A Study of Delay Differential Equations with Applications to Machine Tool Vibrations

Pankaj Wahi

Thesis submitted for the degree of
Doctor of Philosophy
in the Faculty of Engineering
September 2005

Abstract

This thesis addresses several related problems involving delay differential equations (DDEs). DDEs appear in manufacturing processes including machine tool vibrations, robotics, controls, acoustics, traffic dynamics, optics, chemical kinetics, biology, ecology, economics and other areas.

The thesis considers five different problems. The first two problems are mathematical in nature and deal with asymptotic calculations pertaining to DDEs. The third problem involves obtaining some general finite-dimensional ODE approximations for DDEs. The last two problems involve machine tool vibrations.

In the first problem studied, asymptotic expressions are obtained for the large characteristic roots of several delayed systems including first and second order DDEs with single delays, and/or distributed as well as multiple incommensurate delays. An example considering coefficients of disparate magnitude is also analyzed using an alternative asymptotic strategy. These large root asymptotics are complemented with calculations using Padé approximants to find all the roots of these systems.

In the second problem studied, the method of averaging has been used to study strongly nonlinear conservative oscillators perturbed by delayed and/or fractional derivative terms. Fractional derivatives incorporate distributed delayed effect over a time-varying interval. Interesting dynamics is uncovered in the strongly nonlinear case with small delayed terms, where arbitrarily many stable and unstable limit cycles can coexist, and infinitely many simultaneous saddle-node bifurcations can occur (in the asymptotic limit).

In the third problem studied in the thesis, a Galerkin projection technique is presented by which finite-dimensional ODE approximations for DDEs can be obtained in a straightforward fashion. The technique requires neither the system to be near a bifurcation point, nor the delayed terms to have any specific restrictive form, nor even the delay, nonlinearities and/or forcing to be small. An improvement and extension of this technique to higher order DDEs and systems of DDEs is also presented. A detailed numerical convergence analysis of these finite-dimensional projections is performed by approximating the first several characteristic roots of linear DDEs. The order of convergence observed for the Galerkin projection techniques is 2 for large N (i.e., error is proportional to N^{-2}), where N is the dimension of the approximation. Other numerical studies, involving bifurcation diagrams for nonlinear DDEs, show that the qualitative dynamics of the DDEs can be captured satisfactorily with a modest number of shape functions in the Galerkin projection.

In the fourth problem studied, a practical application is considered. A study of a well known regenerative machine tool vibration model near a codimension 2 Hopf bifurcation point is conducted using the method of multiple scales. New analytical expressions are obtained for the double Hopf points. Both sub- and supercritical bifurcations are predicted to occur near the reference point; and analytical conditions on the parameter variations for each type of bifurcation to occur are obtained as well.

Finally, a preliminary study of self-interrupted regenerative turning is performed in the last part of this thesis. To facilitate the analysis, a new approach is proposed to model the regenerative effect in metal cutting. This model automatically incorporates the multiple-regenerative effect accompanying the self-interrupted cutting. Some lower dimensional ODE approximations are obtained for this model using Galerkin projections. Using these ODE approximations, a bifurcation diagram of the regenerative turning process is obtained. It is found that the unstable branch resulting from the subcritical Hopf bifurcation meets the stable branch resulting from the self-interrupted dynamics in a turning point bifurcation. A rough analytical estimate of the turning point tool displacement is also obtained. This estimate helps to identify regions in the space of cutting parameters where loss of stability leads to much greater amplitude self-interrupted motions than in some other regions. Multiple stable periodic solutions and quasiperiodic solutions are observed in some parameter regimes.

The tools developed in this thesis should be useful for people studying delay differential equations, especially focusing on machine tool vibrations. The contents of this thesis may, however, be interesting to a broader audience in the field of nonlinear dynamics.

Acknowledgment

I thank my advisor Dr. Anindya Chatterjee for having guided me throughout this work. He introduced me to the problems studied in this thesis and gave ideas to solve them. I have learnt much in life from him. He has influenced every aspect of my life ranging from the philosophy of life to the philosophy of research. This whole work has been completed only due to his constant encouragement, deep involvement, and above all, his faith in me.

I am ever indebted to my grandparents, parents, uncles, aunts, brothers and sisters, without whose encouragement it would not have been possible for me to take such a big step as pursuing a PhD. They have always shown full faith in me and backed me in all my decisions, even if it required sacrifices on their part. It is their faith in me which gives me the strength to overcome difficulties and the confidence to undertake challenging tasks.

I thank Dr. Tamás Kalmár-Nagy and Prof. Gábor Stépán for discussions influencing portions of this thesis.

I also thank all my professors and teachers for the good training and the precious knowledge that they have imparted to me. They have provided me with the platform from where I can launch my research career.

Next, I thank the *Dynamics Lab* members for providing an excellent environment for working. The healthy discussions, both technical and non-technical, that we have had among ourselves have helped me mature in life. The numerous sleepless nights spent together in the lab debating and discussing various subjects, and the uncountable *Tea Board* visits to restore our energy are unforgettable. I thank all my lab members, Sovan, Satwinder, Srikanth, Mohit, Nandakumar, Jitpal, Amol, Pradipta, Sandeep, Vamshi, Umesh and Pradeep, from whom I have learnt a lot in life. I also thank Prabhu, Vivek, and Venkatesh who served as project assistants in the *Dynamics Lab* for their help.

I enjoyed the company of numerous friends in IISc who made my stay in IISc a new experience altogether and have helped me grow in one way or another. I will remember them throughout my life. I thank them all, especially Sai, Pandey, Sundeep, Munish and Palekar for giving me new insights into research and life.

I express my sincere thanks to the Marie-Curie Actions wing of the European Commission and the Institute for Technical Acoustics, Technical University of Berlin, Germany for selecting me as a Marie-Curie fellow in the European Doctorate in Sound and Vibration Studies program and giving me an opportunity to enrich my research experience.

I thank the Department of Science and Technology (DST) for supporting this work. I also thank the Council for Scientific and Industrial Research (CSIR) for providing financial support for attending the ASME international conference held at Chicago, Illinois, USA in September 2003. I thank the Indian Institute of Science and the Government of India for giving me the opportunity to carry out this research work.

Lastly, I express my sincere thanks to each and every person who has directly or indirectly helped me in reaching this milestone in my life.

Contents

Chapter 1

Introduction

This thesis presents a study of delayed dynamical systems.

The study is motivated by the dynamics of regenerative machine tool vibrations in metal cutting which is modeled as a delayed dynamical system [1-25]. In the literature, the establishment of the regenerative effect as the most important source of tool vibrations has been attributed to Tlusty *et al.* [1], Tobias [2], and Kudinov [3]. The regenerative effect arises from the variation in the chip thickness due to a wavy workpiece surface generated by a vibrating tool during its last pass; the mathematical models involved are delay differential equations (DDEs).

Delayed dynamical systems also appear in many other areas of science and engineering. Delays appear in robotic applications, either through information delay in telemanipulation or through delay in the feedback control [26-30]. Time-delayed feedback control has been used to control complex chaotic systems [31-34]. Surface acoustic wave sensors have been modeled using DDEs [35, 36]. DDEs have also been found useful in an alternative approach to model musical instruments [37-39]. In particular, Barjau and Giblet [39] have provided a comprehensive list of the various useful DDEs for woodwind-like and string instruments considering various losses in the system. Hu and Eberhard [40] have used time delayed systems for modeling wave propagation in longitudinal impacts. Delay differential equations have been used in modeling traffic dynamics [41, 42]. In chemical kinetics, DDEs have been used to account for the reaction time and the time taken for mixing of the reactants [43-46]. Delays have been found to be useful in laser dynamics [47-49]. Neural networks accounting for the delay in the interaction between neurons have appeared in the literature [50, 51]. Apart from these engineering applications, delayed dynamical systems have also been found useful in modeling biological systems [52-55], population dynamics [56] and economic cycles [57].

The contribution of this thesis may be divided roughly into three parts. We present asymptotic calculations pertaining to some mathematical aspects of DDEs; some general finite dimensional ODE approximations for DDEs which could be useful in many of the application areas listed above; and finally a study of some aspects of regenerative machine tool vibrations. In this thesis, we have only considered simple turning processes giving rise to constant coefficient DDEs (as opposed to, say, milling which results in a DDE with periodic coefficients).

In the next section, we briefly provide some background material and models related to metal cutting.

1.1 A SDOF model of machine tool vibrations

A schematic of the turning process in 3-D, and a 2-D projection of the same on the $x-y$ plane, are shown in Figure 1.1.

The tool travels along the negative x-axis with a constant nominal feed rate of C_0 (length units/revolution). The workpiece rotates about the x-axis with a constant angular velocity of $\bar{\Omega}$ radians/time unit. The chip width w is the depth of cut in this cutting process, and is along the negative z-axis. The tool and tool-holder assembly is approximated by a single degree of freedom spring-mass-damper system in the x direction with coefficients k, m and c, respectively. Let the instantaneous chip thickness be denoted by $C(t)$. The equation of motion for the tool is usually given as (e.g., see [8, 12, 14])

$$m\,\ddot{x}(t) + c\,\dot{x}(t) + k\,x(t) = F_x(C(t))\,. \tag{1.1}$$

Alternately, we can write

$$\ddot{x}(t) + 2\,\zeta\,\omega_n\,\dot{x}(t) + \omega_n^2\,x(t) = \frac{F_x(C(t))}{m}\,, \tag{1.2}$$

where $\omega_n = \sqrt{\dfrac{k}{m}}$ is the natural angular frequency of the tool and $\zeta = \dfrac{c}{2\sqrt{m\,k}}$ is the damping ratio. We now

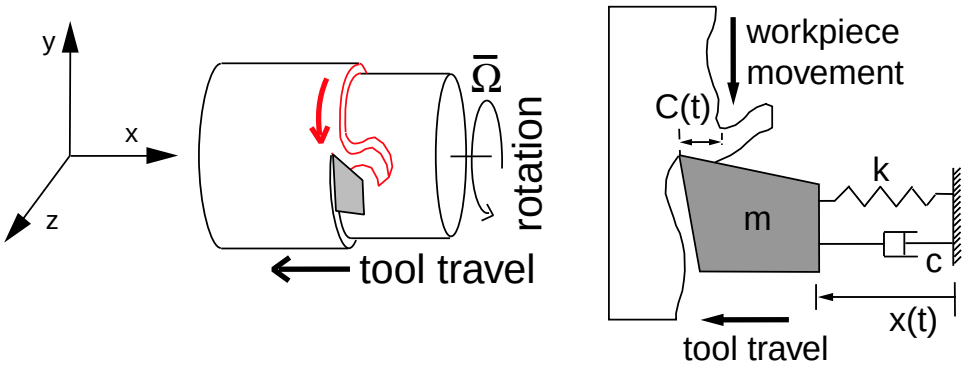

Figure 1.1: A simple single degree of freedom model for tool vibrations.

scale time as $\bar{t} = \omega_n\, t$ (and drop the bar for notational convenience) to obtain

$$\ddot{x}(t) + 2\,\zeta\,\dot{x}(t) + x(t) = \frac{F_x(C(t))}{m\,\omega_n^2}\,. \tag{1.3}$$

In this scaled time, the constant angular velocity of the workpiece is $\Omega = \dfrac{\bar{\Omega}}{\omega_n}$. Also the tool velocity in the x-direction in this scaled time is given by $v = -\dfrac{C_0\,\Omega}{2\pi}$.

Note that the mechanics of cutting is a big field in itself and a number of complicated slip-line field treatments have been proposed in recent times (see, for example, [58, 59] and references therein) to obtain the cutting force as a function of the cutting parameters. However, for people interested in machine tool vibration, a simple and empirical way to obtain the cutting force is from an approximate curve fit to experimental data (see, for example, [7, 20]). Shi and Tobias [7] obtained a third-order polynomial with a negative second-order term suggesting a power law with exponent less than 1, while Kalmár-Nagy *et al.* [20] obtained a power law fit with exponent 0.41. In this thesis, we use the power law model of Taylor [60], also used by Kalmár-Nagy *et al.* [12], given by

$$F_x(C(t)) = K\,w\,C(t)^{3/4}\,,$$

where w is the chip width and K incorporates the dependence on other cutting parameters like cutting velocity, nominal feed, tool geometry etc., all assumed constant for our analyses. Substituting the above expression for $F_x(C(t))$ in Eq. (1.3), we get

$$\ddot{x}(t) + 2\,\zeta\,\dot{x}(t) + x(t) = P C(t)^{3/4}\,, \tag{1.4}$$

where $P = \dfrac{K\,w}{m\,\omega_n^2}$. Equation (1.4) provides the basic model for the tool-workpiece dynamics. In this model, the chip thickness is determined by the tool-workpiece dynamics, and vice versa. The instantaneous chip thickness $C(t)$ is usually given by

$$C(t) = C_0 + x(t-\tau) - x(t)\,, \tag{1.5}$$

where $\tau = 2\pi/\Omega$ is the time period of one revolution (for example, see [12])[1]. Equations (1.4) and (1.5) result in the following delay differential equation (DDE)

$$\ddot{x}(t) + 2\,\zeta\,\dot{x}(t) + x(t) = P\,(C_0 + x(t-\tau) - x(t))^{3/4}\,. \tag{1.6}$$

In chapter 7, we will present an alternative to Eq. (1.5), suitable for self-interrupted cutting. Equation (1.6) is linearized about the constant solution $x(t) \equiv P C_0^{3/4}$ to perform a stability analysis by Kalmár-Nagy *et al.* [12]. This linear stability analysis gives the parameter values for stable steady cutting. In addition, Kalmár-Nagy *et al.* [12] have analytically proven the existence of subcritical instability for Eq. (1.6), which here means that unstable periodic motion exists near the nominally stable cutting; and some stable vibratory motions exist far away as well. Such motions were observed experimentally by Hanna and Tobias [4], and Shi and Tobias [7].

[1] Note that the expression used here actually corresponds to the width of cut which can be different from the actual thickness of the chip material coming out. Though the term chip thickness in manufacturing terminology does not refer to the width of cut, it is common in the machine tool vibration community to use chip thickness to refer to the width of cut. In this thesis, we would stick to the latter nomenclature, and hence use chip thickness and width of cut interchangeably.

At this point, we would like to note that there are various other physical mechanisms giving rise to machine tool vibrations as well. The most notable among them are the temperature and velocity dependent friction between the tool and the chip-workpiece contact surfaces [61-64], and the thermoplastic behavior of the chip wherein the shear stress varies in the plastic deformation zone [61, 65, 66]. This thesis, however, focuses on delay differential equations and applications to tool vibrations arising due to the regenerative effect.

In the next section, we briefly present a more general linear delayed model for machine tool vibration proposed by Stépán, which gives better correspondence with observed stability behavior [8].

1.2 A more general model proposed by Stépán

In this more general delayed model, two qualitatively different delays are introduced. The first one is a "long" discrete time delay $\tau = \dfrac{2\pi}{\Omega}$, where Ω is the speed of workpiece rotation in rad/sec. This is the time period of one revolution. The second one is a "short" continuous delay $h = \dfrac{2L}{\Omega D}$, where L is the length of the tool-chip contact region and D is the diameter of the workpiece. This is the time during which the tool and the chip are in contact.

The linear model of regenerative machine tool vibration in the x-direction, considering both the long discrete and the short continuous delays, is given by Stépán [8] as

$$\ddot{x}(t) + 2\,\psi\,\omega_n\,\dot{x}(t) + \omega_n^2\,x(t) + \frac{k_1}{m}\int_{-h}^{0} W(\theta)\,x(t+\theta)\,d\theta - \frac{k_1}{m}\int_{-\tau-h}^{-\tau} W(\tau_1+\theta)\,x(t+\theta)\,d\theta = 0\,, \tag{1.7}$$

where $\omega_n = \sqrt{\dfrac{k}{m}}$ is the natural angular frequency of the tool, $\psi = \dfrac{c}{2\sqrt{m\,k}}$ is the damping ratio, k_1 is the slope of the F_x versus $C(t)$ curve[2] at $C(t) = C_0$, and $W(\theta)$ with $\theta \in [-h, 0]$, represents the traction distribution function over the tool-chip contact region.

When $W(\theta) = \delta(\theta)$, there is only the long discrete delay τ, and on suitable rescaling of time, Stépán obtains

$$\ddot{x}(t) + 2\,\psi\,\dot{x}(t) + (1+p)\,x(t) - p\,x(t-\tau_1) = 0\,, \tag{1.8}$$

where $p = \dfrac{k_1}{m\,\omega_n^2}$, and $\tau_1 = \omega_n\,\tau$. Equation (1.8) is also derived in [12]. If $\tau_1 = 1$, for simplicity, we have

$$\ddot{x} + 2\psi\dot{x} + (1+p)\,x - p\,x(t-1) = 0\,. \tag{1.9}$$

We will study the characteristic roots of Eq. (1.9) in detail in section 2.3 of chapter 2.

When $W(\theta) \neq \delta(\theta)$ in Eq. (1.7), we have an integro-DDE which represents a distributed delay effect. If $W(\theta)$ is approximated by more than one Dirac-delta function, e.g., $W(\theta) = \delta(\theta) + \delta(\theta + h)$, we get a delayed system with multiple delays which could be incommensurate. Note that systems with incommensurate delays are not amenable to analysis using Pontryagin's criteria [67] (see also [68]). But we will consider such systems in our analysis in the next chapter. Note that incommensurate delays can also arise in other applications, e.g., a system where a microphone picks up signals from two unequally distant speakers and gives it as a feedback to the amplifier driving them.

1.3 Layout of the thesis

Chapters 2 and 3 deal with asymptotic calculations for some DDEs. In chapter 2, we have developed asymptotic expressions for the large characteristic roots of some linear constant coefficient DDEs which in combination with a few roots using Padé approximants give us all the characteristic roots. Material from this chapter has been published in [69]. Some earlier results were also presented at [70] and [71]. In chapter 3, we study strongly nonlinear conservative oscillators perturbed by delayed and/or fractional derivative terms. Material from this chapter has been published in [72].

Chapters 4 and 5 constitute the second part of the thesis. In chapter 4, we present a novel Galerkin projection technique to obtain finite-dimensional ODE approximations for DDEs in a straightforward fashion. The technique requires neither the system to be near a bifurcation point, nor the delayed terms to have any specific restrictive form, nor even the delay, nonlinearities and/or forcing to be small. This work has been published in [73] and was also presented at [74]. In chapter 5, the Galerkin projection technique has been

[2]Here $C(t)$ is the chip thickness as before, and F_x is the x-component of the cutting force.

improved and extended to higher order DDEs and systems of DDEs. A detailed numerical convergence analysis of these Galerkin projection techniques is also presented. Material from this chapter has been presented at [75].

Chapters 6 and 7 deal with studies of regenerative machine tool vibrations. In chapter 6, a well known regenerative machine tool vibration model (a delay differential equation) is studied near a codimension 2 Hopf bifurcation point. Material from this chapter has been published in [76] and was also presented at [77]. In chapter 7, a study of the *self-interrupted* turning process is presented.

Finally, some concluding discussion is presented in chapter 8.

Chapter 2

Characteristic roots of delayed systems

In this chapter, we find *all* the characteristic roots of some linear constant coefficient delay differential equations (DDEs). These DDEs are infinite-dimensional systems and have transcendental characteristic equations with infinitely many characteristic roots. In this chapter, we develop asymptotics for the large roots of some DDEs. The material of this chapter has been published in [69] and was presented in [70] and [71].

2.1 Introduction

The simplest linear DDEs have constant coefficients, as in

$$\dot{x}(t) = \alpha x(t) + \beta x(t-\Delta)\,, \tag{2.1}$$

where $\Delta > 0$. The solution of Eq. (2.1) is a sum of terms of the form $e^{\lambda t}$, [56, 68, 78, 79, 80], where λ satisfies

$$\lambda = \alpha + \beta e^{-\lambda\Delta}\,.$$

This equation determines the infinitely many *characteristic roots* of the DDE, impossible to find in closed form. If all these roots have negative real parts, then all solutions decay to zero and the system is stable. A root with a positive real part implies an exponentially growing solution (system unstable).

The study of linear constant coefficient DDEs is important since analysis of general nonlinear DDEs often begins with a preliminary study of the *linearized* DDE (e.g., [12]). Analysts often seek conditions under which the system is stable. This search is nontrivial because there are infinitely many characteristic roots not obtainable in closed form. Significant stability results have, nevertheless, been obtained (e.g., sections 1.2 and 1.4 in [56], Theorems $4.1-4.3$ in section 11.4, Theorems $5.1-5.3$ in section 11.5 in [68], chapter 10 in [78] and chapter 2 in [80], etc.; see also [81, 82]). The above references contain results pertaining to either all roots having negative real parts, or specific parameter values for which a pure imaginary pair exists. It is also possible to count the number of roots in the right half of the complex plane [80, 83].

Whether the system is stable or not, it is of further interest to find out *where* the characteristic roots lie. The geometrical distribution of these characteristic roots is important in proving theorems on series expansion and asymptotic behavior of solutions; see Bellman and Cooke [78]. Results in similar directions have also been obtained for specific equations by others (e.g., section 1.4 of [68], section 11.3 of [84]). These theorems show for certain DDEs, e.g., that there are finitely many roots in any vertical or horizontal strip in the complex plane.

Numerical algorithms for finding the characteristic roots of linear constant coefficient DDEs have been given in [85, 86]. However, they are computationally efficient for finding the first few roots only. Sandquist and Rogers [87] have sought the characteristic roots for scalar linear first order DDEs; they consider a single delay, and graphically determine the roots of a transcendental equation in one variable.

As mentioned above, in this chapter we aim to determine *all* the roots of some linear constant coefficient DDEs. Our approach is based on asymptotic calculations for the *large* roots, a Padé approximant for a small number of roots that are not large, and numerics (the Newton-Raphson method) to refine these roots. Alternative asymptotics are also used for the not very large roots of a DDE involving coefficients of disparate magnitude.

It may be noted that Bellman and Cooke [78] have obtained leading order asymptotics for characteristic roots of a class of DDEs with multiple commensurate delays. In contrast, here we find correction terms in the expansions, giving very accurate estimates. Moreover, incommensurate delays are included in our study. Finally, DDEs with coefficients of disparate magnitude are considered as well.

This chapter is organized as follows. Sections 2.2 through 2.5 concentrate on the large roots of four different DDEs of increasing levels of difficulty including first and second order DDEs with single and/or multiple

incommensurate and/or distributed delays. Sections 2.2 and 2.3 consider simpler first and second order cases. In section 2.4, we consider a first order DDE with multiple incommensurate and distributed delays. The last example is that of a DDE with multiple incommensurate delays with coefficients of disparate magnitude studied in section 2.5. Some concluding remarks are made in section 2.6.

2.2 A preliminary example

We begin with the equation (e.g., [68, 56])

$$\dot{x} + a\,x(t-1) = 0\,. \tag{2.2}$$

Assuming $x(t) = C\,e^{\lambda\,t}$ as usual, we obtain

$$\lambda + a\,e^{-\lambda} = 0 \tag{2.3}$$

Letting $\lambda = \alpha + i\,\beta$ and separating real and imaginary parts, we obtain

$$\alpha + a\,e^{-\alpha}\cos\beta = 0\,, \tag{2.4}$$

$$\beta - a\,e^{-\alpha}\sin\beta = 0\,. \tag{2.5}$$

We assume a is nonzero and $\mathcal{O}(1)$ compared to $|\lambda|$, and that $\beta \geq 0$ ($-\beta$ gives another solution).

Proposition 1 *In the large roots of Eq. (2.3), $\alpha < 0$ and $\alpha = \mathcal{O}(\ln\beta)$.*

Proof If, in the large roots, α is not large (i.e., is bounded or $\mathcal{O}(1)$) then Eq. (2.5) gives the contradiction $\beta = \mathcal{O}(1)$. If α is large and positive, then Eq. (2.4) gives the contradictory $\alpha = o(1)$. Therefore, α is large and *negative*. Then Eq. (2.4) implies, in the asymptotic limit, that $\cos\beta = 0$, which gives $\sin\beta = \pm 1$. By Eq. (2.5) we can show that, for integer $N \gg 1$,

$$\alpha \sim -\ln\left(\frac{\beta}{|a|}\right) \quad \text{and} \quad \beta \sim \left(2N + \frac{\mathrm{sgn}(a)}{2}\right)\pi\,. \quad \bullet$$

Roots found numerically by the Newton-Raphson method, along with the asymptotic approximations themselves, agree well in Fig. 2.1.

2.3 A second order DDE

We now consider the equation derived in chapter 1,

$$\ddot{x}(t) + 2\,\psi\,\dot{x}(t) + (1+p)\,x(t) - p\,x(t-1) = 0\,, \tag{2.6}$$

For this equation, for small p, all characteristic roots lie in the left half plane[12]. Here, we develop large-root asymptotics for p nonzero and finite. Note that second order delayed systems have long been of interest due to mechanical applications [81, 82, 88].

In Eq. (1.9), we let $x = C\,e^{\lambda t}$, set $\lambda = \alpha + i\,\beta$, and separate real and imaginary parts to get

$$\alpha^2 - \beta^2 + 2\,\psi\,\alpha + 1 + p - p\,e^{-\alpha}\cos\beta = 0\,, \tag{2.7}$$

$$2\,\alpha\,\beta + 2\,\psi\,\beta + p\,e^{-\alpha}\sin\beta = 0\,. \tag{2.8}$$

We now eliminate large regions of the complex plane from our consideration. We divide the upper half plane qualitatively into the regions shown in Fig. 2.2, and investigate them one by one. The lower half plane is symmetrical, hence excluded. We will eliminate regions *not* containing any roots. In the shaded area roots are not large, and our asymptotics do not hold.

Proposition 2 *For Eq. (2.6), large roots have large α and occur only in the left half of region 3, Fig. 2.2.*

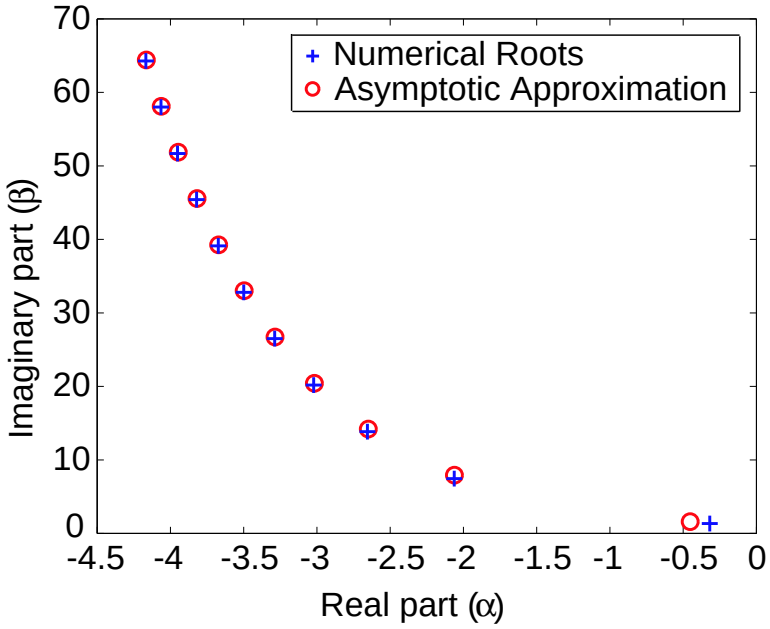

Figure 2.1: Roots of Eq. (2.3) for $a = 1$.

Proof If α is $\mathcal{O}(1)$ in the large roots, it leaves an unbalanced β^2 in Eq. (2.7). So α is large.

First consider regions 1 and 2, as well as the right half of region 3. Since $\alpha > 0$ here, $0 < e^{-\alpha} < 1$. In Eq. (2.7), since large α means $\alpha^2 \gg \alpha$, we balance the two largest terms to get $\alpha^2 \sim \beta^2$. Using this in Eq. (2.8), we find nothing can balance the large term $2\alpha\beta$.

Next, consider regions 4 and 5. Here, $e^{-\alpha}$ is exponentially large compared to both α and β as well as algebraic powers thereof. Equations (2.7) and (2.8) then lead to the contradictory

$$\cos^2\beta + \sin^2\beta \ll 1.$$

By elimination, only the left half of region 3 contains large roots. •

Proposition 3 *Equations (2.7) and (2.8) are satisfied by* $\alpha = -2\ln\beta + \ln|p| + o(1)$ *and* $\beta = \left(2N + \dfrac{1+sgn(p)}{2}\right)\pi + o(1)$, *for integer* $N \gg 1$.

Proof By proposition 2, $\beta \gg |\alpha| \gg 1$ for the large roots. We substitute $\alpha = \mu\ln\beta + z$ in Eqs. (2.7) and (2.8), with the assumption that $|z| \ll \ln\beta$, to get

$$\mu^2(\ln\beta)^2 + 2\mu(z+\psi)\ln\beta + z^2 - \beta^2 + 2\psi z + 1 + p - p\,\beta^{-\mu}e^{-z}\cos\beta = 0\,, \tag{2.9}$$

$$2\mu\beta\ln\beta + 2z\beta + 2\psi\beta + p\,\beta^{-\mu}e^{-z}\sin\beta = 0\,. \tag{2.10}$$

In Eq. (2.9), β^2 is asymptotically bigger than all other terms (including $\mu^2(\ln\beta)^2 \sim \alpha^2$) except possibly $p\,\beta^{-\mu}\,e^{-z}\cos\beta$, so these two terms must balance each other. Note, $p \neq 0$. This gives

$$\beta^{-\mu}\,e^{-z}\cos(\beta) = \mathcal{O}\left(\beta^2\right)\,. \tag{2.11}$$

Taking absolute values and then logarithms,

$$-\mu\ln\beta + \ln|\cos\beta| \sim 2\ln\beta\,,$$

where we have dropped z since it is smaller than $\ln\beta$.

In the above, we could conceivably have $0 < |\cos\beta| \ll 1$, and in fact small enough that $\ln|\cos\beta| = \mathcal{O}(\ln\beta)$. This, however, requires $\beta^{-\mu}e^{-z} \gg \beta^2$ which leaves a large term $\beta^{-\mu}e^{-z}\sin\beta$ (with $\sin\beta \sim \pm 1$) unbalanced in Eq. (2.10). Therefore, to balance terms, we must let $\mu = -2$. Then Eqs. (2.9) and (2.10), on dividing by β^2 and dropping smaller terms, give

$$p\,e^{-z}\,\cos\beta \sim -1, \tag{2.12}$$

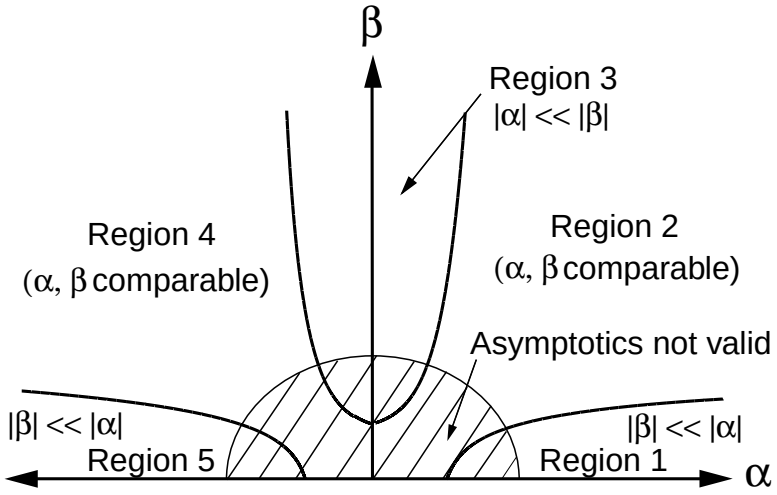

Figure 2.2: Regions considered in the complex plane.

$$p\,e^{-z}\,\sin\beta = o(1) \tag{2.13}$$

Since $pe^{-z} = 0$ violates Eq. (2.12), we must have $\sin\beta = o(1)$ from Eq. (2.13), whence $\cos\beta \sim \pm 1$. Consequently, $pe^{-z} \sim \mp 1$. The result follows. •

We can now develop formal series as follows (assuming $p > 0$; the other case is analogous). Having balanced β^2 terms, we still retain $\mathcal{O}(\beta)$ terms, which are relatively smaller by a factor of $\mathcal{O}(1/N)$. Accordingly, we write (note the slightly different form for α, now dependent explicitly on N):

$$\beta \;=\; (2N+1)\pi \;+\; \frac{\beta_1}{N} \;+\; \frac{\beta_2}{N^2} + \cdots \tag{2.14}$$

$$\alpha \;=\; -2\ln[(2N+1)\pi] \;+\; \ln p \;+\; \frac{\alpha_1}{N} \;+\; \frac{\alpha_2}{N^2} + \cdots \tag{2.15}$$

Substituting into Eqs. (2.9) and (2.10), expanding in series, collecting terms (using MAPLE), and solving for the unknown coefficients, we obtain:

$$\begin{aligned}
\beta_1 \;&=\; -\frac{2\ln(2N\pi) \;-\; \psi \;-\; \ln p}{\pi}\,,\\
\beta_2 \;&=\; \frac{2\ln(2N\pi) - \psi - \ln p - 2}{2\pi}\,,\\
\alpha_1 \;&=\; 0\,,\\
\alpha_2 \;&=\; -\frac{1}{4\pi^2}\,(-1 + 8\ln\pi\ln N + 8\ln\pi\ln 2 + 8\ln 2\ln N - 4\ln(2N\pi)\ln p\\
&\qquad\qquad - 4\psi\ln(2N\pi) + 2\ln p + 2\psi\ln p + 2\psi^2 \;-\; p \;+\; 4\psi)\,.
\end{aligned}$$

While collecting terms above, we have treated $\ln N$ as $\mathcal{O}(1)$ compared to N.

The above approximations agree well with roots obtained using Newton-Raphson; see Fig. 2.3. There are just three relatively small roots (one real, one complex pair) not captured by the asymptotics; those are not plotted here.

2.4 A DDE with multiple and distributed delays

Consider

$$\dot{x}(t) + a_1\,x(t) + a_2\,x(t - 1/\sqrt{2}) + a_3\,x(t-1) + a_4\int_0^1 x(t-s)\cos s\,ds = 0\,, \tag{2.16}$$

with $a_3 \neq 0$. The characteristic equation is (we multiply by $\lambda^2 + 1$ to simplify the expression, but introduce spurious roots at $\lambda = \pm i$ which we ignore)

$$-a_4\,e^{(-\lambda)}\,\lambda\,\cos(1) + a_4\,e^{(-\lambda)}\,\sin(1) + a_4\,\lambda + a_3\,e^{(-\lambda)}\,\lambda^2 + a_2\,e^{(-\lambda)} + a_2\,e^{(-\lambda/\sqrt{2})}\,\lambda^2$$

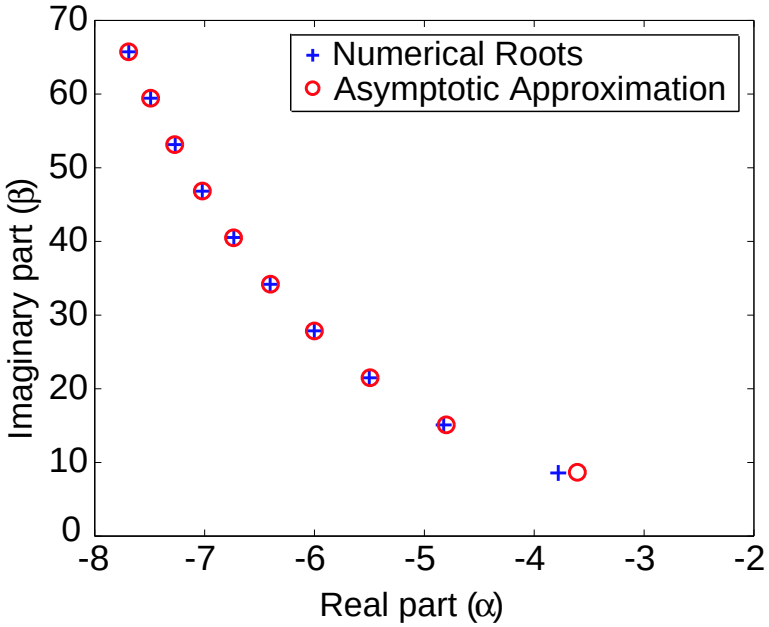

Figure 2.3: Roots of Eq. (2.6) with $\psi = 0.1$ and $p = 2$.

$$+ a_2\, e^{(-\lambda/\sqrt{2})} + a_1\,\lambda^2 + a_1 + \lambda^3 + \lambda = 0\,.$$

Substituting $\lambda = \alpha + i\,\beta$ and separating real and imaginary parts, we get

$$\begin{aligned}
&-a_4\, e^{-\alpha}\,\alpha\,\cos 1\,\cos\beta - a_4\, e^{-\alpha}\,\beta\,\cos 1\,\sin\beta + a_4\, e^{-\alpha}\,\sin 1\,\cos\beta + a_4\,\alpha - a_3\, e^{-\alpha}\,\beta^2\,\cos\beta \\
&+2\,a_3\, e^{-\alpha}\,\alpha\,\beta\,\sin\beta + a_3\, e^{-\alpha}\,\alpha^2\,\cos\beta + a_3\, e^{-\alpha}\,\cos\beta + 2\,a_2\, e^{-\alpha/\sqrt{2}}\,\alpha\,\beta\,\sin(\beta/\sqrt{2}) \\
&+a_2\, e^{-\alpha/\sqrt{2}}\,\alpha^2\,\cos(\beta/\sqrt{2}) - a_2\, e^{-\alpha/\sqrt{2}}\,\beta^2\,\cos(\beta/\sqrt{2}) + a_2\, e^{-\alpha/\sqrt{2}}\,\cos(\beta/\sqrt{2}) \\
&+ a_1\,\alpha^2 - a_1\,\beta^2 + a_1 + \alpha^3 - 3\,\alpha\,\beta^2 + \alpha = 0\,, \qquad (2.17)
\end{aligned}$$

$$\begin{aligned}
&a_4\, e^{-\alpha}\,\alpha\,\cos 1\,\sin\beta - a_4\, e^{-\alpha}\,\beta\,\cos 1\,\cos\beta - a_4\, e^{-\alpha}\,\sin 1\,\sin\beta + a_4\,\beta - a_3\, e^{-\alpha}\,\alpha^2\,\sin\beta \\
&+2\,a_3\, e^{-\alpha}\,\alpha\,\beta\,\cos\beta + a_3\, e^{-\alpha}\,\beta^2\,\sin\beta - a_3\, e^{-\alpha}\,\sin\beta + 2\,a_2\, e^{-\alpha/\sqrt{2}}\,\alpha\,\beta\,\cos(\beta/\sqrt{2}) \\
&-a_2\, e^{-\alpha/\sqrt{2}}\,\alpha^2\,\sin(\beta/\sqrt{2}) + a_2\, e^{-\alpha/\sqrt{2}}\,\beta^2\,\sin(\beta/\sqrt{2}) - a_2\, e^{-\alpha/\sqrt{2}}\,\sin(\beta/\sqrt{2}) \\
&+ 2\,a_1\,\alpha\,\beta + 3\,\alpha^2\,\beta - \beta^3 + \beta = 0\,. \qquad (2.18)
\end{aligned}$$

We again eliminate regions of the complex plane from consideration.

Lemma 1 *In that portion of region 3 where $\beta \gg |\alpha| \gg 1$, Eqs. (2.17) and (2.18) simplify to*

$$\begin{aligned}
&2a_3 e^{-\alpha}\alpha\beta\sin\beta - a_3 e^{-\alpha}\beta^2\cos\beta + 2a_2 e^{-\alpha/\sqrt{2}}\,\alpha\beta\sin(\beta/\sqrt{2}) \\
&\qquad - a_2 e^{-\alpha/\sqrt{2}}\beta^2\cos(\beta/\sqrt{2}) - 3\alpha\beta^2 = \mathrm{DST}\,, \qquad (2.19)
\end{aligned}$$

and

$$\begin{aligned}
&2a_3 e^{-\alpha}\alpha\beta\cos\beta + a_3 e^{-\alpha}\beta^2\sin\beta + 2a_2 e^{-\alpha/\sqrt{2}}\alpha\beta\cos(\beta/\sqrt{2}) \\
&\qquad + a_2 e^{-\alpha/\sqrt{2}}\beta^2\sin(\beta/\sqrt{2}) - \beta^3 = \mathrm{DST}\,, \qquad (2.20)
\end{aligned}$$

where DST *stands for "demonstrably smaller terms".*

Proof Consider first the coefficients of $e^{-\alpha}\cos\beta$ among the terms appearing in Eq. (2.17), i.e.,

$$-a_4\alpha\cos 1, \quad a_4\sin 1, \quad -a_3\beta^2, \quad a_3\alpha^2 \quad \text{and} \quad a_3.$$

The largest of these is $-a_3\beta^2$, so we drop the other four. Similarly, of the two terms containing $e^{-\alpha}\sin\beta$, one is dropped; among terms containing $e^{-\alpha/\sqrt{2}}\cos(\beta/\sqrt{2})$, all but one are dropped; among the rest excluding the term with $e^{-\alpha/\sqrt{2}}\sin(\beta/\sqrt{2})$, only $3\alpha\beta^2$ needs to be retained. Similar simplifications are made for Eq. (2.18) (details omitted). •

Proposition 4 *The large roots of Eqs. (2.17) and (2.18) have large α and lie only in the left half of region 3, Fig. 2.2.*

Proof For large roots, $\alpha = \mathcal{O}(1)$ leaves β^3 unbalanced in Eq. (2.18). So α is large.

We first drop regions 1 and 2 from our consideration, as follows. In these regions, terms containing $e^{-\alpha}$ can be dropped, being smaller than other terms, giving:

$$a_4\,\alpha + a_1\,\alpha^2 - a_1\,\beta^2 + a_1 + \alpha^3 - 3\,\alpha\,\beta^2 + \alpha = o(1)\,, \tag{2.21}$$

$$a_4\,\beta + 2\,a_1\,\alpha\,\beta + 3\,\alpha^2\,\beta - \beta^3 + \beta = o(1)\,. \tag{2.22}$$

In region 1, the largest term α^3 is unbalanced in Eq. (2.21). In region 2, the leading terms in Eqs. (2.21) and (2.22) give $\alpha^3 \sim 3\alpha\beta^2$ and $3\alpha^2\beta \sim \beta^3$, which have no nonzero solutions.

Now we drop the right half of region 3, as follows. By lemma 1, Eqs. (2.19) and (2.20) hold in this region. Since $\alpha > 0$ in the right half, we have $0 < e^{-\alpha} < e^{-\alpha/\sqrt{2}} < 1$. This leaves the largest term β^3 unbalanced in Eq. (2.20).

We next consider regions 4 and 5. Here, $\alpha < 0$ (and large), so $e^{-\alpha} \gg e^{-\alpha/\sqrt{2}}$, which in turn is much greater than both α and β as well as algebraic powers thereof. Hence, retaining only the terms containing $e^{-\alpha}$ in Eqs. (2.17) and (2.18), we get

$$\begin{aligned} &a_4\sin 1\cos\beta - a_4\alpha\cos 1\cos\beta - a_4\beta\cos 1\sin\beta + a_3\alpha^2\cos\beta \\ &\qquad + 2a_3\alpha\beta\sin\beta - a_3\beta^2\cos\beta + a_3\cos\beta = \text{DST}\,, \end{aligned} \tag{2.23}$$

and

$$\begin{aligned} &a_4\alpha\cos 1\sin\beta - a_4\beta\cos 1\cos\beta - a_4\sin 1\sin\beta - a_3\alpha^2\sin\beta \\ &\qquad + 2a_3\alpha\beta\cos\beta + a_3\beta^2\sin\beta - a_3\sin\beta = \text{DST}\,. \end{aligned} \tag{2.24}$$

In region 4, the quadratic terms in α and β dominate in Eqs. (2.23) and (2.24), giving (since $a_3 \neq 0$)

$$-\alpha^2\sin\beta + 2\alpha\beta\cos\beta + \beta^2\sin\beta = \text{DST}\,, \tag{2.25}$$

$$\alpha^2\cos\beta + 2\alpha\beta\sin\beta - \beta^2\cos\beta = \text{DST}\,. \tag{2.26}$$

Multiplying Eq. (2.25) with $\sin\beta$, Eq. (2.26) with $\cos\beta$, and subtracting, we find

$$\beta^2 - \alpha^2 = \text{DST},$$

which means $\beta \sim \alpha$. However, that in turn leads to the contradictory

$$\cos\beta = o(1) \quad \text{and} \quad \sin\beta = o(1), \quad \text{i.e.,} \quad \cos^2\beta + \sin^2\beta \ll 1\,. \tag{2.27}$$

In region 5, α^2 dominates in Eqs. (2.25) and (2.26), giving the same contradiction Eq. (2.27).
Hence, we conclude that asymptotically large roots lie only in the left half of region 3. •

Proposition 5 *Equations (2.17) and (2.18) are satisfied by $\alpha = -\ln\beta + \ln|a_3| + o(1)$ and $\beta = \left(2N + \frac{sgn(a_3)}{2}\right)\pi + o(1)$.*

Proof By proposition 4 and lemma 1, we have the simplified equations, Eqs. (2.19) and (2.20) (reproduced below).

$$\begin{aligned} &2a_3e^{-\alpha}\alpha\beta\sin\beta - a_3e^{-\alpha}\beta^2\cos\beta + 2a_2e^{-\alpha/\sqrt{2}}\alpha\beta\sin(\beta/\sqrt{2}) \\ &\qquad - a_2e^{-\alpha/\sqrt{2}}\beta^2\cos(\beta/\sqrt{2}) - 3\alpha\beta^2 = \text{DST}\,, \end{aligned} \tag{2.28}$$

and

$$2a_3e^{-\alpha}\alpha\beta\cos\beta + a_3e^{-\alpha}\beta^2\sin\beta + 2a_2e^{-\alpha/\sqrt{2}}\alpha\beta\cos(\beta/\sqrt{2}) + a_2e^{-\alpha/\sqrt{2}}\beta^2\sin(\beta/\sqrt{2}) - \beta^3 = \mathrm{DST}\,. \tag{2.29}$$

Here $\alpha < 0$ and $|\alpha| \gg 1$ so that $e^{-\alpha} \gg e^{-\alpha/\sqrt{2}} \gg 1$. In Eq. (2.28), $e^{-\alpha}\beta^2\cos\beta$ is asymptotically larger than any other term unless $\cos\beta = o(1)$, whence $\sin\beta \sim \pm 1$. Using this in Eq. (2.29), the two largest terms have magnitudes $e^{-\alpha}\,\beta^2$ and β^3. This gives

$$a_3e^{-\alpha}\beta^2\sin\beta - \beta^3 = \mathrm{DST}\,.$$

For $a_3 > 0$, we require $\sin\beta \sim 1$ which leads to

$$\beta = (2N + 1/2)\pi + o(1) \qquad \text{and} \qquad \alpha = -\ln\beta + \ln a_3 + o(1)\,, \tag{2.30}$$

while for $a_3 < 0$, we require $\sin\beta \sim -1$ and hence,

$$\beta = (2N - 1/2)\pi + o(1) \qquad \text{and} \qquad \alpha = -\ln\beta + \ln|a_3| + o(1)\,,$$

for large integer N. •

We now find two correction terms in a formal series. The procedure is somewhat more complicated than before.

The second largest terms in Eqs. (2.19) and (2.20) are of $\mathcal{O}(\beta^{-(1-\frac{1}{\sqrt{2}})})$ compared to β^3. This suggests a formal series in powers of $N^{-(1-\frac{1}{\sqrt{2}})}$. However, there are terms of $\mathcal{O}(\beta^{-1})$, $\mathcal{O}(\beta^{-2})$, etc., whose powers are not integer multiples of $1 - \dfrac{1}{\sqrt{2}}$, and so the formal series should have mixed powers of $N^{-(1-\frac{1}{\sqrt{2}})}$ and N^{-1}. We therefore anticipate a series of the form

$$\beta \,=\, (2N+1/2)\pi \,+\, \frac{\beta_1}{N^{(1-\frac{1}{\sqrt{2}})}} \,+\, \frac{\beta_2}{N^{2(1-\frac{1}{\sqrt{2}})}} + \cdots + \frac{\beta_{11}}{N} + \frac{\beta_{12}}{N^2} + \cdots + \text{ mixed powers}\,.$$

Note, however, that the first mixed power is of the form

$$\frac{1}{N^{1-\frac{1}{\sqrt{2}}}} \times \frac{1}{N} \ll \frac{1}{N}\,,$$

and so if we retain only the first two small corrections, then we have the somewhat simpler expression

$$\beta \,=\, (2N+1/2)\pi \,+\, \frac{\beta_1}{N^{(1-\frac{1}{\sqrt{2}})}} \,+\, \frac{\beta_2}{N^{2(1-\frac{1}{\sqrt{2}})}} \,+\, \text{h.o.t.} \tag{2.31}$$

where "h.o.t." stands for higher order terms. Note that $1/\sqrt{2} \approx 0.7$ and so (roughly) $N^{-(1-\frac{1}{\sqrt{2}})} \approx N^{-0.3}$. Similarly, $N^{-2(1-\frac{1}{\sqrt{2}})} \approx N^{-0.6} \gg N^{-1} \gg$ "mixed powers".

For analytical convenience, we take the leading order solution for α as $\alpha = -\ln\beta + z$, where $z \ll \ln\beta$ and express the correction z in a series as

$$z \,=\, \ln(a_3) \,+\, \frac{z_1}{N^{(1-\frac{1}{\sqrt{2}})}} \,+\, \frac{z_2}{N^{2(1-\frac{1}{\sqrt{2}})}} + \text{h.o.t.}\,. \tag{2.32}$$

Substituting α in Eqs. (2.19) and (2.20) and dividing throughout by β^3, we get

$$-1 \,+\, a_3\,e^{-z}\,\sin(\beta) \,+\, a_2\,\sin\left(\frac{\beta}{\sqrt{2}}\right)e^{-z/\sqrt{2}}\,\beta^{-(1-\frac{1}{\sqrt{2}})} + \mathcal{O}\left(\frac{\ln\beta}{\beta}\right) = 0\,, \tag{2.33}$$

$$a_3\,e^{-z}\,\cos(\beta) \,+\, a_2\,\cos\left(\frac{\beta}{\sqrt{2}}\right)e^{-z/\sqrt{2}}\,\beta^{-(1-\frac{1}{\sqrt{2}})} + \mathcal{O}\left(\frac{\ln\beta}{\beta}\right) = 0\,. \tag{2.34}$$

Substituting Eqs. (2.31) and (2.32) in Eqs. (2.33) and (2.34), followed by expanding and collecting terms finally gives[1]

$$\beta_1 \,=\, 2^{\frac{-2+\sqrt{2}}{2}}\,\pi^{\frac{-2+\sqrt{2}}{2}}\,a_2\,a_3^{-\frac{1}{\sqrt{2}}}\,\cos\left(\frac{(4N+1)}{2\sqrt{2}}\pi\right),$$

[1] Our calculations were done using MAPLE 6 (Windows), which, for these irrational powers, needs a little patience. We found it useful to do the expansion one term at a time. For each term, we divided by the (known) largest surviving power of N, and then asked for the limit as $N \to \infty$.

$$\beta_2 = \frac{1}{8\pi^2}\left(2^{\sqrt{2}}\pi^{\sqrt{2}}\, a_2^2\, a_3^{-\sqrt{2}}\, \left(1-\sqrt{2}\right)\sin\left(\frac{(4N+1)}{\sqrt{2}}\pi\right)\right),$$

$$z_1 = 2^{\frac{-2+\sqrt{2}}{2}}\,\pi^{\frac{-2+\sqrt{2}}{2}}\, a_2\, a_3^{-\frac{1}{\sqrt{2}}}\, \sin\left(\frac{(4N+1)}{2\sqrt{2}}\pi\right),$$

$$z_2 = -\frac{1}{8\pi^2}\left(2^{\sqrt{2}}\,\pi^{\sqrt{2}}\, a_2^2\, a_3^{-\sqrt{2}}\, \left(1-\sqrt{2}\right)\cos\left(\frac{(4N+1)}{\sqrt{2}}\pi\right)\right).$$

Figure 2.4 shows some of the characteristic roots of Eq. (2.16) obtained numerically using the Newton-Raphson method along with the asymptotic approximations, which are in good agreement.

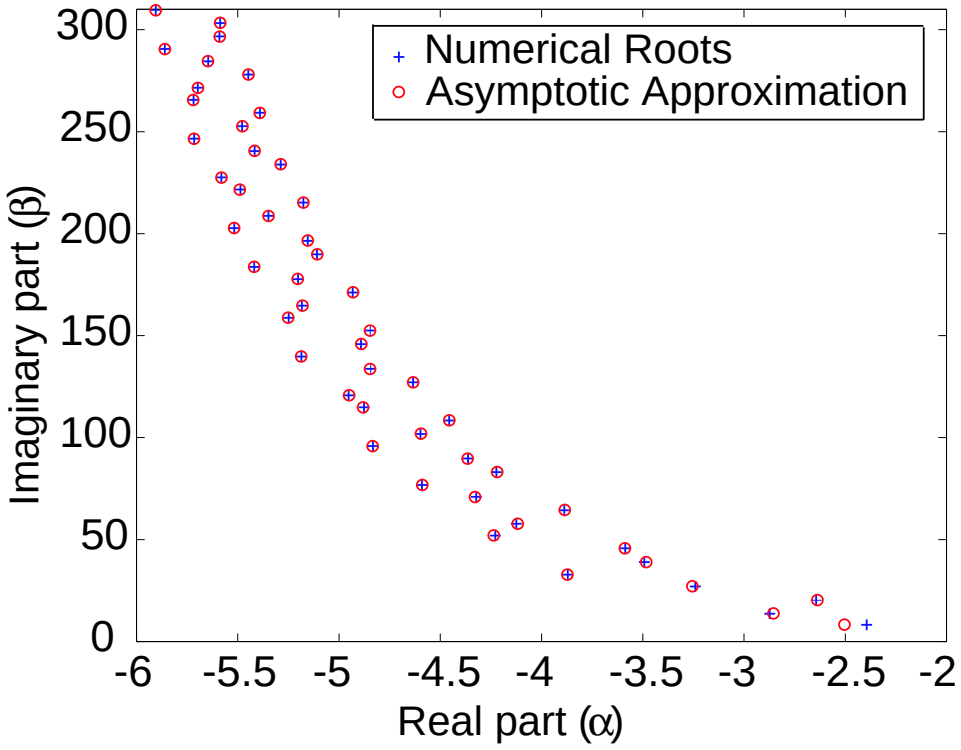

Figure 2.4: Characteristic roots of Eq. (2.16) for $a_1 = a_2 = a_3 = a_4 = 1$.

Remark 1 The smaller characteristic roots of DDEs can be found using Padé approximants ([89, 90]). These, along with the asymptotics above, can give *all* the roots. The procedure requires arbitrary precision arithmetic (in, e.g., MAPLE). See appendix A.

2.5 Asymptotics on coefficients

In the above DDEs the term with the largest delay essentially determined the large roots. For DDEs with multiple delays, however, if the coefficients of delayed terms have disparate magnitudes, then the above asymptotics may only begin to hold for extremely large roots. In such cases, we could develop alternative asymptotic expansions. A relevant example of such systems is addressed in [91]. Here, we present another example:

$$\dot{x}(t) + \frac{x(t-1/\sqrt{2})}{\epsilon} + a\,x(t-1) = 0\,, \tag{2.35}$$

where $0 < \epsilon \ll 1$. Note that this is a special case of Eq. (2.16) with $a_2 = 1/\epsilon$, $a_3 = a$ and $a_1 = a_4 = 0$. Substituting $\lambda = \alpha + i\beta$ and separating real and imaginary parts, we get

$$\alpha + \frac{e^{-\alpha/\sqrt{2}}\cos(\beta/\sqrt{2})}{\epsilon} + ae^{-\alpha}\cos\beta = 0\,, \tag{2.36}$$

$$\beta - \frac{e^{-\alpha/\sqrt{2}}\sin(\beta/\sqrt{2})}{\epsilon} - ae^{-\alpha}\sin\beta = 0\,. \tag{2.37}$$

Remark 2 The above two equations each have three terms. However, there are regimes of root magnitudes for which, in each equation, two of the terms are much bigger than the third. Our analytical search for roots will focus on these regimes. In what follows, we adopt the following convention. If the $m^{\rm th}$ and $n^{\rm th}$ terms, with $m = 1, 2, 3$ and $n = 1, 2, 3$, are negligible compared to the other terms in Eqs. (2.36) and (2.37) respectively, then we refer to it as "Case (m, n)". The large root asymptotics developed in the previous section correspond to Case $(2, 2)$.

Remark 3 The leading order solution of Eq. (2.16) given by Eq. (2.30) also represents roots of Eq. (2.35), under Case (2,2). Substituting Eq. (2.30) in Eq. (2.37), the first and third terms turn out to be of $\mathcal{O}(N)$ while the second term is of $\mathcal{O}\left(\dfrac{N^{1/\sqrt{2}}}{\epsilon}\right)$. Hence, the second term is negligible for $N \gg \dfrac{N^{1/\sqrt{2}}}{\epsilon}$, i.e., $N \gg \epsilon^{-(2+\sqrt{2})}$.

Alternatively, the asymptotic expressions of Eqs. (2.31) and (2.32), for the roots of Eq. (2.16), are based on the correction term being $o(1)$. For Eq. (2.35), viewed as a special case of Eq. (2.16) (with $a_2 = 1/\epsilon$), substitution of β_1 found in section 2.4 in the series solution for β, i.e., Eq. (2.31) gives the first correction term to be

$$\frac{2^{\frac{-2+\sqrt{2}}{2}}\,\pi^{\frac{-2+\sqrt{2}}{2}}\,a^{-\frac{1}{\sqrt{2}}}}{\epsilon\,N^{(1-\frac{1}{\sqrt{2}})}}\cos\left(\frac{(4N+1)}{2\sqrt{2}}\pi\right).$$

For the above to be $o(1)$, we require $N \gg \epsilon^{-(2+\sqrt{2})}$, matching the above.

The asymptotics developed below are therefore for N smaller than the above estimate. How much smaller is a somewhat tricky issue as discussed later.

By remark 2, our analytical search for the roots will concentrate on regimes where two of the three terms in each equation, i.e., Eqs. (2.36) and (2.37), are much larger than the third one. Accordingly we have 9 different possibilities, one of which, Case $(2, 2)$, has been dealt with in the previous section. Here, we check the remaining possibilities one by one for the existence of roots and obtain expressions for them.

Proposition 6 *Case (1,1) yields a set of solutions for Eqs. (2.36) and (2.37).*

Proof Equations (2.36) and (2.37) simplify to

$$\frac{e^{-\alpha/\sqrt{2}}\cos(\beta/\sqrt{2})}{\epsilon} = -ae^{-\alpha}\cos\beta + \mathrm{ST}\,, \tag{2.38}$$

$$\frac{e^{-\alpha/\sqrt{2}}\sin(\beta/\sqrt{2})}{\epsilon} = -ae^{-\alpha}\sin\beta + \mathrm{ST}\,, \tag{2.39}$$

where "ST" stands for an asymptotically smaller term. Squaring Eqs. (2.38) and (2.39) and adding, in the asymptotic limit we get

$$\frac{e^{-\sqrt{2}\,\alpha}}{\epsilon^2} = a^2 e^{-2\,\alpha}\,, \tag{2.40}$$

whence to leading order we have

$$\alpha \;=\; (2+\sqrt{2})\ln(\epsilon a)\,. \tag{2.41}$$

Substituting α in Eqs. (2.38) and (2.39) and rearranging, we get in the asymptotic limit

$$a^{-(1+\sqrt{2})}\epsilon^{-(2+\sqrt{2})}\left(\cos(\beta/\sqrt{2}) + \cos\beta\right) = 0\,,$$

$$a^{-(1+\sqrt{2})}\epsilon^{-(2+\sqrt{2})}\left(\sin(\beta/\sqrt{2}) + \sin\beta\right) = 0\,.$$

Again squaring and adding we get

$$2a^{-(1+\sqrt{2})}\epsilon^{-(2+\sqrt{2})}\left(1 + \cos\left(\frac{\beta}{2+\sqrt{2}}\right)\right) = 0\,.$$

which requires $\cos\left(\dfrac{\beta}{2+\sqrt{2}}\right) = -1$, whence

$$\beta \;=\; (2N+1)(2+\sqrt{2})\pi\,. \tag{2.42}$$

Equations (2.41) and (2.42) give solutions for Eqs. (2.36) and (2.37). •

We further investigate these roots for small ϵ and large N as follows. Substituting Eqs. (2.41) and (2.42) in Eq. (2.37), we note that the first term is of $\mathcal{O}(N)$ while the second and the third term are of $\mathcal{O}(\epsilon^{-(2+\sqrt{2})})$. Hence, the assumption that the first term is negligible for Case $(1,1)$ is valid as long as $N \ll \epsilon^{-(2+\sqrt{2})}$. Note that this is complementary to Case $(2,2)$ where $N \gg \epsilon^{-(2+\sqrt{2})}$ (by remark 3).

We proceed to a correction term. We add corrections β_1 and α_1 to the leading order solutions for β and α, i.e., in Eqs. (2.41) and (2.42), respectively. We substitute α and β in Eqs. (2.36) and (2.37), expand in a Taylor series about $\alpha_1 = \beta_1 = 0$, drop quadratic and higher order terms, and solve for β_1 and α_1 to get

$$\beta_1 = \frac{\epsilon^{2+\sqrt{2}}\, a^{1+\sqrt{2}} \left((4N+2)\pi \cos\left((2+\sqrt{2})(2N+1)\pi\right) + 2\ln(a\epsilon) \sin\left((2+\sqrt{2})(2N+1)\pi\right)\right)}{-3+2\sqrt{2}},$$

$$\alpha_1 = \frac{\epsilon^{2+\sqrt{2}}\, a^{1+\sqrt{2}} \left((4N+2)\pi \sin\left((2+\sqrt{2})(2N+1)\pi\right) - 2\ln(a\epsilon) \cos\left((2+\sqrt{2})(2N+1)\pi\right)\right)}{-3+2\sqrt{2}}.$$

Since we are interested in $N \ll \epsilon^{-(2+\sqrt{2})}$ for this case we find, self-consistently, that $\beta_1 = o(1)$ and $\alpha_1 = o(1)$. This concludes Case $(1,1)$.

Remark 4 In the above, we established the range of β (or equivalently N) over which the asymptotic expressions hold, i.e., $\beta \ll \epsilon^{-(2+\sqrt{2})}$. In what follows, such sharp estimates on β may not always be easily obtainable. Sometimes, for simplicity, we will fix β at some ϵ-independent range of magnitudes and take the limit as $\epsilon \to 0$. Eventually, numerics will bear out the final analytical approximations.

Lemma 2 *If r is an irrational number and either $\sin\theta = 0$ or $\cos\theta = 0$, then $\sin(r\theta) \neq 0$ and $\cos(r\theta) \neq 0$.*

Proof $\sin\theta = 0$ requires $\theta = n\pi$, for some integer n. However, $\sin(r\theta) = 0$ requires $r\theta = m\pi$, for some integer m. Simultaneous satisfaction of both the above requirements imply, contradictorily, that $r = \dfrac{m}{n}$. Similar contradictions arise for the other cases. •

Proposition 7 *Case (2,1) can be eliminated.*

Proof From Eqs. (2.36) and (2.37), we have

$$\alpha = -ae^{-\alpha}\cos\beta + \mathrm{ST}\,, \tag{2.43}$$

$$\frac{e^{-\alpha/\sqrt{2}}\sin(\beta/\sqrt{2})}{\epsilon} = -ae^{-\alpha}\sin\beta + \mathrm{ST}\,. \tag{2.44}$$

Squaring and adding, we get in the asymptotic limit

$$\frac{e^{-\sqrt{2}\,\alpha}\sin^2(\beta/\sqrt{2})}{\epsilon^2} + \alpha^2 = a^2 e^{-2\,\alpha}\,. \tag{2.45}$$

There are three possibilities now: $\alpha \gg 1$, $\alpha = \mathcal{O}(1)$ and $\alpha \ll -1$.

1. If $\alpha \gg 1$, the RHS of Eq. (2.45), i.e., $a^2\, e^{-2\,\alpha} = o(1)$. However, in the LHS, $\alpha^2 \gg 1$ while the first term is positive, giving a contradiction.

2. If $\alpha = \mathcal{O}(1)$, the first term remains unbalanced in Eq. (2.45) unless $\sin^2(\beta/\sqrt{2}) \ll 1$. However, Case $(2,1)$ implies for Eq. (2.36) that $\cos^2(\beta/\sqrt{2}) \ll 1$ as well, giving a contradiction because $\sin^2(.) + \cos^2(.) = 1$.

3. If $\alpha \ll -1$, then $\alpha^2 \ll e^{-2\,\alpha}$ and Eq. (2.45) simplifies to

$$\frac{e^{-\sqrt{2}\,\alpha}\sin^2(\beta/\sqrt{2})}{\epsilon^2} = a^2 e^{-2\,\alpha} + \mathrm{ST}\,. \tag{2.46}$$

   Also, Case (2,1) implies for Eq. (2.36) that $\cos(\beta/\sqrt{2}) = o(1)$, whence $\sin^2(\beta/\sqrt{2}) \sim 1$. In that case, Eq. (2.46) simplifies to Eq. (2.40) which has Eq. (2.41) as the leading order solution for α. Substituting Eq. (2.41) for α in Eq. (2.44), we require in the asymptotic limit

$$\sin(\beta/\sqrt{2}) + \sin\beta = 2\sin\left(\frac{2+\sqrt{2}}{4}\beta\right)\cos\left(\frac{2-\sqrt{2}}{4}\beta\right) = 0\,,$$

   which contradicts our prior conclusion that $\cos(\beta/\sqrt{2}) = 0$ in the asymptotic limit[2] (by lemma 2).

[2]Note that we have considered β fixed as $\epsilon \to 0$. An argument allowing β to grow as $\epsilon \to 0$ can be developed, but is trickier and avoided here.

Thus, Case $(2,1)$ gives no roots. •

Proposition 8 *Cases (3,1), (1,2) and (3,2) can also be eliminated.*

Proof The proof resembles that of proposition 7 and is not given here to save space. •

Proposition 9 *The three Cases* $(m,3)$*,* $m = 1,2,3$ *lead to one set of solutions for Eqs. (2.36) and (2.37).*

Proof

1. For Case (1,3), from Eqs. (2.36) and (2.37) we get

$$\frac{e^{-\alpha/\sqrt{2}}\cos(\beta/\sqrt{2})}{\epsilon} = -ae^{-\alpha}\cos\beta + \mathrm{ST}\,, \tag{2.47}$$

$$\beta = \frac{e^{-\alpha/\sqrt{2}}\sin(\beta/\sqrt{2})}{\epsilon} + \mathrm{ST}\,. \tag{2.48}$$

Note that Case (.,3) implies that $\beta \gg ae^{-\alpha}|\sin\beta|$. Accordingly, we have two subcases, in the asymptotic limit, viz., $\sin\beta = 0$ and $\sin\beta \neq 0$.

(a) If $\sin\beta = 0$ in the asymptotic limit, we have $\cos\beta = \pm 1$. In that case, solving Eq. (2.47) for α, we get

$$\alpha = (2+\sqrt{2})\ln\left(\frac{\epsilon a}{|\cos(\beta/\sqrt{2})|}\right).$$

Substituting the above in Eq. (2.48), we will require

$$\epsilon^{(2+2\sqrt{2})/\sqrt{2}}\, a^{(2+\sqrt{2})/\sqrt{2}}\,\beta = \sin(\beta/\sqrt{2})\,\cos^{\frac{2+\sqrt{2}}{\sqrt{2}}}(\beta/\sqrt{2})\,.$$

In the asymptotic limit as $\epsilon \to 0$, we will require either $\sin(\beta/\sqrt{2}) = 0$ or $\cos(\beta/\sqrt{2}) = 0$ which contradicts $\sin\beta = 0$ (by lemma 2).

(b) If $\sin\beta \neq 0$ in the asymptotic limit, we have $\beta \gg ae^{-\alpha}$. Also, from Eq. (2.48), we have $\dfrac{e^{-\alpha/\sqrt{2}}}{\epsilon} \geq \beta \gg ae^{-\alpha}$. Hence, for balance in Eq. (2.47), we require $\cos(\beta/\sqrt{2}) = 0$ (in the asymptotic limit), whence

$$\beta \;=\; (2N+1/2)\sqrt{2}\,\pi + o(1)\,. \tag{2.49}$$

Substituting the above for β in Eq. (2.48) and solving for α, we get

$$\alpha \;=\; -\sqrt{2}\ln\Big(\epsilon(2N+1/2)\sqrt{2}\,\pi\Big) + o(1)\,. \tag{2.50}$$

This concludes Case $(1,3)$.

2. For Case (2,3), we have

$$\alpha = -ae^{-\alpha}\cos\beta + \mathrm{ST}\,, \tag{2.51}$$

$$\beta = \frac{e^{-\alpha/\sqrt{2}}\sin(\beta/\sqrt{2})}{\epsilon} + \mathrm{ST}\,. \tag{2.52}$$

Again $\beta \gg ae^{-\alpha}|\sin\beta|$, giving two subcases as before.

(a) If $\sin\beta = 0$, we have $\cos\beta = \pm 1$ and Eq. (2.51) reduces, in the asymptotic limit, to

$$\alpha \pm ae^{-\alpha} = 0\,.$$

The above has at most one solution for α which, in turn, is $\mathcal{O}(1)$. In that case, $e^{-\alpha/\sqrt{2}} = \mathcal{O}(1)$ and Case (2,3) requires $\cos(\beta/\sqrt{2}) = 0$ contradicting $\sin\beta = 0$.

(b) If $\sin\beta \neq 0$ in the asymptotic limit, we have $\beta \gg ae^{-\alpha}$. Also from Eq. (2.52), we have $\dfrac{e^{-\alpha/\sqrt{2}}}{\epsilon} \geq \beta$. Now, Case (2,.) requires $\dfrac{e^{-\alpha/\sqrt{2}}\cos(\beta/\sqrt{2})}{\epsilon} \ll ae^{-\alpha} \ll \beta$. This is possible only when $\cos(\beta/\sqrt{2}) = 0$ giving Eqs. (2.49) and (2.50) as the solutions again.

3. For Case (3,3), we get from Eqs. (2.36) and (2.37)

$$\alpha = -\frac{e^{-\alpha/\sqrt{2}}\cos(\beta/\sqrt{2})}{\epsilon} + \mathrm{ST}\,, \tag{2.53}$$

$$\beta = \frac{e^{-\alpha/\sqrt{2}}\sin(\beta/\sqrt{2})}{\epsilon} + \mathrm{ST}\,. \tag{2.54}$$

In the asymptotic limit, Eqs. (2.53) and (2.54) are the same as Eqs. (2.4) and (2.5) with $a = 1/\epsilon$ and the delay being $1/\sqrt{2}$ instead of 1. From proposition 1, we get the same expressions for α and β as given in Eqs. (2.49) and (2.50).

Thus, all Cases $(m, 3)$, $m = 1, 2, 3$ give the same solutions given by Eqs. (2.49) and (2.50). •

Remark 5 All three cases (.,3) lead to the same solution set. A finer analysis of small terms might tell them apart. Note also that these solutions rest on $\beta \gg 1$, which implies "large" roots (though not larger than that allowed by remark 4). As will be seen in numerics, all but a small number of roots are in fact captured accurately.

Remark 6 In the above, roots in different magnitude regimes were captured by different scalings of the nominally small/large expansion terms. Equations (2.49) and (2.50) apply for N somewhat large, but not larger than $\epsilon^{-(2+\sqrt{2})}$. Moreover, there ϵ itself is small. Elsewhere, we have held N fixed as $\epsilon \to 0$. Below, to obtain correction terms to the leading order solutions, we set $\epsilon = \Delta/N^{1-\frac{1}{\sqrt{2}}}$, where $\Delta = o(1)$ since $N \ll \epsilon^{-(2+\sqrt{2})}$. However, now Δ will be held constant while we consider asymptotics for large N. These different scalings are motivated by mathematical convenience alone, always keeping in mind that we are finally interested in some finite nonzero values of ϵ and N, and it matters little how we get there. In final justification of these ideas, numerics and approximations will match below.

For finding a correction term, we first scale ϵ as mentioned in remark 6, then substitute $\beta = (2N+1/2)\pi\sqrt{2}+\beta_1$ and $\alpha = -\sqrt{2}\ln(\epsilon(2N+1/2)\pi\sqrt{2})+\alpha_1$ in Eqs. (2.36) and (2.37), expand in a Taylor series about $\alpha_1 = \beta_1 = 0$ till first order, solve for α_1 and β_1, retain the largest power of N (a key step in simplifying very long expressions), and reinsert $\Delta = \epsilon N^{1-\frac{1}{\sqrt{2}}}$ to finally get

$$\beta_1 = \frac{2^{1+\frac{3}{\sqrt{2}}}\,\pi^{1+\sqrt{2}}\,\epsilon^{\sqrt{2}}\,a\,\cos((2N+1/2)\,\pi\,\sqrt{2})}{4\,\pi^2\,N^{(1-\sqrt{2})} + 2^{3\sqrt{2}}\,\epsilon^{2\sqrt{2}}\,\pi^{2\sqrt{2}}\,a^2\,N^{(\sqrt{2}-1)} + 2^{2+\frac{3}{\sqrt{2}}}\,\pi^{1+\sqrt{2}}\,\epsilon^{\sqrt{2}}\,a\,\sin((2N+1/2)\,\pi\,\sqrt{2})}\,, \tag{2.55}$$

$$\alpha_1 = \frac{2^{1+\frac{3}{\sqrt{2}}}\,\pi^{1+\sqrt{2}}\,\epsilon^{\sqrt{2}}\,a\,\sin((2N+1/2)\,\pi\,\sqrt{2}) + 2^{3\sqrt{2}}\,\pi^{2\,\sqrt{2}}\,\epsilon^{2\,\sqrt{2}}\,a^2\,N^{\sqrt{2}-1}}{4\,\pi^2\,N^{(1-\sqrt{2})} + 2^{3\sqrt{2}}\,\epsilon^{2\sqrt{2}}\,\pi^{2\sqrt{2}}\,a^2\,N^{(\sqrt{2}-1)} + 2^{2+\frac{3}{\sqrt{2}}}\,\pi^{1+\sqrt{2}}\,\epsilon^{\sqrt{2}}\,a\,\sin((2N+1/2)\,\pi\,\sqrt{2})}\,. \tag{2.56}$$

Figure 2.5 shows the converged roots obtained from Newton-Raphson iterations, each starting from a different initial point on a large, uniform grid (exhaustive search); as well as the above analytical estimates. Agreement is good except for a single root near the origin.

2.6 Concluding remarks

We have obtained asymptotic approximations for the roots of the characteristic equations of some linear DDEs with constant coefficients. The term with the largest delay dominates in the asymptotic expansions for the large roots. A few smaller roots obtained using a Padé approximant can complement these asymptotic expressions to give all the characteristic roots of a DDE. However, if a very large coefficient is associated with a term with a smaller delay (equivalently, the term with the largest delay has a small coefficient), the large root asymptotics are useful only for extremely large roots. For such cases, determining the remaining roots using the Padé approximant is impractical and alternative asymptotic expansions can be developed. This study provides practical insight into the location of characteristic roots of DDEs on the complex plane, and may be useful for further theoretical studies as well.

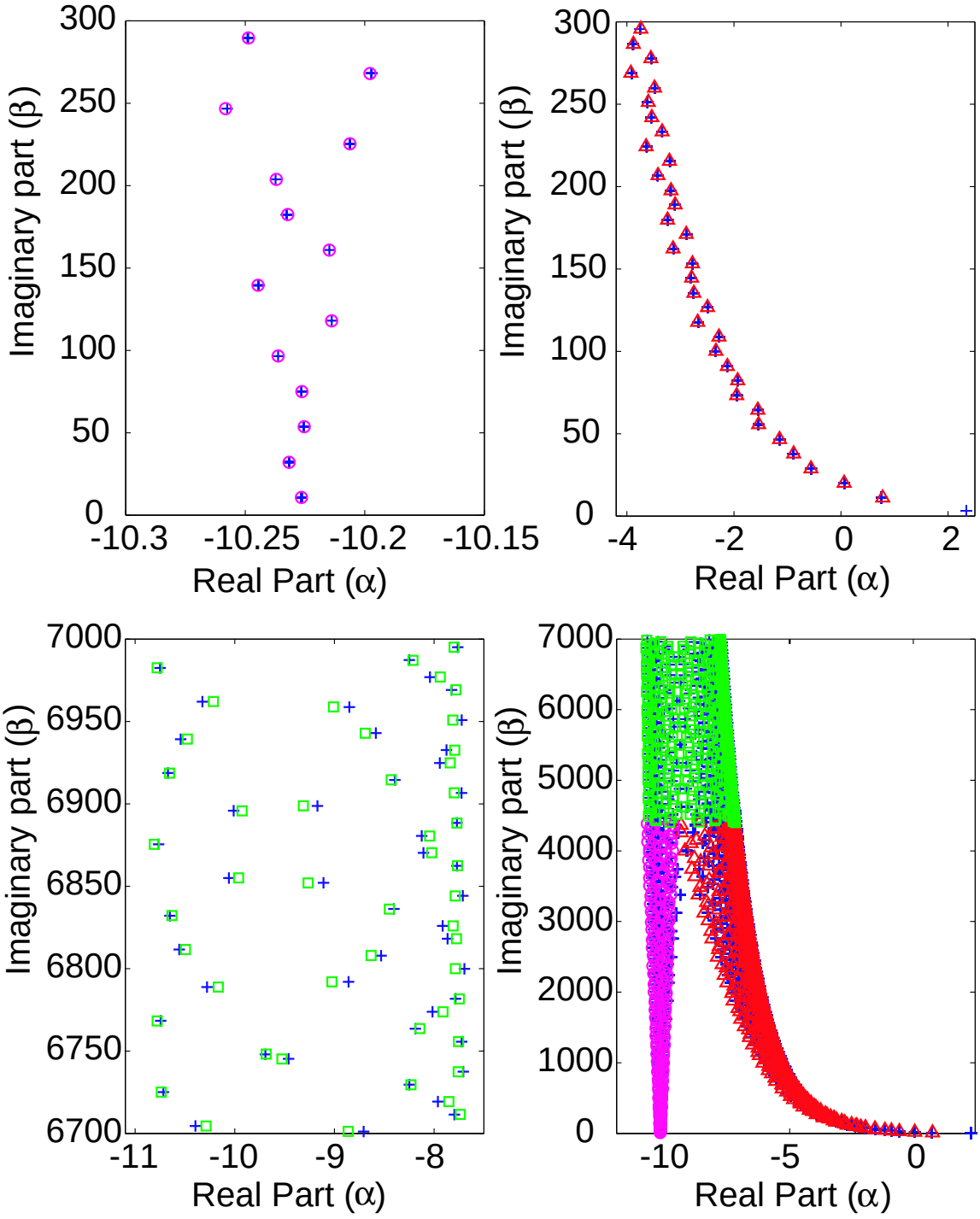

Figure 2.5: Roots of Eqs. (2.36) and (2.37) for $a = 1$ and $\epsilon = 0.05$. Plus signs: Newton-Raphson. Circles: asymptotic, Case (1,1). Triangles: asymptotic, Case (.,3). Rectangles: asymptotic, Case (2,2).

Chapter 3

Averaging with small fractional damping and delayed terms

In this chapter, we use the method of averaging to study small perturbations of conservative oscillators. The unperturbed conservative oscillators need not be linear. The perturbations studied involve delayed terms as well as fractional derivative terms (fractional derivatives incorporate a distributed delay effect over a time-varying interval). The material of this chapter has been published in [72].

3.1 Introduction

Differential equations with delayed terms (DDEs) have applications in many areas of science and engineering as mentioned in chapter 1. Fractional derivatives (which incorporate distributed delay effects with an infinite delay) are, among other things, useful in describing the frequency dependent damping behavior of many materials [92, 93, 94, 95].

We first consider problems where the unperturbed system is *linear*.

Analytical treatment of even linear problems involving delayed terms or fractional derivatives is nontrivial. However, when the delayed terms or the fractional derivative terms in the equation are small, the systems can be studied analytically using perturbation methods.

The method of multiple scales, which is similar to the method of averaging [96], has been used to study linear oscillators perturbed by small delayed terms [97, 98, 99]. If the delayed term is small but the delay itself is large, then the method of multiple scales is applicable with some modifications (for example, see [91]).

For linear oscillators perturbed by small fractional derivative terms, Li *et al.* [100] have used averaging. Their approach indirectly recovers the averaged equations after several modifications of the averaging method for the *periodic* case. The problem, however, is directly amenable to averaging for the *aperiodic* case, as discussed below, for which a short and simple procedure exists [101]. A similar problem has also been studied using multiple scales by Rossikhin and Shitikova [102].

In this chapter, after briefly studying the aforementioned linear/weakly nonlinear cases involving delayed terms and/or fractional derivatives, we use averaging to study the dynamics of some *strongly nonlinear* conservative oscillators with small perturbations in the form of delays and/or fractional derivatives. This is the main contribution of the present chapter. The method of averaging, implemented in an approximate sense as in [103], gives "slow flows" governing the evolution of amplitude and phase of the oscillations under study. The slow flow equations are ODEs, do not contain fractional derivatives or delayed terms, and are easy to study further using standard numerical and/or analytical methods for ODEs.

3.2 Background and numerics

3.2.1 Delay differential equations

Consider a DDE of the form

$$\dot{x}(t) = H\left(x(t), x(t-s_1), x(t-s_2), \cdots, x(t-1)\right) , \tag{3.1}$$

where x could be a vector and $0 < s_1 < s_2 < \cdots < s_n = 1$ are finite time delays. Assuming $s_n = 1$ is allowed because time can be scaled to make it so. At instant t, the evolution of x depends explicitly on values it took in the immediately preceding unit interval, $[t-1, t]$.

For the numerical integration of DDEs in this thesis, we use the following method. We fit a cubic spline over an interval somewhat longer than unity, say $[t-1-10h, t]$; and interpolate, using the fitted spline, at all the desired time instants in the past. The portion of stored history longer than unity is optional. It is used here because splines on intervals fit better at points not too close to the endpoints. This interpolation scheme is convenient for software like Matlab, which has inbuilt commands for splines. Once the interpolated values are available, we simply use a fixed-step fourth order Runge-Kutta method. Note that all numerics in this chapter are solely for checking the accuracy of analytical approximations.

3.2.2 Differential equations with fractional derivatives

We adopt the Riemann-Liouville definition of the fractional derivative [104],

$$D_a^q[x(t)] \equiv \frac{d^q x(t)}{[d(t-a)]^q} \equiv \frac{1}{\Gamma(n-q)} \frac{d^n}{dt^n} \left[\int_a^t \frac{x(u)}{(t-u)^{q-n-1}} du \right],$$

where n is the smallest integer greater than or equal to q and Γ represents the Gamma function. For systems starting from rest (a case studied by many authors) we have $x(t) = 0$ for $t < 0$, so $D_{-\infty}^q$ is identical to D_0^q and we drop the subscript a. In this chapter, we assume $0 < q < 1$, the case most relevant to structural damping. Hence,

$$D^q x(t) = \frac{1}{\Gamma(1-q)} \frac{d}{dt} \int_0^t \frac{x(u)}{(t-u)^q} du = \frac{1}{\Gamma(1-q)} \left[\frac{x(0)}{t^q} + \int_0^t \frac{\dot{x}(t-u)}{u^q} du \right].$$

The latter form above is useful to us. In it, the first term has a singularity at $t = 0$, and the integral involves a singular kernel. The singularity due to the first term can be treated[1] using a local series expansion near $t = 0$, but for simplicity we assume $x(0) = 0$ as in [105, 106]. Moreover, we change variables to $\bar{u} = u^{1-q}$, which removes the singularity in the kernel to give

$$D^q x(t) = \frac{1}{\Gamma(2-q)} \int_0^{t^{(1-q)}} \dot{x}(t - \bar{u}^{1/(1-q)})\, d\bar{u}\,.$$

Uniformly spaced points in the original time t are non-uniformly spaced in $\bar{u}$. However, fitting a spline to $\dot{x}(t)$ and interpolating at uniformly spaced $\bar{u}$ values, the integral can be evaluated numerically (Simpson's rule). In this way, knowing the history of $\dot{x}(t)$, we evaluate $D^q x(t)$. Finally, a modified fourth order Runge Kutta routine, with access to the history needed for the integral, is used to integrate forward in time. Note, again, that our numerics are solely for verifying analytical approximations.

We mention two final points. First, the cubic spline interpolant has higher order accuracy than Simpson's rule; so, for integration, we should interpolate at a fine mesh. Second, there might be numerical difficulties if q approaches 0 or 1; here, we focus on q away from these limits (e.g., $q = 1/2$).

3.3 Weakly nonlinear oscillations

3.3.1 The method of averaging

The classical method of averaging (see, e.g., [101, 108, 109]) is applicable to systems of the form

$$\dot{x} = \epsilon\, G(x, t)\,, \quad 0 < \epsilon \ll 1\,. \tag{3.2}$$

In this section, we study

$$\ddot{x}(t) + x(t) = \epsilon \bar{F}\,, \tag{3.3}$$

where $\bar{F}$ can depend on delayed values and fractional derivatives of x.

We now cast Eq. (3.3) in the form of Eq. (3.2) (a routine procedure). For $\epsilon = 0$, the solution to Eq. (3.3) is $x(t) = R\sin(t+\phi)$ for R and ϕ arbitrary constants. For small $\epsilon \neq 0$ we let

$$x(t) = R(t)\, \sin\left(t + \phi(t)\right), \tag{3.4}$$

where $R(t)$ and $\phi(t)$ both change *slowly* with time. We also incorporate the usual constraint,

$$\dot{x}(t) = R(t)\, \cos\left(t + \phi(t)\right). \tag{3.5}$$

[1] Initial conditions for linear problems have also been included in, e.g., Laplace transform based treatments [107].

Proceeding in the usual manner [101, 108, 109], we finally obtain

$$\dot{R} = \epsilon \cos(t+\phi)\, F \tag{3.6}$$

$$\dot{\phi} = -\epsilon \frac{\sin(t+\phi)}{R} F\,, \tag{3.7}$$

where F is simply $\bar{F}$ with Eqs. (3.4) and (3.5) plugged in. Equations (3.6) and (3.7) have the form of Eq. (3.2). Now, depending on whether the function G is periodic or aperiodic in its explicit dependence on time t, we have two cases :

1. If $G = G(\cdot, t)$ is periodic in t, i.e., $G(\cdot, t+T_0) = G(\cdot, t)$ for some $0 < T_0 < \infty$, then the correct averaging procedure (see Theorem 3.2.10 in [101]) is to hold x constant in the right hand side of Eq. (3.2)[2], while t-averaging over the time period T_0, as in
$$\frac{1}{T_0}\int_0^{T_0} G\, dt.$$
2. If G is aperiodic in t, the correct averaging procedure (see Theorem 3.3.3 in [101]) is to average over an "infinitely" long time, as in (holding x constant)
$$\lim_{T\to\infty} \frac{1}{T}\int_0^{T} G\, dt.$$

3.3.2 Weakly nonlinear oscillation with delayed terms

For illustration, consider

$$\ddot{x}(t) + x(t) = -2\zeta\dot{x}(t) - \mu x(t)^3 + 2u x_s(t) + 2v\dot{x}_s(t)\,, \tag{3.8}$$

where we introduce the notation $x_s(t) = x(t-s)$ and $\dot{x}_s(t) = \dot{x}(t-s)$, and ζ, μ, u and v are small quantities. This is the same equation as in section 2.1 of [98], but without forcing. In [98], the method of multiple scales was used; here, we will briefly demonstrate the use of averaging. We substitute $\zeta = \epsilon\bar{\zeta}$, $\mu = \epsilon\bar{\mu}$, $u = \epsilon\bar{u}$ and $v = \epsilon\bar{v}$, where $0 < \epsilon \ll 1$. Note that we have replaced the delay τ (used in [98]) by s. We now have

$$\ddot{x}(t) + x(t) = \epsilon\left(-2\bar{\zeta}\dot{x}(t) - \bar{\mu}x(t)^3 + 2\bar{u}x_s(t) + 2\bar{v}\dot{x}_s(t)\right). \tag{3.9}$$

Substituting $x(t) = R(t)\sin(t+\phi(t))$ and following the routine steps described above, we obtain

$$\begin{aligned}\dot{R}(t) = \epsilon\,\Big(&-\bar{\mu}\,R(t)^3\cos(t+\phi(t))\sin^3(t+\phi(t)) + 2\,\bar{u}\,R_s(t)\,\cos(t+\phi(t))\sin(t-s+\phi_s(t))\\ &+2\,\bar{v}\,R_s(t)\,\cos(t+\phi(t))\cos(t-s+\phi_s(t)) + 2\,\bar{\zeta}\,R(t)\,\sin^2(t+\phi(t)) - 2\,\bar{\zeta}\,R(t)\Big)\end{aligned}$$

and

$$\begin{aligned}\dot{\phi}(t) = -\epsilon\,\frac{\sin(t+\phi(t))}{R(t)}\,\Big(&-2\,\bar{\zeta}\,R(t)\,\cos(t+\phi(t)) - \bar{\mu}\,R(t)^3\sin^3(t+\phi(t))\\ &+2\,\bar{u}\,R_s(t)\,\sin(t-s+\phi_s(t)) + 2\,\bar{v}\,R_s(t)\,\cos(t-s+\phi_s(t))\Big)\,,\end{aligned}$$

where we again denote delays using $R_s(t) = R(t-s)$ and $\phi_s(t) = \phi(t-s)$. For averaging, R and ϕ are to be held constant while t-averaging the right hand sides of the above equations. Hence, we substitute $R(t) = R_s(t) = R$ and $\phi(t) = \phi_s(t) = \phi$, which gives

$$\begin{aligned}\dot{R} = \epsilon\,R\,\Big(&-\bar{\mu}\,R^2\cos(t+\phi)\sin^3(t+\phi) + 2\,\bar{u}\,\cos(t+\phi)\sin(t-s+\phi)\\ &+2\,\bar{v}\cos(t+\phi)\cos(t-s+\phi) + 2\,\bar{\zeta}\,\left(\sin(t+\phi)\right)^2 - 2\,\bar{\zeta}\Big)\end{aligned}$$

and

$$\dot{\phi} = -\epsilon\,\sin(t+\phi)\left(-2\,\bar{\zeta}\,\cos(t+\phi) - \bar{\mu}\,R^2\sin^3(t+\phi) + 2\,\bar{u}\,\sin(t-s+\phi) + 2\,\bar{v}\,\cos(t-s+\phi)\right).$$

The right hand sides of both equations above are 2π-periodic in t. Averaging gives

$$\dot{R} = -\epsilon\,R\left(\bar{u}\,\sin(s) - \bar{v}\,\cos(s) + \bar{\zeta}\right) \tag{3.10}$$

and

$$\dot{\phi} = -\frac{\epsilon}{8}\left(-3\,\bar{\mu}\,R^2 + 8\,\bar{v}\sin(s) + 8\,\bar{u}\,\cos(s)\right). \tag{3.11}$$

Going back to the old variables ζ, μ, u and v, we get the same results as obtained using multiple scales in [98]. For further verification, we have plotted the numerical solution of Eq. (3.8) along with that of the averaged equations, i.e., Eqs. (3.10) and (3.11) in Fig. 3.1. The match is good.

We now turn to systems with light fractional derivative damping.

[2]Or to hold R and ϕ constant in the right hand sides of Eqs. (3.6) and (3.7).

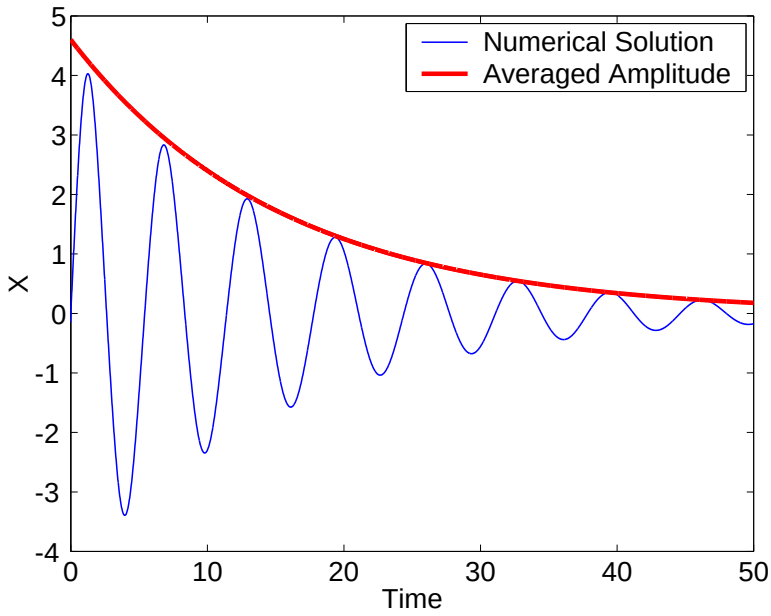

Figure 3.1: Solution of Eq. (3.8) and Eqs. (3.10) and (3.11) for $s = 1$, $\zeta = \mu = u = v = 0.05$. Initial conditions: $x(\eta) = 5\sin(\eta)$, $\dot{x}(\eta) = 5\cos(\eta)$, for $\eta \in [-1, 0]$, $R(0) = 4.65$, $\phi(0) = 0$. For a discussion of the choice of initial conditions, see Appendix B.

3.3.3 Weakly nonlinear oscillations with fractional damping

In what follows we take $q = 1/2$ in our fractional derivative, appropriate for a large variety of viscoelastic damping materials (see appendix C for $q \neq 1/2$). To demonstrate the averaging calculation in this case, we consider

$$\ddot{x}(t) + \epsilon D^{1/2}x(t) + x(t) = \delta(t)\,. \tag{3.12}$$

In the above $\delta(t)$ represents an instantaneous impulse [3] at $t = 0$, and $0 < \epsilon \ll 1$ (light damping). After the impulse has acted, we have the initial conditions $x(t) = 0$ for $t \leq 0$, and $\dot{x}(0^+) = 1$; and the governing equation for $t > 0$ is

$$\ddot{x}(t) + x(t) = -\epsilon D^{1/2}x(t)\,. \tag{3.13}$$

We again assume $x(t) = R(t)\sin(t + \phi(t))$ as described above, and obtain

$$\dot{R} = -\epsilon\,\cos(t+\phi)\,D^{1/2}x(t)\,, \tag{3.14}$$

$$\dot{\phi} = \epsilon\,\frac{\sin(t+\phi)}{R}D^{1/2}x(t)\,. \tag{3.15}$$

For averaging, we write $D^{1/2}x(t)$ in terms of $R(t)$ and $\phi(t)$ as

$$D^{1/2}\,x(t) = \frac{1}{\Gamma(1/2)}\int_0^t \frac{\dot{x}_s(t)}{\sqrt{s}}ds = \frac{1}{\sqrt{\pi}}\int_0^t \frac{R_s(t)\cos(t+\phi_s(t)-s)}{\sqrt{s}}ds\,. \tag{3.16}$$

We then write (recalling that we will set $R(t) = R_s(t) = R$ and $\phi(t) = \phi_s(t) = \phi$, to be held constant within the averaging integral)

$$\begin{aligned} D^{1/2}\,x(t) &= \frac{1}{\sqrt{\pi}}\int_0^t \frac{R\cos(t+\phi-s)}{\sqrt{s}}ds \\ &= \frac{R\cos(t+\phi)}{\sqrt{\pi}}\int_0^t \frac{\cos(s)}{\sqrt{s}}ds + \frac{R\sin(t+\phi)}{\sqrt{\pi}}\int_0^t \frac{\sin(s)}{\sqrt{s}}ds\,. \end{aligned} \tag{3.17}$$

[3] The instantaneous impulse is the Dirac delta function, which is a generalized function that is zero everywhere except at $t = 0$, undefined at $t = 0$, and whose integral over any nonzero interval containing $t = 0$ is unity.

The integrals above are aperiodic functions of t (case 2 in section 3.3.1), so we use an infinite time average (unlike the case with merely delayed x). Substituting for $D^{1/2}x(t)$ in Eq. (3.14) will require evaluation of

$$\lim_{T\to\infty}\frac{1}{T}\int_0^T \cos\left(t+\phi\right)\left\{\frac{R\cos(t+\phi)}{\sqrt{\pi}}\int_0^t\frac{\cos(s)}{\sqrt{s}}ds+\frac{R\sin(t+\phi)}{\sqrt{\pi}}\int_0^t\frac{\sin(s)}{\sqrt{s}}ds\right\}dt\,. \tag{3.18}$$

Integrating the first term above by parts, we get

$$\lim_{T\to\infty}\frac{R}{4\sqrt{\pi}}\left\{\left[\left(\frac{2\,t}{T}+\frac{\sin(2\,t)}{T}\right)\int_0^t\frac{\cos(s)}{\sqrt{s}}ds\right]_0^T-\frac{1}{T}\int_0^T\left[(2\sqrt{t}\cos(t)+\frac{\sin(2\,t)\cos(t)}{\sqrt{t}}\right]dt\right\}.$$

The above can be simplified to

$$\frac{R}{2\sqrt{\pi}}\lim_{T\to\infty}\left[\int_0^T\frac{\cos(s)}{\sqrt{s}}ds-\frac{1}{T}\int_0^T\sqrt{t}\cos(t)dt\right]. \tag{3.19}$$

Integrating the second term above by parts, we have

$$\int_0^T\sqrt{t}\cos(t)dt=\left.\sqrt{t}\sin(t)\right|_0^T-\int_0^T\frac{\sin(t)}{2\sqrt{t}}dt\,.$$

Substituting for $\displaystyle\int_0^T\sqrt{t}\cos(t)$ in Eq. (3.19), we get (on dropping terms that go to zero)

$$\frac{R}{2\sqrt{\pi}}\lim_{T\to\infty}\int_0^T\frac{\cos(s)}{\sqrt{s}}ds=\frac{R}{2\sqrt{2}}\,.$$

Thus, the first term of expression (3.18) is

$$\lim_{T\to\infty}\frac{1}{T}\int_0^T\frac{R\cos^2(t+\phi)}{\sqrt{\pi}}\int_0^t\frac{\cos(s)}{\sqrt{s}}ds=\frac{R}{2\sqrt{2}}\,.$$

By similar calculations,

$$\lim_{T\to\infty}\frac{1}{T}\int_0^T\frac{R\cos(t+\phi)\sin(t+\phi)}{\sqrt{\pi}}\int_0^t\frac{\sin(s)}{\sqrt{s}}ds=0\,.$$

Using the above, we get the averaged equations for $\dot{R}$ as

$$\dot{R}=-\epsilon\,\frac{1}{2\,\sqrt{2}}\,R.$$

In a similar fashion, we also get

$$\dot{\phi}=\epsilon\,\frac{1}{2\,\sqrt{2}}\,.$$

The above results could be obtained using the following alternative and informal argument. The integrals $\displaystyle\int_0^t\frac{\sin(s)}{\sqrt{s}}ds$ and $\displaystyle\int_0^t\frac{\cos(s)}{\sqrt{s}}ds$ are bounded for small t in spite of the singular integrand in the latter. In the infinite-time average, therefore, only the behaviors for $t\to\infty$ matter. For large t, we have

$$\int_0^t\frac{\cos(s)}{\sqrt{s}}\,ds=\sqrt{\frac{\pi}{2}}+\frac{\sin(t)}{\sqrt{t}}+\mathcal{O}\left(t^{-3/2}\right) \tag{3.20}$$

and

$$\int_0^t\frac{\sin(s)}{\sqrt{s}}\,ds=\sqrt{\frac{\pi}{2}}-\frac{\cos(t)}{\sqrt{t}}+\mathcal{O}\left(t^{-3/2}\right). \tag{3.21}$$

For our averaging purposes, we need to retain only the leading order, or constant, terms. The contributions from the correction terms go to zero. Therefore, *for our purposes*, on substituting Eqs. (3.20) and (3.21) in Eq. (3.17), we have

$$D^{1/2}x(t)\;=\;\frac{R\cos(t+\phi)}{\sqrt{2}}+\frac{R\sin(t+\phi)}{\sqrt{2}}+\;\text{negligible terms.} \tag{3.22}$$

Substituting Eq. (3.22) in Eqs. (3.14) and (3.15) and dropping the negligible terms, we get

$$\dot{R}=-\epsilon\,\frac{R}{\sqrt{2}}\,\left(\cos^2(t+\phi)+\sin(t+\phi)\,\cos\left(t+\phi\right)\right), \tag{3.23}$$

$$\dot{\phi} = \epsilon \frac{1}{\sqrt{2}} \left(\sin\left(t+\phi\right) \cos(t+\phi) + \sin^2(t+\phi) \right). \tag{3.24}$$

On averaging the above, where we note that the aperiodicity is gone and we are back to the periodic case, we obtain exactly as above

$$\dot{R} = -\epsilon \frac{1}{2\sqrt{2}} R \tag{3.25}$$

and

$$\dot{\phi} = \epsilon \frac{1}{2\sqrt{2}}. \tag{3.26}$$

These equations govern the evolution of the amplitude R and phase ϕ of the unforced oscillations (though there is an instant of forcing, we examine the subsequent unforced oscillations only). The solution for R is compared in Fig. 3.2 with the exact solution for the original equation (using the Laplace transform; see [104]). The match is excellent.

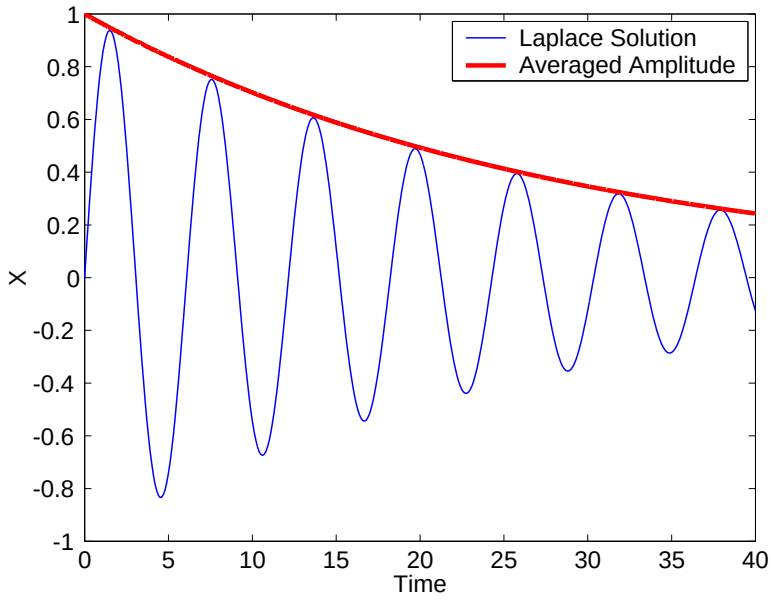

Figure 3.2: Impulse response of Eq. (3.12) for $\epsilon = 0.1$. Initial conditions: $x(0) = 0$ and $\dot{x}(0) = 1$. The solution of Eq. (3.25) is also shown for $R(0) = 1$.

We have now succeeded in averaging harmonic oscillators slightly perturbed with delayed terms and fractional derivatives. For the delayed terms, our results match those obtained earlier by other authors using the method of multiple scales. For fractional derivatives, we have shown how aperiodic averaging can be used more simply than the approach developed in [100].

We now move on to strongly nonlinear oscillators, where the main contributions of this chapter lie.

3.4 Strongly nonlinear oscillations

In this section, we adapt a recently developed technique called harmonic balance based averaging [103] to tackle small perturbations of some *strongly* nonlinear oscillators.

3.4.1 Harmonic balance based averaging

Averaging can not only be used to study small perturbations of the harmonic oscillator, but also (in principle at least) to perturbations of strongly nonlinear oscillators. However, there are practical difficulties in applying averaging to such strongly nonlinear problems. An approximate method for doing the averaging, called harmonic balance based averaging (HBBA) [103], is used in this chapter. The method is outlined here for completeness. Consider

$$\ddot{x} + g(x, \dot{x}) = \epsilon F, \tag{3.27}$$

where F is possibly a function of x, $\dot{x}$, $D^{1/2}x$ and/or $x(t-1)$ or $\dot{x}(t-1)$, and $g(x,\dot{x})$ has a two-parameter family of periodic solutions. Consider Eq. (3.27) for $\epsilon = 0$,

$$\ddot{x} + g(x,\dot{x}) = 0\,. \tag{3.28}$$

Equation (3.28) has a periodic solution expressible abstractly as $x = \tilde{h}(R,\omega(R),t)$, where R represents the amplitude of the solution, and the time period is $T = 2\pi/\omega(R)$. The general solution is then

$$x = \tilde{h}(R,\omega(R),t+\tilde{\phi})\,, \tag{3.29}$$

where both R and $\tilde{\phi}$ are arbitrary constants (defining a two-parameter family of periodic solutions). We rescale time through

$$\frac{d\tau}{dt} = \omega(R(\tau))\,,$$

where $\omega(R(\tau))$ is the same as in Eq. (3.29). Letting primes denote τ-derivatives, Eq. (3.27) becomes

$$\omega^2 x^{''} + \omega\frac{\partial\omega}{\partial R}R^{'}x^{'} + g = \epsilon F\,. \tag{3.30}$$

In τ-time, the unperturbed solution (Eq. (3.29)) may be rewritten as some new function

$$x = h(R,\phi,\tau) \tag{3.31}$$

that is 2π-periodic in τ, and where R and ϕ are constants for $\epsilon = 0$. We will take the above to be the solution for Eq. (3.30), with R and ϕ as slowly varying functions of τ for $0 < \epsilon \ll 1$. We also choose the constraint equation

$$x^{'} = \frac{\partial h}{\partial\tau}\,. \tag{3.32}$$

From Eqs. (3.31) and (3.32), we obtain

$$\frac{\partial h}{\partial R}R^{'} + \frac{\partial h}{\partial\phi}\phi^{'} = 0\,. \tag{3.33}$$

Similarly, from Eqs. (3.30) and (3.32), we obtain

$$\omega^2\left\{\frac{\partial^2 h}{\partial\tau^2} + \frac{\partial^2 h}{\partial\tau\partial R}R^{'} + \frac{\partial^2 h}{\partial\tau\partial\phi}\phi^{'}\right\} + \omega\frac{\partial\omega}{\partial R}\frac{\partial h}{\partial\tau}R^{'} + g = \epsilon F\,. \tag{3.34}$$

In Eq. (3.34), we have

$$\omega^2\frac{\partial^2 h}{\partial\tau^2} + g = 0$$

because h is an exact solution. Thus, we obtain

$$\left(\omega^2\frac{\partial^2 h}{\partial\tau\partial R} + \omega\frac{\partial\omega}{\partial R}\frac{\partial h}{\partial\tau}\right)R^{'} + \omega^2\frac{\partial^2 h}{\partial\tau\partial\phi}\phi^{'} = \epsilon F\,. \tag{3.35}$$

Solving Eqs. (3.33) and (3.35), we obtain (using subscripts to denote partial derivatives)

$$R^{'} = -\epsilon\frac{h_\phi F}{\omega^2\left(h_R h_{\tau\phi} - h_\phi h_{\tau R}\right) - \omega\omega_R h_\tau h_\phi}\,, \tag{3.36}$$

$$\phi^{'} = \epsilon\frac{h_R F}{\omega^2\left(h_R h_{\tau\phi} - h_\phi h_{\tau R}\right) - \omega\omega_R h_\tau h_\phi}\,. \tag{3.37}$$

Equations (3.36) and (3.37) can be τ-averaged in principle. Subsequently, using the fact that $\dot{\tau} = \omega$, we can recover the slow flow for R and ϕ in terms of the original unscaled time t.

The harmonic balance approximations of HBBA enter at this point. Since we do not have $\tilde{h}$ in closed form, we use an approximation of the form

$$\tilde{h} \approx C_0(R) + R\sin(\omega(R)t) + \sum_{k=2}^{N}\left\{B_k(R)\sin(k\omega(R)t) + C_k(R)\cos(k\omega(R)t)\right\}\,,$$

where R represents the amplitude of oscillation, the angular frequency $\omega(R)$ determines the fundamental period, and the B_k's, C_k's and ω are known functions of R obtained using harmonic balance (or, in fact, any other good approximation method). Replacing $\omega(R)t$ with $\tau + \phi$, we get an approximation to h from $\tilde{h}$.

Substituting the above approximations for h and ω in Eqs. (3.36) and (3.37) provides closed form approximations to the true $\mathcal{O}(\epsilon)$ vector field, in the form of Eq. (3.2), and which can in principle be averaged. However, averaging typically presents difficulties in practice in that the required integrals cannot be found in closed form. Here again, we use harmonic balance.

We assume the quantity to be averaged can be written as $\dfrac{r_1(R,\phi,\tau)}{r_2(R,\phi,\tau)}$, where r_1 and r_2 are trigonometric polynomials. We choose an integer $N \geq 1$ and approximate

$$\frac{r_1(R,\phi,\tau)}{r_2(R,\phi,\tau)} \approx a_0 + \sum_{k=1}^{N} \left(a_k \cos k\tau + a_{k+N} \sin k\tau\right) ,$$

which in turn we rewrite as

$$r_1(R,\phi,\tau) \approx r_2(R,\phi,\tau) \times \left\{ a_0 + \sum_{k=1}^{N} \left(a_k \cos k\tau + a_{k+N} \sin k\tau\right) \right\} . \tag{3.38}$$

The above yields a system of $2N+1$ simultaneous linear equations by harmonic balance [103], which are solved for a_k, $k = 0, 1, \cdots, 2N$. The coefficient a_0 then approximates the average. If k harmonics are used in the initial approximation to the periodic solutions, and if N harmonics are used in the averaging procedure described above, then the procedure is referred to as (k, N) averaging.

3.4.2 Delayed terms

Consider a cubic oscillator with light delayed damping

$$\ddot{x}(t) + x(t)^3 = -\epsilon x(t-1) . \tag{3.39}$$

We take two term harmonic balance and assume a solution of the form

$$x = R \sin \omega t + \nu R \sin 3\omega t . \tag{3.40}$$

On balancing harmonics (see, e.g., [103]), we find $\nu \approx -3/67$. Also, $\omega \approx 8R/9$. The approximate solution h of Eq. (3.31) is

$$x = R \left(\sin(\tau + \phi) - \frac{3}{67} \sin(3\tau + 3\phi) \right) . \tag{3.41}$$

Also, $x(t-1) = x(\tau - \omega)$. Substituting for $F = -x(\tau - \omega)$ in Eqs. (3.36) and (3.37) (the expressions are lengthy and not reproduced here), and carrying out $(2, 6)$ averaging, we get

$$R' = \frac{\epsilon}{R} \left(0.41284 \sin\left(\frac{8R}{9}\right) + 0.00226 \sin\left(\frac{8R}{3}\right) \right) ,$$

$$\phi' = \frac{\epsilon}{R^2} \left(0.41599 \cos\left(\frac{8R}{9}\right) + 0.00116 \cos\left(\frac{8R}{3}\right) \right) .$$

Multiplying the above with $\omega(R)$, we get the averaged equations in the original time t as

$$\dot{R} = \epsilon \left(0.36697 \sin\left(\frac{8R}{9}\right) + 0.00201 \sin\left(\frac{8R}{3}\right) \right) , \tag{3.42}$$

and

$$\dot{\phi} = \frac{\epsilon}{R} \left(0.36977 \cos\left(\frac{8R}{9}\right) + 0.00103 \cos\left(\frac{8R}{3}\right) \right) . \tag{3.43}$$

It is interesting to note, in the slow flows above, the trigonometric dependence on R. This is a consequence of the delay as well as the strong nonlinearity. The slow flow predicts infinitely many limit cycles. For limit cycles with very large R, however, ϵ may need to be very small indeed for the approximation to be good.

Solving the above two equations numerically along with

$$\dot{\tau} = \omega(R) = \frac{8}{9} R$$

gives the response of the system through Eq. (3.41). Results are shown in Fig. 3.3. Note that the maximum value of the approximate solution is actually $x = \dfrac{70}{67}R$, and so a $\dfrac{70}{67}$ scaled version of R has been plotted to represent the averaged amplitude. The match is good, both for amplitude and phase (the latter shows a small error over many cycles).

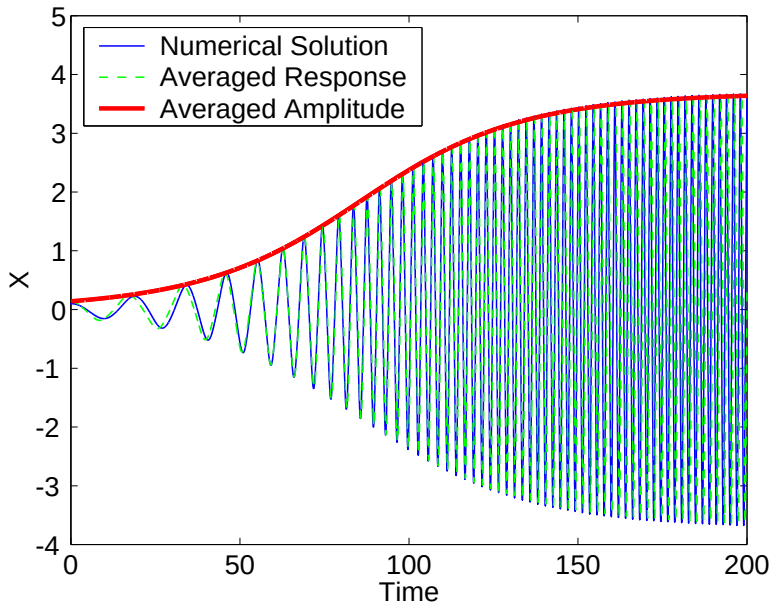

Figure 3.3: Numerical solution of Eq. (3.39) and Eqs. (3.42) and (3.43) for $\epsilon = 0.1$. Initial conditions: $x(\eta) = 0.1\cos(\eta)$, $\dot{x}(\eta) = -0.1\sin(\eta)$, $\eta \in [-1, 0]$, $R(0) = 0.14$, $\phi(0) = \frac{\pi}{2}$. 'Averaged amplitude' refers to $\frac{70}{67}R$.

3.4.3 Fractional damping

We now consider the same cubic oscillator, but with light fractional damping

$$\ddot{x} + x^3 = -\epsilon D^{1/2}x\,. \tag{3.44}$$

We use the same two term harmonic balance as before.

The relation between $D^{1/2}x(t)$ and $D^{1/2}x(\tau)$ is obtained by introducing $u = \omega s$ in

$$D^{1/2}x(t) = \frac{1}{\Gamma(1/2)}\int_0^t \frac{\dot{x}(t-s)}{\sqrt{s}}ds = \frac{1}{\Gamma(1/2)}\int_0^\tau \frac{\omega x^{'}(\tau-u)}{\sqrt{u}/\sqrt{\omega}}\frac{du}{\omega}\,,$$

where, for our averaging purposes, ω is constant within the integral. This results in

$$D^{1/2}x(t) = \sqrt{\omega}D^{1/2}x(\tau)\,.$$

Using simplifications similar to those of section 3.3.3, we find that we may use

$$D^{1/2}x(\tau) = \frac{2}{201}R^{3/2}\left(-3\sqrt{3}\sin(3\tau+3\phi) + 67\cos(\tau+\phi) + 67\sin(\tau+\phi) - 3\sqrt{3}\cos(3\tau+3\phi)\right)\,. \tag{3.45}$$

Substituting for $F = -D^{1/2}x$ in Eqs. (3.36) and (3.37), we get the slow flow equations governing the evolution of R and ϕ. After $(2,6)$ averaging and multiplying by $\omega(R)$, we obtain

$$\dot{R} = -0.24697\sqrt{R}\,\epsilon\,, \tag{3.46}$$

$$\dot{\phi} = \frac{0.24770}{\sqrt{R}}\,\epsilon\,. \tag{3.47}$$

For numerical comparisons, initial conditions for the averaged equations are obtained as follows. As mentioned earlier, $x(0) = 0$ and $\dot{x}(0) > 0$. From Eq. (3.41),

$$x(0) = R(0)\left(\sin(\phi(0)) - \frac{3}{67}\sin(3\phi(0))\right) = 0,$$

where $R(0) \neq 0$ implies $\phi(0) = 0$. Also

$$\dot{x}(0) = \left.\frac{dx(\tau)}{d\tau}\right|_{\tau=0}\left.\frac{d\tau}{dt}\right|_{\tau=0} = R(0)\left(\cos(\phi(0)) - \frac{9}{67}\cos(3\phi(0))\right)\omega(R(0))$$

$$= \frac{8}{9} R^2(0) \left(\cos(\phi(0)) - \frac{9}{67} \cos(3\phi(0)) \right) .$$

Substituting $\phi(0) = 0$ and solving, we get

$$R(0) = \sqrt{\frac{9}{8}} \sqrt{\frac{67}{58}} \sqrt{\dot{x}(0)} = \sqrt{\frac{603}{464}} \sqrt{\dot{x}(0)} = 1.14 \sqrt{\dot{x}(0)} .$$

The numerically computed averaged amplitude, $\frac{70}{67} R$ as before, compares well with the full numerical solution in Fig. 3.4.

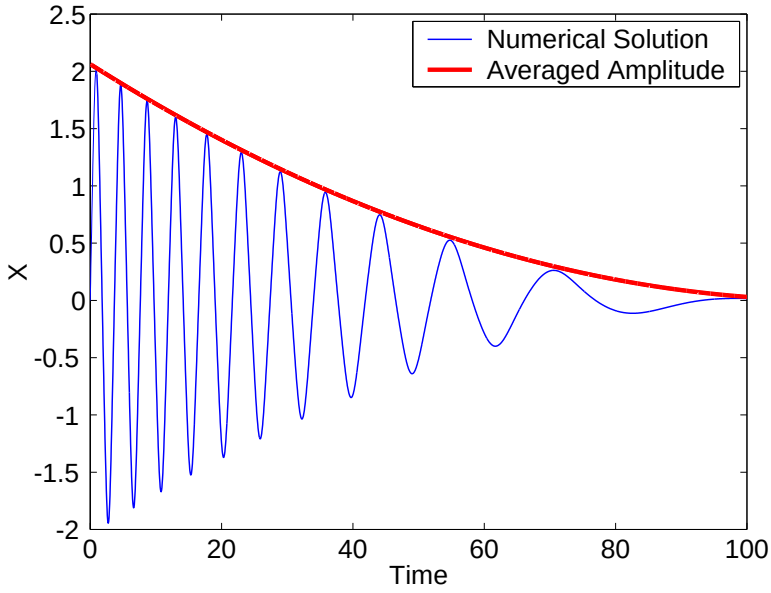

Figure 3.4: Numerical solution of Eq. (3.44) and Eqs. (3.46) and (3.47) for $\epsilon = 0.1$. Initial conditions : $x(0) = 0$, $\dot{x}(0) = 3$, $R(0) = 1.14 \times \sqrt{3} = 1.9745$, $\phi(0) = 0$.

3.4.4 Coexisting traditional, delayed and fractional damping

It is interesting to consider the following system, which has three types of damping (traditional, delayed and fractional order)

$$\ddot{x}(t) + x(t)^3 = -\epsilon \left(\alpha \, \dot{x}(t) + \beta \, D^{1/2} x(t) + \gamma \, \dot{x}(t-1) \right) . \tag{3.48}$$

Proceeding as above, the averaged equations are

$$\dot{R} = \epsilon \left(-0.33155 \, \alpha \, R - 0.32619 \, \gamma \, R \cos\left(\frac{8R}{9}\right) - 0.00536 \, \gamma \, R \cos\left(\frac{8R}{3}\right) - 0.24697 \, \beta \, \sqrt{R} \right) ,$$

$$\dot{\phi} = \epsilon \left(0.24770 \, \frac{\beta}{\sqrt{R}} + 0.32868 \, \gamma \, \sin\left(\frac{8R}{9}\right) + 0.00274 \, \gamma \, \sin\left(\frac{8R}{3}\right) \right) .$$

Figures 3.5 through 3.8 present numerical results for Eq. (3.48) and the averaged equations, for different values of α, β and γ.

For $\gamma = 0$, i.e., in the absence of delayed damping, the amplitude evolves as

$$\dot{R} = \epsilon \sqrt{R} \left(-0.33155 \, \alpha \, \sqrt{R} - 0.24697 \, \beta \right) .$$

There are no limit cycles.

For $\beta = 0$, the oscillator has traditional as well as delayed damping. The equation for amplitude is then

$$\dot{R} = \epsilon \, R \left(-0.33155 \, \alpha \, - 0.32619 \, \gamma \, \cos\left(\frac{8R}{9}\right) - 0.00536 \, \gamma \, \cos\left(\frac{8R}{3}\right) \right) .$$

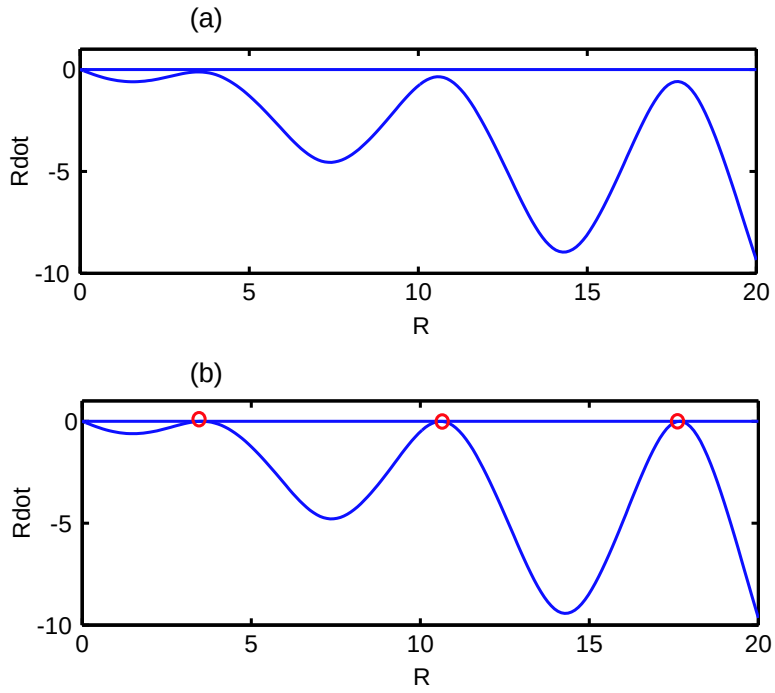

Figure 3.5: $\dot{R}$ versus R for $\beta = 0$, (a) $\alpha = 1$, $\gamma = 0.9$, (b) $\alpha = 1$, $\gamma = 1$.

Plots of $\dot{R}$ versus R for two sets of α and γ are shown in Fig. 3.5. For $\gamma = 0.9$ and $\alpha = 1$, all the solutions approach $R = 0$ (there are no limit cycles). Holding $\alpha = 1$ fixed and increasing γ through 1, there occur infinitely many simultaneous saddle-node bifurcations, and infinitely many pairs of stable and unstable limit cycles are born (by first order averaging). Numerical solutions are shown in Fig. 3.6 for $\gamma = 0.9$ and $\alpha = 1$. The amplitude decay rates correspond well with Fig. 3.5.

Finally, we consider $\alpha = 0$, when traditional linear damping is absent. Now the amplitude evolution is given by

$$\dot{R} = \epsilon \sqrt{R} \left(-0.32619\, \gamma \sqrt{R} \cos\left(\frac{8R}{9}\right) - 0.00536\, \gamma \sqrt{R} \cos\left(\frac{8R}{3}\right) - 0.24697\, \beta \right).$$

There are now infinitely many limit cycles whenever γ is nonzero; for large R the first order (delayed) damping term overwhelms the half order derivative.

A plot of $\dot{R}$ versus R for two sets of β and γ is shown in Fig. 3.7. A phase plot of the original system for $\epsilon = 0.06$, $\alpha = 0$, $\beta = 1$ and $\gamma = 1$ is given in Fig. 3.8 shows the first few stable limit cycles. The correspondence with Fig. 3.7(a) is good.

3.4.5 A nonanalytic system

The strong cubic nonlinearity considered above could be tackled exactly (without harmonic balance approximations) using elliptic functions as well (e.g., [110]). However, HBBA can handle a much broader range of nonlinearities. To demonstrate, we now consider the nonanalytic system

$$\ddot{x}(t) + x(t)\,|x(t)| + \epsilon \left(\alpha\, \dot{x}(t) + \beta\, D^{1/2} x(t) + \gamma\, \dot{x}(t-1) \right) = 0\,. \tag{3.49}$$

Using a two term harmonic balance identical to Eq. (3.40), we obtain $\omega \approx \dfrac{63}{68}\sqrt{R}$ and approximate h as

$$x = R \left(\sin(\tau + \phi) - \frac{53}{2005} \sin(3\tau + 3\phi) \right).$$

Proceeding as before and using $(2, 6)$ averaging, we obtain

$$\dot{R} = \epsilon\, R^{3/4} \left(-0.29340\, \beta - 0.40050\, \alpha\, R^{1/4} - 0.39785\, \gamma\, R^{1/4} \cos\left(\frac{63}{68}\sqrt{R}\right) - 0.00265\, \gamma\, R^{1/4} \cos\left(\frac{189}{68}\sqrt{R}\right) \right)$$

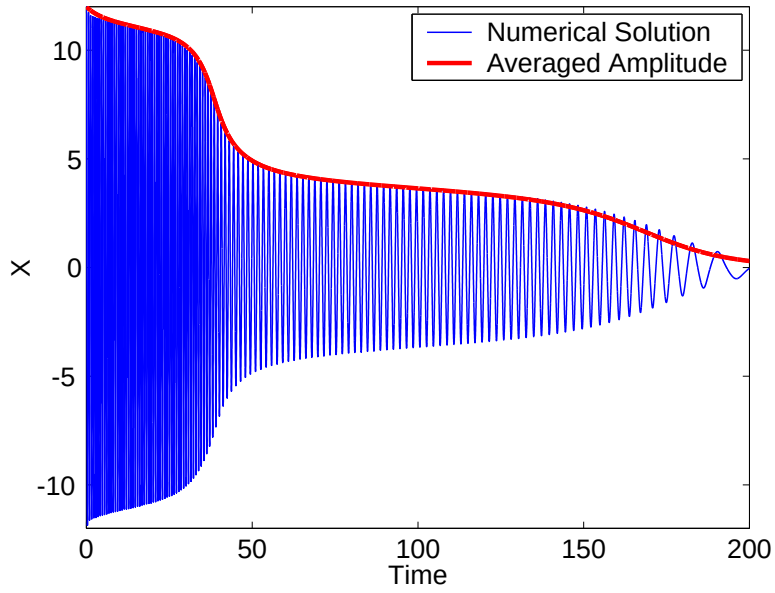

Figure 3.6: Numerical solution of Eq. (3.48) and the corresponding averaged equations for $\epsilon = 0.1$, $\beta = 0$, $\alpha = 1$, $\gamma = 0.9$. Initial conditions : $x(\eta) = 12\cos(\eta)$, $\dot{x}(\eta) = -12\sin(\eta)$, $\eta \in [-1, 0]$, $R(0) = 67/70 \times 12 = 11.4857$, $\phi(0) = \frac{\pi}{2}$.

and

$$\dot{\phi} = \frac{\epsilon}{R^{1/4}} \left(0.29214\,\beta + 0.39729\,\gamma\,R^{1/4} \sin\left(\frac{63}{68}\sqrt{R}\right) + 0.00065\,\gamma\,R^{1/4} \sin\left(\frac{189}{68}\sqrt{R}\right)\right).$$

Numerical results, in Fig. 3.9, are good. Thus, nonanalyticity in the unperturbed equation does not lead to any trouble while using HBBA.

3.5 Concluding remarks

The method of averaging has been applied to study small perturbations to conservative oscillators which may be strongly nonlinear. The perturbations studied include delayed terms and fractional derivative terms. Averaging for the case of fractional derivatives corresponds to the general or aperiodic case and involves an infinite time average which, however, can be replaced using asymptotic arguments by a simpler finite time average corresponding to a periodic case.

A slightly perturbed harmonic oscillator is studied first to validate the averaging procedure in the presence of delays and fractional derivative terms. For strongly nonlinear systems, the recently developed approximate technique of HBBA [103] is used. Strongly nonlinear systems with cubic nonlinearity as well as a *nonanalytic* nonlinearity are considered (the latter is not easily tractable using, say, elliptic functions). The averaged dynamics closely match the full numerical solutions in all cases, verifying the validity of the averaging procedure as well as the harmonic balance approximations therein. Moreover, interesting dynamics is uncovered in the strongly nonlinear case with small delayed terms, where arbitrarily many stable and unstable limit cycles can coexist, and infinitely many simultaneous saddle-node bifurcations can occur (in the asymptotic limit).

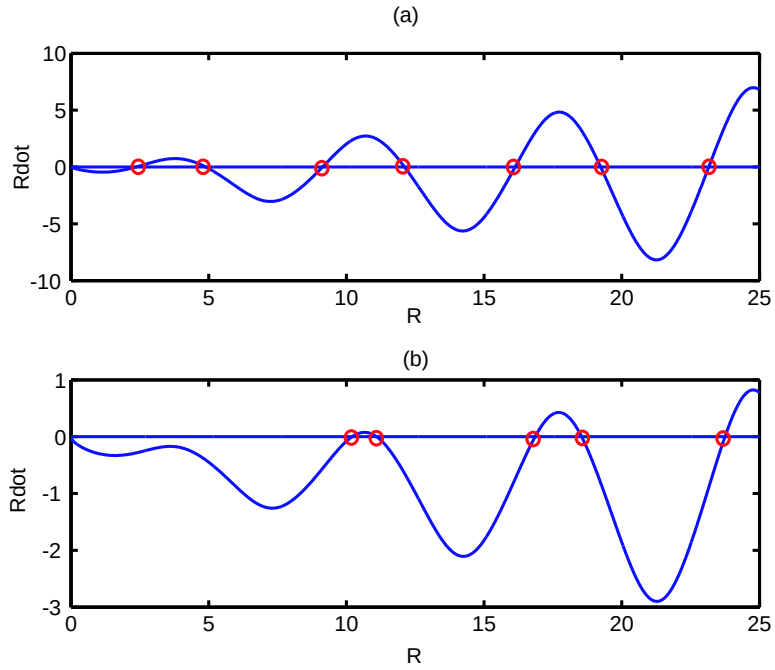

Figure 3.7: Plot of $\dot{R}$ versus R for $\alpha = 0$, (a) $\beta = 1$, $\gamma = 1$, (b) $\beta = 1$, $\gamma = 0.25$.

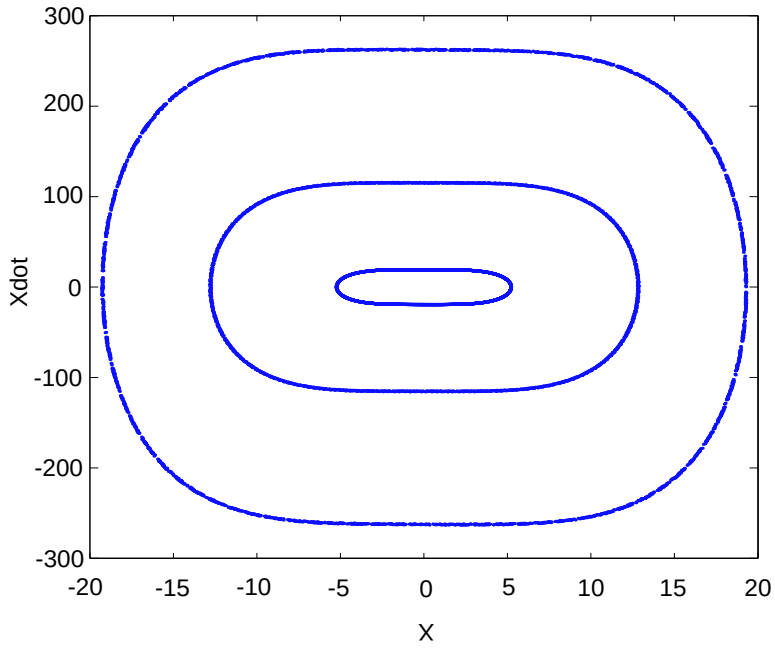

Figure 3.8: Phase plot of Eq. (3.48) for $\alpha = 0$, $\beta = 1$, $\gamma = 1$ and $\epsilon = 0.06$.

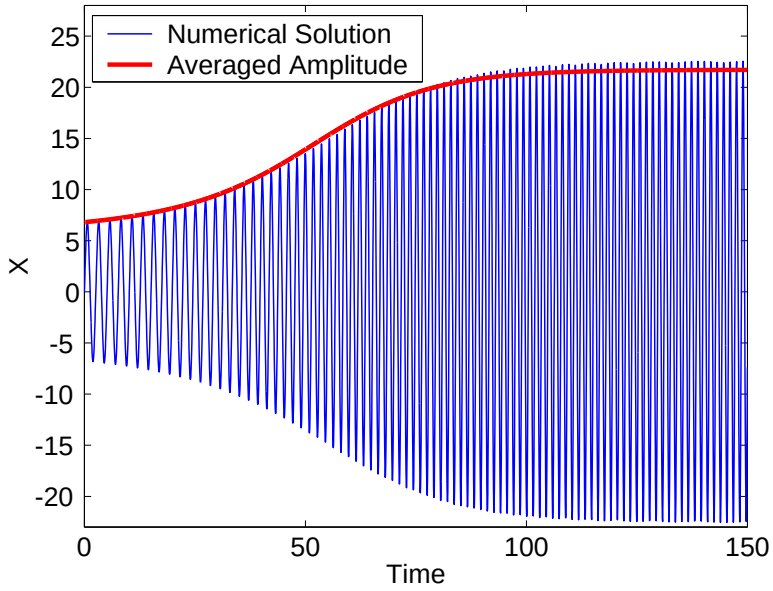

Figure 3.9: Numerical solution of Eq. (3.49) along with the numerical solution of the corresponding averaged equations for $\epsilon = 0.1$, $\alpha = 0.1$, $\beta = 1$, $\gamma = 1$. Initial conditions : $x(\eta) = 0$, $\eta \in [-1, 0]$, $\dot{x}(\eta) = 0$, $\eta \in [-1, 0)$, $\dot{x}(0) = 15$, $R(0) = 6.6$, $\phi(0) = 0$.

Chapter 4

Galerkin projections

This chapter presents a simple and effective Galerkin technique for obtaining low dimensional systems of ordinary differential equations (ODEs) which approximate the dynamics of the DDEs. The technique requires neither the system to be near a bifurcation point, nor the delayed terms to have any specific restrictive form, nor even the delay, nonlinearities and/or forcing to be small. The material of this chapter was published in [73] and also presented in [74].

4.1 Introduction

Although DDEs are infinite dimensional, their dynamics is often effectively restricted to a fairly small number of dimensions. Methods of describing and/or computing such low dimensional dynamics and their low dimensional descriptions are therefore of broad practical interest. This chapter presents a simple and effective Galerkin technique for obtaining low dimensional systems of ordinary differential equations (ODEs) which approximate the dynamics of the DDEs.

Several numerical techniques for direct forward simulations of DDEs, not explicitly based on low dimensional projections, are known [111, 112, 113, 114]. For the most part, these tend to be more complicated than (say) the most popular methods for ODEs. Moreover, a lot of easily available software exists for numerical analysis of ODEs, while the same is not yet true for DDEs. Thus projections giving ODEs from DDEs are of practical as well as academic interest.

Formal mathematical treatment of lower dimensional projections for DDEs tend to be complicated by the awkward functional analytic setting such calculations need for rigorous justification [68, 84]. Perhaps consequently, practical Galerkin projections for DDEs have so far been restricted to harmonic balance or variations thereof, to find either periodic or quasiperiodic solutions [9, 115, 116, 117, 118]. Harmonic balance is, however, limited in that it cannot be used to study transient behavior, the stability or instability of periodic solutions (except through additional Floquet theory calculations, see [9]), and complex aperiodic (chaotic) solutions.

If the delayed terms in a DDE are small, then straightforward application of well known perturbation methods can lead to low dimensional descriptions of the dynamics (see, e.g., [97, 98, 99]). The problem is more challenging when the delayed terms are not small. Available analytical techniques used for such cases include center manifold reductions near Hopf bifurcations [119, 120, 121, 122], direct treatment via normal forms at such near-bifurcation points (bypassing the center manifold reductions) [123, 124, 125], as well as direct application of the method of multiple scales at such points (bypassing normal forms) [9, 126]. Such descriptions, restricted near bifurcation points, are not well suited for detailed parameter studies.

A different analytical approach, not based on the usual perturbation methods, is provided by Roussel [45], who develops approximate descriptions of the low dimensional dynamics using "smallness" in the delay interval as well as simplifications afforded by assuming "long-time" behavior. Roussel's approach is limited to certain classes of DDEs, and not easily amenable to systematic refinement.

Another general approach to obtaining finite dimensional approximations for DDEs consists of developing maps to describe the evolution of the system over discrete time intervals (often equal to the delay interval) [23, 127, 128]. Within this approach is included the idea of temporal finite elements [127], where the delay interval is split into a number of subintervals over which (cubic Hermite) polynomials are used as shape functions; subsequently, the dynamics from delay interval to delay interval is expressed by a map. In the case of linear DDEs, the map is simple, and given by matrices of size proportional to the number of subintervals used. A related, but simpler, approach called semi-discretization [128] involves piecewise-constant approximations over subintervals within the delay interval; this also leads to maps.

Here, in contrast to the above approaches, we will use a Galerkin projection technique to directly obtain a set of ODEs that will provide excellent finite-dimensional approximations for the dynamics of several DDEs

(verified by comparisons with direct numerical simulations). Transient, periodic and aperiodic solutions will all be captured very satisfactorily by the low dimensional systems of ODEs. We note that ODEs have been obtained from DDEs using other, conceptually different, approaches [85, 129].

4.2 Theory

4.2.1 Delay differential equations

Many DDEs or Retarded Functional Differential Equations (RFDEs) can be written in the form

$$\dot{x}(t) \,=\, f\left(t, x(t), x_{\tau_1}(t), x_{\tau_2}(t), \cdots, x_{\tau_n}(t)\right), \quad \text{for } t > 0, \text{ and } x_s(0) \equiv x(-s) = X(s), s \in (0, \tau_n], \tag{4.1}$$

where $X(s)$ is a given "initial function." In the above, we define

$$x_\tau(t) \equiv x(t-\tau),$$

and assume n is a finite number, with

$$0 < \tau_1 < \tau_2 < \cdots < \tau_n = 1.$$

Note that if the largest delay in the system is *finite*, then scaling of time can always make it equal to unity. It will be clear below that we can easily include the more general case where f also depends on one or more quantities of the form (see pages $2-8$ of [68] for examples of applications)

$$\tilde{z} \equiv \int_0^1 z(s)\, g(x(t-s))\, ds\,,$$

where $z(s)$ represents a distributed delayed effect and g is some possibly nonlinear function. Including one or more such terms, we may write our general DDE as[1]

$$\dot{x}(t) \,=\, f\left(t, x(t), x_{\tau_1}(t), x_{\tau_2}(t), \cdots, x_{\tau_n}(t), \tilde{z}_1, \tilde{z}_2, \cdots\right), \quad \text{with } x(-s) = X(s), s \in (0, \tau_n]\,. \tag{4.2}$$

Note that $\dot{x}(t)$ does not depend on delayed values of itself, i.e., terms like $\dot{x}(t-\Delta)$; such equations, called *neutral* equations, where the highest order derivatives themselves appear with delayed arguments, are not considered here because their dynamics can be more complex than for DDEs.

By Eq. (4.2), $\dot{x}$ at time t depends on the values of x at various times within the interval $[t-1, t]$. Therefore, in the interval $(0,1)$, $\dot{x}$ has the same order of differentiability as x in the interval $(-1,0)$. For example, if x is discontinuous for $t \in (-1,0)$, then $\dot{x}$ is discontinuous for $t \in (0,1)$ but x is continuous there. In this way, as time proceeds, the solution gets smoother and smoother (this is *not* the case for neutral equations, which we avoid here). For this reason, in this chapter, we assume the solution is as smooth as necessary.

While calculating the evolution of $x(t)$, we need to keep track of the solution over the immediately preceding unit interval of time. To this end, we define an instantaneous local time interval $[0,1]$ with a local variable s. In this local interval, the function $x(t)$ coincides with a function $F(t,s)$ given by

$$F(t,s) \,=\, x_s(t) \,=\, x(t-s)\,. \tag{4.3}$$

The DDE governs the evolution of $F(t,s)$ with t.

4.2.2 Finite dimensional approximation

We approximate the function $F(t,s)$ by

$$F(t,s) \,=\, a_0(t) \,+\, a_1(t)\, s \,+\, \sum_{k=1}^{N-2} a_{k+1}(t)\, \sin(k\pi s)\,, \tag{4.4}$$

where N is a finite number that we choose. Note that any function of interest can be expressed on a finite interval as a Fourier sine series superposed on a straight line, as shown in Fig. 4.1.

Also, we automatically have

$$x(t) \,\equiv\, F(t,0) \,=\, a_0(t)\,. \tag{4.5}$$

The other components $a_i(t)$ represent other dimensions in the dynamics, and will be coupled with $a_0(t)$ in the ODEs we seek.

[1] We have retained for clarity the terms $x_\tau(t)$ although they could be written as $\displaystyle\int_0^1 \delta(s-\tau)\, x(t-s)\, ds$, where δ represents the Dirac delta function.

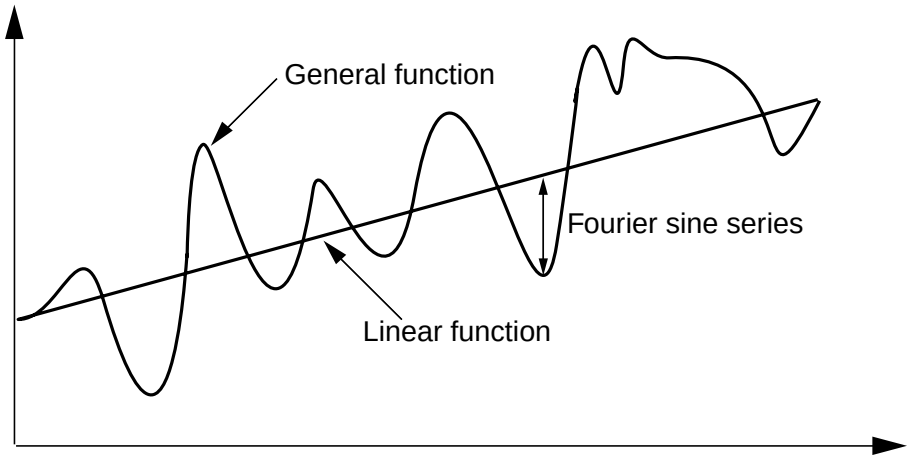

Figure 4.1: On a finite interval, an arbitrary function = a linear function + a Fourier sine series.

4.2.3 Standard Galerkin projections

Usually, in Galerkin projections for ODEs like

$$\dot{x} - f(t, x) = 0\,,$$

one substitutes an approximate solution of the form

$$x(t) \approx \sum_{i=1}^{N} a_i\, \phi_i(t)\,,$$

where the a_i are undetermined constants and the ϕ_i are user-selected shape functions. One then sequentially multiplies the residual with N distinct weighting functions (most commonly chosen to be the shape functions ϕ_i themselves), integrates over an interval of interest, and sets the integral equal to zero in each case. This process yields N simultaneous algebraic equations for the a_i.

In contrast, for PDEs of the form (say)

$$u_t - f(t, y, u, u_y, u_{yy}) = 0\,,$$

one substitutes an approximate solution given by

$$u(t, y) \approx \sum_{i=1}^{N} a_i(t)\, \phi_i(y)\,,$$

where the $a_i(t)$ are now undetermined functions of time and the $\phi_i(y)$ are user-selected shape functions. One then sequentially multiplies the residual with N functions of y (often the ϕ_i themselves), integrates over y, sets the integrals equal to zero, and obtains N simultaneous ODEs for the $a_i(t)$.

Our aim, for DDEs, is to obtain a system of ODEs governing the evolution of a finite number of state variables. A straightforward Galerkin procedure seems somewhat awkward now (unlike the situation where one seeks periodic solutions, uses harmonic balance, and obtains algebraic equations). For example, consider the equation

$$\dot{x}(t) + x(t-1) = 0\,.$$

Galerkin projections involve inner products, which usually mean integration; and here the logical integration domain seems to be a moving window of unit length. Since we also wish to retain some time dependence at the end of the integration process, we must both integrate over a time-like variable while holding some time-like variable constant. These issues motivate our Galerkin procedure.

4.2.4 Galerkin procedure for DDEs

As will be clear, our procedure pays particular attention to the right endpoint of the unit interval. Subsequently, attention is paid to the whole unit interval. The steps in the procedure are given below.

1. Differentiating Eq. (4.5) with respect to t, we obtain

$$\dot{a}_0(t) \;= \dot{x}(t)\,. \tag{4.6}$$

In the above, we substitute into the right hand side the quantity f from the right hand side of the original DDE, i.e., Eq. (4.2), where in turn quantities like $x_{\tau_1}(t)$ are obtained by substituting $s = \tau_1$ in Eq. (4.4). This gives an explicit equation of the form

$$\dot{a}_0(t) \;= f_{re}\,, \tag{4.7}$$

where the subscript "re" denotes right endpoint.

2. We now turn to the interior of the unit interval. Here, from Eq. (4.3), we have

$$F(t,s) = x(t-s)\,.$$

The above implies

$$\frac{\partial F}{\partial t} + \frac{\partial F}{\partial s} \;= 0\,. \tag{4.8}$$

Substituting Eq. (4.4) in the above we get

$$\dot{a}_0(t) + \dot{a}_1(t)\,s + \sum_{k=1}^{N-2} \dot{a}_{k+1}(t)\sin(k\pi s) + a_1(t) + \sum_{k=1}^{N-2} a_{k+1}(t)k\pi\cos(k\pi s) = 0\,.$$

The above equation cannot hold identically but gives us, instead, the framework for a Galerkin projection. Having obtained a condition for the evolution of $a_0(t)$ (Eq. (4.7)), we now seek the evolutions of the remaining $N-1$ coefficients $a_i(t)$. Accordingly, we take inner products with the shape functions multiplying these coefficients, to obtain the following $N-1$ equations:

$$\int_0^1 \left\{ \dot{a}_0(t) + \dot{a}_1(t)\,s + \sum_{k=1}^{N-2} \dot{a}_{k+1}(t)\sin(k\pi s) + a_1(t) + \sum_{k=1}^{N-2} a_{k+1}(t)k\pi\cos(k\pi s) \right\} \cdot\; s\,ds = 0 \tag{4.9}$$

and

$$\int_0^1 \left\{ \dot{a}_0(t) + \dot{a}_1(t)\,s + \sum_{k=1}^{N-2} \dot{a}_{k+1}(t)\sin(k\pi s) + a_1(t) + \sum_{k=1}^{N-2} a_{k+1}(t)\,k\pi\cos(k\pi s) \right\} \cdot \sin(m\pi s)\,ds = 0\,, \tag{4.10}$$

for $m = 1, 2, \cdots, N-2$.

Note that the above integrals are not dependent on the original DDE. Only the assumed form of Eq. (4.4) enters these calculations. However, $\dot{a}_0(t)$, itself determined by Eq. (4.7), drives the other $\dot{a}_i(t)$ in Eqs. (4.9) and (4.10).

3. Combining Eqs. (4.7), (4.9) and (4.10), we obtain N simultaneous linear algebraic equations in the N unknowns, $\dot{a}_0, \dot{a}_1, \cdots, \dot{a}_{N-1}$, which gives our system of ODEs for subsequent analysis.

4.3 Examples

In this section, we will apply the foregoing method to several different DDEs. In each case, suitable comparisons will be made between numerical results obtained directly from the DDE and those obtained from the ODEs. In what follows, numerical solutions of nonlinear DDEs were all obtained using a fixed step fourth order Runge Kutta routine adapted to remember, interpolate and incorporate past values.

4.3.1 A linear DDE

Consider

$$\dot{x}(t) \;+ x(t) \;+ x(t - 1/\sqrt{2}) \;+ x(t-1) \;+ \int_0^1 x(t-s)\,\cos(s)\,ds = 0\,. \tag{4.11}$$

We note that the characteristic roots of this equation is studied in detail in chapter 2. Taking $N = 4$, we obtain

$$F(t,s) = a_0(t) + a_1(t)s + a_2(t)\sin(\pi s) + a_3(t)\sin(2\pi s).$$

Equation (4.7), applied to Eq. (4.11), becomes

$$\dot{a}_0 = -\left\{ F(t,0) + F(t,1/\sqrt{2}) + F(t,1) + \int_0^1 F(t,s)\cos(s)\,ds \right\} .$$

The remaining three equations needed are given by Eqs. (4.9) and (4.10). Finally, we obtain

$$\begin{aligned}
\dot{a}_0 &= -3.8415\,a_0 - 2.0889\,a_1 - 1.3413\,a_2 + 0.8888\,a_3 \,, \\
\dot{a}_1 &= 4.5463\,a_0 + 1.2887\,a_1 + 4.2390\,a_2 - 11.6582\,a_3 \,, \\
\dot{a}_2 &= 1.9968\,a_0 + 0.5660\,a_1 - 0.9908\,a_2 + 8.9568\,a_3 \,, \\
\dot{a}_3 &= 1.4471\,a_0 + 0.4102\,a_1 - 1.3174\,a_2 - 3.7109\,a_3 \,.
\end{aligned}$$

The eigenvalues of the coefficient matrix in the above system of ODEs are $-0.1662 \pm 2.4979\,i$ and $-3.4611 \pm 3.9056\,i$. The first one matches well with the numerically obtained $-0.1639 \pm 2.4749\,i$.

Table 4.1: Characteristic roots of Eq. (4.11)

N	Roots					
4	-0.1662 $\pm\ 2.4979\,i$	$\mathbf{-3.4611}$ $\mathbf{\pm 3.9056}\,i$	–	–	–	–
6	-0.1675 $\pm\ 2.4826\,i$	-1.1387 $\pm\ 8.8467\,i$	$\mathbf{-4.7083}$ $\mathbf{\pm 5.0461}\,i$	–	–	–
8	-0.1670 $\pm\ 2.4784\,i$	-1.7552 $\pm\ 8.9150\,i$	-0.9704 $\pm\ 14.6150\,i$	$\mathbf{-5.6091}$ $\mathbf{\pm 6.1852}\,i$	–	–
10	-0.1650 $\pm\ 2.4770\,i$	-2.1044 $\pm\ 8.7924\,i$	-1.5400 $\pm\ 14.6970\,i$	-0.6828 $\pm\ 20.6504\,i$	$\mathbf{-6.5094}$ $\mathbf{\pm 7.3185}\,i$	–
12	-0.1647 $\pm\ 2.4763\,i$	-2.2899 $\pm\ 8.6498\,i$	-1.9803 $\pm\ 14.7132\,i$	-1.1054 $\pm\ 20.7812\,i$	-0.6164 $\pm\ 26.7833\,i$	$\mathbf{-7.2903}$ $\mathbf{\pm 8.4698}\,i$
14	-0.1647 $\pm\ 2.4760\,i$	-2.3819 $\pm\ 8.5320\,i$	-2.3482 $\pm\ 14.6663\,i$	-1.4425 $\pm\ 20.8671\,i$	-1.0126 $\pm\ 26.9623\,i$	-0.5678 $\pm 32.8533\,i$
16	-0.1645 $\pm\ 2.4756\,i$	-2.4022 $\pm\ 8.4484\,i$	-2.6084 $\pm\ 14.5422\,i$	-1.6974 $\pm\ 20.8954\,i$	-1.3125 $\pm\ 27.1081\,i$	-0.9378 $\pm 32.9952\,i$
18	-0.1643 $\pm\ 2.4756\,i$	-2.4070 $\pm\ 8.3957\,i$	-2.7790 $\pm\ 14.3950\,i$	-1.8982 $\pm\ 20.8933\,i$	-1.5513 $\pm\ 27.2184\,i$	-1.2372 $\pm 33.1424\,i$
20	-0.1643 $\pm\ 2.4754\,i$	-2.4150 $\pm\ 8.3598\,i$	-2.9001 $\pm\ 14.2541\,i$	-2.0729 $\pm\ 20.8792\,i$	-1.7611 $\pm\ 27.3073\,i$	-1.5008 $\pm 33.2691\,i$
Numerical	-0.1639 $\pm\ 2.4749\,i$	-2.3946 $\pm\ 8.2369\,i$	-2.8736 $\pm\ 13.6232\,i$	-2.6442 $\pm\ 20.2466\,i$	-3.2404 $\pm\ 27.0141\,i$	-3.8703 $\pm 32.8338\,i$

The match improves with increasing N, as shown in Tab. 4.1. The last row of Tab. 4.1 represents the roots of the characteristic equation of Eq. (4.11) found numerically using the Newton-Raphson method to 12 significant digits (not all shown here). Hence, we have treated them as the exact roots and the Galerkin projection roots are compared with these numerically found roots. In the first five rows of the tabulated results, a spurious root of steadily increasing magnitude and with fairly large negative real part (corresponding to rapid decay) is shown in boldface. It is seen that as N increases, this root eventually goes off far into the left half plane (see also Tab. 4.2). All other roots are seen converging towards their correct values (numerically found values as described above).

Table 4.2: Spurious root goes off into left half plane.

N	14	16	18	20
	-7.9866 $\pm\ 9.6362\,i$	-8.8018 $\pm\ 10.730\,i$	-9.6101 $\pm\ 11.7743\,i$	-10.3091 $\pm\ 12.8320\,i$

It is worthwhile to examine the pair of spurious roots in some detail. The pair of spurious roots represent rapidly decaying dynamics that plays no significant role over the time-scale of interest. The presence of this pair

of spurious roots is thus an insignificant artifact of the approximation scheme. As the approximation is refined, i.e., N increased, this root increases in magnitude and goes off to infinity towards the far left of the complex plane. Note that the correct large characteristic roots for this equation, found using asymptotics in [69], have real parts logarithmically related to the imaginary parts. The spurious roots obtained here are not one of these large roots in disguise.

The above discussion has a parallel with an issue in computing the natural frequencies of a structure using the finite element method. If we fix a range of frequencies (say $0 - 1000$ Hz) and refine the FE mesh further and further, the frequencies within this range converge to their exact values. However, for any given mesh the highest frequencies obtained are unreliable. Similarly for our problem, if we fix a circle of some radius around the origin and refine the approximation, i.e., increase N, the approximate roots contained in that semi-circle will converge to their exact values. The pair of spurious roots will eventually leave this circle, go into the far left half of the complex plane and become dynamically insignificant.

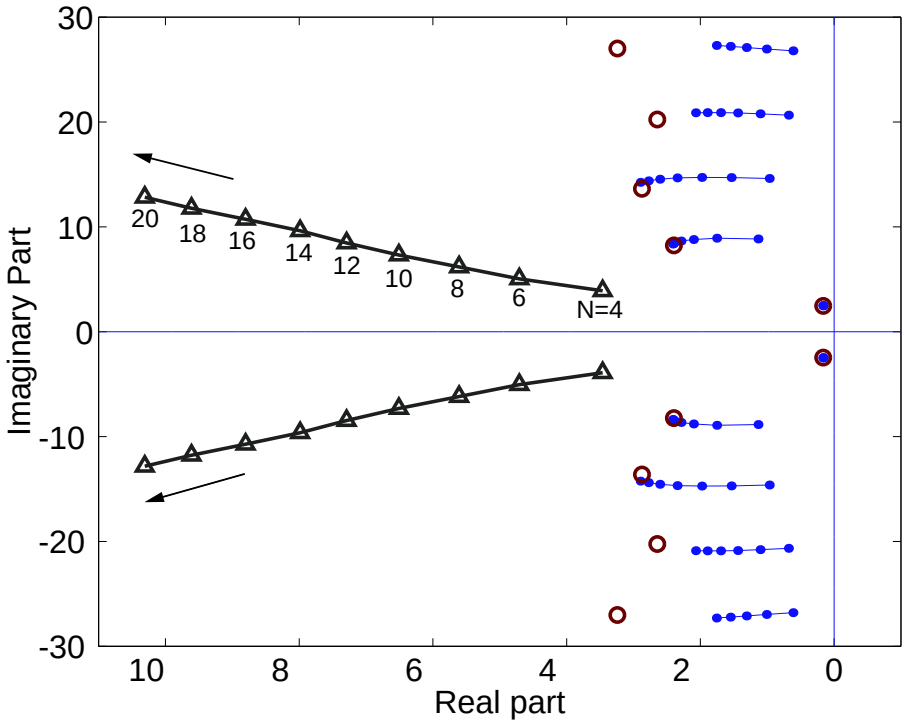

Figure 4.2: Characteristic roots of Eq. (4.11). Dots : converging roots through Galerkin Projection. Triangles : spurious roots. Circles : exact roots.

Note that several excellent methods for computing the characteristic roots of linear constant coefficient DDEs are available [69, 130, 86, 131], as are methods for determining the stability of given DDEs without necessarily finding the characteristic roots [14,15,39-42].The present Galerkin projection is not meant to compete with them. The foregoing example merely serves to illustrate the convergence of results obtained using this method, whose main utility is expected to be in obtaining ODE representations of *nonlinear* DDEs.

4.3.2 A nonlinear DDE

We now consider a periodically forced DDE with a single linear delayed term and an undelayed cubic nonlinearity,

$$\dot{x}(t) + b_1\, x(t-1) + b_2\, x(t)^3 = F \sin(\omega t)\,. \tag{4.12}$$

The system of nonlinear ODEs corresponding to Eq. (4.12) for $N = 5$ is presented below for clarity of expression

$$\dot{a}_0 = F \sin(\omega t) - b_1 a_0 - b_1 a_1 - b_2 a_0^3\,,$$

$$\dot{a}_1 = \frac{-1}{5\,(6\,\pi^2 - 49)} \left(45\,\pi^2 F \sin(\omega t) - 400\,F \sin(\omega t) - 276\,a_4 \pi + 400\,b_1 a_1 + 45\,a_1 \pi^2 - 45\,\pi^2 b_1 a_1\right.$$

$$-400\,a_1 - 45\,\pi^2 b_1 a_0 - 45\,\pi^2 b_2 a_0^3 - 60\,a_2\pi + 400\,b_1 a_0 + 400\,b_2 a_0^3 + 96\,a_3\pi\big)\ ,$$

$$\dot{a}_2 = \frac{-2}{15\,\pi(6\,\pi^2 - 49)}\big(45\,a_1\pi^2 - 45\,\pi^2 b_1 a_0 - 45\,\pi^2 b_1 a_1 + 45\,\pi^2 F\sin(\omega t) - 45\,\pi^2 b_2 a_0^3$$
$$-270\,F\sin(\omega t) + 828\,a_4\pi - 120\,a_3\pi^3 + 270\,b_1 a_1 - 270\,a_1$$
$$+270\,b_1 a_0 + 270\,b_2 a_0^3 + 180\,a_2\pi + 692\,a_3\pi\big)\ ,$$

$$\dot{a}_3 = \frac{-1}{15\,\pi(6\,\pi^2 - 49)}\big(135\,\pi^2 F\sin(\omega t) - 1200\,F\sin(\omega t) + 2700\,a_4\pi - 432\,a_4\pi^3 + 1200\,b_1 a_1$$
$$+135\,a_1\pi^2 - 135\pi^2 b_1 a_1 - 1200 a_1 - 135\,\pi^2 b_1 a_0 - 135\,\pi^2 b_2 a_0^3$$
$$-2140\,a_2\pi + 240\,a_2\pi^3 + 1200\,b_1 a_0 + 1200\,b_2 a_0^3 + 288\,a_3\pi\big)\ ,$$

$$\dot{a}_4 = \frac{-2}{5\,\pi(6\,\pi^2 - 49)}\big(-620\,a_3\pi + 30\,b_2 a_0^3 + 30\,b_1 a_1 + 30 b_1 a_0 - 30F\sin(\omega t) + 5\,a_1\pi^2 + 92\,a_4\pi$$
$$+20\,a_2\pi + 72\,a_3\pi^3 - 30\,a_1 + 5\,\pi^2 F\sin(\omega t) - 5\,\pi^2 b_2 a_0^3 - 5\pi^2 b_1 a_1 - 5\,\pi^2 b_1 a_0\big)\ .$$

But for computational purposes, we use $N = 9$ and choose the initial function as identically zero (all 9 state variables in the Galerkin projection also start from zero initial conditions). Results from direct numerical integration of the DDE and the corresponding ODEs are compared for two sets of parameter values, and somewhat different qualitative behaviors, in Figs. 4.3 and 4.4. In both cases, the match is very good both in the transient as well as the steady state behavior.

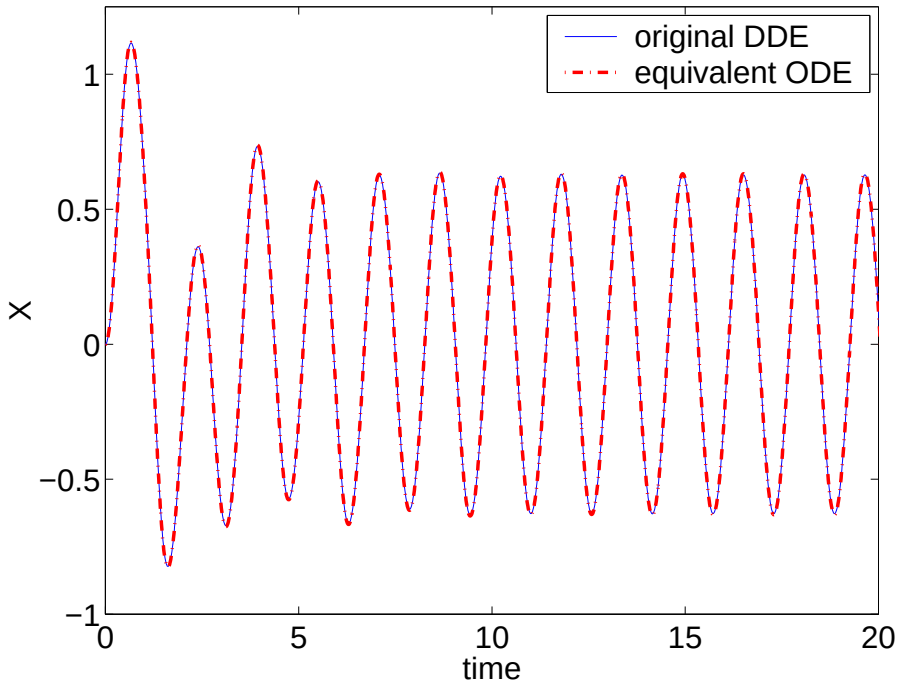

Figure 4.3: Numerical solution of Eq. (4.12) and the corresponding system of ODEs for $b_1 = b_2 = 1$, $F = 3$, $\omega = 4$, and $N = 9$.

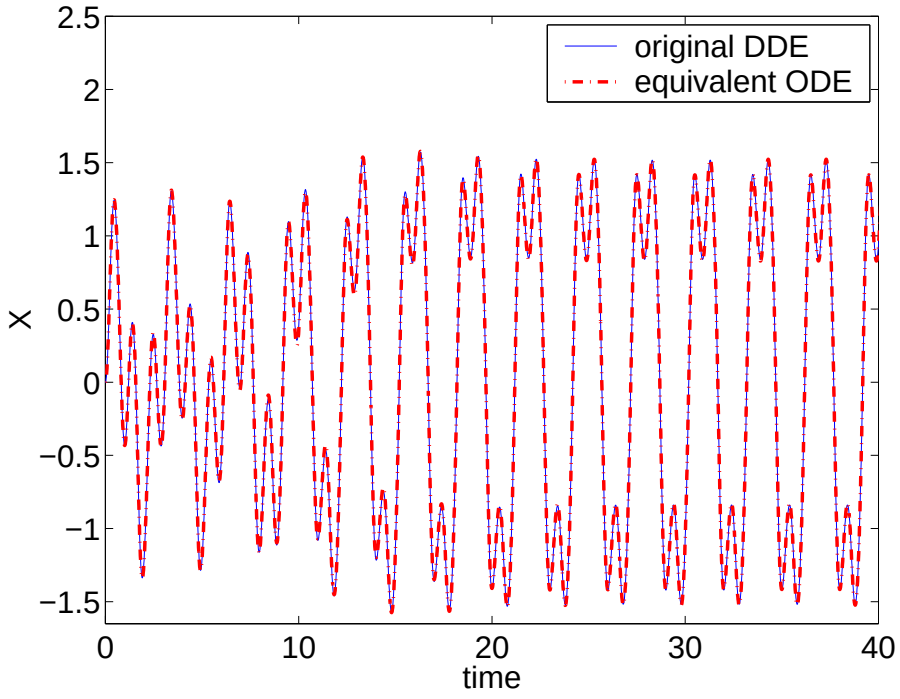

Figure 4.4: Numerical solution of Eq. (4.12) and the corresponding system of ODEs for $b_1 = 3\pi/4$, $b_2 = \pi/4$, $F = 3\pi/2$, $\omega = 2\pi$, $N = 9$.

4.3.3 More than one delay

We now consider

$$\dot{x}(t) + b_1\, x(t-1) + b_2\, x(t)^3 + b_3\, x(t-1/2) = F \sin(\omega t)\,, \tag{4.13}$$

which has two different delays.

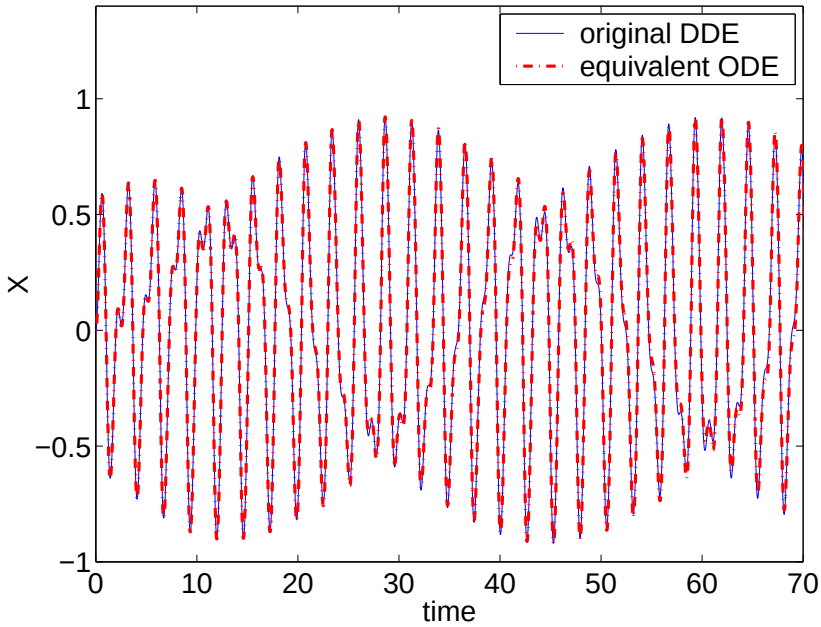

Figure 4.5: Numerical solution of Eq. (4.13) and the corresponding system of ODEs for $b_1 = b_2 = b_3 = F = \pi/2$, $\omega = 3\pi/2$, $N = 15$.

In this case good accuracy is achieved with $N = 15$, as seen from Fig. 4.5 (as before, all initial conditions were taken to be zero). With smaller N, the modulations in the solution were qualitatively present but quantitatively less accurate.

4.3.4 A nonlinear delayed term

Consider

$$\dot{x}(t) + b_1 x(t-1) + b_2 x(t)^3 + b_3 x(t-1/2)^2 = F \sin(\omega t)\,. \tag{4.14}$$

Results, shown in Fig. 4.6 for $N = 9$ and zero initial conditions, are very good.

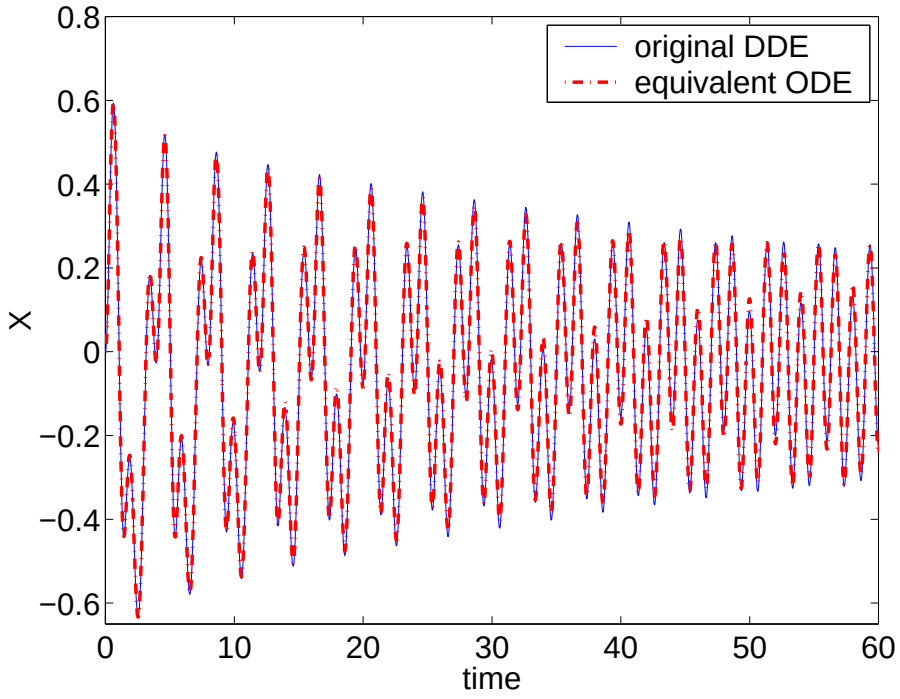

Figure 4.6: Numerical solution of Eq. (4.14) and the corresponding system of ODEs for $b_1 = b_2 = b_3 = F = \pi/2$, $\omega = 3\pi/2$, $N = 9$.

4.4 Parameter studies

The numerical study of any system often involves systematic investigation of the effects of changing parameters. The results are often displayed in bifurcation diagrams. Galerkin projections can be useful in this regard both in easy incorporation of bifurcation analysis algorithms for ODEs, as well as potential savings in run time (our own ODE calculations took 3 to 5 times less computer time than our corresponding DDE calculations, but further study with codes geared for efficiency is needed to verify this aspect).

We first study Eq. (4.12) under varying b_1, which represents the strength of the delayed term. For each b_1, we numerically solve the equations at hand (DDE or ODE), and locate those instants in time when $\dot{x} = 0$; we then find the values of x at those times and plot them, using dots, against the varying parameter. Results are shown in Figs. 4.7 through 4.9, for the original DDE, for ODEs with $N = 5$, and for $N = 9$ respectively. The pointwise match between DDE and ODE improves with increasing N; however, a qualitative picture that might be accurate enough for most purposes is obtained for a modest value of N.

In each figure, the two curves seen for near-zero values of the bifurcation parameter represent a single periodic motion (which has two points within each period when $\dot{x} = 0$).

Figure 4.10 shows zoomed portions of Figs. 4.7 through 4.9 with finer details. It is seen that the match is not perfect, but better for $N = 9$ than for $N = 5$.

It was mentioned above that in generating Figs. 4.7 through 4.9, the ODE solutions were obtained about three to five times (depending on N) more quickly than the DDE results. Thus, the Galerkin procedure allowed, at least in our study, significant savings in time at a modest cost in accuracy. More rigorous tests with well

written DDE codes, as well as possibly more efficient implementations of the Galerkin projections, may shed further light on the issue of time savings with the present Galerkin procedure. An anonymous reviewer of the journal version of this work [73] has expressed the opinion that the Galerkin projection may not, in the end, compete as well against DDE codes as our abovementioned results may suggest. Resolution of this question is a matter of future work.

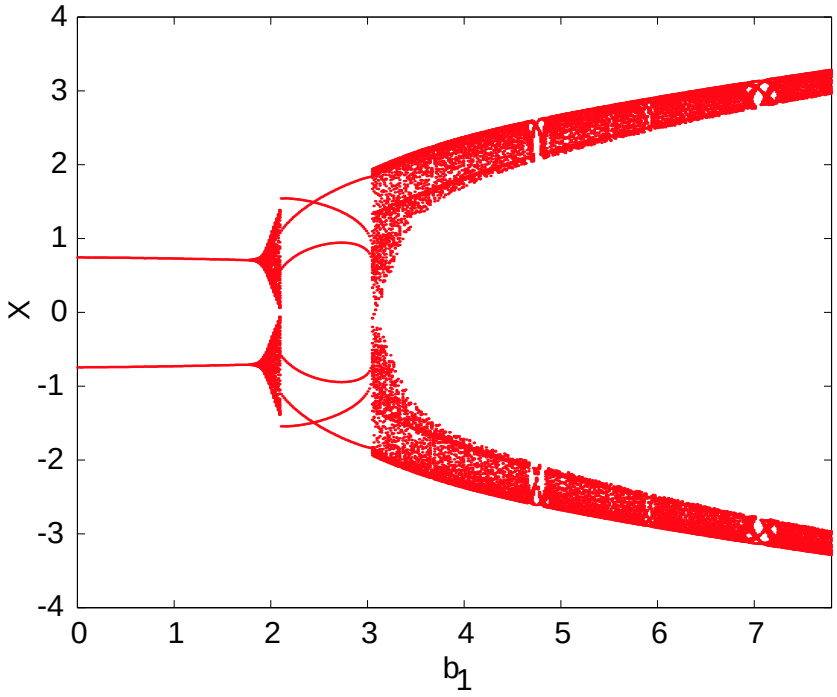

Figure 4.7: Equation (4.12) by direct numerical simulation: $b_2 = \pi/4$, $F = 3\pi/2$, $\omega = 2\pi$.

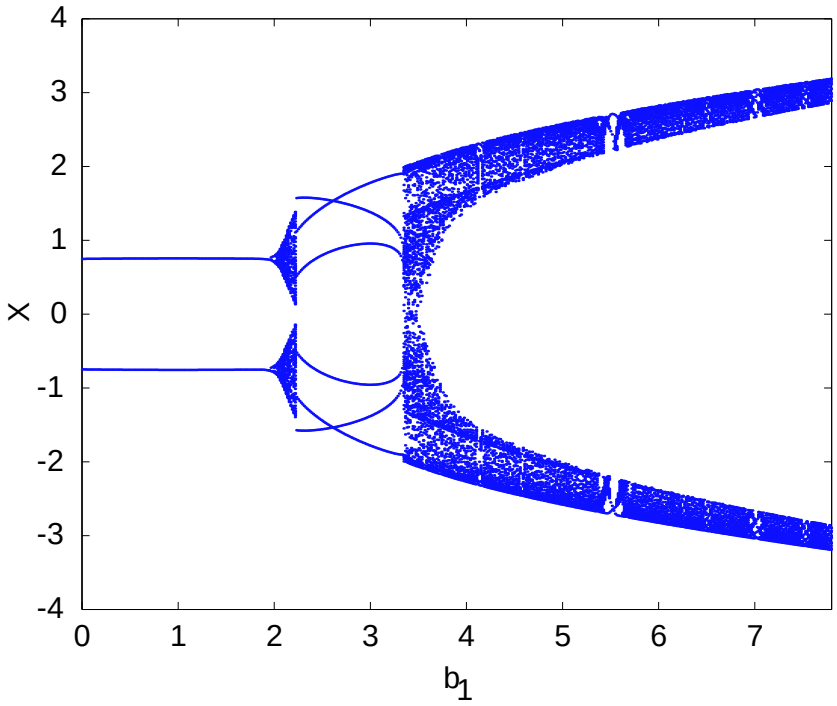

Figure 4.8: Equation (4.12) by numerical simulation of ODEs: same parameter as in Fig. 4.7, $N = 5$.

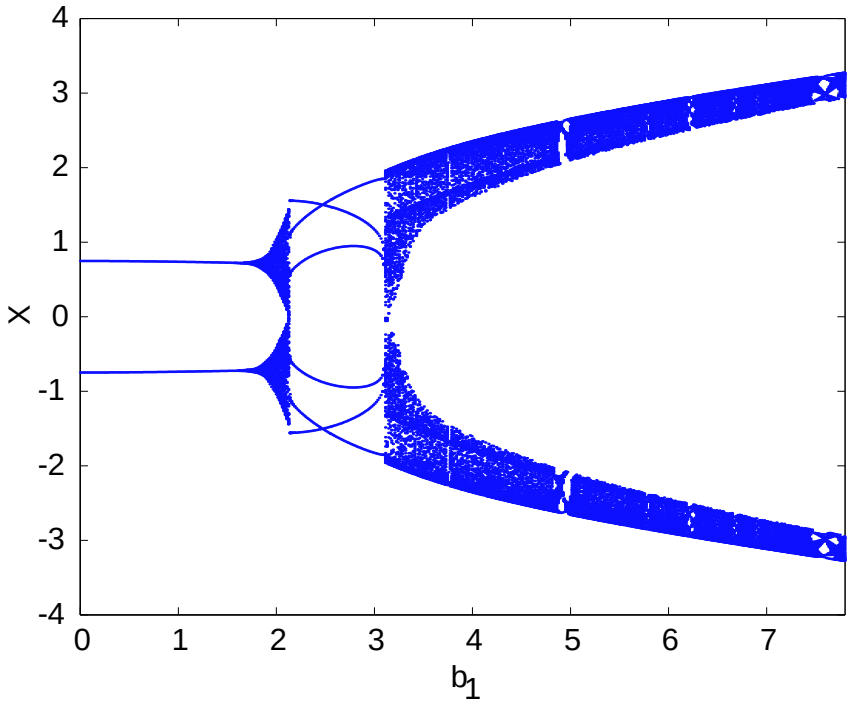

Figure 4.9: Same parameters as Fig. 4.7 with $N = 9$.

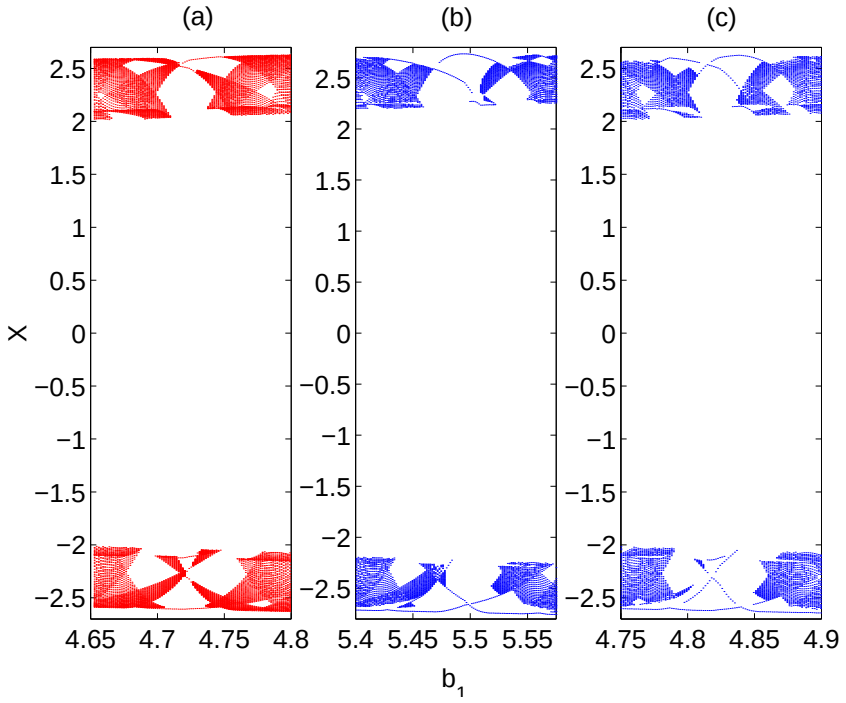

Figure 4.10: Zoomed portions, with finer details, of (a) Fig. 4.7, (b) Fig. 4.8, and (c) Fig. 4.9.

Next, we also generate bifurcation diagrams for Eqs. (4.13) and (4.14). Results are shown in Figs. 4.11 and 4.12 for Eq. (4.13), and Figs. 4.13 and 4.14 for Eq. (4.14). For both cases, the agreement is good between the bifurcation diagrams obtained from the original DDE and the reduced ODEs.

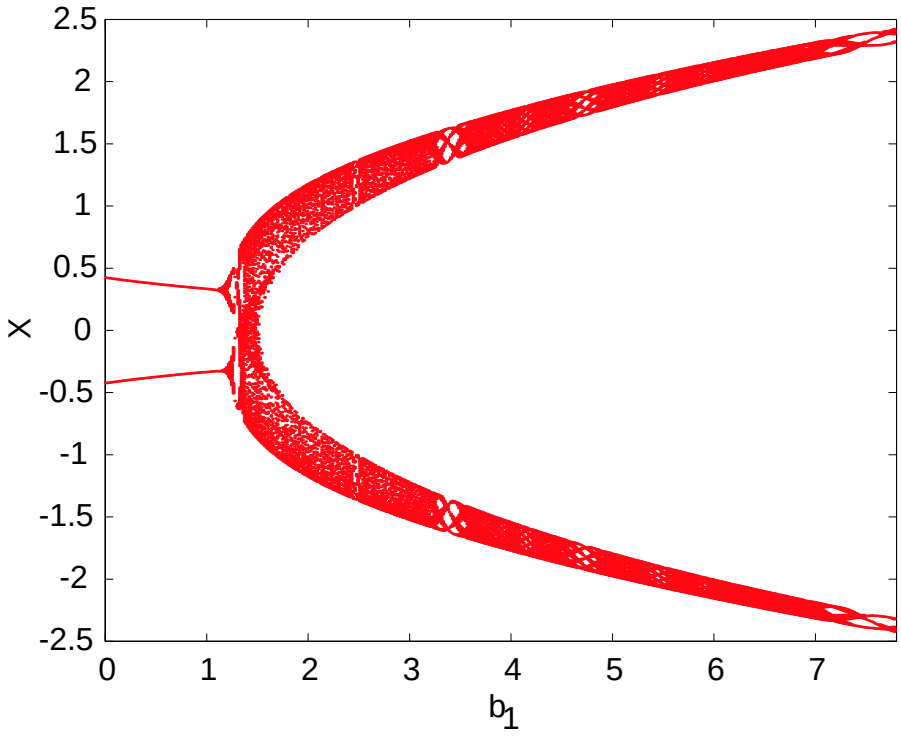

Figure 4.11: Equation (4.13) by direct numerical simulation: $b_2 = b_3 = F = \pi/2$, $\omega = 3\pi/2$.

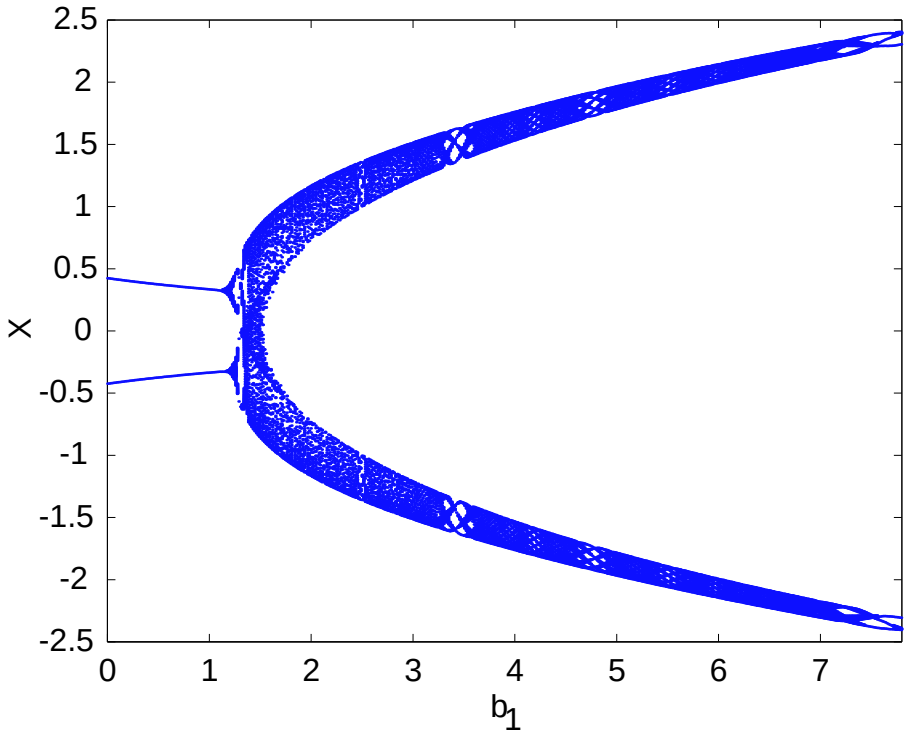

Figure 4.12: Equation (4.13) by numerical simulation of ODEs: same parameters as in Fig. 4.11, $N = 15$.

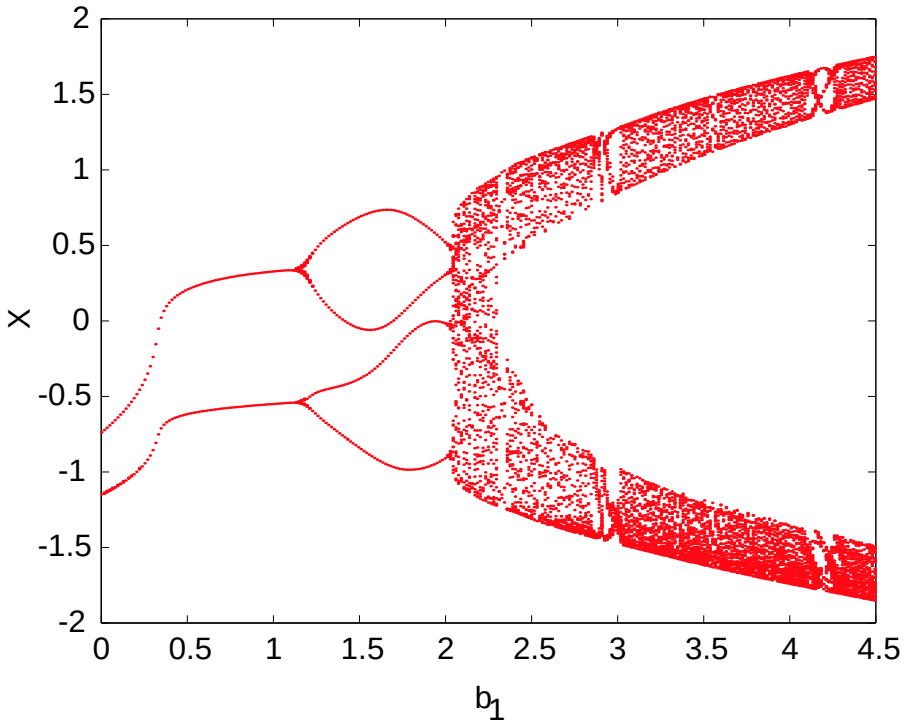

Figure 4.13: Equation (4.14) by direct numerical simulation: $b_2 = b_3 = F = \pi/2$, $\omega = 3\pi/2$.

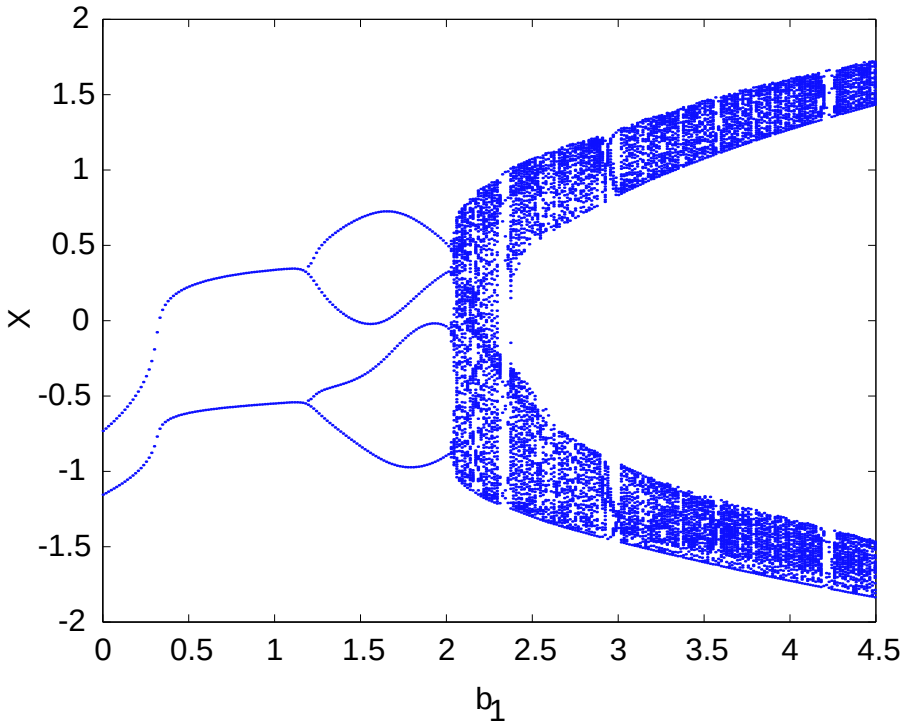

Figure 4.14: Equation (4.14) by numerical simulation of ODEs: same parameters as in Fig. 4.13, $N = 9$.

4.5 Concluding remarks

We have presented a Galerkin projection technique by which finite-dimensional ODE approximations for DDEs can be obtained in a straightforward fashion. The technique requires neither the system to be near a bifurcation point, nor the delayed terms to have any specific restrictive form, nor even the delay, nonlinearities and/or forcing to be small. The method presented here is not applicable to neutral systems.

We have shown through several numerical examples that the systems of ODEs obtained using this procedure can in fact accurately capture the dynamics of the DDEs under study. The accuracy of solutions increases with increasing numbers of shape functions used in the Galerkin projection. We expect the present technique to be useful in detailed numerical studies, including parameter studies, of nonlinear DDEs. In this preliminary work, we have presented the basic procedure and demonstrated its effectiveness using several numerical examples.

A numerical study of the convergence of this technique is presented in the next chapter, where we also improve and extend this technique to higher order DDEs and systems of DDEs.

Chapter 5

Improvement and extension of the Galerkin procedure

In this chapter, we first present a brief numerical study of the performance and convergence of the Galerkin technique presented in the previous chapter by approximating the characteristic roots of linear constant coefficient DDEs. Then, we present a modification of the Galerkin technique that gives better performance. For demonstration, we use this modified technique to obtain finite dimensional descriptions used for approximating the characteristic roots of several linear constant coefficient DDEs. While the Galerkin technique itself is useful for nonlinear time-varying problems as well, its application to the linear constant coefficient problem serves as a detailed numerical investigation of its performance.

We also extend the technique to higher order DDEs and systems of DDEs.

Natarajan and Chatterjee have developed a finite element implementation of this improved scheme [134]. Vivek Natarajan also did several of the calculations in this chapter, under my supervision. Some material from this chapter was presented in [75].

5.1 Introduction

To illustrate the basic issues relevant to this chapter, consider the DDE

$$\dot{x} = -x(t-1).$$

Its characteristic equation is

$$\lambda + e^{-\lambda} = 0,$$

which is transcendental and has infinitely many roots as mentioned in chapter 2. Such equations typically cannot be solved in closed form.

A Galerkin projection technique has been developed in the previous chapter to obtain finite-dimensional ODE approximations for DDEs. Here, we first present a brief numerical study of its performance and convergence. We then present a modification to the Galerkin procedure henceforth called the modified Galerkin projection, which outperforms the one presented in the previous chapter. We use both these techniques to find the first several characteristic roots of some linear constant coefficient DDEs. For large N, where N is the dimension of the approximation, the error in approximating a given root goes to zero like N^{-2}. For any given N, the modified Galerkin technique provides a larger number of accurate estimates than the technique presented in the previous chapter. This modified technique, and its detailed numerical evaluation, are the main contributions of this chapter. A smaller contribution of this chapter is the extension of the technique to higher order DDEs.

As mentioned in chapter 2, several methods for finding the first few characteristic roots of linear DDEs exist in the literature [85, 86, 133]. The approach in [86, 133] is to approximate the solution operator by a finite-dimensional matrix that maps the function from one delay interval to another. The characteristic roots are then the logarithms of the eigenvalues of that matrix. The approximating matrix in [133] is based on subspace iteration of the integration operator of the DDE, while in [86] the matrix is based on a finite-difference scheme. In [85], the DDE is reduced to a system of ODEs by using a finite-difference scheme over the delay interval. The characteristic roots are then directly obtained as the eigenvalues of the coefficient matrix associated with the ODEs. Our approach, like [85], obtains a system of ODEs, but is conceptually different in that it is based on global shape functions and a Galerkin projection (as opposed to finite differences in time).

In this chapter, the modified Galerkin procedures will be applied to several different DDEs. These are

1. $\dot{x} + x(t-1) = 0$, which is the simplest case.

2. $\dot{x} + x + x(t-1/\sqrt{2}) + x(t-1) + \int_0^1 x(t-u)\cos(u)\,du = 0$, which is a first order DDE with multiple incommensurate delays as well as a distributed delay effect also studied in chapter 2.

3. $\ddot{x} + 0.2\,\dot{x}(t-1/2) + 3x - 2x(t-1) = 0$, which is a second order DDE.

4. $\dot{x} + 10x + x(t-1) + 2y(t-1) = 0$ and $\dot{y} + 10y + x(t-1) + y(t-1) = 0$, which is a system of two coupled DDEs.

5. $\dot{x} + 10x + x(t-1/\sqrt{2}) + y(t-1) = 0$, $\dot{y} + 10y + z(t-1) = 0$ and $\dot{z} + 10z + x(t-1) = 0$, which is a system of three coupled DDEs with incommensurate delays.

In the next section, we briefly present the Galerkin technique again with a pictorial representation of the technique for clarity and then perform a detailed performance analysis of the same. To this end, we write the reduced system from the previous chapter using a matrix notation that clarifies algorithmic issues.

5.2 The Galerkin procedure of chapter 4

Consider a general DDE with finite and nonzero, possibly distributed, delays

$$\dot{x}(t) \;=\; \hat{f}\,(t, x(t), \text{delayed values of}\, x(t))\,. \tag{5.1}$$

We let the largest delay be unity (by scaling time if necessary). We define the function

$$F(t,s) \;=\; x_s(t) \;=\; x(t-s)\,, s \in [0,1]. \tag{5.2}$$

In the interior of the s-interval we have from Eq. (5.2)

$$\frac{\partial F}{\partial t} + \frac{\partial F}{\partial s} \;=\; 0. \tag{5.3}$$

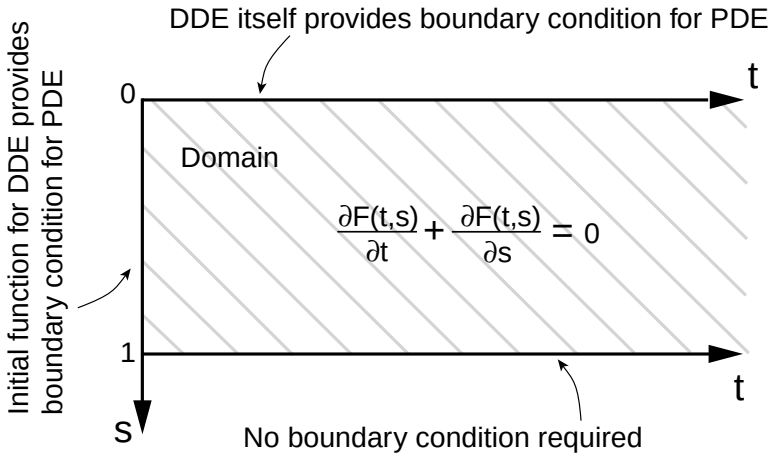

Figure 5.1: PDE from DDE

Figure 5.1 depicts our strategy pictorially. We have replaced the real-line domain with a semi-infinite strip in the (t,s) plane. In this semi-infinite domain the PDE defined in Eq. (5.3) is the governing equation. On the edge $t = 0$, s goes from 0 to 1 and the initial function of the DDE acts as the boundary condition for the PDE. On the semi-infinite edge where $s = 0$ and $t > 0$, the DDE itself acts as the boundary condition as will be seen below. No boundary condition is needed on the other semi-infinite edge where $s = 1$ and $t > 0$.

We now develop our approximation scheme. We approximate

$$F(t,s) \;\approx\; a_0(t) \;+\; a_1(t)\,s \;+\; \sum_{k=1}^{N-2} a_{k+1}(t)\,\sin(k\pi s)\,, \tag{5.4}$$

where N is finite. From Eqs. (5.2) and (5.4), we have $x(t) \equiv F(t,0) = a_0(t)$, which on differentiation with respect to t gives

$$\dot{a}_0(t) = \dot{x}(t) = f\left(t, a_0(t), a_1(t), a_2(t), \cdots, a_{N-1}(t)\right), \tag{5.5}$$

where the function f is obtained by substituting Eqs. (5.2) and (5.4) in $\hat{f}$ of Eq. (5.1). Equation (5.5) defines the boundary condition on the semi-infinite edge where $s = 0$ and $t > 0$, as it governs the evolution of the function $F(t,s)$ on this boundary.

Substituting Eq. (5.4) in Eq. (5.3), we define

$$r(t,s) = \dot{a}_0(t) + \dot{a}_1(t)\, s + \sum_{k=1}^{N-2} \dot{a}_{k+1}(t) \sin(k\pi s) + a_1(t) + \sum_{k=1}^{N-2} a_{k+1}(t) k\pi \cos(k\pi s), \tag{5.6}$$

where $r(t,s)$ is called the residual. The residual is made orthogonal to the shape functions (this is the Galerkin projection) to obtain the following $N-1$ equations:

$$\int_0^1 \left\{ \dot{a}_0(t) + \dot{a}_1(t)\, s + \sum_{k=1}^{N-2} \dot{a}_{k+1}(t) \sin(k\pi s) + a_1(t) + \sum_{k=1}^{N-2} a_{k+1}(t) k\pi \cos(k\pi s) \right\} \cdot s\, ds = 0 \tag{5.7}$$

and

$$\int_0^1 \left\{ \dot{a}_0(t) + \dot{a}_1(t)\, s + \sum_{k=1}^{N-2} \dot{a}_{k+1}(t) \sin(k\pi s) + a_1(t) + \sum_{k=1}^{N-2} a_{k+1}(t)\, k\pi \cos(k\pi s) \right\} \cdot \sin(m\pi s)\, ds = 0, \tag{5.8}$$

for $m = 1, 2, \cdots, N-2$.

Equations (5.5), (5.7) and (5.8) constitute N ODEs which can be written in the form

$$\mathbf{A}\dot{\mathbf{a}} + \mathbf{B}\mathbf{a} = \mathbf{b}(\mathbf{a}, t), \tag{5.9}$$

where $\mathbf{A}$ and $\mathbf{B}$ are $N \times N$ matrices, $\mathbf{a}$ is a vector containing a_i and $\mathbf{b}(\mathbf{a},t)$ is a vector with a single nonzero element representing time varying and/or nonlinear terms from the DDE (Eq. (5.1)). Almost all elements of both $\mathbf{A}$ and $\mathbf{B}$ can be evaluated once and for all, independent of the specific DDE (the last $N-1$ rows as determined by Eqs. (5.7) and (5.8)). Expressions for the elements of $\mathbf{A}$ and $\mathbf{B}$ are given in Tables 5.1 and 5.2, respectively.

Table 5.1: Coefficients of $\dot{a}_i s$ using old residual.

Equation No.	$\dot{a}_0$	$\dot{a}_1$	$\dot{a}_{k+1},\ \ k = 1, \cdots, N-2$
5.7	$\frac{1}{2}$	$\frac{1}{3}$	$\frac{(-1)^{k+1}}{k\pi}$
5.8	$\frac{2}{m\pi}$ for m odd, 0 otherwise.	$\frac{(-1)^{m+1}}{m\pi}$	$\frac{1}{2}$ for $k = m$, 0 otherwise.

For a linear constant coefficient DDE, $\mathbf{b}(\mathbf{a},t) = \mathbf{0}$ and hence Eq. (5.9) represents an eigenvalue problem of the form $\dot{\mathbf{a}} = \mathbf{C}\,\mathbf{a}$, where $\mathbf{C} = -\mathbf{A}^{-1}\mathbf{B}$. Eigenvalues of the matrix $\mathbf{C}$ approximate the first several characteristic roots of the DDE under consideration[1].

For a numerical study of the performance of the Galerkin technique, we consider

$$\dot{x} + x(t-1) = 0. \tag{5.10}$$

Using Eqs. (5.2) and (5.4) this can be written as

$$\dot{a_0} + a_0 + a_1 = 0. \tag{5.11}$$

Hence along with Eqs. (5.7) and (5.8) we have N ODEs which can be written as $\dot{\mathbf{a}} = \mathbf{C}\,\mathbf{a}$.

[1]For the invertibility of $\mathbf{A}$, see Appendix D.

Table 5.2: Coefficients of $a_i s$ using old residual.

Equation No.	a_0	a_1	$a_{k+1},\ \ k = 1, \cdots, N-2$
5.7	0	$\frac{1}{2}$	$-\frac{2}{k\pi}$ for k odd , 0 otherwise .
5.8	0	$\frac{2}{m\pi}$ for m odd , 0 otherwise .	$\frac{2km}{m^2-k^2}$ for $k+m$ odd , 0 otherwise .

For any characteristic root of the DDE, absolute error is $|\lambda_{exact} - \lambda_c|$, where λ_{exact} is the highly accurate characteristic root of the DDE via Newton-Raphson and λ_c is the eigenvalue of $\mathbf{C}$ closest to λ_{exact}. The absolute errors for the first and second characteristic roots of Eq. (5.10) are calculated for different values of N and plotted on a log-log scale in Fig. 5.2 (right). On fitting a straight line, it is observed that the error is proportional to N^{-2} for large N.

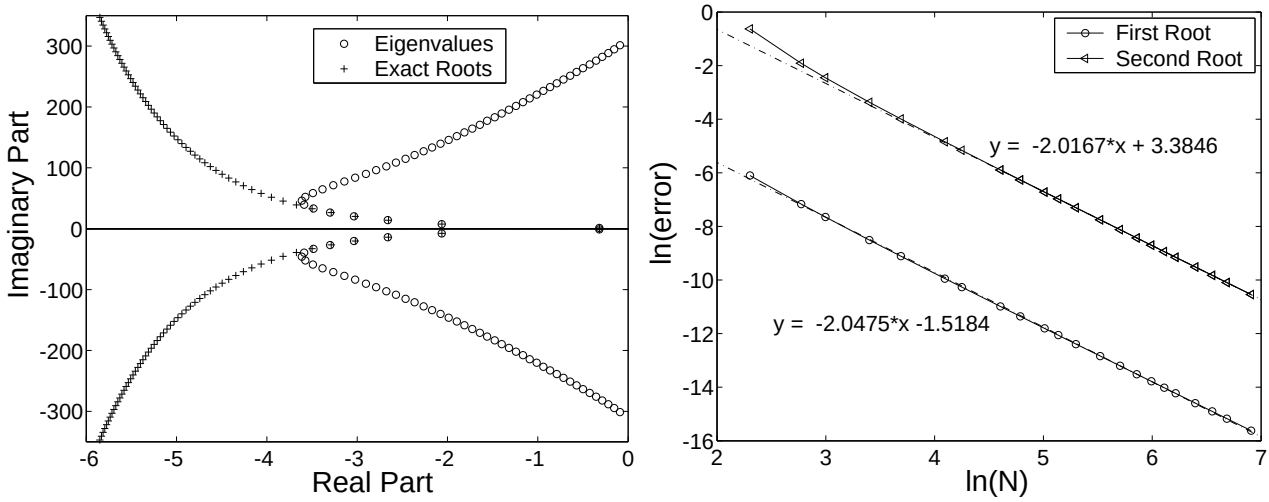

Figure 5.2: Left: Eigenvalues of $\mathbf{C}$ for $N = 100$ and exact roots of Eq. (5.10). By exact, we mean highly accurate roots numerically obtained via Newton-Raphson. Right: Convergence with N of first two characteristic roots of Eq. (5.10).

Figure 5.2 (left) shows the exact characteristic roots of the DDE, along with the eigenvalues of the matrix $\mathbf{C}$ for $N = 100$. We stress again that the exact roots of the DDE are the roots obtained via Newton-Raphson with a high degree of accuracy. The first few eigenvalues (about 12) are accurate to plotting precision.

Overall, the numerical results may be summarized as follows. As N increases, individual eigenvalues converge to the corresponding exact (in the sense mentioned above) characteristic roots of the DDE. Also, the number of eigenvalue estimates with error less than some given tolerance increases with N.

In the next section we present an analysis of a second order DDE with a delayed derivative which motivates the modification in the Galerkin procedure by which a much larger number of accurate estimates will be obtained.

5.3 A second order DDE

From Eq. (5.3), we note that $-\dfrac{\partial F(t,s)}{\partial s}$ and $\dfrac{\partial F(t,s)}{\partial t}$ are the same and both of them can be used for approximating $\dot{x}(t-s)$. However, in numerical implementations of the Galerkin procedure for higher order systems which involve terms of the form $\dot{x}(t-\tau)$, we have observed that the results obtained are better if we use $\dfrac{\partial F(t,s)}{\partial t}$.

To clarify the issue, consider the second order DDE

$$\ddot{x} + 20\dot{x} + 2\dot{x}(t-1) + 20x(t-1) + 100x = 0\,. \tag{5.12}$$

From Eq. (5.3), we can write Eq. (5.12) as either

$$\left.\frac{\partial^2 F}{\partial t^2}\right|_{s=0} + 20\left.\frac{\partial F}{\partial t}\right|_{s=0} + 2\left.\frac{\partial F}{\partial t}\right|_{s=1} + 20\,F|_{s=1} + 100\,F|_{s=0} = 0 \tag{5.13}$$

or

$$\left.\frac{\partial^2 F}{\partial t^2}\right|_{s=0} + 20\left.\frac{\partial F}{\partial t}\right|_{s=0} - 2\left.\frac{\partial F}{\partial s}\right|_{s=1} + 20\,F|_{s=1} + 100\,F|_{s=0} = 0. \tag{5.14}$$

Equations (5.7) and (5.8) still continue to be useful for both the equations. For the above two equations using the approximation presented in the previous chapter, we note that a_0 would be the only variable with a second derivative involved here. Accordingly, introducing a new variable $y = \dot{a}_0$, we can write both the system of equations, i.e., Eqs. (5.7), (5.8) and (5.13) or Eqs. (5.7), (5.8) and (5.14), as $\mathbf{A}\dot{\mathbf{a}} + \mathbf{B}\mathbf{a} = 0$, where $\mathbf{a} = \{y, a_0, a_1, \cdots, a_{N-1}\}^T$. Again the eigenvalues of $\mathbf{C} = -\mathbf{A}^{-1}\mathbf{B}$ would approximate the first few characteristic roots of the DDE, Eq. (5.12). The results for both the cases are presented in Fig. 5.3.

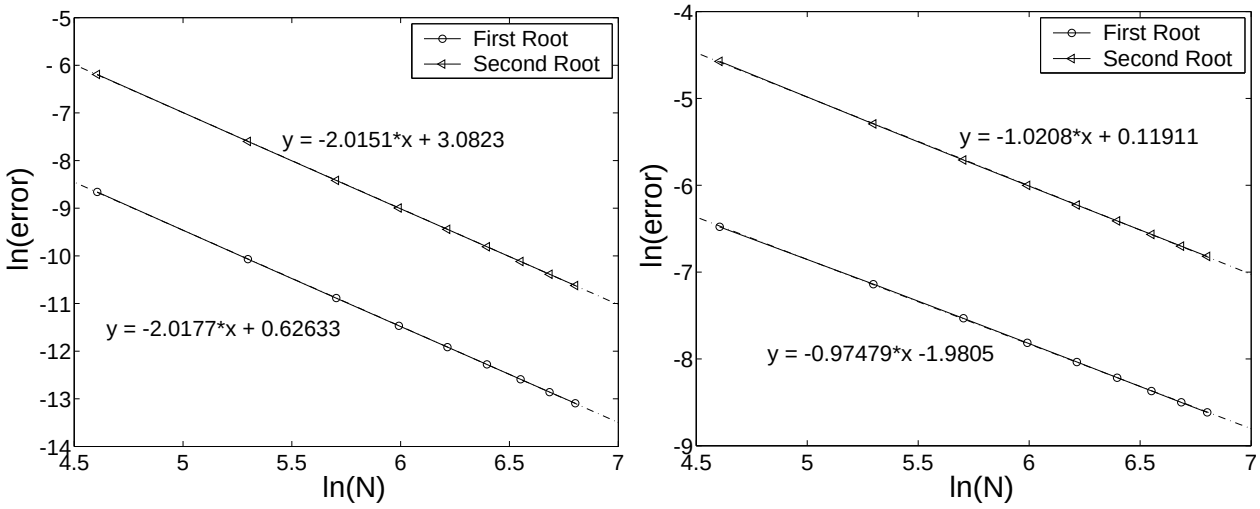

Figure 5.3: Left: From Eq. (5.13). Right: From Eq. (5.14).

It is clear from the figure that using the t-derivative (Eq. (5.13)) gives better convergence (N^{-2} against N^{-1} for the s-derivative (Eq. (5.14)).

The above observation suggest that using the s-derivative of the function $F(t,s)$ is probably not a good idea at least for the choice of the shape functions used in this work. This motivates our modification of the Galerkin procedure presented in the next section.

5.4 Modified Galerkin procedure

Motivated by the analysis presented in the previous section, we replace Eq. (5.3) by

$$\int_0^s \left(\frac{\partial F(t,s)}{\partial t} + \frac{\partial F(t,s)}{\partial s}\right) ds = \int_0^s \frac{\partial F(t,s)}{\partial t}\, ds + F(t,s) - F(t,0) = 0, \quad s \in [0,1]\,, \tag{5.15}$$

so as to get rid of the s-derivative. A pictorial representation of our modified strategy would be similar to Fig. 5.1, except that the governing equation inside the domain would now be given by Eq. (5.15) instead of Eq. (5.3).

We now proceed with our approximation scheme. Substituting Eq. (5.4) for $F(t,s)$ in Eq. (5.15), we define

$$r_m(t,s) = \dot{a}_0(t)\,s + \dot{a}_1(t)\,\frac{s^2}{2} + \sum_{k=1}^{N-2} \dot{a}_{k+1}(t)\frac{(1-\cos(k\pi s))}{k\pi} + a_1(t)\,s + \sum_{k=1}^{N-2} a_{k+1}(t)\sin(k\pi s)\,, \tag{5.16}$$

where r_m is a residual (the m-subscript for "modified" is used to differentiate from the r of Eq. (5.6)). Again making this modified residual orthogonal to the shape functions used in Eq. (5.4), we obtain

$$\int_0^1 \left\{ \dot{a}_0(t)\,s + \dot{a}_1(t)\,\frac{s^2}{2} + \sum_{k=1}^{N-2} \dot{a}_{k+1}(t)\frac{(1-\cos(k\pi s))}{k\pi} + a_1(t)\,s + \sum_{k=1}^{N-2} a_{k+1}(t)\sin(k\pi s) \right\} \cdot\, s\,ds = 0 \tag{5.17}$$

and

$$\int_0^1 \left\{ \dot{a}_0(t)\,s + \dot{a}_1(t)\,\frac{s^2}{2} + \sum_{k=1}^{N-2} \dot{a}_{k+1}(t)\frac{(1-\cos(k\pi s))}{k\pi} + a_1(t)\,s + \sum_{k=1}^{N-2} a_{k+1}(t)\sin(k\pi s) \right\} \cdot\, \sin(m\pi s)\,ds = 0\,, \tag{5.18}$$

for $m = 1, 2, \cdots, N-2$.

Equations (5.5), (5.17) and (5.18) now constitute N ODEs which are written in the form

$$\mathbf{A_m}\,\dot{\mathbf{a}} + \mathbf{B_m}\,\mathbf{a} = \mathbf{b}(\mathbf{a}, t)\,,$$

where $\mathbf{a}$ and $\mathbf{b}(\mathbf{a},t)$ have the same meaning as before, and where $\mathbf{A_m}$ and $\mathbf{B_m}$ are new (modified) $N \times N$ matrices. For linear constant coefficient DDEs, we obtain $\dot{\mathbf{a}} = \mathbf{C_m}\,\mathbf{a}$, where $\mathbf{C_m} = -{\mathbf{A_m}}^{-1}\mathbf{B_m}$. The eigenvalues of $\mathbf{C_m}$ approximate the first several characteristic roots of the DDE [2]. The $N-1$ rows of matrices $\mathbf{A_m}$ and $\mathbf{B_m}$, determined by Eqs. (5.17) and (5.18), are again independent of the specific DDE. They are given in Tables 5.3 and 5.4, respectively.

Table 5.3: Coefficients of $\dot{a}_i s$ using modified residual.

Equation No.	$\dot{a}_0$	$\dot{a}_1$	$\dot{a}_{k+1},\ \ k = 1, \cdots, N-2$
5.17	$\frac{1}{3}$	$\frac{1}{8}$	$\frac{1}{2k\pi} + \frac{2}{k^3\pi^3}$ for k odd, $\quad \frac{1}{2k\pi}$ otherwise.
5.18	$\frac{(-1)^{m+1}}{m\pi}$	$\frac{1}{2m\pi} - \frac{2}{m^3\pi^3}$ for m odd, $-\frac{1}{2m\pi}$ otherwise.	$\frac{-2m}{k\pi^2(m^2-k^2)} + \frac{1-(-1)^m}{km\pi^2}$ for $k+m$ odd, $\frac{1-(-1)^m}{km\pi^2}$ otherwise.

We now consider the same equation as was considered in section 5.2, i.e.,

$$\dot{x} + x(t-1) = 0\,. \tag{5.19}$$

Equation (5.11) holds, and along with Eqs. (5.17) and (5.18) gives N ODEs which can be written as $\dot{\mathbf{a}} = \mathbf{C_m}\,\mathbf{a}$.

Figure 5.4 shows the eigenvalues of $\mathbf{C_m}$, for $N = 100$ (left) and $N = 200$ (right), along with the exact roots (highly accurate roots via Newton-Raphson) of Eq. (5.19). The y-axis for both the plots in Fig. 5.4 is the same.

Two points may be noted. First, for fixed N (say $N = 100$), this method provides many more usefully accurate roots than the method presented in chapter 4 (Fig. 5.2 (left)). Second, as N increases (say from 100 to 200) the number of useful roots increases as well. Quantitative comparisons of the performance of the two procedures will be presented later (Table 5.5).

Convergence for this method, corresponding to Fig. 5.2 (right) for the earlier procedure, is shown in Fig. 5.5.

[2] For the invertibility of $\mathbf{A_m}$, see Appendix D

Table 5.4: Coefficients of $a_i s$ using modified residual.

Equation No.	a_0	a_1	$a_{k+1},\ \ k = 1, \cdots, N-2$
5.17	0	$\frac{1}{3}$	$\frac{(-1)^{k+1}}{k\pi}$
5.18	0	$\frac{(-1)^{m+1}}{m\pi}$	$\frac{1}{2}$ for $k = m\,,\quad 0$ otherwise.

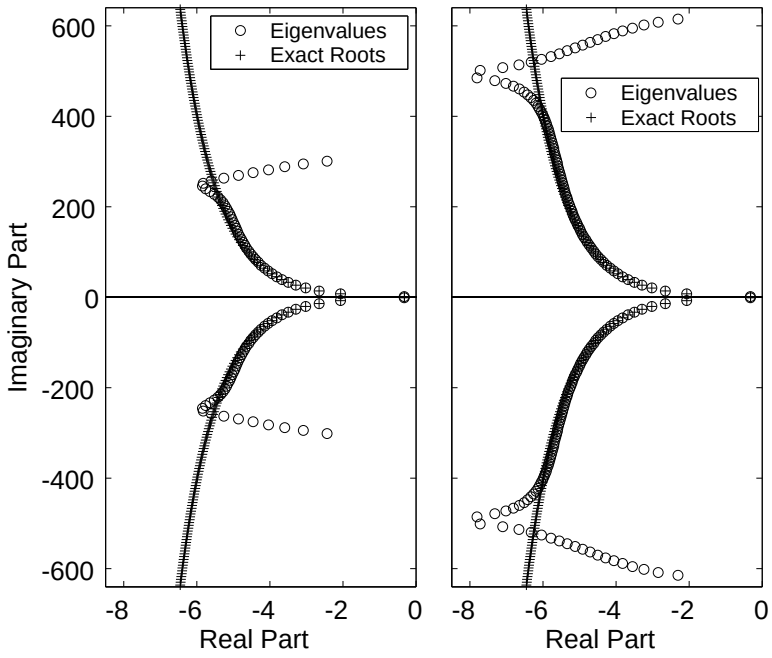

Figure 5.4: Eigenvalues of $\mathbf{C_m}$ for $N = 100$ (left) and 200 (right) along with exact roots (highly accurate numerical roots) of Eq. (5.19).

Again, the error goes to zero like N^{-2}. However, the coefficients of N^{-2} for the modified method are much smaller than that for the method presented in chapter 4 which can be seen from the coefficients in the linear fits. This means that the modified method not only gives more usefully accurate roots, but for any given root and N, the error in the root is much smaller for the modified method. For example, for $\ln(N) \approx 5$, $\ln(error) \approx -6$ for the first root in Fig. 5.2, while $\ln(error) \approx -10$ in Fig. 5.5.

We next consider a first order DDE with incommensurate delays as well as a distributed delay studied before in chapters 2 and 4,

$$\dot{x} + x + x(t - 1/\sqrt{2}) + x(t-1) + \int_0^1 x(t-u)\,\cos(u)\,du = 0\,. \tag{5.20}$$

Using Eqs. (5.2) and (5.4) this can be written as

$$\dot{a_0} + 3a_0 + a_1\left(1 + \frac{1}{\sqrt{2}}\right) + \sum_{k=1}^{N-2} a_{k+1}\sin\left(\frac{k\pi}{\sqrt{2}}\right) + \int_0^1 \left(a_0 + a_1 u + \sum_{k=1}^{N-2} a_{k+1}\sin(k\pi u)\right)\cos(u)du = 0. \tag{5.21}$$

Again, along with Eqs. (5.17) and (5.18), we have N ODEs which can be written as $\dot{\mathbf{a}} = \mathbf{C_m}\,\mathbf{a}$.

Figure 5.6 (left) shows the eigenvalues of $\mathbf{C_m}$ for $N = 100$ and the exact roots (in the sense defined earlier) of Eq. (5.20). About 40 eigenvalues are visibly close to their corresponding exact roots. Figure 5.6 (right) shows

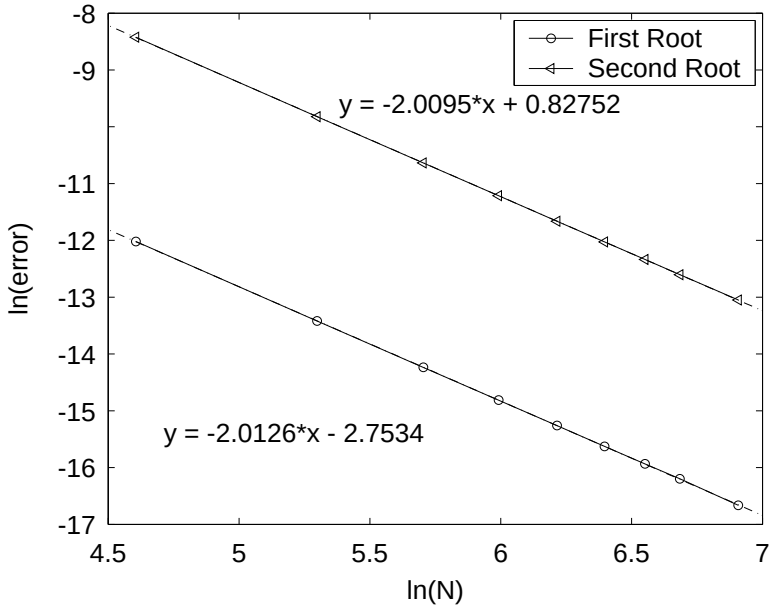

Figure 5.5: Convergence with N of first two characteristic roots of Eq. (5.19).

absolute error versus N for the first two characteristic roots of Eq. (5.20), on a log-log scale. The order of the method is 2 again.

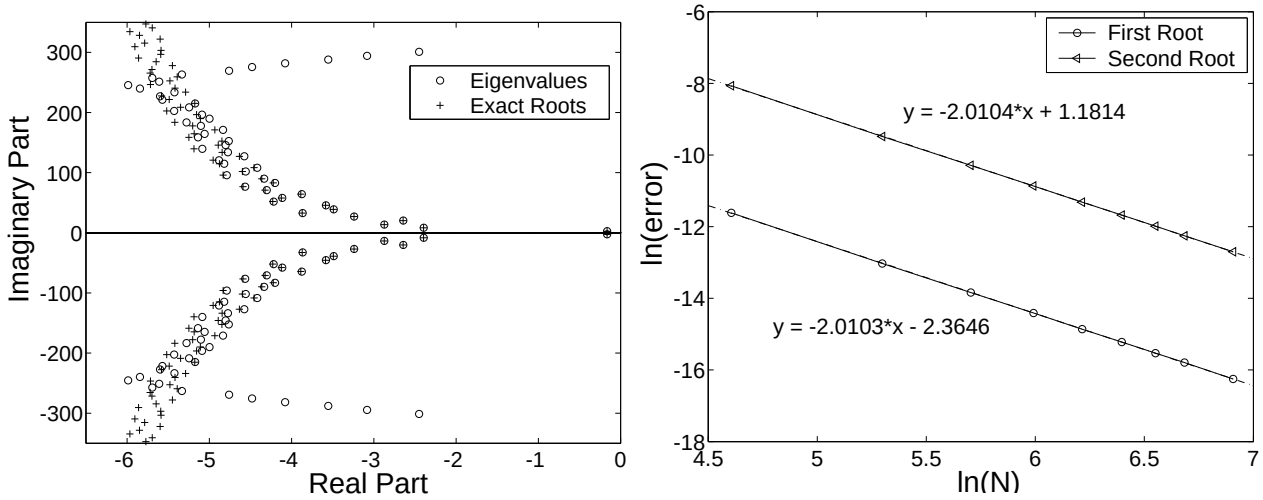

Figure 5.6: Left: Eigenvalues of $\mathbf{C_m}$ for $N = 100$ and exact roots (in the sense defined earlier) of Eq. (5.20). Right: Convergence with N of first two characteristic roots of Eq. (5.20).

For comparison, the performance of the original Galerkin projection (chapter 4) is presented in Fig. 5.7.

5.5 Higher order DDEs

The procedure for second order DDEs shown in section 5.3 is simple. Still higher orders require some extra calculations.

In this section, we briefly present another second order example before moving to higher order cases. Consider

$$\ddot{x} + 0.2\,\dot{x}(t - 1/2) + 3x - 2x(t - 1) = 0\,. \tag{5.22}$$

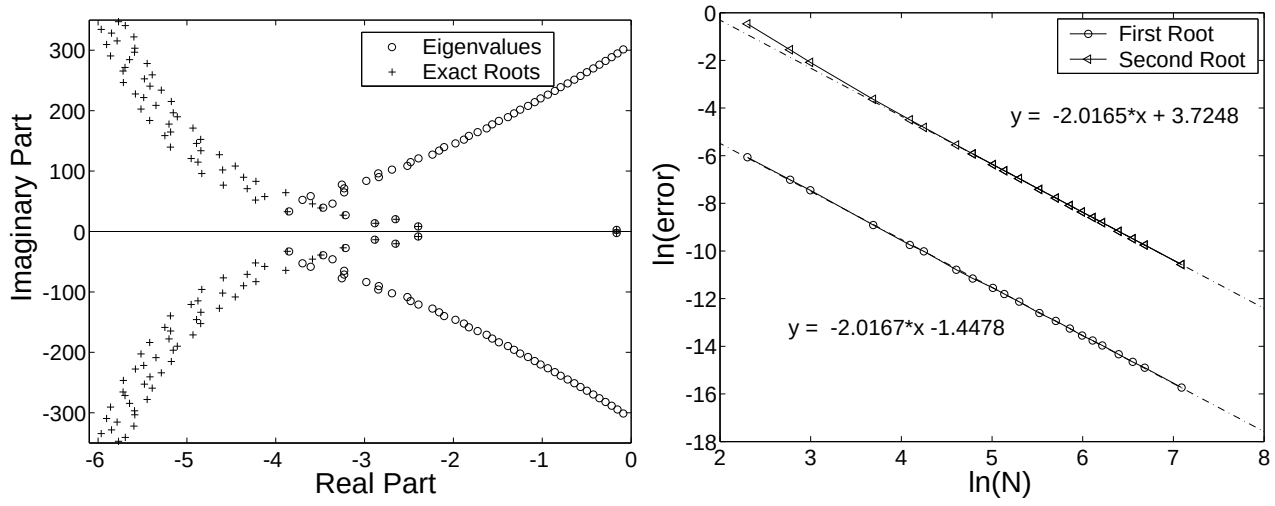

Figure 5.7: Left: Eigenvalues of $\mathbf{C}$ for $N = 100$ and exact roots (in the sense defined earlier) of Eq. (5.20). Right: Convergence with N of first two characteristic roots of Eq. (5.20).

Using Eqs. (5.2) and (5.4) this can be written as

$$\ddot{a}_0 + 0.2\dot{a}_0 + 0.1\dot{a}_1 + 0.2\sum_{k=1}^{N-2} \dot{a}_{k+1}\sin(k\pi/2) + 3a_0 - 2(a_0 + a_1) = 0\,. \tag{5.23}$$

Equations (5.17) and (5.18) continue to be useful in this case. Again noting that a_0 is the only variable with a second derivative and introducing a new variable $y = \dot{a}_0$, we can write the system of equations, i.e., Eqs. (5.17), (5.18) and (5.23), as $\mathbf{A_m}\dot{\mathbf{a}} + \mathbf{B_m}\mathbf{a} = 0$, where $\mathbf{a} = \{y, a_0, a_1, \cdots, a_{N-1}\}^T$.

Figure 5.8 (left) shows the eigenvalues for $N = 100$ and the exact roots (in the sense defined earlier) of Eq. (5.22). About 30 eigenvalues are close to the exact roots. Figure 5.8 (right) shows error versus N for the first and second characteristic roots of Eq. (5.22) on a log-log scale. The order of convergence is 2, as before.

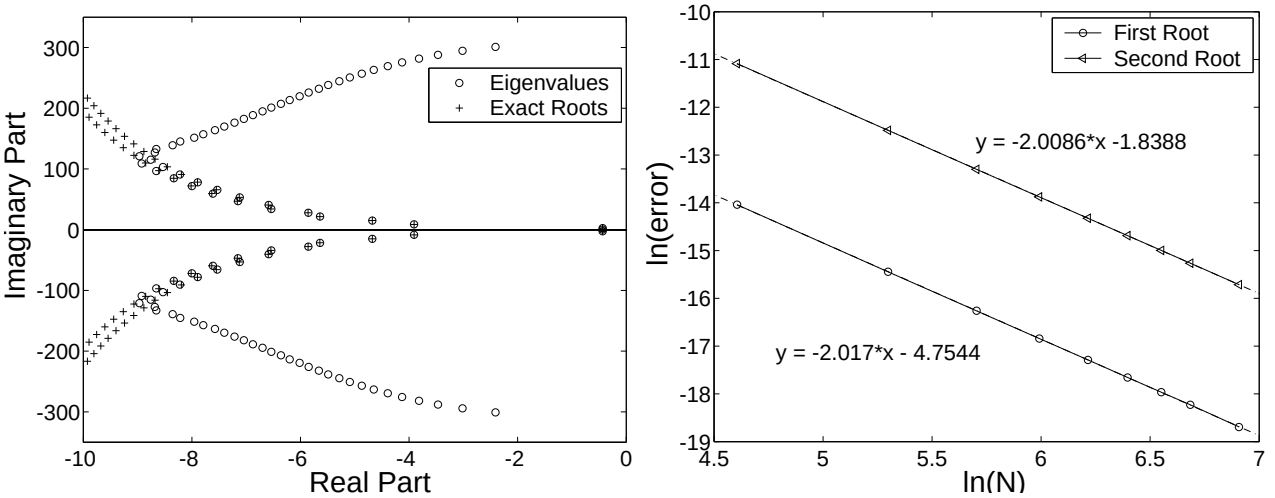

Figure 5.8: Left: Eigenvalues of $\mathbf{C_m}$ for $N = 100$ and exact roots (in the sense defined earlier) of Eq. (5.22). Right: Convergence with N of first two characteristic roots of Eq. (5.22).

Figure 5.9 presents the same results as Fig. 5.8 but obtained using the method of chapter 4. As before, the new method outperforms the old one.

More generally, any second order DDE can be reduced using Eqs. (5.2) and (5.4) to an equation which will consist only of $\dot{a}_i$ and a_i along with $\ddot{a}_0$, and the above procedure will be applicable.

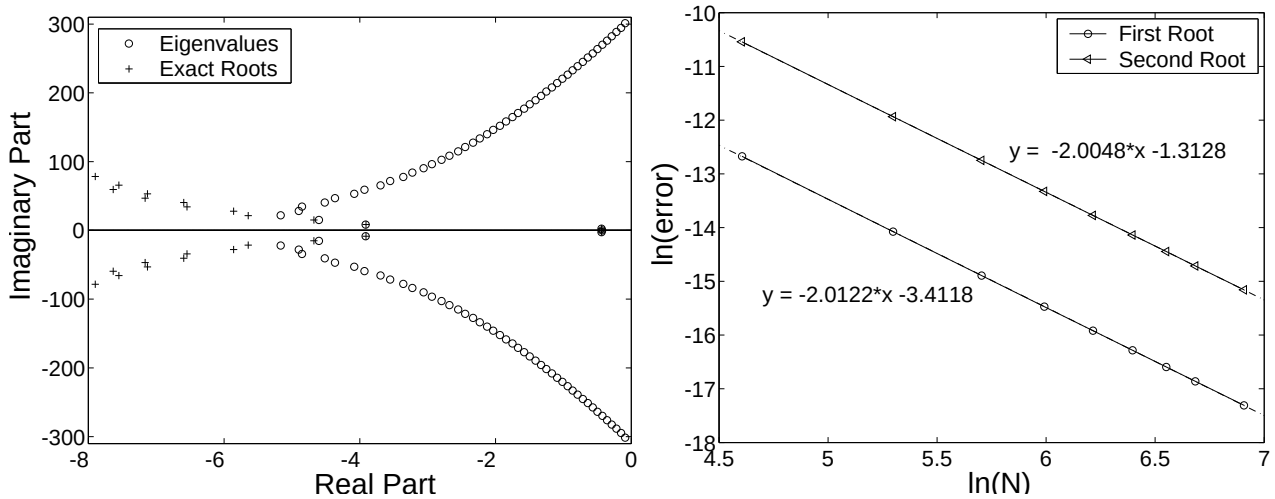

Figure 5.9: Left: Eigenvalues of $\mathbf{C}$ for $N = 100$ and exact roots (in the sense defined earlier) of Eq. (5.22). Right: Convergence with N of first two characteristic roots of Eq. (5.22).

5.5.1 System of two DDEs

The system of two coupled linear DDEs is an example related to the second order linear DDE. This system can be reduced to an equivalent second order linear DDE. For illustration, consider

$$\dot{x} + 10x + x(t-1) + 2y(t-1) = 0\,, \tag{5.24}$$

$$\dot{y} + 10y + x(t-1) + y(t-1) = 0\,. \tag{5.25}$$

We will replace this system with an equivalent second order DDE, as follows. The characteristic equation for the system is

$$\lambda^2 + 2\lambda e^{-\lambda} + 20\lambda - e^{-2\lambda} + 20e^{-\lambda} + 100 = 0\,. \tag{5.26}$$

By inspection, a second order DDE with the same characteristic equation is

$$\ddot{x} + 2\dot{x}(t-1) + 20\dot{x} - x(t-2) + 20x(t-1) + 100x = 0\,. \tag{5.27}$$

On scaling time by $t = 2\tau$, Eq. (5.27) is transformed to

$$x'' + 4x'(\tau - 1/2) + 40x' - 4x(\tau - 1) + 80x(\tau - 1/2) + 400x = 0\,, \tag{5.28}$$

where $(')$ denotes τ-derivative. We can now proceed as we did for Eq. (5.22). Figure 5.10 (left) shows the eigenvalues of $\mathbf{C_m}$ for $N = 100$ and the exact roots (in the sense defined earlier) of Eq. (5.28). Around 28 eigenvalues are visibly close to the roots of the DDE. The roots of the original system, Eqs. (5.24) and (5.25), can be obtained from these roots upon division by 2 (because of time scaling).

Figure 5.10 (right) shows error versus N on a log-log scale for the first and second characteristic roots of Eq. (5.28). The order of convergence is 2 again.

5.5.2 DDEs of order higher than 2

For DDEs of order higher than 2, the equivalent of Eq. (5.23) generally contains higher derivatives of the a_i $(i > 0)$. To illustrate, consider the following DDE.

$$\dddot{x} + \ddot{x}(t-1) + x = 0. \tag{5.29}$$

Substituting Eqs. (5.2) and (5.4) into Eq. (5.29) gives (equivalent to Eq. (5.23))

$$\dddot{a}_0 + \ddot{a}_0 + \ddot{a}_1 + a_0 = 0. \tag{5.30}$$

Note the second derivative of a_1.

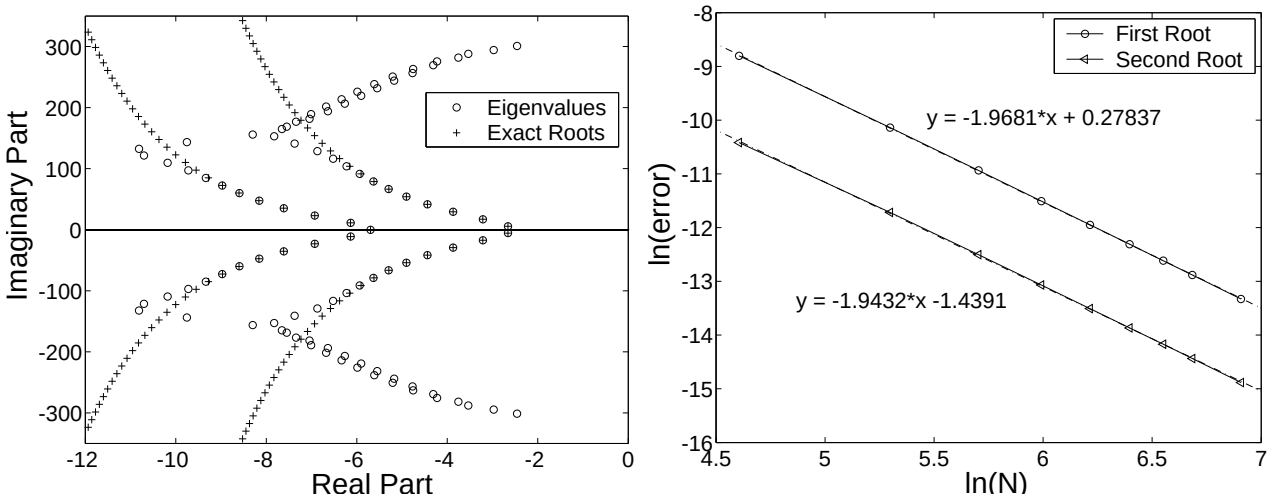

Figure 5.10: Left: Eigenvalues of $\mathbf{C_m}$ for $N = 100$ and exact roots (in the sense defined earlier) of Eq. (5.28). Right: Convergence with N of first two characteristic roots of Eq. (5.28).

In such cases, we proceed as follows. We can write Eqs. (5.17) and (5.18) in the form

$$\hat{\mathbf{A}}_\mathbf{m}\dot{\mathbf{c}} + \hat{\mathbf{B}}_\mathbf{m}\mathbf{c} + a_0\mathbf{w_1} + \dot{a_0}\mathbf{w_2} = 0, \tag{5.31}$$

where $\hat{\mathbf{A}}_\mathbf{m}$ and $\hat{\mathbf{B}}_\mathbf{m}$ are $(N-1)\times(N-1)$ matrices, $\mathbf{w_1}$ and $\mathbf{w_2}$ are vectors of size $N-1$, and $\mathbf{c} = \{a_1, a_2, \cdots, a_{N-1}\}^T$, i.e., all the a_i excluding a_0. For clarity, we mention that $\hat{\mathbf{A}}_\mathbf{m}$, $\hat{\mathbf{B}}_\mathbf{m}$, $\mathbf{w_1}$ and $\mathbf{w_2}$ are just sub-matrices of the matrices $\mathbf{A_m}$ and $\mathbf{B_m}$ defined earlier. Equation (5.31) is solved for $\dot{\mathbf{c}}$ to get

$$\dot{\mathbf{c}} = -\hat{\mathbf{A}}_\mathbf{m}^{-\mathbf{1}}(\hat{\mathbf{B}}_\mathbf{m}\mathbf{c} + a_0\mathbf{w_1} + \dot{a_0}\mathbf{w_2}). \tag{5.32}$$

Equation (5.32) is differentiated as many times as required, substituting for $\dot{\mathbf{c}}$ after each differentiation to get the higher derivatives of $a_i, i = 1, \cdots, N-1$, in terms of $\dot{a}_i$, a_i, a_0 and derivatives of a_0. For example

$$\ddot{\mathbf{c}} = \hat{\mathbf{A}}_\mathbf{m}^{-1}(-\hat{\mathbf{B}}_\mathbf{m}\dot{\mathbf{c}} - \dot{a_0}\mathbf{w_1} - \ddot{a_0}\mathbf{w_2}), \tag{5.33}$$

which can be used to write Eq. (5.30) in terms of a_i, $\dot{a}_i$, a_0, $\dot{a_0}$, $\ddot{a}_0$ and $\dddot{a_0}$. Similarly

$$\dddot{\mathbf{c}} = \hat{\mathbf{A}}_\mathbf{m}^{-1}(-\hat{\mathbf{B}}_\mathbf{m}\ddot{\mathbf{c}} - \ddot{a_0}\mathbf{w_1} - \dddot{a_0}\mathbf{w_2}). \tag{5.34}$$

In the above we can substitute for $\ddot{\mathbf{c}}$ from Eq. (5.33) and get $\dddot{a_i}$, $i \geq 1$, in terms of a_i, $\dot{a}_i$, a_0, $\dot{a_0}$, $\ddot{a}_0$ and $\dddot{a_0}$. In this way, any higher order DDE can be written using a_i, $\dot{a}_i$, a_0, and higher derivatives of a_0 alone. Finally we represent this rewritten DDE and Eqs. (5.17) and (5.18) in the form $\mathbf{A_m}\dot{\mathbf{a}} + \mathbf{B_m}\mathbf{a} = 0$ where $\mathbf{a}$ is a vector containing a_i, a_0 and several derivatives of a_0.

Now that we can treat a scalar DDE of order M, we consider systems of M first order DDEs. The first step is to find the characteristic equation of the given system. An equivalent M^{th} order linear DDE can then be identified (along the lines of section 5.3, Eqs. (5.24) and (5.25)) which will have the same characteristic equation.

As an example, we now consider the following system of three coupled DDEs:

$$\dot{x} + 10x + x(t - 1/\sqrt{2}) + y(t-1) = 0\,, \tag{5.35}$$
$$\dot{y} + 10y + z(t-1) = 0\,, \tag{5.36}$$
$$\dot{z} + 10z + x(t-1) = 0\,. \tag{5.37}$$

The characteristic equation of this system is

$$\lambda^3 + 30\lambda^2 + e^{-\lambda/\sqrt{2}}\lambda^2 + 300\lambda + 20e^{-\lambda/\sqrt{2}}\lambda + 100e^{-\lambda/\sqrt{2}} + e^{-3\lambda} + 1000 = 0\,. \tag{5.38}$$

An equivalent third order DDE is

$$\dddot{x} + 30\ddot{x} + \ddot{x}(t - 1/\sqrt{2}) + 300\dot{x} + 20\dot{x}(t - 1/\sqrt{2}) + 100x(t - 1/\sqrt{2}) + x(t-3) + 1000x = 0\,. \tag{5.39}$$

Scaling time by $t = 3\tau$, we get

$$x'''+90x''+3x''\left(\tau-\frac{1}{3\sqrt{2}}\right)+2700x'+180x'\left(\tau-\frac{1}{3\sqrt{2}}\right)+2700x\left(\tau-\frac{1}{3\sqrt{2}}\right)+27x(\tau-1)+27000x=0\,. \quad (5.40)$$

Equation (5.40) can now be analyzed and its characteristic roots obtained as described above. These roots are 3 times the characteristic roots of the original system. Figure 5.11 (left) shows the eigenvalues of $\mathbf{C_m}$ for $N = 100$ and the exact roots (in the sense defined earlier) of Eq. (5.40). About 24 eigenvalues seem accurate to plotting accuracy.

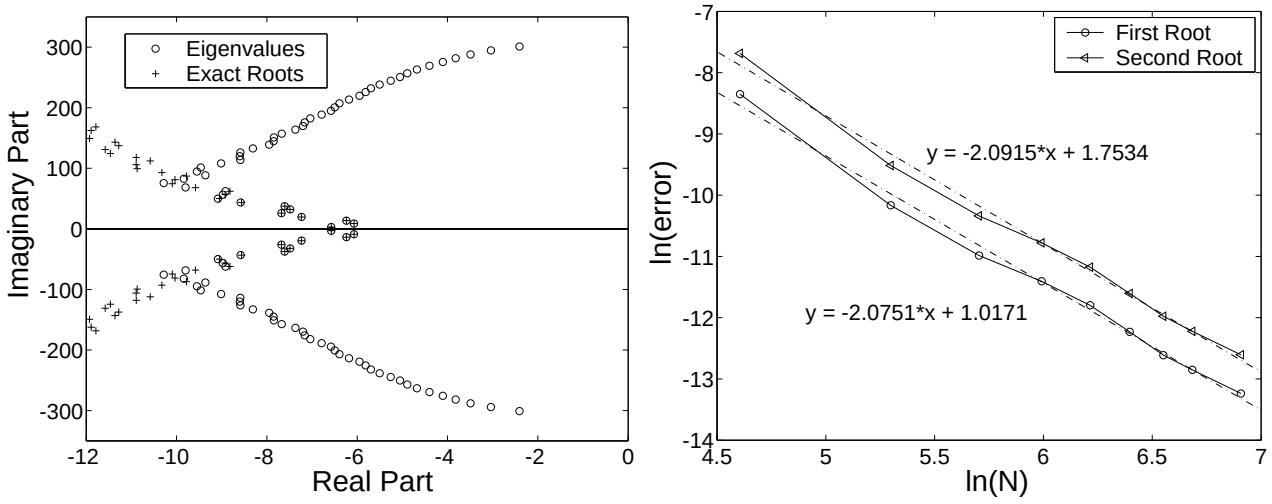

Figure 5.11: Left: Eigenvalues of $\mathbf{C_m}$ for $N = 100$ and exact roots (in the sense defined earlier) of Eq. (5.40). Right: Convergence with N of first two characteristic roots of Eq. (5.40).

Figure 5.11 (right) shows on a log-log scale, error versus N for the first and second characteristic roots of Eq. (5.40). Once again, the error goes to zero like N^{-2}.

5.6 Comparison between the two methods

We consider two measures for gauging the performance of the Galerkin projections. The first is the order of convergence, which is N^{-2} for both methods. The second and more important measure of performance is the number of usefully accurate eigenvalues (by usefully accurate, we mean something like, for example, close enough to the actual root that Newton-Raphson iteration can reliably take over). It is in the second measure that the modified method outperforms the old one (of chapter 4). The number of eigenvalues p that lie within some specified distance from the characteristic roots of the DDE are used here as the number of usefully accurate eigenvalues. These estimates can be refined further using Newton-Raphson method to get arbitrarily accurate roots of the DDE. Table 5.5 shows this number p, for the five DDEs considered here, using both the old and the modified methods, taking $N = 200$ and and the error tolerance as 0.05.

Table 5.5: Number of eigenvalues p with error ≤ 0.05 and $N = 200$.

Equation No.	p from old method	p from modified method
5.19	12	72
5.20	10	74
5.22	7	39
5.28	7	47
5.40	2	28

5.7 Concluding remarks

In this chapter, we have presented a modified Galerkin procedure. We have used this modified procedure as well as the Galerkin procedure of chapter 4 for calculating the first several characteristic roots of some constant coefficient DDEs. The methods can be implemented easily. The order of these methods is 2 (i.e., for an $N \times N$ matrix approximation, the error in any root goes to zero like N^{-2}). The modified procedure gives us several usefully accurate roots which can be rapidly refined further using Newton-Raphson iteration. Though the Galerkin techniques are also applicable to nonlinear DDEs, we have restricted ourselves to linear DDEs in this chapter.

Our procedures also allow for special-purpose low dimensional models using specialized shape functions, e.g., from experimental data using proper orthogonal decomposition [135, 136, 137]. Such applications are not considered here.

We mention that the conceptually different framework of finite differencing has also been used to obtain characteristic roots of DDEs [85, 86], often with faster convergence (e.g., N^{-3}, N^{-5}). These fast converging methods have their strengths, but are not in conflict with the present approach for the following two reasons.

First, Newton-Raphson refinement requires $\mathcal{O}(N)$ calculations added to the $\mathcal{O}(N^3)$ for the eigenvalue solver (i.e., Newton-Raphson refinement is essentially free). So the number of usefully accurate roots is more important than the asymptotic convergence rate, and that is fairly good for the modified method presented in this chapter.

Secondly, other shape functions may give faster than N^{-2} convergence. Here, we have laid the foundation for such investigations, e.g., involving finite element implementations with faster convergence.

Chapter 6

Regenerative tool chatter near a codimension 2 Hopf point

With this chapter, we begin to study systems relevant to metal cutting. We first study a double Hopf bifurcation in a tool vibration DDE derived from Hanna and Tobias [4] and Kalmár-Nagy *et al.* [12]. The double Hopf point considered in this chapter corresponds to high-speed cutting. The material from his chapter has also been published in [76] and presented at [77].

6.1 Introduction

The regenerative effect in metal cutting is an important source of undesirable vibrations in machine tools [2], leading to poor surface finish and enhanced tool wear. Mathematical models of such vibrations are delay differential equations (DDEs). Stépán [8] has listed several DDEs relevant to machine tool vibrations, and addressed stability analyses of the same.

Linear stability analyses of constant coefficient DDEs relevant to machine tools [8, 9, 12] are usually presented in the form of stability charts containing various stability "lobes." The stability chart depicts the boundary between stable and unstable regimes. Hopf bifurcations in these models arise when parameter values cross these stability boundaries. Points of intersection of curves defining different stability lobes indicate codimension 2 Hopf bifurcations. These points are of practical interest since they represent local optima in operating conditions: in a finite neighborhood of cutting speeds, they represent the greatest possible stable chip width (or material removal rate).

In this chapter, we use direct multiple scales (bypassing a center manifold reduction, as discussed below) to study a double Hopf bifurcation in a tool vibration DDE derived from Hanna and Tobias [4] and Kalmár-Nagy *et al.* [12]. The double Hopf point considered here corresponds to high-speed cutting. We use a nonstandard definition of the associated small parameter ϵ that allows us to *not* treat the vibration amplitude as extremely small near the bifurcation point. We do treat the damping in the system as small, thereby obtaining analytical expressions for the nominal double Hopf points. These double Hopf points are all resonant. Both sub- and supercritical Hopf bifurcations are observed here, depending on how two key parameters vary near the double Hopf point. Numerical simulations are used to verify analytical simplifications and approximations.

The analytical technique adopted here follows easily from prior related work on ODEs, PDEs and DDEs. Codimension 2 (or double) Hopf bifurcations arising in systems of nonlinear ODEs have been studied using the method of multiple scales by Yu [138]. In PDEs, center manifold reductions and normal form theory [139, 140] or multiple scales [141, 142] have been used. Simple Hopf bifurcations arising in DDEs have also been studied using center manifold reductions [12, 119, 120, 121, 122], normal form theory (bypassing the center manifold reductions) [123, 124, 125], and the method of multiple scales or MMS (bypassing the normal forms as well) [9, 10, 126]. Fofana [13] used center manifold reductions to study double Hopf bifurcations in a DDE model for regenerative machine tool chatter, while Stépán and Haller [26] used the theory of normal forms along with a center manifold analysis for a DDE model for robot control. The application of the methods given in [13, 26] is more difficult for the tool vibration DDE considered herein, primarily because of the non-symmetric nonlinearity and the complicated center manifold reduction. Our approach, being more direct, is simpler than that in [13, 26].

Quasi-periodic tool motion has been experimentally observed for thread cutting by Stépán [14]. A bifurcation diagram near the double Hopf point representing the "most likely scenario" is also proposed therein. A qualitative discussion of quasiperiodic motions along with possible loss of contact (between tool and workpiece) is also presented in [16]. In this chapter we complement the above two works; we directly and analytically treat

a double Hopf point and obtain mathematical descriptions of the slow dynamics near this point.

This chapter is organized as follows. In section 6.2, we briefly outline the derivation of the machine tool vibration DDE studied herein. Linear stability analysis of the DDE is presented in section 6.3, wherein we also obtain analytical expressions for the double Hopf points. Multiple scales analysis of the DDE near a double Hopf bifurcation point is presented in section 6.4. Some analysis and verification of the slow flow equations obtained using MMS are given in section 6.5. Conclusions are presented in section 6.6.

6.2 A SDOF model for tool vibration

We will consider the non-dimensionalized 1 DOF model for regenerative tool vibrations derived in [12], but with an added stiffening cubic nonlinearity in the restoring force (as in [4]). The governing equation then will be:

$$\ddot{x}(t) + 2\,\zeta\,\dot{x}(t) + (1+p)\,x(t) + \alpha x(t)^3 - p\,x(t-\tau) = \frac{3p}{10}\left\{(x(t)-x(t-\tau))^2 - (x(t)-x(t-\tau))^3\right\}, \tag{6.1}$$

where α is small (in a sense defined below), p is a parameter proportional to chip width, and τ, the time-delay, is inversely proportional to the cutting speed.

A derivation of Eq. (6.1) is outlined below.

We start with Eq. (1.4) derived in chapter 1. In this chapter, we wish to account for the structural nonlinearities and hence we assume that the spring has a weak stiffening cubic nonlinearity which modifies the equation to

$$\ddot{x}(t) + 2\,\zeta\,\dot{x}(t) + x(t) + k_3 x(t)^3 = PC(t)^{3/4}, \tag{6.2}$$

where P is a parameter proportional to the chip width as defined in chapter 1 and $k_3 \ll 1$.

The instantaneous chip thickness (see footnote 1) $C(t)$ is given by

$$C(t) = C_0 + x(t-\tau) - x(t) = C_0 + x_\tau(t) - x(t), \tag{6.3}$$

where $\tau = 2\pi/\Omega$ is the time period of one revolution.

Now we substitute the above equation for the instantaneous chip thickness in Eq. (6.2), set the origin of $x(t)$ at the steady-state deflection due to the cutting force at the nominal chip thickness C_0 to obtain

$$\ddot{x}(t) + 2\,\zeta\,\dot{x}(t) + x(t) + \alpha x(t)^3 = P(C_0 + x_\tau(t) - x(t))^{3/4} - PC_0^{3/4},$$

Now expanding the right hand side of the above equation locally in a power series about C_0 up to third order, rearranging and nondimensionalizing as in [12], we obtain

$$\ddot{x}(t) + 2\,\zeta\,\dot{x}(t) + (1+p)\,x(t) + \alpha\,x(t)^3 - p\,x_\tau(t) = \frac{3\,p}{10}\left\{(x(t)-x_\tau(t))^2 - (x(t)-x_\tau(t))^3\right\}, \tag{6.4}$$

where $\alpha = \dfrac{25\,k_3}{144\,C_0^2}$ and $p = \dfrac{3\,P}{4\,C_0^{1/4}}$ is the nondimensional bifurcation parameter proportional to the chip width w for a given C_0. The only difference between Eq. (6.4) and the one derived in [12] is the presence of $\alpha x(t)^3$. We assume $\alpha \ll 1$.

6.3 Linearization

Linearizing Eq. (6.4) about $x(t) \equiv 0$, we get

$$\ddot{x}(t) + 2\,\zeta\,\dot{x}(t) + (1+p)\,x(t) - p\,x_\tau(t) = 0. \tag{6.5}$$

A stability analysis of Eq. (6.5) is given in [12]. Here, the stability boundaries showing the first two lobes in the $p-\tau$ plane for $\zeta = 0$ and $\zeta = 0.1$ are plotted in Fig. 6.1. $\mathrm{Q} = (2\pi, 5/8) = (6.283, 0.625)$ and $\mathrm{Q}' = (5.980, 0.877)$ represent double Hopf points for $\zeta = 0$ and $\zeta = 0.1$, respectively. Observe that, though the presence of small nonzero damping affects the stability boundary, the curves near Q and Q′ are qualitatively very similar.

The numerical values of ζ reported in the literature generally correspond to very light damping ($\zeta = 0.02 - 0.03$ [10], $\zeta = 0.025$ [14], $\zeta = 0.0417$ [17], $\zeta = 0.03$ [18], $\zeta = 0.0138$ [19], $\zeta = 0.0135$ [20], $\zeta = 0.01$ [21], $\zeta = 0.0038$ [22], $\zeta = 0.0032$ [24]). Accordingly, we drop the damping term from Eq. (6.5) to get the following *unperturbed* linear equation

$$\ddot{x}(t) + (1+p)\,x(t) - p\,x_\tau(t) \;=\; 0. \tag{6.6}$$

The characteristic equation corresponding to Eq. (6.6) is

$$\lambda^2 + (1+p) - pe^{-\lambda\,\tau} = 0.$$

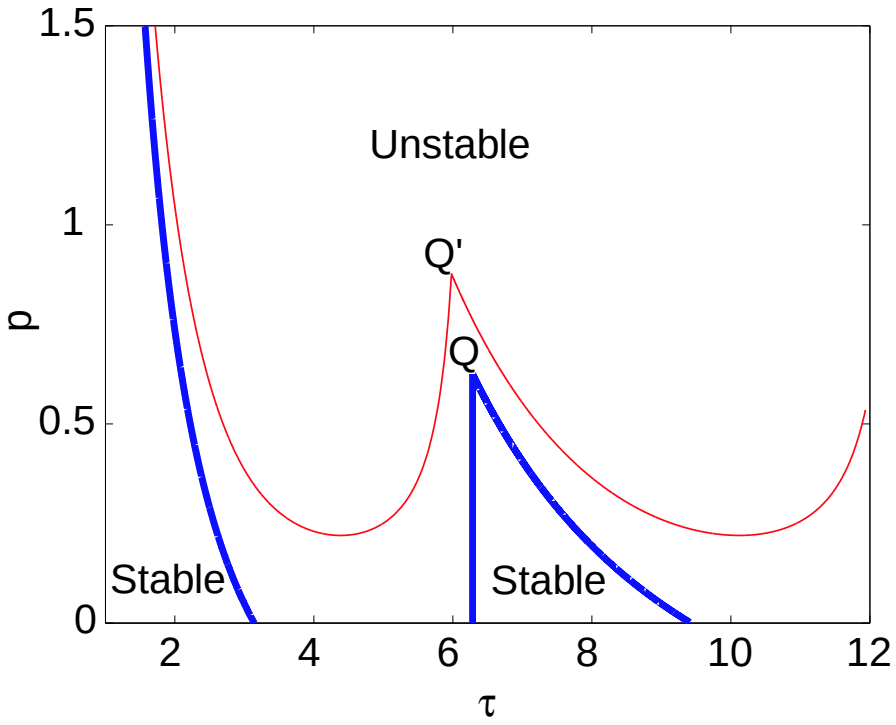

Figure 6.1: Stability boundary of Eq. (6.5), thick line: $\zeta = 0$ and thin line: $\zeta = 0.1$.

On the stability boundary, the characteristic equation has a pair of pure imaginary roots with all other roots having negative real parts. To find the stability boundary, we substitute $\lambda = \pm i\,\omega$, with $\omega \geq 0$, into the above and obtain

$$-\omega^2 + 1 + p - p\cos(\omega\,\tau) + i\,p\sin(\omega\,\tau) \;= 0\,.$$

Separating real and imaginary parts, we get

$$1 - \omega^2 + p\,(1 - \cos(\omega\,\tau)) \;=\; 0\,, \tag{6.7}$$

$$p\sin(\omega\,\tau) \;=\; 0\,. \tag{6.8}$$

An immediate observation is that $p = 0$ and $\omega = 1$ satisfies the above equations. However, this corresponds to not cutting at all; we are ultimately interested in $p > 0$.

From Eq. (6.8), we get for $p \neq 0$, either $\omega\tau = 2N\pi$ or $\omega\tau = (2M+1)\pi$, for some integers N and M (for ease of identification, N represents even multiples of π, and M represents odd).

First consider an even case. When $\omega\tau = 2N\pi$, from Eq. (6.7) we get $\omega = 1$ and hence, $\tau = 2N\pi$. In this case, p remains indeterminate (i.e., this solution is valid for all p). The indeterminacy in p is represented by the thick vertical line in Fig. 6.1.

Now consider an odd case. When $\omega\tau = (2M+1)\pi$, from Eq. (6.7) we get

$$p = \frac{\omega^2 - 1}{2}.$$

Since $p \geq 0$ by assumption, we must have $\omega \geq 1$. Since

$$\tau = \frac{(2M+1)\pi}{\omega},$$

we then have $\tau \leq (2M+1)\pi$. Finally, for $\tau = 2M\pi < (2M+1)\pi$, this solution branch intersects the even solution branch labeled using the symbol N as discussed above (see also the thick lines in Fig. 6.1).

By the foregoing, we simultaneously have two solutions in (τ, p) space whenever $N = M$. These are given by

1. $\omega_1\tau = 2N\pi$, whence $\omega_1 = 1$ and $\tau = 2N\pi$, and

2. $\omega_2\tau = (2N+1)\pi$, whence

$$\omega_2 = \frac{2N+1}{2N} \text{ and } p = \frac{4N+1}{8N^2}.$$

In other words, at $\tau = 2N\pi$ and $p = \dfrac{4N+1}{8N^2}$, we have two pairs of pure imaginary roots corresponding to $\omega_1 = 1$ and $\omega_2 = \dfrac{2N+1}{2N}$ (all such points are resonant).

Note that the solution branches obtained above intersect at other points in (τ, p) space as well; but those points are all already unstable by virtue of being above some other branch. Thus, the above set of intersections represents all possible double Hopf points on the stability boundary in parameter space.

We will henceforth restrict attention to the case $N = 1$, whereby $\tau = 2\pi$, $p = 5/8$ and the two frequencies are $\omega_1 = 1$ and $\omega_2 = 3/2$.

For this choice of the parameters, the first few of the remaining roots (found numerically) are -0.1544, $-0.3150 \pm 2.445\,i$, $-0.4499 \pm 3.452\,i$ and $-0.5400 \pm 4.458\,i$. For a special case of Eq. (6.5) with $\tau = 1$, it has been shown analytically in [69] that the large roots have logarithmically large negative real parts, i.e., for a large root λ, $\mathrm{Re}(\lambda) = \mathcal{O}(-\ln|\lambda|)$. The above numerically obtained roots, though not very large, already confirm this predicted asymptotic trend. Hence, all the λ's except the pure imaginary ones obtained above have negative real parts and this choice of parameters, i.e., $(\tau, p) = (2\pi, 5/8) = (6.283, 0.625)$, represents a double Hopf point on the stability boundary. The rest of this chapter presents an analysis of Eq. (6.4) in the neighbourhood of this double Hopf point.

Note from Fig. 6.1 that in the presence of a small amount of damping the double Hopf point shifts a little. For $\zeta = 0.1$, it is

$$(\tau, p) = (5.980, 0.877) = (2\pi - 0.303, 5/8 + 0.252)\,. \tag{6.9}$$

This will be accounted for by detuning and perturbing the parameters as described in the next section.

6.4 Multiple scales

Scaling: To perform multiple scales analysis, we could scale $x(t)$ as $\epsilon\, y(t)$, where ϵ is some "small" parameter (as in [9, 10, 11]). However, this restricts $x(t)$ to be infinitesimal. Instead, noting that $p = 5/8$ for the double Hopf point, we take $3\,p/10 = 3/16 = 0.1875$ as ϵ in Eq. (6.4), allowing $x(t) = \mathcal{O}(1)$ with respect to this ϵ. The multiple-scales analysis that follows is based on the smallness of ϵ, and so is strictly valid only in the limit as $\epsilon \to 0$, while our interest lies in the strictly finite $\epsilon = 3/16$. However, it will be seen that the analysis gives useful qualitative insights into the behavior of the system. Numerical values match imperfectly but acceptably well. For further discussion on the nonrigorous modeling decision implicit in this scaling, see appendix E.

Detuning: To indirectly account for variations in τ near the double Hopf point, we stretch time as $\bar{t} = (1+\epsilon\,\Delta)t$ (and then drop the overbar for notational simplicity). A delay of 2π in this new time scale represents a time delay of $\dfrac{2\pi}{(1+\epsilon\,\Delta)}$ in the original time t. An increase in Δ thus corresponds to a decrease in the delay (or an increase in the rotational speed of the workpiece). In the above, we mean that Δ is arbitrary while ϵ is really the finite-nonzero number 3/16. However, the analysis will be based on asymptotics for small ϵ (see appendix E).

Further scaling: We substitute $p = \dfrac{5}{8} + \epsilon p_1$ to account for the variation in p near the double Hopf point. Again, we mean here that p_1 is arbitrary while ϵ is really the finite-nonzero number 3/16. However, as mentioned above, the analysis will be based on asymptotics for small ϵ (see appendix E). In a similar spirit, we set $\zeta = \epsilon\zeta_1$ and $\alpha = \epsilon\alpha_1$.

Now, scaling as above, we get from Eq. (6.4)

$$(1+\epsilon\Delta)^2\ddot{x}(t) + 2\,\epsilon\,(1+\epsilon\Delta)\,\zeta_1\dot{x}(t) + \left(\frac{13}{8} + \epsilon\,p_1\right)x(t) - \left(\frac{5}{8} + \epsilon\,p_1\right)x_{2\pi}(t)$$

$$+\,\epsilon\,\alpha_1\,x(t)^3 = \frac{3}{10}\left(\frac{5}{8} + \epsilon\,p_1\right)\left((x(t) - x_{2\pi}(t))^2 - (x(t) - x_{2\pi}(t))^3\right)\,,$$

where we rearrange the coefficient on the right hand side to get

$$(1+\epsilon\Delta)^2\ddot{x}(t) + 2\,\epsilon\,(1+\epsilon\Delta)\,\zeta_1\dot{x}(t) + \left(\frac{13}{8} + \epsilon\,p_1\right)x(t) - \left(\frac{5}{8} + \epsilon\,p_1\right)x_{2\pi}(t)$$

$$+\,\epsilon\,\alpha_1\,x(t)^3 = \frac{3}{16}\left(1+\frac{8}{5}\epsilon\,p_1\right)\left((x(t)-x_{2\pi}(t))^2-(x(t)-x_{2\pi}(t))^3\right)\,.$$

So far, in spite of our declared intentions of using $\epsilon = 3/16$, we have not really done so. Now setting $3/16 = \epsilon$ in the right hand side above, we finally get

$$(1+\epsilon\Delta)^2\ddot{x}(t) + 2\,\epsilon\,(1+\epsilon\Delta)\,\zeta_1\dot{x}(t) + \left(\frac{13}{8}+\epsilon\,p_1\right)x(t) - \left(\frac{5}{8}+\epsilon\,p_1\right)x_{2\pi}(t)$$

$$+\,\epsilon\,\alpha_1\,x(t)^3 = \epsilon\left(1+\frac{8}{5}\epsilon\,p_1\right)\left((x(t)-x_{2\pi}(t))^2-(x(t)-x_{2\pi}(t))^3\right)\,.$$

Dividing throughout by $(1+\epsilon\Delta)^2$, we obtain

$$\ddot{x}(t) + \frac{2\,\epsilon\,\zeta_1}{(1+\epsilon\Delta)}\dot{x}(t) + \frac{1}{(1+\epsilon\Delta)^2}\left[\left(\frac{13}{8}+\epsilon\,p_1\right)x(t) - \left(\frac{5}{8}+\epsilon\,p_1\right)x_{2\pi}(t)\right] + \frac{\epsilon\,\alpha_1}{(1+\epsilon\Delta)^2}x(t)^3$$

$$= \frac{\epsilon}{(1+\epsilon\Delta)^2}\left(1+\frac{8}{5}\epsilon\,p_1\right)\left((x(t)-x_{2\pi}(t))^2-(x(t)-x_{2\pi}(t))^3\right)\,. \tag{6.10}$$

So far, no small-ϵ approximations have been made. Solution of the above equation with $\epsilon = 3/16$ is exactly equivalent to solution of the original unscaled equation. Now, making a small-ϵ approximation, we expand the above in a Taylor series and retain terms up to $\mathcal{O}(\epsilon)$ to get

$$\ddot{x}(t) + \frac{13}{8}x(t) - \frac{5}{8}x_{2\pi}(t) = \epsilon\left(2\,\Delta\left(\frac{13}{8}x(t)-\frac{5}{8}x_{2\pi}(t)\right) - 2\,\zeta_1\dot{x}(t) - \alpha_1\,x(t)^3 - p_1\,B + B^2 - B^3\right), \tag{6.11}$$

where $B = x(t) - x_{2\pi}(t)$.

For $\epsilon = 0$ Eq. (6.11) is linear and hence has as general solution an infinite linear combination of terms of the form $e^{\lambda t}$. Of these infinitely many λ's, there are two pairs of pure imaginary roots given by $\pm i$ and $\pm\frac{3}{2}i$, with all other roots having negative real parts. Thus, after the transients are dead, we have the following steady state solution

$$x(t) = A_1\sin t + A_2\cos t + A_3\sin\left(\frac{3t}{2}\right) + A_4\cos\left(\frac{3t}{2}\right)\,, \tag{6.12}$$

where A_1, A_2, A_3 and A_4 are arbitrary constants. We will take the above as the solution to the unperturbed equation, i.e., Eq. (6.11) with $\epsilon = 0$ (see also Nayfeh *et al.* [9, 10, 11] and the discussion in Das and Chatterjee [126]).

We introduce two time scales as: t, the original time scale and $T = \epsilon\,t$. The solution to Eq. (6.11) is assumed to be a function of these two time scales and it is further assumed that the solution can be expressed as

$$x(t) = X(t,T) = X_0(t,T) + \epsilon X_1(t,T) + \cdots\,. \tag{6.13}$$

Substituting Eq. (6.13) in Eq. (6.10), we get

$$\frac{\partial^2 X_0}{\partial t^2} + \frac{13}{8}X_0 - \frac{5}{8}X_0(t-2\pi) + \epsilon\left\{\frac{\partial^2 X_1}{\partial t^2} + \frac{13}{8}X_1 - \frac{5}{8}X_1(t-2\pi) + 2\frac{\partial^2 X_0}{\partial t\,\partial T}\right.$$

$$+2\,\zeta_1\frac{\partial X_0}{\partial t} + \frac{\partial X_0}{\partial T}(t-2\pi) + \alpha_1\,X_0^3 + p_1\,(X_0 - X_0(t-2\pi)) + \frac{5}{4}\,\Delta\,X_0(t-2\pi)$$

$$\left.-\frac{13}{4}\Delta\,X_0 + \frac{5\,\pi}{4} - (X_0 - X_0(t-2\pi))^2 + (X_0 - X_0(t-2\pi))^3\right\} + \mathcal{O}(\epsilon^2) = 0\,. \tag{6.14}$$

where, for brevity, we have shown the t-dependence for delayed quantities only. To lowest order, Eq. (6.14) becomes

$$\frac{\partial^2 X_0}{\partial t^2} + \frac{13}{8}X_0 - \frac{5}{8}X_0(t-2\pi) = 0\,. \tag{6.15}$$

The solution of Eq. (6.15) (by Eq. (6.12)) is

$$X_0 = A_1\sin t + A_2\cos t + A_3\sin\left(\frac{3t}{2}\right) + A_4\cos\left(\frac{3t}{2}\right)\,, \tag{6.16}$$

where $A_i = A_i(T), i = 1,2,3,4$.

Substituting Eq. (6.16) into Eq. (6.14) and simplifying, at the next order we obtain

$$\frac{\partial^2 X_1}{\partial t^2} + \frac{13}{8} X_1 - \frac{5}{8} X_1(t-2\pi) + \sum_{m=0}^{9} N_m \cos\left(\frac{m\,t}{2}\right) + \sum_{m=1}^{9} M_m \sin\left(\frac{m\,t}{2}\right) = 0\,, \tag{6.17}$$

where N_i and M_i are given by some lengthy expressions found using MAPLE. In what follows, $\dfrac{\partial A_i}{\partial T}, i = 1, 2, 3, 4,$ are written simply as $\dfrac{dA_i}{dT}$ because slower time scales are not retained and $A_i = A_i(T)$ only. The various coefficients N_i and M_i are

$$N_0 = -2\,A_4^2 - 2\,A_3^2\,,$$

$$N_1 = \frac{3}{4}\,\alpha_1\,A_2^2\,A_4 + \frac{3}{2}\,\alpha_1\,A_1\,A_2\,A_3 - \frac{3}{4}\,\alpha_1\,A_1^2\,A_4\,,$$

$$N_2 = \frac{3}{4}\,\alpha_1\,A_1^2\,A_2 + \frac{3}{2}\,\alpha_1\,A_2\,A_3^2 + \frac{3}{2}\,\alpha_1\,A_2\,A_4^2 - 2\,\Delta\,A_2 + \frac{3}{4}\,\alpha_1\,A_2^3 + \frac{5}{4}\,\pi\,\frac{dA_2}{dT} + 2\,\zeta_1\,A_1 + 2\,\frac{dA_1}{dT}\,,$$

$$N_3 = 6\,A_3^2\,A_4 - \frac{5}{4}\,\pi\,\frac{dA_4}{dT} + 3\,\zeta_1\,A_3 + 2\,p_1\,A_4 + \frac{3}{2}\,\alpha_1\,A_2^2\,A_4 + \frac{3}{4}\,\alpha_1\,A_3^2\,A_4 - \frac{9}{2}\,\Delta\,A_4 + \frac{3}{4}\,\alpha_1\,A_4^3 + \frac{3}{2}\,\alpha_1\,A_1^2\,A_4 + 3\,\frac{dA_3}{dT} + 6\,A_4^3\,,$$

$$N_4 = \frac{3}{2}\,\alpha_1\,A_1\,A_3\,A_4 - \frac{3}{4}\,\alpha_1\,A_2\,A_3^2 + \frac{3}{4}\,\alpha_1\,A_2\,A_4^2\,,$$

$$N_5 = 0\,,$$

$$N_6 = -2\,A_4^2 + 2\,A_3^2 + \frac{1}{4}\,\alpha_1\,A_2^3 - \frac{3}{4}\,\alpha_1\,A_1^2\,A_2\,,$$

$$N_7 = -\frac{3}{2}\,\alpha_1\,A_1\,A_2\,A_3 + \frac{3}{4}\,\alpha_1\,A_2^2\,A_4 - \frac{3}{4}\,\alpha_1\,A_1^2\,A_4\,,$$

$$N_8 = -\frac{3}{2}\,\alpha_1\,A_1\,A_3\,A_4 - \frac{3}{4}\,\alpha_1\,A_2\,A_3^2 + \frac{3}{4}\,\alpha_1\,A_2\,A_4^2\,,$$

$$N_9 = 2\,A_4^3 - \frac{3}{4}\,\alpha_1\,A_3^2\,A_4 - 6\,A_3^2\,A_4 + \frac{1}{4}\,\alpha_1\,A_4^3\,,$$

$$M_1 = \frac{3}{2}\,\alpha_1\,A_1\,A_2\,A_4 + \frac{3}{4}\,\alpha_1\,A_1^2\,A_3 - \frac{3}{4}\,\alpha_1\,A_2^2\,A_3\,,$$

$$M_2 = -2\,\frac{dA_2}{dT} - 2\,\Delta\,A_1 + \frac{5}{4}\,\pi\,\frac{dA_1}{dT} - 2\,\zeta_1\,A_2 + \frac{3}{2}\,\alpha_1\,A_1\,A_4^2 + \frac{3}{4}\,\alpha_1\,A_1\,A_2^2 + \frac{3}{2}\,\alpha_1\,A_1\,A_3^2 + \frac{3}{4}\,\alpha_1\,A_1^3\,,$$

$$M_3 = -3\,\zeta_1\,A_4 + 2\,p_1\,A_3 - 9/2\,\Delta\,A_3 - \frac{5}{4}\,\pi\,\frac{dA_3}{dT} + \frac{3}{4}\,\alpha_1\,A_3^3 + \frac{3}{4}\,\alpha_1\,A_3\,A_4^2 + 6\,A_3^3 - 3\,\frac{dA_4}{dT} + \frac{3}{2}\,\alpha_1\,A_2^2\,A_3 + 6\,A_3\,A_4^2 + 3/2\,\alpha_1\,A_1^2\,A_3\,,$$

$$M_4 = \frac{3}{2}\,\alpha_1\,A_2\,A_3\,A_4 + \frac{3}{4}\,\alpha_1\,A_1\,A_3^2 - \frac{3}{4}\,\alpha_1\,A_1\,A_4^2\,,$$

$$M_5 = 0\,,$$

$$M_6 = -\frac{1}{4}\,\alpha_1\,A_1^3 + \frac{3}{4}\,\alpha_1\,A_1\,A_2^2 - 4\,A_3\,A_4\,,$$

$$M_7 = \frac{3}{2}\,\alpha_1\,A_1\,A_2\,A_4 - \frac{3}{4}\,\alpha_1\,A_1^2\,A_3 + \frac{3}{4}\,\alpha_1\,A_2^2\,A_3\,,$$

$$M_8 = \frac{3}{2}\,\alpha_1\,A_2\,A_3\,A_4 - \frac{3}{4}\,\alpha_1\,A_1\,A_3^2 + \frac{3}{4}\,\alpha_1\,A_1\,A_4^2\,,$$

$$M_9 = -2\,A_3^3 + \frac{3}{4}\,\alpha_1\,A_3\,A_4^2 + 6\,A_3\,A_4^2 - \frac{1}{4}\,\alpha_1\,A_3^3\,.$$

Now to avoid secular terms in the solution, the coefficients of $\sin t$, $\cos t$, $\sin\left(\frac{3\,t}{2}\right)$ and $\cos\left(\frac{3\,t}{2}\right)$ in Eq. (6.17) are set to zero, i.e., $M_2 = 0, N_2 = 0, M_3 = 0$ and $N_3 = 0$. Solving these four equations, we obtain $\frac{dA_1}{dT}$, $\frac{dA_2}{dT}$, $\frac{dA_3}{dT}$ and $\frac{dA_4}{dT}$.

Finally the evolution of A_1, A_2, A_3 and A_4 in the original time scale t can be obtained as

$$\dot{A}_i = \epsilon\frac{\partial A_i}{\partial T} + \mathcal{O}(\epsilon^2)\,, \qquad i = 1, 2, 3, 4\,.$$

The expressions obtained (using MAPLE) up to $\mathcal{O}(\epsilon)$ are

$$\begin{aligned}
\dot{A}_1 = \frac{\epsilon}{64 + 25\,\pi^2}\,\big\{&40\,\pi\,\zeta_1\,A_2 - 64\,\zeta_1\,A_1 + 40\,\pi\,\Delta\,A_1 + 64\,\Delta\,A_2 - 24\,\alpha_1\,A_2^3 - 24\,\alpha_1\,A_1^2\,A_2 - 15\,\pi\,\alpha_1\,A_1\,A_2^2 \\
&-15\,\pi\,\alpha_1\,A_1^3 - 30\,\pi\,\alpha_1\,A_1\,A_3^2 - 30\,\pi\,\alpha_1\,A_1\,A_4^2 - 48\,\alpha_1\,A_2\,A_3^2 - 48\,\alpha_1\,A_2\,A_4^2\big\}\,, \\
\dot{A}_2 = \frac{-\epsilon}{64 + 25\,\pi^2}\,\big\{&40\,\pi\,\zeta_1\,A_1 + 64\,\zeta_1\,A_2 - 40\,\pi\,\Delta\,A_2 + 64\,\Delta\,A_1 - 24\,\alpha_1\,A_1^3 - 24\,\alpha_1\,A_1\,A_2^2 + 15\,\pi\,\alpha_1\,A_1^2\,A_2 \\
&+15\,\pi\,\alpha_1\,A_2^3 + 30\,\pi\,\alpha_1\,A_2\,A_3^2 + 30\,\pi\,\alpha_1\,A_2\,A_4^2 - 48\,\alpha_1\,A_1\,A_3^2 - 48\,\alpha_1\,A_1\,A_4^2\big\}\,, \\
\dot{A}_3 = \frac{-\epsilon}{144 + 25\,\pi^2}\,\big\{&144\,\zeta_1\,A_3 + 60\,\pi\,\zeta_1\,A_4 + 90\,\pi\,\Delta\,A_3 - 216\,\Delta\,A_4 + 288\,A_4^3 + 288\,A_3^2\,A_4 - 15\,\pi\,\alpha_1\,A_3\,A_4^2 \\
&-15\,\pi\,\alpha_1\,A_3^3 - 120\,\pi\,A_3^3 - 120\,\pi\,A_3\,A_4^2 + 36\,\alpha_1\,A_4^3 + 36\,\alpha_1\,A_3^2\,A_4 + 72\,\alpha_1\,A_1^2\,A_4 \\
&+72\,\alpha_1\,A_2^2\,A_4 - 30\,\pi\,\alpha_1\,A_1^2\,A_3 - 30\,\pi\,\alpha_1\,A_2^2\,A_3 - 40\,\pi\,p_1\,A_3 + 96\,p_1\,A_4\big\}\,, \\
\dot{A}_4 = \frac{\epsilon}{144 + 25\,\pi^2}\,\big\{&60\,\pi\,\zeta_1\,A_3 - 144\,\zeta_1\,A_4 - 90\,\pi\,\Delta\,A_4 - 216\,\Delta\,A_3 + 288\,A_3^3 + 288\,A_3\,A_4^2 + 15\,\pi\,\alpha_1\,A_3^2\,A_4 \\
&+ 15\,\pi\,\alpha_1\,A_4^3 + 120\,\pi\,A_3^2\,A_4 + 120\,\pi\,A_4^3 + 36\,\alpha_1\,A_3^3 + 36\,\alpha_1\,A_3\,A_4^2 + 72\,\alpha_1\,A_1^2\,A_3 \\
&+72\,\alpha_1\,A_2^2\,A_3 + 30\,\pi\,\alpha_1\,A_1^2\,A_4 + 30\,\pi\,\alpha_1\,A_2^2\,A_4 + 40\,\pi\,p_1\,A_4 + 96\,p_1\,A_3\big\}\,.
\end{aligned}$$

We finally change to polar co-ordinates using

$$A_1 = R_1\cos(\phi_1) \quad \text{and} \quad A_2 = R_1\sin(\phi_1)\,,$$

and

$$A_3 = R_2\cos\left(\frac{3\phi_2}{2}\right) \quad \text{and} \quad A_4 = R_2\sin\left(\frac{3\phi_2}{2}\right)\,.$$

Solving for $\dot{R}_1$, $\dot{R}_2$, $\dot{\phi}_1$ and $\dot{\phi}_2$, we obtain till $\mathcal{O}(\epsilon)$

$$\dot{R}_1 = \epsilon\frac{\left(40\,\pi\,\Delta - 64\,\zeta_1 - 15\,\pi\,\alpha_1\,R_1^2 - 30\,\pi\,\alpha_1\,R_2^2\right)\,R_1}{25\,\pi^2 + 64}\,, \tag{6.18}$$

$$\dot{R}_2 = \epsilon\frac{(40\,\pi\,p_1 - 144\,\zeta_1 - 90\,\pi\,\Delta + 120\,\pi\,R_2^2 + 15\,\pi\,\alpha_1\,R_2^2 + 30\,\pi\,\alpha_1\,R_1^2)\,R_2}{25\,\pi^2 + 144}\,, \tag{6.19}$$

$$\dot{\phi}_1 = \epsilon\frac{-8\,(5\,\pi\,\zeta_1 - 3\,\alpha_1\,R_1^2 - 6\,\alpha_1\,R_2^2 + 8\,\Delta)}{25\,\pi^2 + 64}\,, \tag{6.20}$$

and

$$\dot{\phi}_2 = \epsilon\frac{8\,(8\,p_1 + 5\,\pi\,\zeta_1 - 18\,\Delta + 3\,\alpha_1\,R_2^2 + 6\,\alpha_1\,R_1^2 + 24\,R_2^2)}{25\,\pi^2 + 144}\,. \tag{6.21}$$

The above system can be studied effectively as a two-dimensional system of equations involving R_1 and R_2 only (Eqs. (6.18) and (6.19)) because the amplitude equations are decoupled from the angular variables (at least till first order). The bifurcation structure of Eqs. (6.18) and (6.19) in the $p_1/\zeta_1 - \Delta/\zeta_1$ plane is shown in Fig. 6.2, where the plane is divided into 5 regions with distinct behaviors.

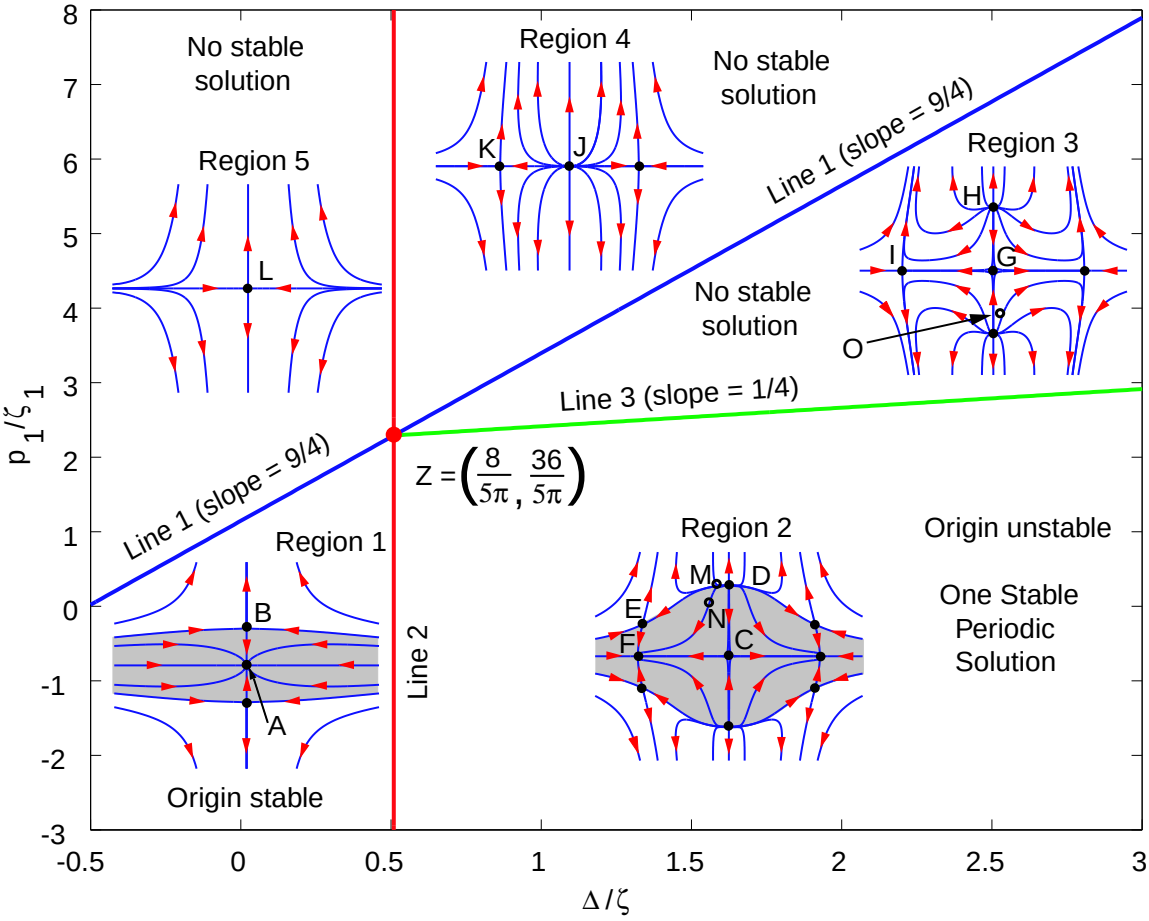

Figure 6.2: Bifurcation structure of Eqs. (6.18) and (6.19). Numerically, for $\zeta = 0.1$ or $\zeta_1 = \dfrac{0.1}{\epsilon} = \dfrac{8}{15}$, Z represents $(p, \tau) = (5.979, 0.854)$, agreeing well with numerics (Eq. (6.9)). For each of the phase portraits above, the horizontal axis represents R_1 and the vertical axis represents R_2.

6.5 Analysis

In region 1, there are two qualitatively different fixed points (along with reflections of the same) marked A and B in Fig. 6.2. Point A, the origin, is a stable node while point B is a saddle representing an unstable periodic solution of Eq. (6.10). The basin of attraction of A is shaded grey.

On crossing line 2 and entering region 2, we find two more qualitatively different fixed points (along with reflections of the same totalling six new equilibria). This results in a total of four qualitatively different fixed points marked C, D, E and F in Fig. 6.2. Point C, the origin, has lost stability and become a saddle while the fixed point F is a stable node, representing a stable periodic solution of Eq. (6.10). The overall basin of attraction for stable periodic solutions is again shaded grey.

Numerical simulation results of Eq. (6.10) in region 2, with $\zeta_1 = 1$, $\alpha_1 = 1$, $\Delta = 8/(5\pi)+1/4$ and $p_1 = 36/(5\pi)$ are plotted in Fig. 6.3. The steady state amplitude found numerically is 0.75, comparing reasonably if imperfectly with 0.82 predicted from first order MMS.

Numerical simulations for two typical points marked M and N in Fig. 6.2, region 2 (one outside the basin of attraction and one inside it) also show behavior consistent with that predicted by the phase portrait (see Figs. 6.4 and 6.5).

Figure 6.4 shows a numerical simulation corresponding to the point M in Fig. 6.2, region 2. M lies just outside the grey region and the solution starting from M is thrown out to infinity eventually. The phase portrait predicts that at the beginning of rapid growth in the amplitude which corresponds to the trajectory being very close to the saddle point, both frequencies, i.e., $\omega = 1$ and $\omega = 3/2$ should be present in the solution. For $\zeta_1 = 1$, $\alpha_1 = 1$, $\Delta = 8/(5\pi) + 1/4$ and $p_1 = 36/(5\pi)$, the fixed point D in Fig. 6.2, region 2, is $R_1 = 0, R_2 = 0.41$. However, the numerically estimated value from other detailed simulation-searches of Eq. (6.10) is $R_1 = 0, R_2 = 0.53$. Guided

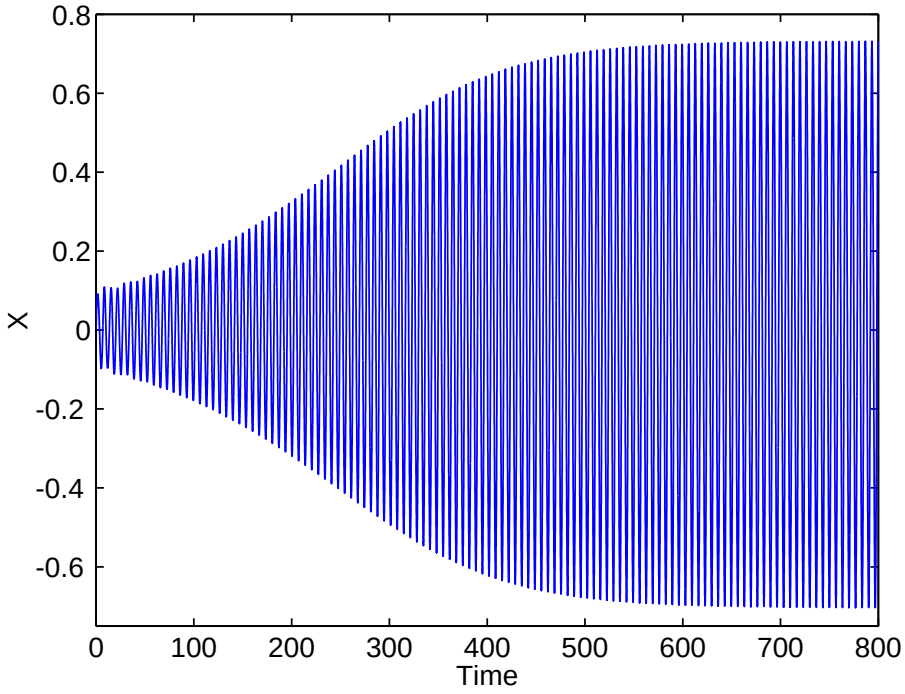

Figure 6.3: Numerical solution of Eq. (6.10) for $\zeta_1 = 1$, $\alpha_1 = 1$, $\Delta = 8/(5\pi) + 1/4$ and $p_1 = 36/(5\pi)$. Initial conditions: $x(\eta) = 0.1\sin(\eta), \dot{x}(\eta) = 0.1\cos(\eta), \eta \in [-2\pi, 0]$.

by this numerical value, we choose $R_1 = 0.031, R_2 = 0.55$ to represent the point M. Accordingly, the initial function for the DDE is $x(\eta) = 0.55\sin(3\eta/2) + 0.031\sin(\eta), \dot{x}(\eta) = 0.825\cos(3\eta/2) + 0.031\cos(\eta), \eta \in [-2\pi, 0]$. The numerical solution of Eq. (6.10) thus obtained is plotted in Fig. 6.4 (top). Figure 6.4 (middle and bottom) shows the power spectral density (PSD) of the numerical solution till the onset of instability (beginning of rapid growth), i.e., till $t \approx 250$, on semilog and linear scales, respectively. There are clearly two dominant frequencies, close to 1 and 3/2 (the difference observed is technically $\mathcal{O}(\epsilon)$, and arises from Eqs. (6.20) and (6.21)). Other frequencies involving relatively smaller amplitudes are seen here as well; these represent various harmonics and linear combinations of the two dominant frequencies.

Figure 6.5 corresponds to the point N in Fig. 6.2, region 2. The phase portrait predicts that an initially higher value of R_2 will eventually decay to $R_2 = 0$. For the same parameter values as used for the point M (Fig. 6.4), we use $R_1 = 0.051, R_2 = 0.5$ to represent the point N. The numerical solution of Eq. (6.10) for the initial function $x(\eta) = 0.5\sin(3\eta/2) + 0.051\sin(\eta), \dot{x}(\eta) = 0.75\cos(3\eta/2) + 0.051\cos(\eta), \eta \in [-2\pi, 0]$, is shown in Fig. 6.5 (top). PSD's of the solution over two time windows, early and late, clearly show the decay of R_2 over time. It is also clear that R_1 stabilizes to 0.75 as in Fig. 6.3 (and compares reasonably well with the analytical prediction of 0.82).

On crossing from region 2 to region 3 along line 3, a reverse subcritical pitchfork bifurcation occurs in the amplitude equations. Note that a pitchfork bifurcation in the amplitude equations corresponds to a Hopf bifurcation in the original system. No stable bounded solutions remain either for the amplitude equations or Eq. (6.10). Numerical simulation of a point marked O in Fig. 6.2, region 3, for $\zeta_1 = 1$, $\alpha_1 = 1$, $\Delta = 8/(5\pi) + 1$ and $p_1 = 36/(5\pi) + 1$ is shown in Fig. 6.6. The initial function is $x(\eta) = 0.6\sin(3\eta/2) + 0.0001\sin(\eta), \dot{x}(\eta) = 0.9\cos(3\eta/2) + 0.0001\cos(\eta), \eta \in [-2\pi, 0]$, which represents a point very close to the R_2 axis. The phase portrait predicts that R_2, the frequency $= 3/2$ component, should decay initially with R_1, the frequency $= 1$ component, growing. The solution should slow down near the saddle point marked I in Fig. 6.2, region 3, before eventually blowing up. All of these are observed in Fig. 6.6, from direct numerical simulation of Eq. (6.10).

On entering region 4 from region 3 along line 1, two unstable nodes merge with the saddle at the origin in another reverse pitchfork bifurcation, leaving a single unstable node at the origin (point J). Again there are no stable bounded solutions.

On crossing from region 4 to region 5 along line 2, the saddles and the unstable node at the origin merge in yet another reverse pitchfork bifurcation, leaving a single saddle at the origin (point L). Here also, there are no stable bounded solutions.

Thus, regions 1 and 2 provide stable bounded solutions of the original equation while regions 3, 4 and 5

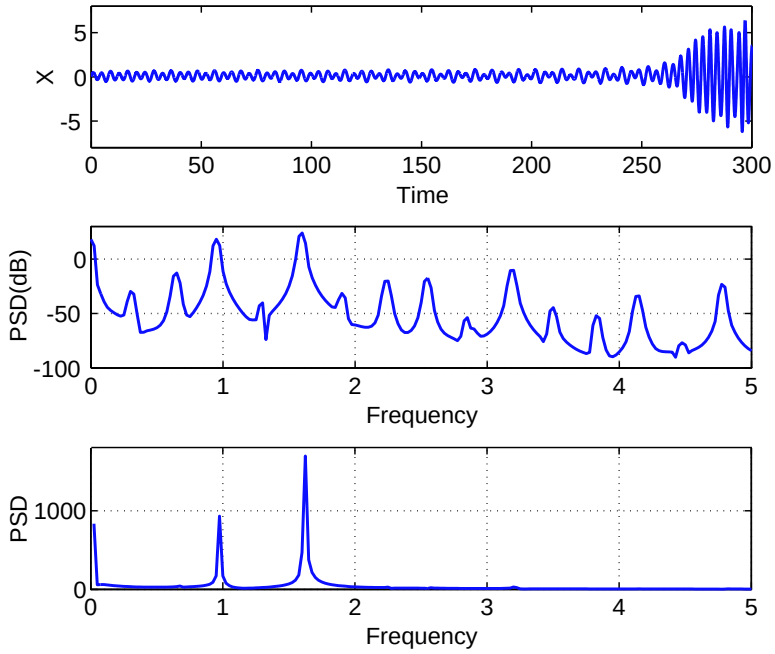

Figure 6.4: Numerical solution of Eq. (6.10) for $\zeta_1 = 1$, $\alpha_1 = 1$, $\Delta = 8/(5\pi) + 1/4$ and $p_1 = 36/(5\pi)$. Initial Conditions: $x(\eta) = 0.55\sin(3\eta/2) + 0.031\sin(\eta), \dot{x}(\eta) = 0.825\cos(3\eta/2) + 0.031\cos(\eta), \eta \in [-2\pi, 0]$. This corresponds to the point M in Fig. 6.2. Middle: PSD of data until beginning of rapid growth, i.e., $t = 85\,\pi \approx 250$ on a log scale. Bottom: PSD on a linear scale showing only two dominant frequencies corresponding to 1 and 3/2 (the difference observed is technically $\mathcal{O}(\epsilon)$, and arises from Eqs. (6.20) and (6.21)).

correspond to no such solutions.

6.6 Concluding remarks

By treating the damping in the system as a small perturbation, analytical expressions have been obtained for all the double Hopf points in the DDE, though the subsequent analysis is restricted to $N = 1$ (the double Hopf point corresponding to a high cutting speed). The unperturbed double-Hopf points obtained herein are all resonant. The direct use of MMS without center manifold reductions simplifies the calculations near the double Hopf point. Our choice of ϵ allowed the previously non-dimensionalized $x(t) = \mathcal{O}(1)$, allowing us to study the dynamics for not-too-small amplitudes. Both sub- and supercritical Hopf bifurcations are observed depending on how two key parameters are varied near the double Hopf point.

Our analysis is not valid for large amplitudes because of our local power series expansion of the expression for the cutting force. For initial conditions outside the domain of attraction of bounded solutions (if any), the amplitudes predicted by our equations become arbitrarily large. For such cases, there are other attractors related to another nonlinearity (see [14] and chapter 7 of this thesis), which involves loss of contact between the tool and the workpiece; this effect has not been considered in this chapter. We note that, for the particular strength of nonlinearity in stiffness proposed by Hanna and Tobias [4], Nayfeh *et al.* [11] showed the presence of bounded global attractors without considering loss of contact; the amplitudes there might be large enough in some physical situation to also lead to loss of contact. For correct physical modeling of the global dynamics of cutting, therefore, models should probably incorporate both nonlinear stiffness as well as loss of contact. However, Prof. Gábor Stépán[1] has suggested that loss of contact may be the more important effect, and I share his views now. For example, in this chapter we have seen that there are significant regions of parameter space where bifurcations are subcritical even with a stiffening nonlinearity. Loss of contact may have a strong role to play in such situations. Accordingly, in the next chapter we incorporate loss of contact but not nonlinear stiffness.

[1] personal communication

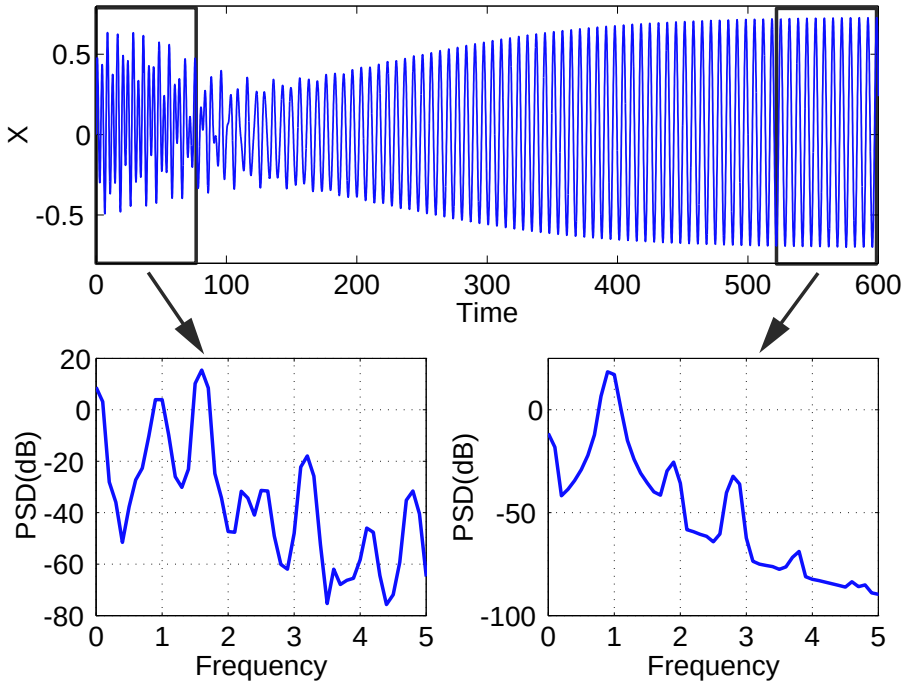

Figure 6.5: Numerical solution of Eq. (6.10) for $\zeta_1 = 1$, $\alpha_1 = 1$, $\Delta = 8/(5\pi) + 1/4$ and $p_1 = 36/(5\pi)$. Initial Conditions: $x(\eta) = 0.5\sin(3\eta/2) + 0.051\sin(\eta), \dot{x}(\eta) = 0.75\cos(3\eta/2) + 0.051\cos(\eta), \eta \in [-2\pi, 0]$. This corresponds to the point N in Fig. 6.2. Bottom left: PSD of data from $t_0 = 0$ to $t_f = 20\,\pi \approx 60$. Bottom right: PSD of data from $t_0 = 170\,\pi \approx 540$ to $t_f = 190\,\pi \approx 600$.

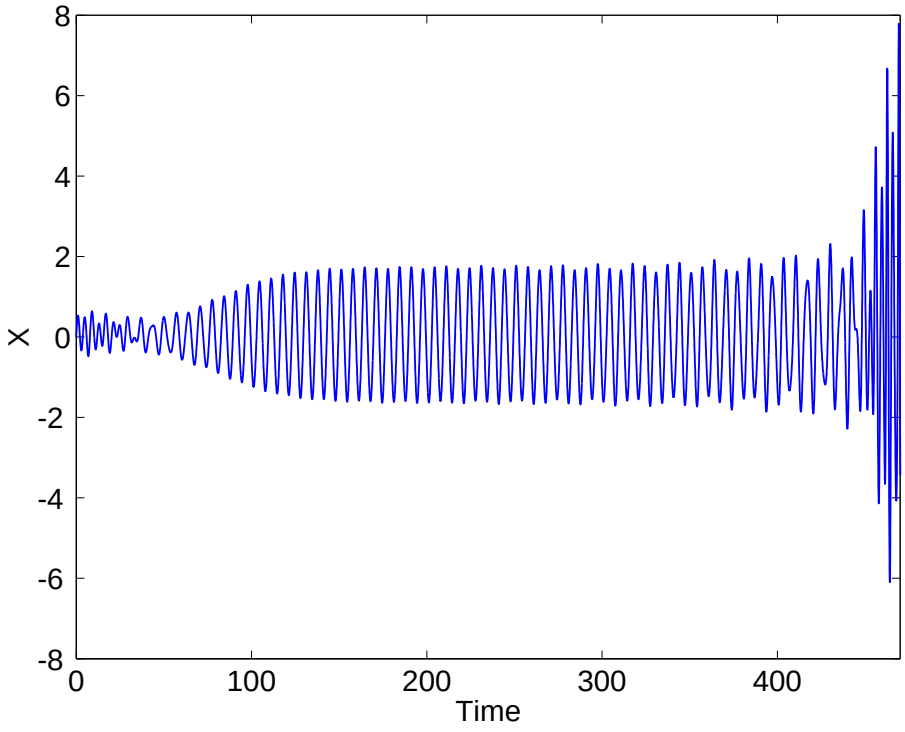

Figure 6.6: Numerical solution of Eq. (6.10) for $\zeta_1 = 1$, $\alpha_1 = 1$, $\Delta = 8/(5\pi) + 1$ and $p_1 = 36/(5\pi) + 1$. Initial Conditions: $x(\eta) = 0.6\sin(3\eta/2) + 0.0001\sin(\eta), \dot{x}(\eta) = 0.9\cos(3\eta/2) + 0.0001\cos(\eta), \eta \in [-2\pi, 0]$. This corresponds to point O in Fig. 6.2.

Chapter 7

Self-interrupted regenerative turning

As pointed out in chapter 6, for correct physical modeling of the global dynamics of cutting, models should incorporate intermittent loss of contact due to large amplitude vibrations. Such cutting is called *self-interrupted*.

7.1 Introduction

In this chapter, we study the self-interrupted regenerative turning arising after the loss of linear stability of steady cutting. Self-interrupted machining occurs due to a loss of contact between the tool and the workpiece when the relative vibrations between the tool and the workpiece grow large. Self-interruption can give rise to globally stable periodic solutions under broad parameter ranges where the primary bifurcation to instability is subcritical.

We develop a new approach to model the regenerative effect in turning operations. The dynamics of the cutting process is modeled using a direct approach which leads to a partial differential equation (PDE) along with an ordinary differential equation (ODE). The coupled PDE-ODE model describes the full dynamics of the turning process, in the sense that the PDE describes the cut surface while the ODE describes the motions of the cutting tool. This model automatically incorporates *self-interruption* due to the loss of contact between the tool and the workpiece as well as the *multiple-regenerative* effects accompanying it.

Recall the basic dynamical model for cutting without loss of contact (Eq. (1.6)). Here, due to loss of contact over some interval, some portion of the workpiece fails to get cut. If it gets cut during the next pass of the tool, then the delay in the DDE jumps from τ to 2τ (multiple regenerative effect [5, 6, 7, 17, 25]). The delay could conceivably be 3τ, 4τ, or higher. These possibilities require tracking of the delay to be used in the DDE model during phases of contact. As will be seen below, our approach requires no such delay tracking while retaining the ability to model self-interruption, at the cost of introducing an extra PDE.

The rest of the chapter is organized as followed. In section 7.2, we present our model for the dynamics of chip formation. In section 7.3, we present numerical simulation results of the model using a finite-difference scheme as well as Galerkin projections. Some qualitative aspects of the solution are also discussed. The bifurcation structure of the regenerative turning process along with some discussion of the same is presented in section 7.4. In section 7.5, we present some solutions other than single globally stable periodic solutions. Concluding remarks are made in section 7.6.

7.2 Chip formation

In this chapter, we will use Eq. (1.4), which is reproduced below

$$\ddot{x}(t) + 2\,\zeta\,\dot{x}(t) + x(t) = PC(t)^{3/4}\,, \tag{7.1}$$

where the parameter P is proportional to the chip width (or depth of cut). We note that studies focusing on the effect of impact during re-entry after loss of contact have appeared in the literature [62, 143]. In case we wish to incorporate an impulsive impact interaction at re-entry, Eq. (7.1) should be modified to

$$\ddot{x}(t) + 2\,\zeta\,\dot{x}(t) + x(t) = PC(t)^{3/4} + sgn(\dot{C}(t))\,\delta(C(t))\,g(\dot{C}(t))\,,$$

where $g(\dot{C}(t)) \geq 0$ incorporates the effect of impact. However, we have modeled re-entry as smooth in this work, and will work with Eq. (7.1).

Our modeling approach is independent of any particular model for tool-workpiece dynamics, and could be trivially extended to other models (e.g., incorporating nonlinear tool stiffness, nonlinear damping, impacts, etc.). We restrict attention to impact-free re-entry and linear tool dynamics for greatest simplicity.

Given the governing equation for the tool-workpiece dynamics, it remains to determine the instantaneous chip thickness $C(t)$. In cutting with sustained contact, the instantaneous chip thickness $C(t)$ (see footnote 1) is

$$C(t) = C_0 + x(t-\tau) - x(t)\,, \tag{7.2}$$

where C_0 is the nominal chip thickness and $\tau = 2\pi/\Omega$ is the time period of one revolution of the workpiece [12, 14, 16, 76]. However, when the relative displacement becomes so large that the tool leaves the workpiece, the above definition of the instantaneous chip thickness no longer remains valid. Delayed displacements from more than one immediate pass have to be considered (hence, the possible delays of $2\tau, 3\tau$, etc.).

We use a new approach to model chip formation which is somewhat similar in spirit to that of Batzer *et al.* [25], in that we both define the cut surface by essentially the same function L (defined below). However, their application (drilling) is different from ours; we introduce a new solution method; and we also present new results specific to turning operations.

A schematic of the turning process is shown in Fig. 7.1. The tool travels along the negative x-direction with a velocity v and the workpiece rotates about the positive x-axis at an angular rate Ω. The tool velocity is related to the nominal chip thickness C_0 by

$$v = \frac{C_0\,\Omega}{2\pi}\,.$$

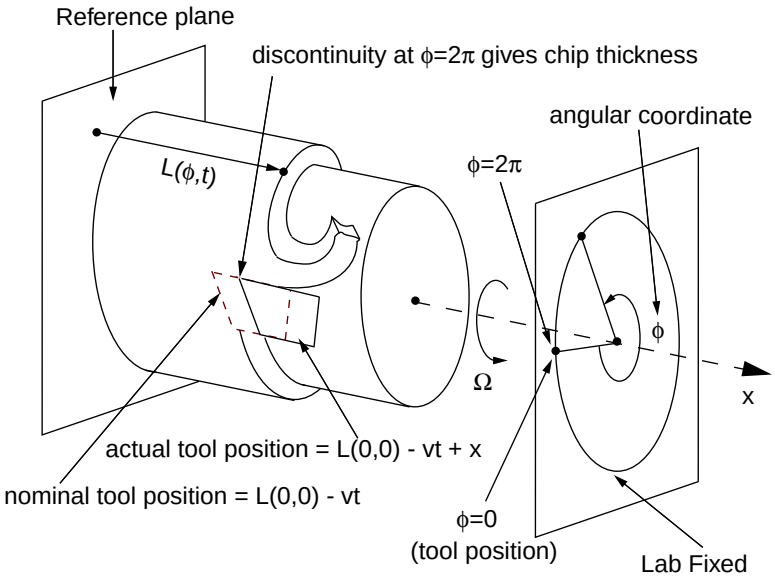

Figure 7.1: A schematic of turning process.

We define a function $L(\phi, t), \phi \in [0, 2\pi]$, which represents the perpendicular distance of points on the cut surface from a reference plane as shown in Fig. 7.1. The angle ϕ is measured in lab-fixed coordinates, $\phi = 0 \equiv 2\pi$ representing the position of the tool. Note that even though $\phi = 0$ and $\phi = 2\pi$ are the same points in the lab-fixed coordinate system, they imply different things for the workpiece. That is, $\phi = 0$ represents the freshly exposed surface just past the tool, while $\phi = 2\pi$ represents the one-revolution old surface location just reaching the tool. In particular, the function $L(\phi, t)$ can have a discontinuity at $\phi = 0 \equiv 2\pi$ which determines the instantaneous chip thickness $C(t)$ (see footnote 1). Thus, the instantaneous chip thickness $C(t)$ is given by

$$C(t) = L(2\pi, t) - L(0, t) \tag{7.3}$$

whenever it is positive, i.e., whenever the tool is in contact with the workpiece. When the tool leaves the workpiece, the chip thickness becomes zero and the discontinuity in the function $L(\phi, t)$ vanishes, i.e.,

$$L(2\pi, t) = L(0, t)\,.$$

The nominal position of the tool is $L(0, 0) - vt$. Due to vibrations, the actual position of the tool is $L(0, 0) - vt + x(t)$. When there is contact between the tool and the workpiece, it follows that $L(0, t) = L(0, 0) - vt + x(t)$. Equation (7.3) then gives

$$C(t) = \max\{L(2\pi, t) - L(0, 0) + vt - x(t), 0\}\,,$$

valid whether the tool is in contact with the workpiece or not. Also, $L(0,0)$ can be taken as zero, giving

$$C(t) = \max\left\{L(2\pi, t) + vt - x(t), 0\right\} . \tag{7.4}$$

The above value of $C(t)$ is to be used in Eq. (7.1).

Now, consider a material point on the cut surface at some angle $\phi \in (0, 2\pi)$. Over a small time duration Δt, the workpiece rotates by an angle $\Delta\phi = \Omega\Delta t$. Therefore,

$$L(\phi + \Omega\Delta t, t + \Delta t) = L\left(\phi, t\right) .$$

It follows that

$$\frac{\partial L}{\partial t} = -\Omega\frac{\partial L}{\partial \phi} . \tag{7.5}$$

The above PDE governs the evolution of $L(\phi, t)$ for $\phi \in (0, 2\pi)$.

We now consider the boundary condition for this PDE. Equation (7.3) is rewritten as

$$L(0, t) = L(2\pi, t) - C(t) , \tag{7.6}$$

where $C(t)$ is given by Eq. (7.4). The above equation expresses the physical fact that $L(2\pi, t)$ and $C(t)$ together determines $L(0, t)$. This equation acts as a boundary condition for the PDE, as will be discussed in greater detail below. It is an important feature of our model. In particular, it automatically and implicitly incorporates any and all regenerative effects.

We now define $\bar{L} = L + vt$. This leads to

$$C(t) = \max\left\{\bar{L}(2\pi, t) - x(t), 0\right\} . \tag{7.7}$$

The PDE is modified to

$$\frac{\partial \bar{L}}{\partial t} = v - \Omega\frac{\partial \bar{L}}{\partial \phi} \tag{7.8}$$

and the boundary condition becomes

$$\bar{L}(0, t) = \bar{L}(2\pi, t) - C(t) . \tag{7.9}$$

Using Eq. (7.7), the boundary condition can be written as

$$\bar{L}(0, t) = \min\left\{\bar{L}(2\pi, t), x(t)\right\} . \tag{7.10}$$

Equations (7.7), (7.8) and (7.10) together define the kinematics of the formation. These in combination with Eq. (7.1) determine the complete dynamics of the regenerative turning process.

A pictorial representation of our approach is provided in Fig. 7.2.

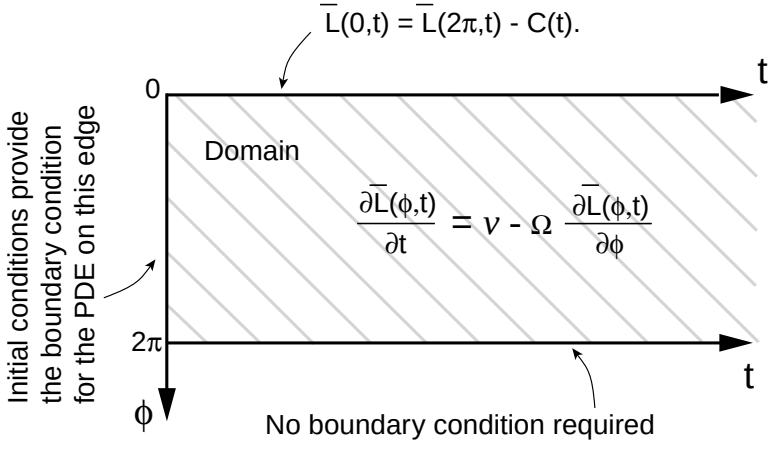

Figure 7.2: Pictorial representation of the chip formation model.

7.3 Numerical results

7.3.1 Finite-difference solution

We use a second-order finite difference scheme to approximate the ϕ-derivative of $\bar{L}(\phi, t)$ in Eq. (7.8). Note that, since $\dfrac{\partial \bar{L}}{\partial \phi}$ has a discontinuity at points where tool-workpiece contact is initiated or lost, the second order finite-difference approximation is not accurate at those isolated points. However, it is accurate at other points, and in our numerical work we have verified that refining the finite-difference mesh does in fact give useful convergence. The algorithmic complication of tracking those discontinuities are therefore avoided. The discretization scheme can be summarized below as

1. Discretize the ϕ-domain $[0, 2\pi]$ into N sub-intervals. Accordingly, the mesh size h is $h = 2\pi/N$.

2. Let the value of the function $\bar{L}(\phi, t)$ at $\phi = 0, h, 2h, \cdots, Nh$ be denoted by $a_0(t), a_h(t)$, $a_{2h}(t), \cdots, a_{Nh}(t)$, respectively.

3. The chip-thickness is calculated using Eq. (7.7) as

$$C(t) = \max\left\{a_{Nh}(t) - x(t), 0\right\} . \tag{7.11}$$

4. Using Eq. (7.10), we get $a_0(t)$ as

$$a_0(t) = \min\left\{a_{Nh}(t), x(t)\right\} . \tag{7.12}$$

   We note from Eq. (7.12) that $a_0(t)$ is a dummy variable and hence, no differential equation is required to govern its evolution.

5. The evolution of the remaining variables $a_{kh}(t), k = 1, 2, \cdots, N$ are obtained by discretizing Eq. (7.8). They are

$$\frac{d}{dt}a_{kh}(t) = v - \Omega\frac{a_{(k+1)h}(t) - a_{(k-1)h}(t)}{2h} , \quad k = 1, 2, \cdots, N-1 , \tag{7.13}$$

$$\frac{d}{dt}a_{Nh}(t) = v - \Omega\frac{3a_{Nh}(t) - 4a_{(N-1)h}(t) + a_{(N-2)h}(t)}{2h} , \tag{7.14}$$

   where Eq. (7.12) is substituted for $a_0(t)$. The one-sided finite-difference derivative in Eq. (7.14) is also second order accurate.

Eqs. (7.13), (7.14), (7.11) and (7.1) determine the dynamics of the turning process. Numerical results for $\zeta = 0.1$, $\Omega = 2$, $v = 1/\pi$, $P = 0.5$ and two different values of N (200 and 300) are presented in Fig. 7.3. Initial conditions are chosen to be all zeros, i.e., $a_i(0) = 0$ for $i = 1, 2, \cdots, N$; $x(0) = 0$ and $\dot{x}(0) = 0$.

The two solutions are near-indistinguishable in Fig. 7.3 (bottom). Hence, for our purposes, we take the solution with $N = 200$ as the exact solution of the set of equations Eqs. (7.7), (7.8), (7.10) and (7.1).

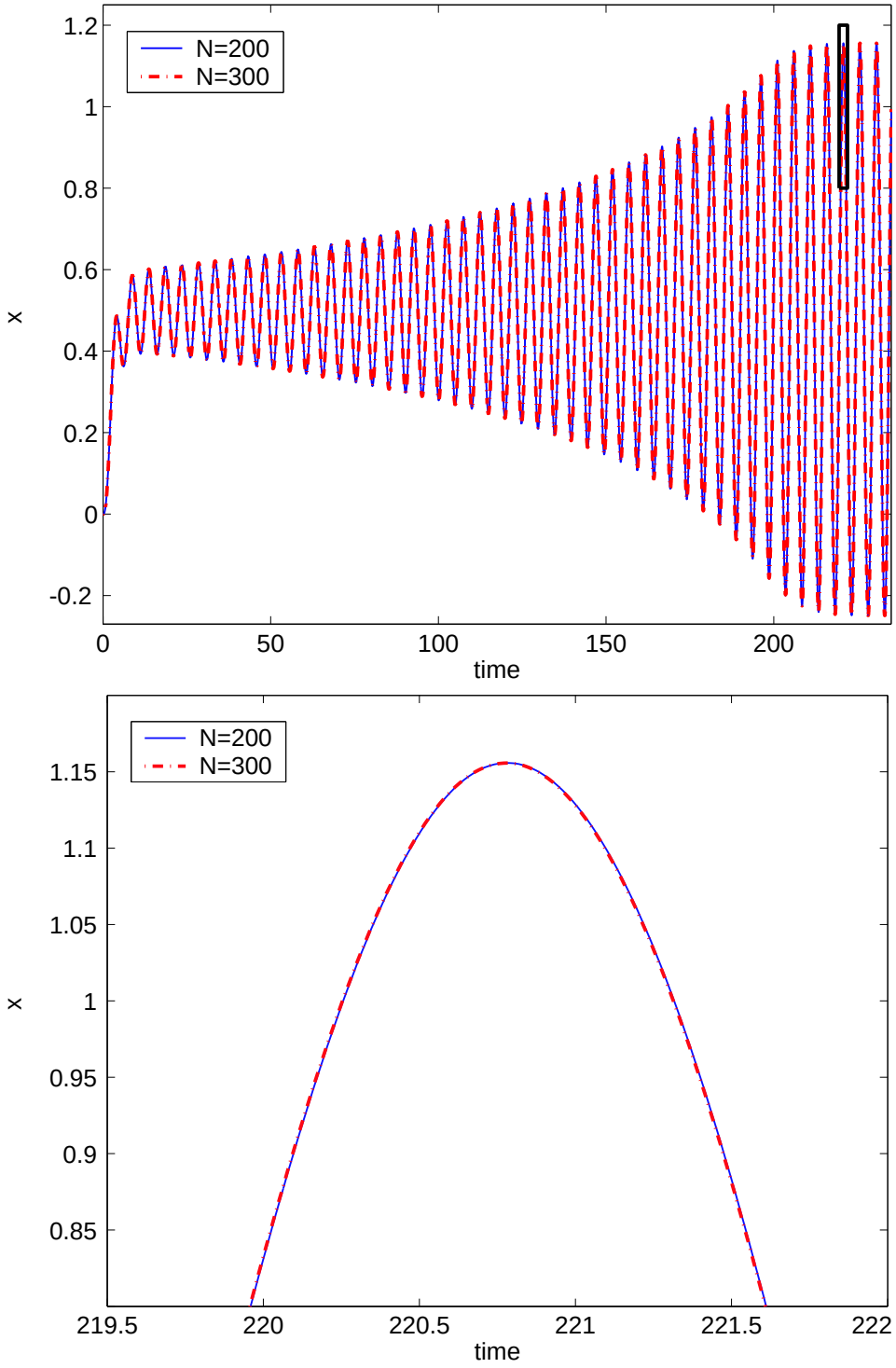

Figure 7.3: Top: Numerical solution of Eqs. (7.13), (7.14), (7.11) and (7.1) for $N = 200$ and $N = 300$. Other parameters are $\zeta = 0.1$, $\Omega = 2$, $v = 1/\pi$, and $P = 0.5$. Initial conditions are chosen to be all zeros, i.e., $a_i(0) = 0$ for $i = 1, 2, \cdots, N$; $x(0) = 0$ and $\dot{x}(0) = 0$. Bottom: A zoomed view of the boxed portion from the top.

7.3.2 Solution using Galerkin projection

Note that Eq. (7.8) is very similar to Eq. (4.8) obtained in chapter 4 where a Galerkin projection was used to obtain a finite set of ODEs (see also [73]). Here, we develop Galerkin projection approximations on similar

lines. We approximate the function $\bar{L}(\phi, t)$ as

$$\bar{L}(\phi, t) \;=\; a_0(t)\left(1 - \frac{\phi}{2\pi}\right) \;+\; a_1(t)\,\frac{\phi}{2\pi} \;+\; \sum_{k=1}^{N-1} a_{k+1}(t)\,\sin\left(\frac{k\phi}{2}\right)\,, \tag{7.15}$$

where N is a finite number that we choose. Note a slight difference in the shape functions (from the ones used in chapter 4) required to account for the different boundary condition (Eq. (7.10)).

We emphasize that our choice of the shape functions represents a smooth function over the domain $\phi \in [0, 2\pi]$. However, the function $\bar{L}(\phi, t)$ potentially has slope discontinuities due to loss and reestablishment of contact. Our choice of shape functions leads to an artificial smoothening of these discontinuities in the Galerkin approximation. However, it will be seen below that this does not introduce significant errors in the approximation and a good match is obtained even with a modest number of shape functions.

From Eq. (7.15), we note that $\bar{L}(0, t) = a_0(t)$ and $\bar{L}(2\pi, t) = a_1(t)$. Hence, the chip thickness from Eq. (7.7) is given as

$$C(t) = \max\left\{a_1(t) - x(t), 0\right\}\,. \tag{7.16}$$

Using Eq. (7.10), we have

$$a_0(t) = \min\left(a_1(t), x(t)\right)\,. \tag{7.17}$$

Once again, $a_0(t)$ acts as a dummy variable. In particular, we take

$$\dot{a}_0(t) = \begin{cases} \dot{x}(t)\,, \;\; x(t) < a_1(t)\,, \\ \dot{a}_1(t)\,, \;\; \text{otherwise}\,. \end{cases} \tag{7.18}$$

Substituting Eq. (7.15) in Eq. (7.8) and rearranging, we get

$$\dot{a}_0(t)\,\left(1 - \frac{\phi}{2\pi}\right) + \dot{a}_1(t)\,\frac{\phi}{2\pi} + \sum_{k=1}^{N-1} \dot{a}_{k+1}(t)\,\sin\left(\frac{k\phi}{2}\right) - v - \frac{\Omega\, a_0(t)}{2\,\pi} + \frac{\Omega\, a_1(t)}{2\,\pi} + \Omega \sum_{k=1}^{N-1} \frac{k\, a_{k+1}(t)}{2}\,\cos\left(\frac{k\phi}{2}\right) \;=\; 0\,.$$

The above equation cannot hold identically, and gives us the framework for the Galerkin projection. We call the left hand side (LHS) of the above equation the residual and make this residual orthogonal to the shape functions corresponding to the real variables, i.e., $a_k(t), k = 1, 2, \cdots, N$. This gives us N equations

$$\int_0^{2\pi} \Bigg\{ \dot{a}_0(t)\,\left(1 - \frac{\phi}{2\pi}\right) \;+\; \dot{a}_1(t)\,\frac{\phi}{2\pi} \;+\; \sum_{k=1}^{N-1} \dot{a}_{k+1}(t)\,\sin\left(\frac{k\phi}{2}\right) \;-\; v \\ - \frac{\Omega\, a_0(t)}{2\,\pi} \;+\; \frac{\Omega\, a_1(t)}{2\,\pi} \;+\; \Omega \sum_{k=1}^{N-1} \frac{k\, a_{k+1}(t)}{2}\,\cos\left(\frac{k\phi}{2}\right) \Bigg\} \;\cdot\; \frac{\phi}{2\pi}\, d\phi = 0 \tag{7.19}$$

and

$$\int_0^{2\pi} \Bigg\{ \dot{a}_0(t)\,\left(1 - \frac{\phi}{2\pi}\right) \;+\; \dot{a}_1(t)\,\frac{\phi}{2\pi} \;+\; \sum_{k=1}^{N-1} \dot{a}_{k+1}(t)\,\sin\left(\frac{k\phi}{2}\right) \;-\; v \\ - \frac{\Omega\, a_0(t)}{2\,\pi} \;+\; \frac{\Omega\, a_1(t)}{2\,\pi} \;+\; \Omega \sum_{k=1}^{N-1} \frac{k\, a_{k+1}(t)}{2}\,\cos\left(\frac{k\phi}{2}\right) \Bigg\} \;\cdot\; \sin\left(\frac{m\phi}{2}\right)\, d\phi = 0\,, \tag{7.20}$$

for $m = 1, 2, \cdots, N-1$. In the above equations, we substitute $a_0(t)$ from Eq. (7.17), $\dot{a}_0(t)$ from Eq. (7.18) and obtain the ODEs in terms of $\dot{a}_i(t)$, $a_i(t)$, $i = 1, 2, .., N$, $\dot{x}(t)$ and $x(t)$.

These equations, i.e., Eqs. (7.16), (7.19) and (7.20) along with Eq. (7.1) define our finite-dimensional ODE model for the turning dynamics.

Numerical simulation results for the parameter values $\zeta = 0.1$, $\Omega = 2$, $v = 1/\pi$, and $P = 0.5$, initial conditions all zeros (same as used in Fig. 7.3), and $N = 25$ are presented in Fig. 7.4.

It can be seen from Fig. 7.4 that the solution of ODEs obtained using Galerkin projection matches very well with the accurate finite-difference solution. The slight difference in phase seen in Fig. 7.4 (bottom) is not of primary importance because the system is autonomous. The match in amplitude and time period is good enough for the bifurcation diagrams to be presented later. We will use Eqs. (7.16), (7.19), (7.20) and (7.1) for detailed parameter studies in section 7.4. Before that, we discuss some qualitative aspects of the solution.

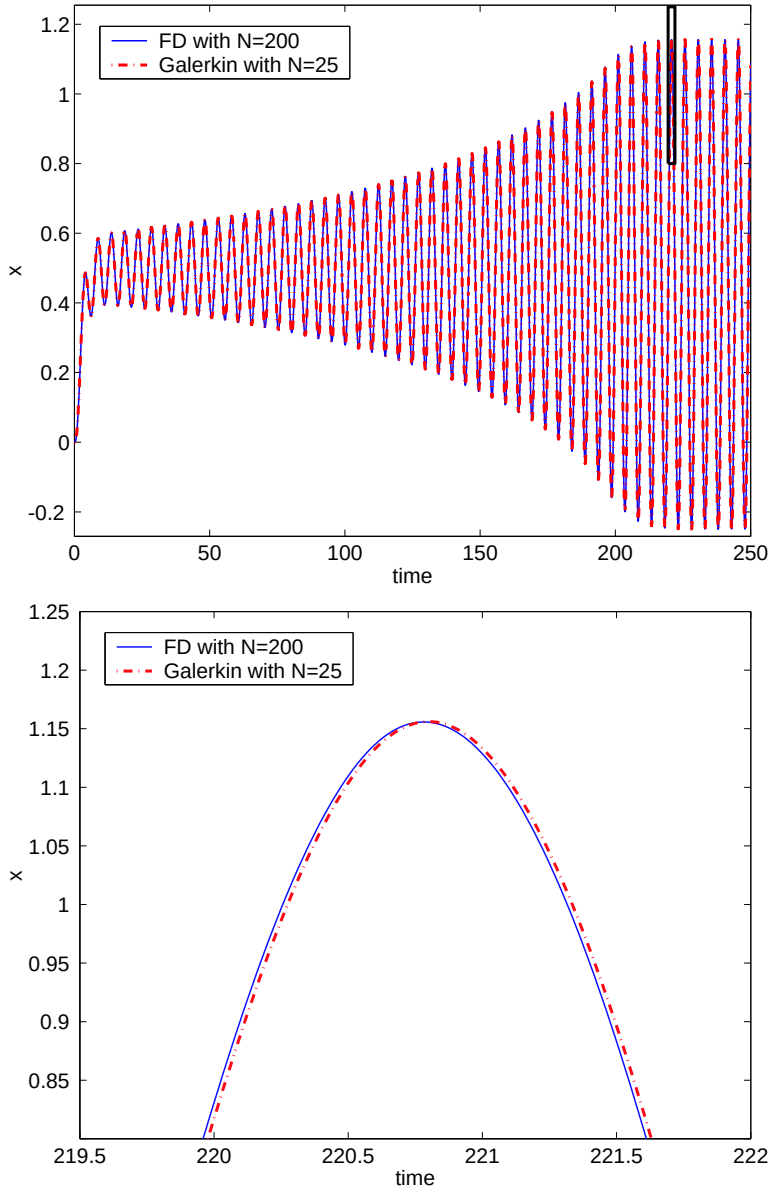

Figure 7.4: Top: Numerical solution of Eqs. (7.16), (7.19), (7.20) and (7.1) for $\zeta = 0.1$, $\Omega = 2$, $v = 1/\pi$, $P = 0.5$, and $N = 25$. Initial conditions: $a_i(0) = 0$ for $i = 1, 2, \cdots, 25$; $x(0) = 0$ and $\dot{x}(0) = 0$. For comparison, the solution obtained using finite-difference with $N = 200$ is also plotted. Bottom: A zoomed view of the boxed portion from the top.

7.3.3 Qualitative aspects of the solution

Figure 7.5 show the function $\bar{L}(\phi, t)$ with $\phi \in [-\pi, \pi]$ and a contour plot of the same on the (ϕ, t) plane. The t-range is from $98\,\pi$ to $100\,\pi$. The time interval depicts two workpiece rotations, but clearly not two solution periods of $x(t)$. The ϕ domain is $[-\pi, \pi]$ using periodic extension to emphasize the discontinuities at $\phi = 0 \equiv 2\pi$. Transients are dead, and the steady state response is seen.

The discontinuity at $\phi = 0$ corresponds to cutting, or contact between tool and workpiece. In particular, the two distinct edges at $\phi = 0$ in Fig. 7.5 represent the profiles of the cut surface. The upper edge represents the cut surface from the previous pass while the lower edge represents the freshly generated surface. The gap between the two edges represents the chip thickness. In the time interval $t \approx [309.5, 310.5]$, the function $\bar{L}(\phi, t)$ is continuous across the edge $\phi = 0$ which corresponds to zero chip thickness, or lack of contact between tool and workpiece.

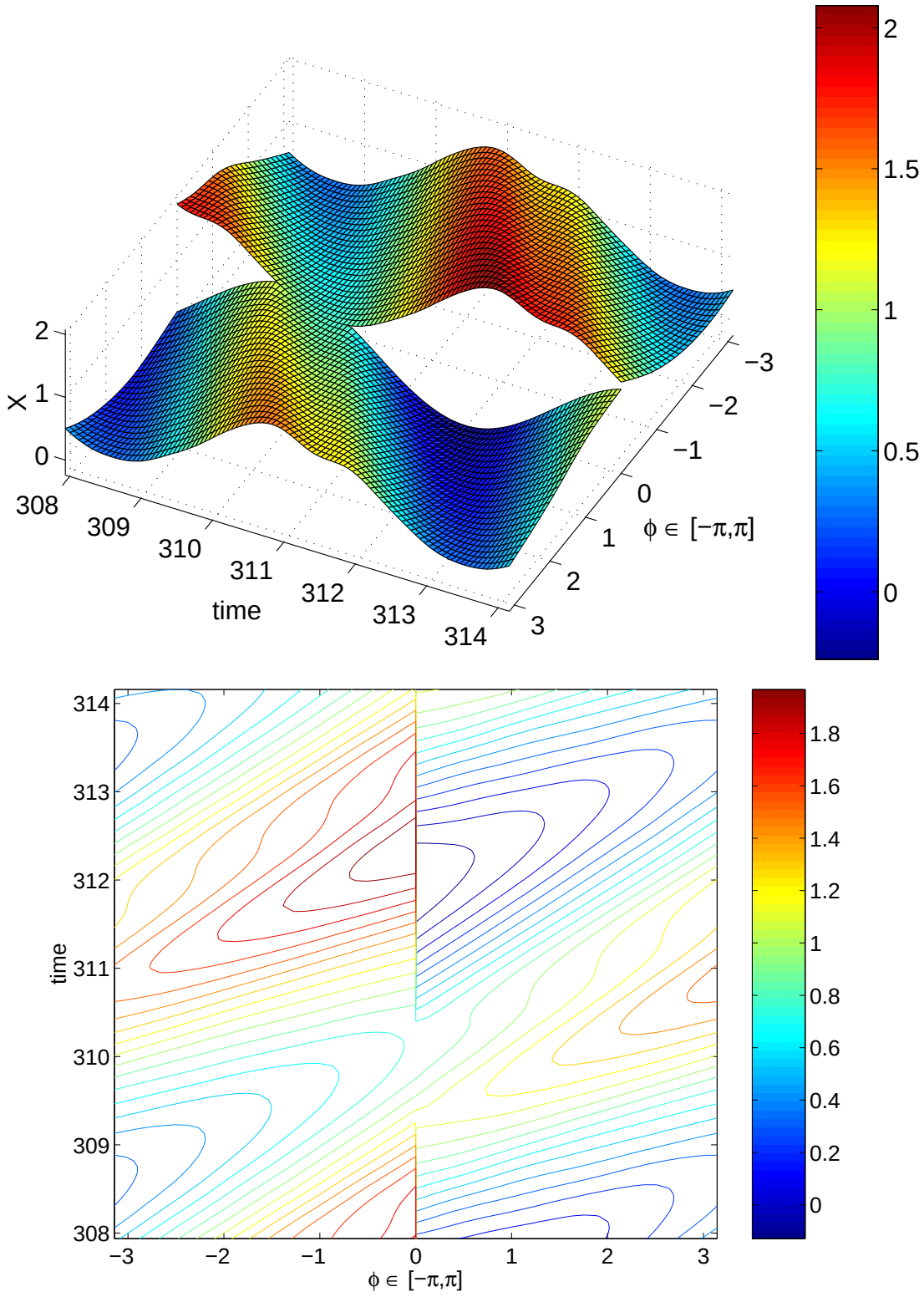

Figure 7.5: Top: $\bar{L}(\phi, t)$ at various instants of time ranging from $98\,\pi$ to $100\,\pi$. Bottom: A contour plot of the top figure. The ϕ domain is $[-\pi, \pi]$ using periodic extension to emphasize the discontinuities at $\phi = 0 \equiv 2\pi$.

7.4 Periodic solutions

7.4.1 Turning points

The bifurcation structure of the regenerative turning process with changing P (or equivalently, the chip width or depth of cut) for $\zeta = 0.1$, $\Omega = 2$, and $v = 1/\pi$ is presented in Fig. 7.6. To generate the bifurcation diagram, we have used a fixed arc-length based continuation scheme in conjunction with a numerical scheme for obtaining periodic solutions of ODEs. Details of the numerical scheme are provided in appendix F. It can be seen in a zoomed view of the boxed portion that the unstable branch from the subcritical Hopf bifurcation (see [12]) and the stable branch from the self-interrupted motion meet in a turning point bifurcation. The point of impending loss of contact occurs on the unstable branch, close to the turning point. At our level of numerical precision, it may be unreliable to try to pinpoint the separation between these two points, and we do not attempt it. For many qualitative purposes, however, the two points may be treated as coincident.

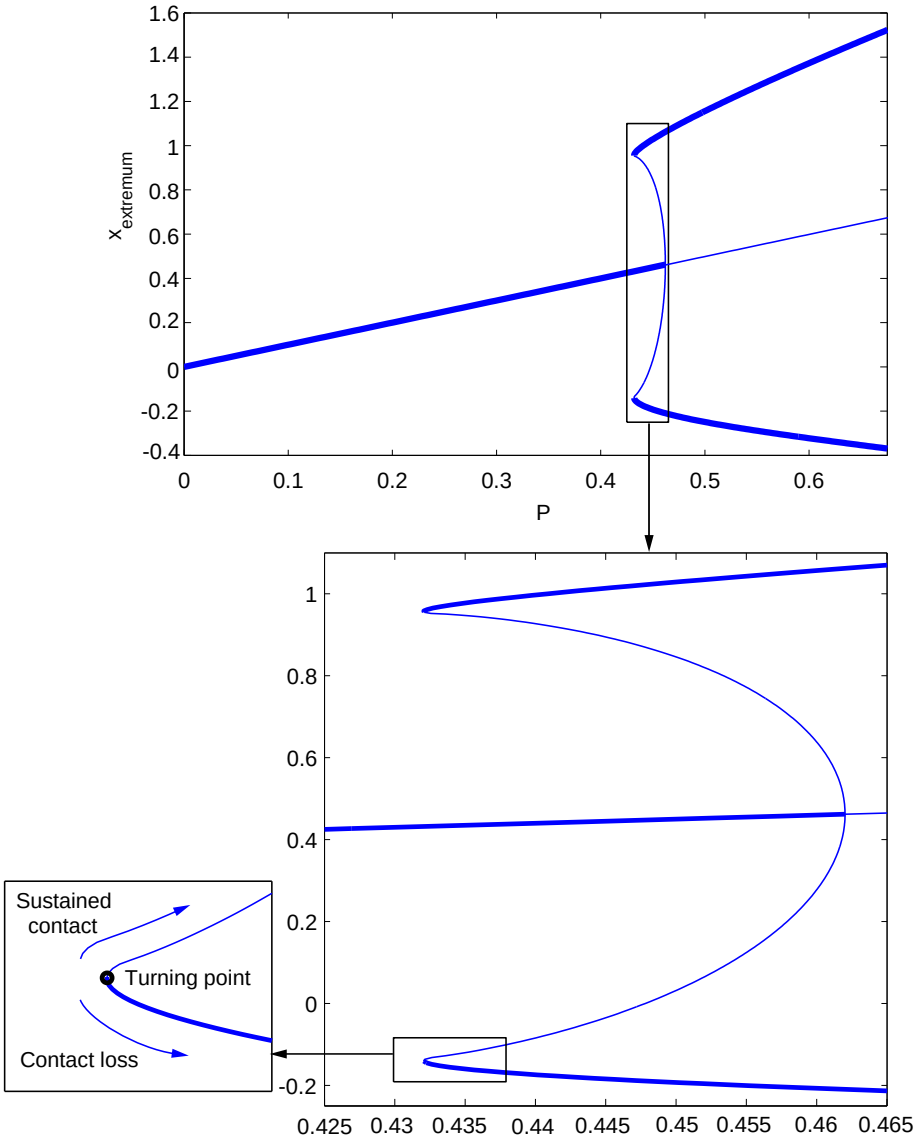

Figure 7.6: Bifurcation diagram for $\zeta = 0.1$, $\Omega = 2$, $v = 1/\pi$ and $N = 25$. Thick lines represent stable solutions while thin lines represent unstable solutions. See text for further details.

In Fig. 7.7, we have plotted the bifurcation diagram for $\zeta = 0.1$, $\Omega = 2$, and $v = 1/\pi$ for different numbers of shape functions in the Galerkin approximation, viz. $N = 5$, $N = 15$ and $N = 25$. The qualitative structure of the bifurcation diagram remains the same. The quantitative agreement between the various bifurcation diagrams improves with increasing N. There is very little difference between the diagrams for $N = 15$ and $N = 25$,

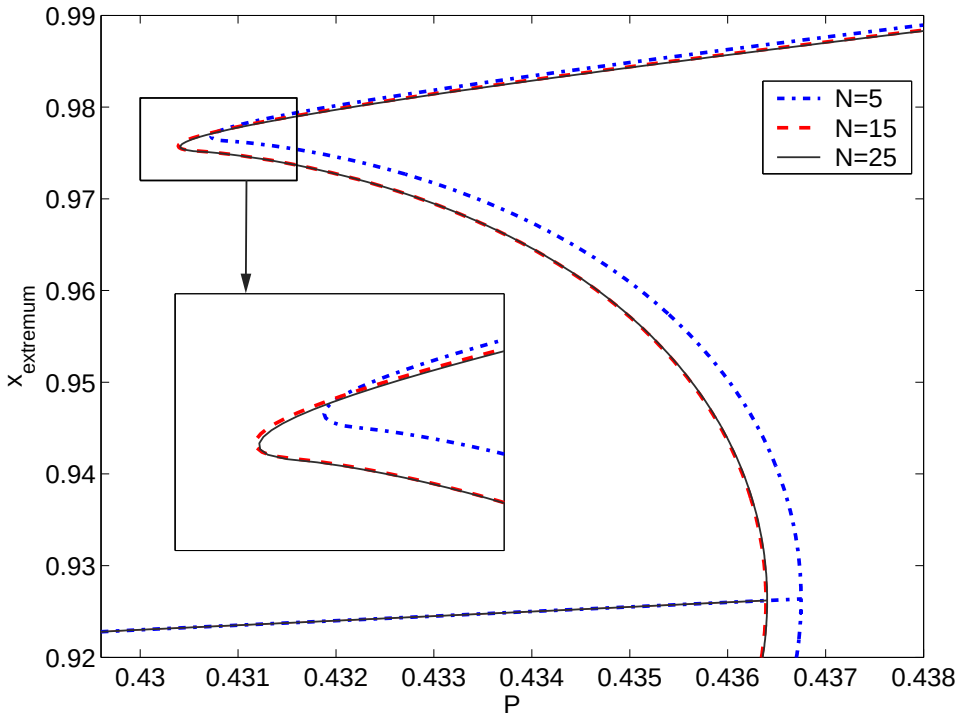

Figure 7.7: Bifurcation diagram for $N = 5$, $N = 15$ and $N = 25$. Parameter values: $\zeta = 0.1$, $\Omega = 2$, and $v = 1/\pi$.

showing convergence of the solution. In general, the number N required for acceptable accuracy will depend on Ω; for example, a very small value of Ω implies many tool oscillations during one workpiece rotation, and large N may be needed to resolve their effect on the cut surface.

Next, we consider the bifurcation diagram for three different values of nondimensionalized damping ζ, viz., $\zeta = 0.05$, $\zeta = 0.1$ and $\zeta = 0.2$, presented in Fig. 7.8. In the figure, we have subtracted $x_{static} = PC_0^{3/4}$, the static displacement due to the nominal cutting force corresponding to the nominal chip thickness, from the extremal x-values in the vertical axis. The bifurcation diagram is not symmetric about zero; this is expected because of the nonlinear cutting force model as well as due to the loss of contact for large enough x.

The turning points are located approximately at $P = 0.935\, P_{critical}$ independent of ζ. Hence, steady cutting is stable under even large perturbations when P is below $0.935\, P_{critical}$. In general, however, the turning point location changes with changing ζ as seen, for example, for $\Omega = 1.2$ in Fig. 7.9. Numerically, we have observed for various values of Ω, that the value of $P/P_{critical}$ at the turning point seems to lie within the interval $[0.92, 0.95]$ for $\zeta \in [0, 0.2]$. This observation may have practical relevance.

7.4.2 Amplitudes at turning points

From Figs. 7.8 and 7.9, we note that the maximal tool displacement at the turning point increases with the damping parameter ζ. The turning point displacement seems to be converging to some specific value as ζ approaches 0. It is about 0.5 (half the nominal chip thickness $C_0 = 1$ for the parameter values of our choice) in Fig. 7.8. This can be interpreted as follows.

The turning point roughly corresponds to the minimum value of the amplitude of the solution for which the tool can leave the workpiece. Approaching the turning point from the unstable branch, there is no loss of contact until (essentially) the turning point. Hence, the usual τ-delayed model can be used as there is no loss of contact. Using Eq. (1.5), we find that the tool leaves the workpiece when

$$x(t) - x(t - \tau) = C_0\,.$$

Now, as a rough approximation, assuming a pure sinusoidal solution $x(t) = A\cos(\omega t)$ about the static deflection x_{static} where A is the amplitude and ω is the angular frequency of the periodic solution, we have

$$A\cos(\omega t) - A\cos(\omega t - \omega\tau) = C_0\,.$$

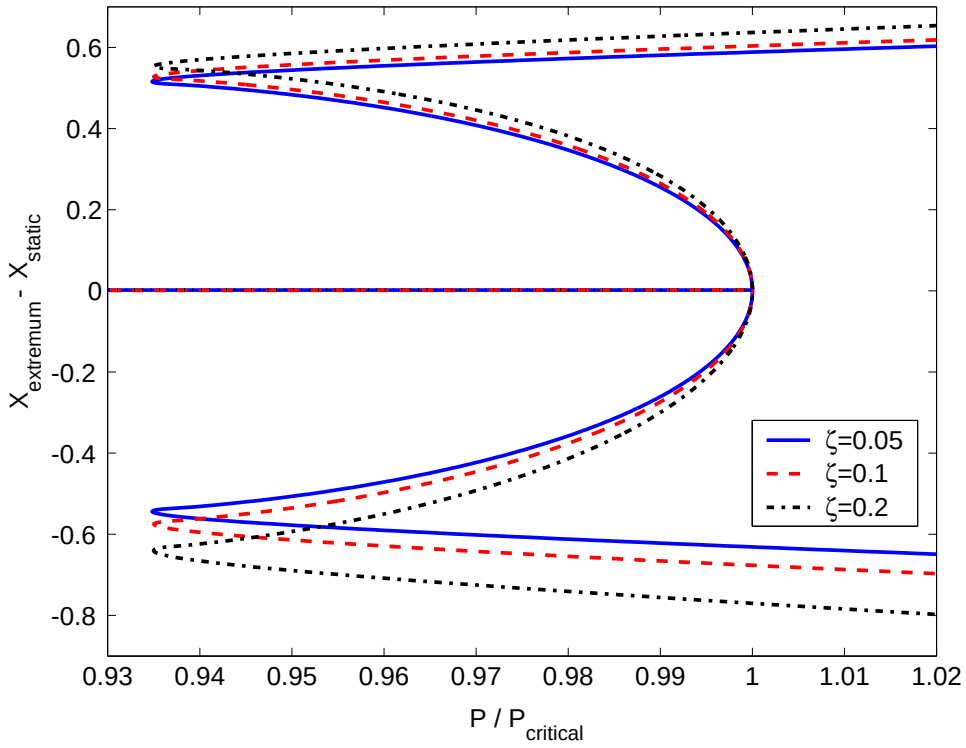

Figure 7.8: Bifurcation diagram for different values of ζ, viz., $\zeta = 0.05$, $\zeta = 0.1$ and $\zeta = 0.2$. Other parameters: $\Omega = 2$, $v = 1/\pi$, $N = 25$.

In addition, we assume that $\omega = \omega_{critical}$, i.e., the time-period of the periodic solutions on the unstable branch do not change much (the time periods obtained from the continuation scheme with $N = 25$ for $\Omega = 2$ and $\zeta = 0.1$ changes from 4.9816 at the stability boundary to 4.9798 at the turning point). Now, the condition for loss of contact can be written as

$$A\cos(\omega_{critical}t - \omega_{critical}\tau) - A\cos(\omega_{critical}t) = C_0\,.$$

We replace $\omega_{critical}t$ by a yet to be determined phase θ, since the tool does not necessarily leave the workpiece at its maximum displacement. This gives us

$$-2A\sin\left(\frac{2\,\theta - \omega_{critical}\tau}{2}\right)\sin\left(\frac{\omega_{critical}\tau}{2}\right) = C_0. \tag{7.21}$$

In addition, for *impending* loss of contact, we must have

$$\max_{\theta}\left\{-2A\sin\left(\frac{2\,\theta - \omega_{critical}\tau}{2}\right)\sin\left(\frac{\omega_{critical}\tau}{2}\right)\right\} = C_0,$$

which occurs when

$$\sin\left(\frac{2\,\theta - \omega_{critical}\tau}{2}\right) = -1$$

or

$$\theta = \frac{3\pi}{2} + \frac{\omega_{critical}\tau}{2}\,.$$

The amplitude for which the tool leaves the workpiece is then given by

$$A = \frac{C_0}{2\,\sin\left(\frac{\omega_{critical}\tau}{2}\right)}\,. \tag{7.22}$$

In the limiting case of zero damping, i.e., $\zeta = 0$, the analysis of chapter 6 shows that $\omega_{critical}\tau = (2M+1)\pi$, for some integer M. Then Eq. (7.22) gives

$$A = \frac{C_0}{2}\,,$$

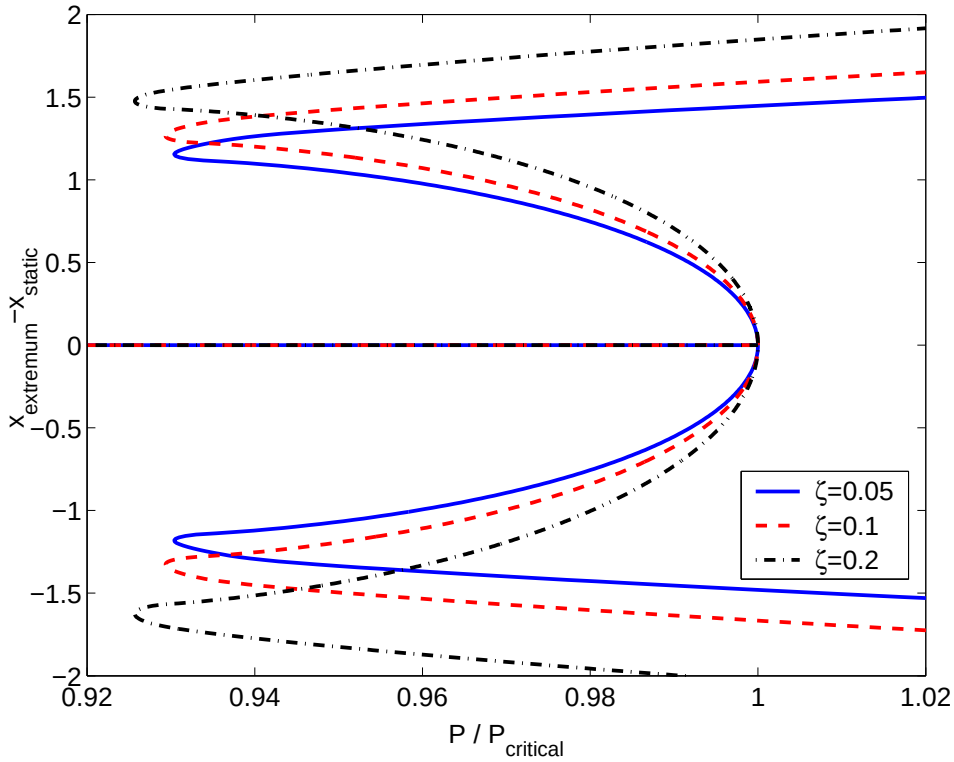

Figure 7.9: Bifurcation diagram for different values of ζ, viz., $\zeta = 0.05$, $\zeta = 0.1$ and $\zeta = 0.2$. Other parameters: $\Omega = 1.2$, $v = 1.2/2\pi$, $N = 25$.

the value observed in Fig. 7.8. Another bifurcation diagram for $\zeta = 0$ and $\Omega = 2.5$, in Fig. 7.10, shows that the tool displacement at the turning point is again about 0.5.

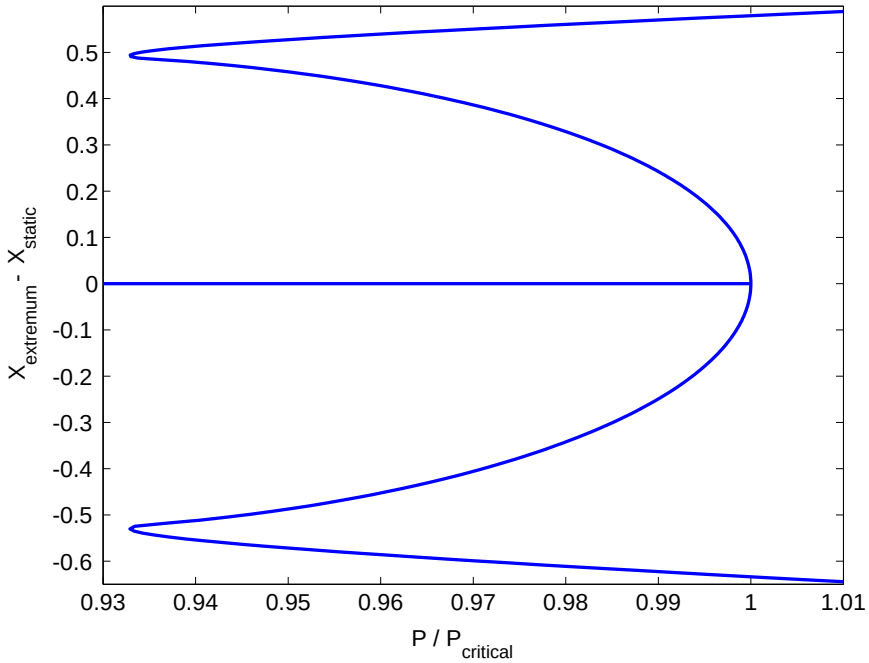

Figure 7.10: Bifurcation diagram for $\zeta = 0$, $\Omega = 2.5$, $v = 2.5/2\pi$ and $N = 25$.

We point out that stable periodic solutions in the case of zero damping, i.e., $\zeta = 0$, are probably strongly influenced by multiple regenerative effects. The system may well be stable for a delay of 2τ or 3τ, although it is unstable for a delay of τ. An investigation of this possibility is left for future work.

However, we note from Fig. 7.9 that the maximal tool displacements at the turning points are quite different from 0.5 and they seem to be converging to a value closer to 1 instead. To better understand this observation, we reexamine the stability analysis of the linearized DDE model presented in section 6.3.

7.4.3 Linear stability reexamined

Figure 6.1 is reproduced below in Fig. 7.11. Note from section 6.2 that P and p are related by $P = \frac{4\,C_0^{1/4} p}{3}$; the vertical axis now shows P for $C_0 = 1$. In Fig. 7.11, we have additionally marked lines corresponding to the values of Ω used in this section. Each lobe of the stability boundary for $\zeta = 0$ consists of three parts: a curved

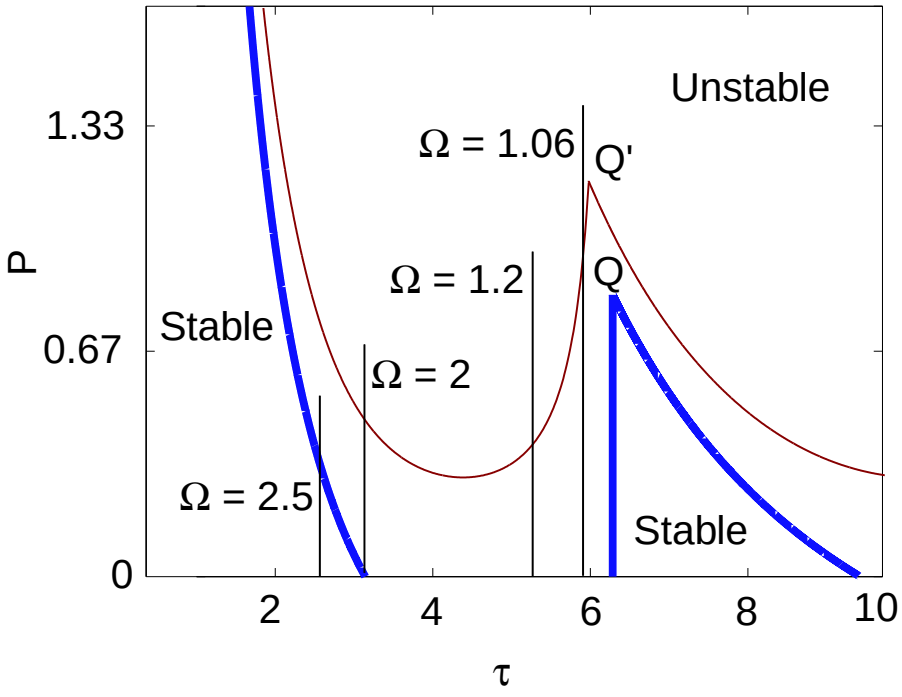

Figure 7.11: Stability boundary from chapter 6. Thick line: $\zeta = 0$ and thin line: $\zeta = 0.1$.

part corresponding to $\omega_{critical}\tau = (2M+1)\pi$, a horizontal part corresponding to $P = 0$ (with $\omega_{critical} = 1$ and a vertical part corresponding to $\omega_{critical}\tau = 2M\pi$. For $\zeta > 0$, the stability lobe is a continuous curve which approaches the $\zeta = 0$ curves as $\zeta \to 0$. Accordingly, for small ζ, and for the first stability lobe we have

$$\sin\left(\frac{\omega_{critical}\tau}{2}\right) \approx 1\,, \text{ for } \tau \in (0, \pi)$$

and

$$\sin\left(\frac{\omega_{critical}\tau}{2}\right) \approx \sin\left(\frac{\tau}{2}\right)\,, \text{ for } \tau \in (\pi, 2\pi)\,.$$

A numerically obtained plot of $\sin\left(\frac{\omega_{critical}\tau}{2}\right)$ versus τ (for values corresponding to the first stability lobe of Fig. 7.11) for different nonzero values of ζ is presented in Fig. 7.12. It can be seen that the $\zeta = 0$ approximation is good for light damping. Figure 7.12 shows that $\sin\left(\frac{\omega_{critical}\tau}{2}\right)$ monotonically decreases with increasing $\tau \in (0, 2\pi)$. Equation (7.22) therefore implies that the amplitude of the stable periodic solutions will monotonically increase with increasing τ (or equivalently decreasing Ω) within the stability lobe. It is clear that points sufficiently far to the left have

$$\sin\left(\frac{\omega_{critical}\tau}{2}\right) = 1$$

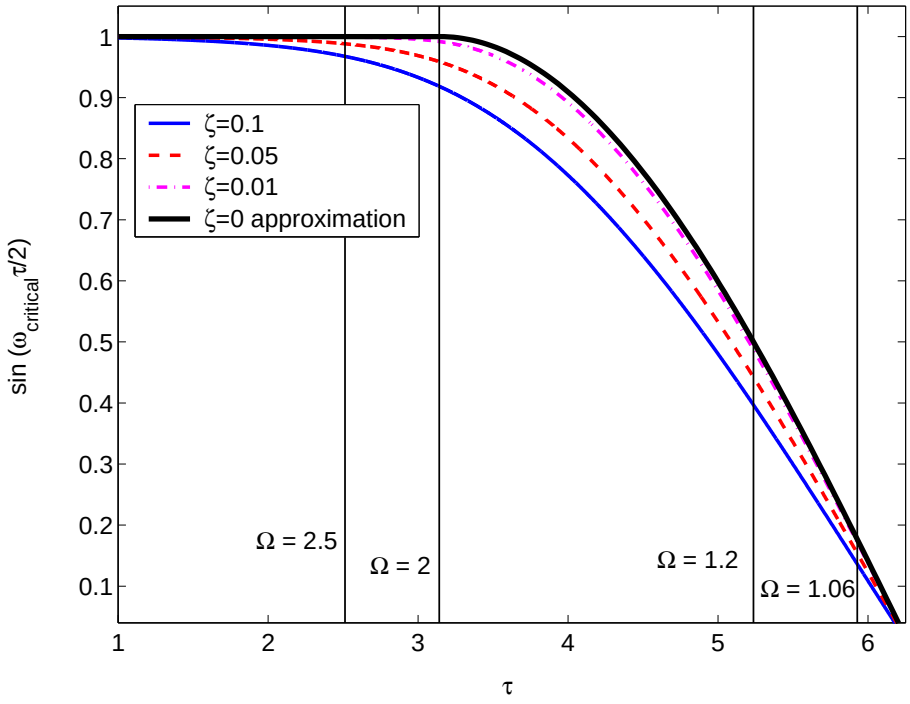

Figure 7.12: $\sin\left(\frac{\omega_{critical}\tau}{2}\right)$ versus τ for the first stability lobe in Fig. 7.11 for different values of ζ.

with corresponding $A = C_0/2$ (Eq. (7.22)), while points sufficiently far to the right of Ω_Z correspond to $\sin\left(\frac{\omega_{critical}\tau}{2}\right)$ taking small values with corresponding A large. In particular, for $\Omega = 1.2$, we find (for small ζ)

$$\sin\left(\frac{\omega_{critical}\tau}{2}\right) \approx 0.5$$

with corresponding $A \approx C_0$, as observed previously in Fig. 7.9.

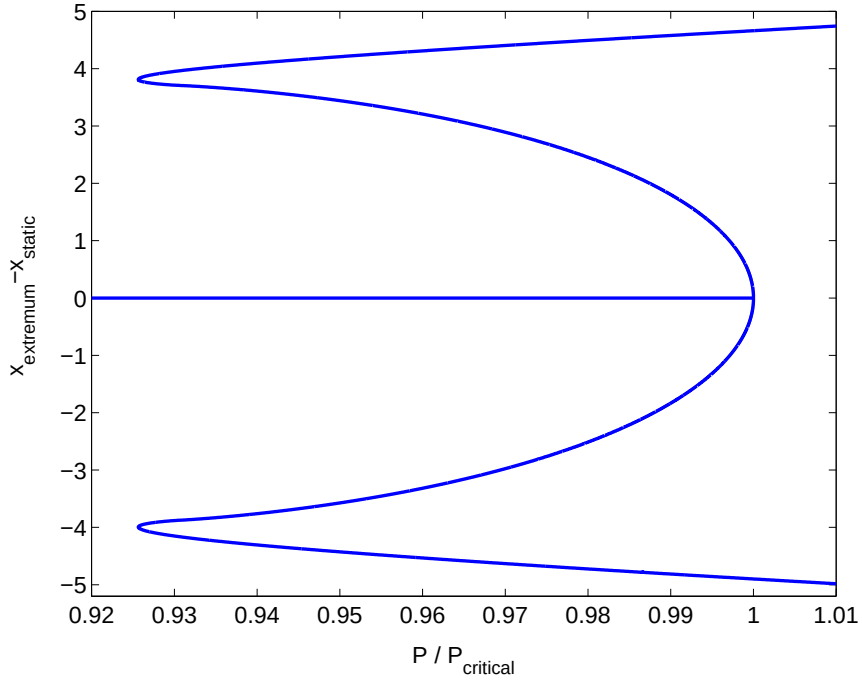

Figure 7.13: Bifurcation diagram for $\zeta = 0.1$, $\Omega = 1.06$, $v = 1.06/2\pi$, and $N = 25$.

The above discussion suggest possibly important practical conclusion. If the stability boundary corresponding to any stability lobe is crossed, in general a subcritical bifurcation will occur and there will immediately arise finite (nonzero) amplitude stable periodic self-interrupted solutions. However, restricting attention to stability loss through the boundary of that same lobe, cutting at higher (conversely, lower) speeds will lower (raise) the amplitude of the ensuing self-interrupted solutions. In the example studied here, and for the first lobe, the variation in amplitude at the turning point can be by as much as a factor of 8 as can be seen in Fig. 7.13. In this figure, the maximal tool displacement at the turning point is approximately 4, 8 times the maximal tool displacement of approximately 0.5 for $\zeta = 0.1$ observed in Fig. 7.8. Note that the relative variation in amplitude in the stable self-interrupted branch between the turning point and the Hopf point is not much (may be 20-30%), in all cases studied so far. In contrast, we have seen that the turning point amplitude can vary by an order of magnitude as Ω is changed. Thus, the position within a given stability lobe range can have an important effect, should stability be lost. In other words, instability under some identifiable cutting conditions can be much worse than under other cutting conditions.

7.5 Other solutions

For $\zeta = 0.1$, the codimension 2 Hopf point occurs at $\Omega = 1.0507$ and $P = 1.1692$. The set of possible solutions near this point depends on how the parameters Ω and P are varied (see, for example, Fig. 6.2). There might be multiple periodic solutions (as shown below) as well as quasiperiodic solutions as discussed in [8, 14, 16]. The quasiperiodic solutions can not be obtained by the numerical procedure described in appendix F. For demonstration of some of the possibilities in quasiperiodic solutions, results of some direct numerical simulations are presented below.

We first consider the bifurcation diagram for $\zeta = 0.1$, $\Omega = 1.05$ (a value close to the codimension 2 Hopf point) and $v = 1.05/2\pi$ in Fig. 7.14. It can be seen from the figure that there are two different branches of

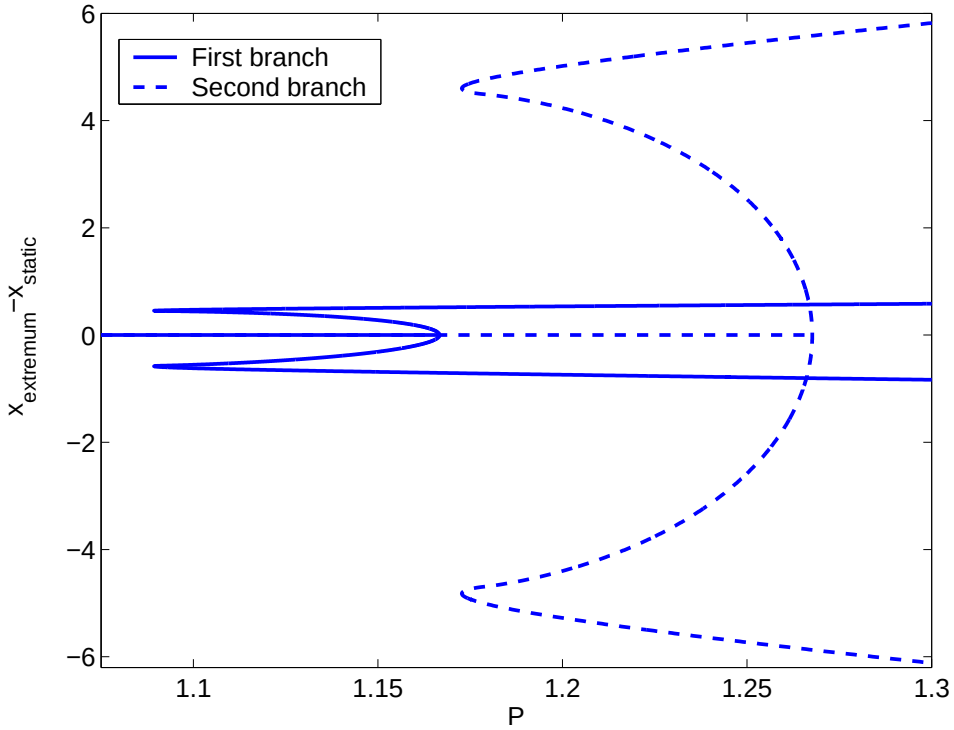

Figure 7.14: Bifurcation diagram for $\zeta = 0.1$, $\Omega = 1.05$, $v = 1.05/2\pi$ and $N = 25$.

periodic solutions. Above $P \approx 1.17$, there are two distinct stable periodic solutions. Numerical simulation results for $\zeta = 0.1$, $\Omega = 1.05$, $v = 1.05/2\pi$, $P = 1.3$, and two different initial conditions quite close to each other are presented in Fig. 7.15.

From Fig. 7.15, we note that slightly different initial conditions lead to two different stable periodic solutions. These stable periodic solutions seem to be separated by an unstable quasiperiodic solution, indicated by quasiperiodic transients in Fig. 7.15 (see Fig. 7.16 as well).

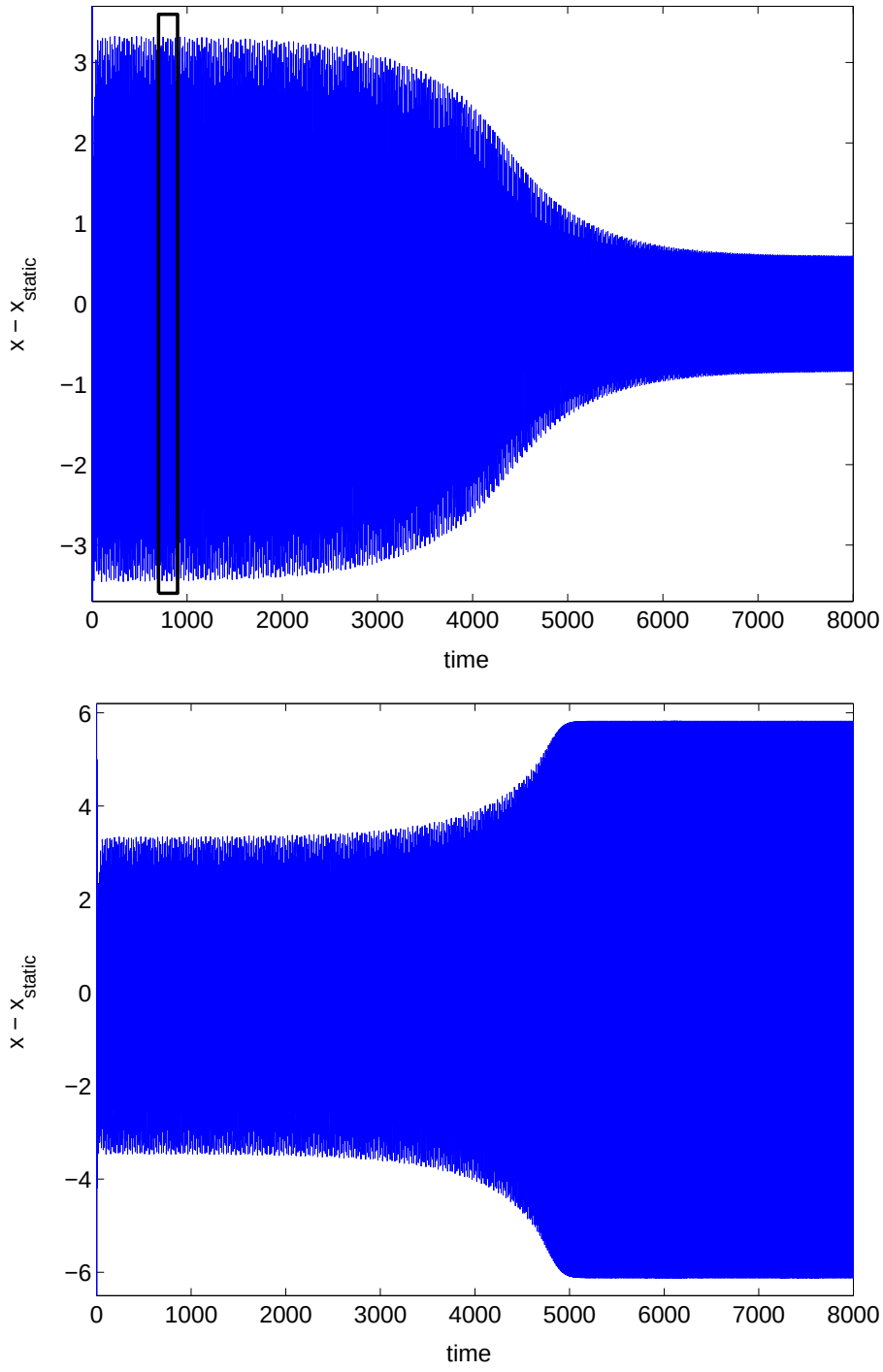

Figure 7.15: Numerical solution of Eqs. (7.16), (7.19), (7.20) and (7.1) for $\zeta = 0.1$, $\Omega = 1.05$, $v = 1.05/2\pi$, $P = 1.3$, and $N = 25$. Top figure initial conditions: $a_i(0) = 0$ for $i = 1, 2, \cdots, 25$; $x(0) = 10.4$ and $\dot{x}(0) = 0$. Bottom figure initial conditions: $a_i(0) = 0$ for $i = 1, 2, \cdots, 25$; $x(0) = 10.43$ and $\dot{x}(0) = 0$

As P is increased further, the periodic solutions eventually lose stability and a quasiperiodic solution can become stable. Numerical simulations for $\zeta = 0.1$, $\Omega = 1.1$, $v = 1.1/2\pi$ and $P = 2.4$, with zero initial conditions, give a stable quasiperiodic solution shown in Fig. 7.17.

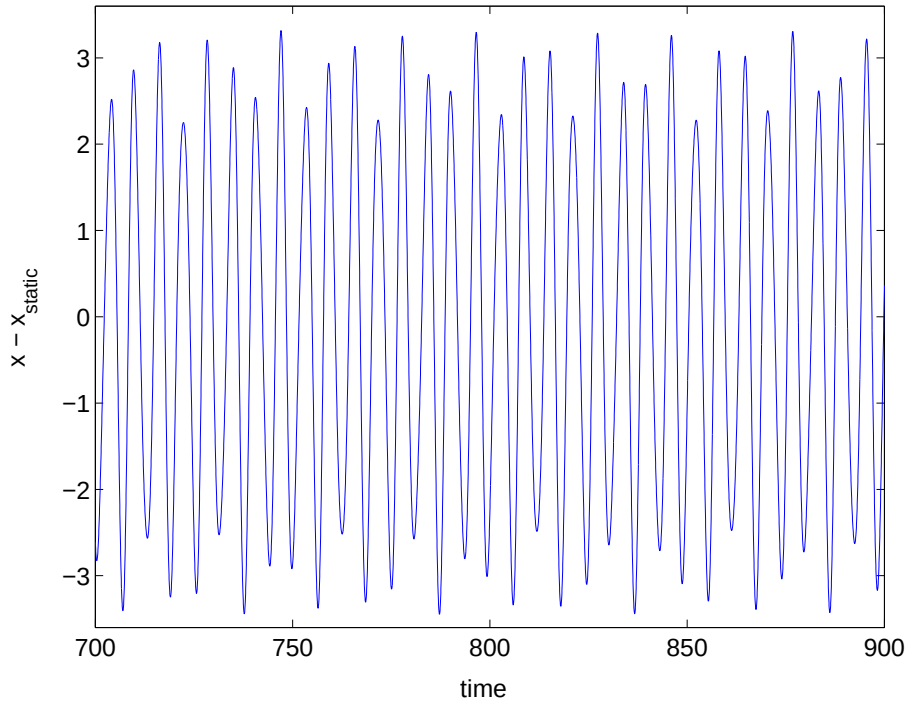

Figure 7.16: A zoomed view of the boxed portion in Fig. 7.15(top).

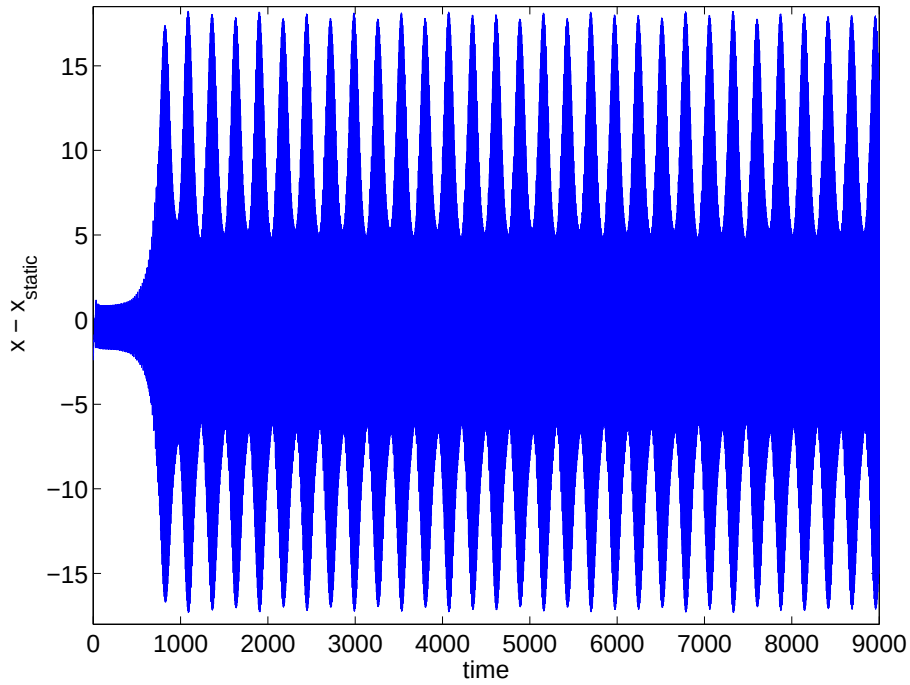

Figure 7.17: Numerical solution of Eqs. (7.16), (7.19), (7.20) and (7.1) for $\zeta = 0.1$, $\Omega = 1.1$, $v = 1.1/2\pi$, $P = 2.4$, and $N = 25$. Initial conditions: $a_i(0) = 0$ for $i = 1, 2, \cdots, 25$; $x(0) = 0$ and $\dot{x}(0) = 0$.

The actual amplitudes obtained here are quite large and may not be of practical interest; also, the P value here is far above the critical value. Nevertheless, from a dynamical systems point of view, these results are interesting and point to a rich, unexplored dynamics in simple models of self-interrupted turning. Perhaps some of that dynamics might eventually prove to have practical relevance as well.

7.6 Concluding remarks

A preliminary analysis of the self-interrupted regenerative turning has been presented in this chapter. A new approach to model the regenerative effect in turning operations has been developed. The dynamics of the cutting process has been modeled using a direct approach which leads to a partial differential equation (PDE) along with an ordinary differential equation (ODE). The PDE describes the cut surface while the ODE describes the motions of the cutting tool. This model automatically incorporates self-interruption due to the loss of contact between the tool and the workpiece in the post-instability region and the multiple-regenerative effects accompanying it. Some lower dimensional ODE approximations have also been obtained for the overall dynamics using Galerkin projections. Using these ODE approximations, we have obtained a bifurcation diagram of the regenerative turning process. It has been found that the unstable branch of periodic solutions resulting from the subcritical Hopf bifurcation and the stable periodic branch resulting from the self-interrupted dynamics meet in a turning point bifurcation. A rough analytical estimate of the turning point tool displacement under light damping has also been obtained and verified numerically. This estimate helps to identify regions in the space of cutting parameters where loss of stability leads to much greater amplitude self-interrupted motions than in some other regions. Multiple stable periodic solutions and quasiperiodic solutions have also been observed beyond the point of initial instability.

Chapter 8

Conclusions

We have studied various aspects of Delay Differential Equations (DDEs) and applied the analysis to practical machine tool vibrations problem.

In chapter 2, we have obtained asymptotic approximations for the roots of the characteristic equations of some linear DDEs with constant coefficients. It has been found that the term with the largest delay dominates in the asymptotic expansions for the large roots. However, for coefficients of disparate magnitude, the large root asymptotics may be useful only for extremely large roots and there are not-very-large roots determined by the smaller delayed terms.

In chapter 3, the method of averaging has been applied to study small perturbations in the form of delayed terms and fractional derivative terms to conservative oscillators which may be strongly nonlinear. Interesting dynamics is uncovered in the strongly nonlinear case with small delayed terms, where arbitrarily many stable and unstable limit cycles can coexist, and infinitely many simultaneous saddle-node bifurcations can occur in the asymptotic limit.

In chapter 4, we have presented a Galerkin projection technique by which finite-dimensional ODE approximations for DDEs can be obtained in a straightforward fashion. The technique requires neither the system to be near a bifurcation point, nor the delayed terms to have any specific restrictive form, nor even the delay, nonlinearities and/or forcing to be small. The accuracy of solutions increases with increasing numbers of shape functions used in the Galerkin projection.

In chapter 5, a numerical convergence study of the Galerkin approximations is presented based on approximation of the first several characteristic roots of some constant coefficient DDEs. A modification and an extension of the Galerkin projection technique to higher order DDEs and system of DDEs is also presented therein. The order of the Galerkin approximations is found to be 2 (i.e., for an $N \times N$ matrix approximation, the error in any root goes to zero like N^{-2}). The modification to the procedure gives us many more usefully accurate roots.

In chapter 6, we have studied the classical single degree of freedom machine tool vibration model, which is a delay differential equation (DDE), near a double Hopf point. By treating the damping in the system as a small perturbation, new analytical expressions have been obtained for all the double Hopf points in the DDE. Both sub- and supercritical Hopf bifurcations are observed depending on how two key parameters are varied near the double Hopf point. However, the region of supercritical bifurcation is limited and globally stable solutions can largely be obtained only by considering loss of contact between the tool and the workpiece. An attempt to incorporate loss of contact is made in the last part of this thesis where we have studied *self-interrupted* turning.

In chapter 7, a preliminary analysis of the self-interrupted regenerative turning has been presented. To facilitate the analysis, a new approach to model the regenerative effect in metal cutting has been proposed. This model has been designed to incorporate self-interruption and multiple-regenerative effects accompanying it. Some lower dimensional ODE approximations have been obtained for the overall dynamics using Galerkin projections. Using these ODE approximations, we have obtained a bifurcation diagram of the regenerative turning process. It has been found that the unstable branch of periodic solutions resulting from the subcritical Hopf bifurcation and the stable periodic branch resulting from the self-interrupted dynamics meet in a turning point bifurcation. A rough analytical estimate of the turning point tool displacement under a light damping assumption has also been obtained. This estimate helps to identify regions in the space of cutting parameters where loss of stability leads to much greater amplitude self-interrupted motions than in some other regions. Multiple stable periodic solutions and quasiperiodic solutions have been observed as well.

The contributions made in this thesis may be viewed, in terms of future work, as follows. The study of characteristic roots of DDEs in chapter 2 sheds light on the locations of roots in the complex plane, possibly useful for future theorems or approximations. Averaging for conservative oscillators (chapter 3) perturbed by small terms involving delays and fractional derivatives is a straightforward addition to the set of nonlinear oscillators amenable to perturbation methods. The Galerkin projection technique presented in chapters 4 and 5 is

a promising technique, potentially useful in detailed numerical studies of delayed systems in different fields. The multiple scales analysis near a codimension 2 Hopf point in chapter 6 may help understand possible complexities in the dynamics of other, similar, systems which are not as easily tractable. The analysis of self-interrupted turning in chapter 7 leads to practical predictions which may be experimentally verified in future work. The new approach therein, to model the regenerative effect along with its lower dimensional ODE approximations, may prove useful in studying the rich dynamics of self-interrupted cutting, which has been only partially uncovered in this thesis.

Appendix A

Smaller Roots of DDEs using Padé approximants

We use MAPLE, to find Padé approximants (as in [89] and [90]) to obtain the smaller roots of the characteristic equations of the DDEs. MAPLE does both symbolic algebra and arbitrary-precision floating point arithmetic. To see the issues involved, consider

$$p - \sqrt{2}e^{-p} - e^{-p/\sqrt{3}} = 0\,. \tag{A.1}$$

Expanding in a Taylor series, we obtain

$$-1 - \sqrt{2} + \left(\sqrt{2} + 1 + \frac{1}{\sqrt{3}}\right) p - \left(\frac{1}{\sqrt{2}} + \frac{1}{6}\right) p^2 + \cdots$$

Retaining terms up to p^{10}, we obtain the Padé approximant of order (5,5). We seek the zeroes of this approximant. The numerator is of the form $\sum_{k=0}^{5} c_k p^k$, where c_0 is

$$6688184704014240 - 1634855556025440\sqrt{6} + 2840749923049920\sqrt{2} - 3855543089257440\sqrt{3}, \tag{A.2}$$

and the other coefficients are comparably lengthy. The first few roots of the numerator polynomial give good approximations to the first few roots of Eq. (A.1). However, the accuracy of the Padé roots increase with the digits of precision used in the floating point arithmetic. Results for the smallest root of Eq. (A.1), which is 1.04464369, are given in Table A.1.

Table A.1: Root improves with precision of arithmetic.

Digits used	6	8	10
First root	1.0452	1.0446398	1.04464353

In practice, to find several roots of a DDE, high order Padé approximants need to be used. The numerator polynomial then involves long/large coefficients. We therefore numerically evaluate the coefficients of the Taylor series at the start, before Padé approximants are calculated. Moreover, many floating point digits are needed for accurate results.

For the three examples studied in chapter 2, we used 650 digits of precision (numerical inaccuracies were observed with our previous choice of 540 digits; no optimization was done on number of digits) and took a Padé approximant of order either $(21, 21)$ or $(22, 22)$ depending on the number of real roots obtained. Results, in Tables A.2 through A.4, show good agreement.

Table A.2: First 6 roots of Eq. (2.2) for $a = 1$.

No.	Padé approximant	Newton-Raphson
1	$-0.3181 + 1.3372\mathrm{i}$	$-0.3181 + 1.3372\mathrm{i}$
2	$-2.0623 + 7.5886\mathrm{i}$	$-2.0623 + 7.5886\mathrm{i}$
3	$-2.6532 + 13.9492\mathrm{i}$	$-2.6532 + 13.9492\mathrm{i}$
4	$-3.0202 + 20.2465\mathrm{i}$	$-3.0202 + 20.2725\mathrm{i}$
5	$-3.2878 + 26.5805\mathrm{i}$	$-3.2878 + 26.5805\mathrm{i}$
6	$-3.4997 + 32.8805\mathrm{i}$	$-3.4985 + 32.8807\mathrm{i}$

Table A.3: First 6 roots of Eq. (2.6) for $p = 2, \psi = 0.1$.

No.	Padé approximant	Newton-Raphson
1	-0.44008	-0.44008
2	$-0.5762 + 2.4326\mathrm{i}$	$-0.5762 + 2.4326\mathrm{i}$
3	$-3.7516 + 8.5961\mathrm{i}$	$-3.7516 + 8.5961\mathrm{i}$
4	$-4.8189 + 15.095\mathrm{i}$	$-4.8190 + 15.095\mathrm{i}$
5	$-5.4984 + 21.4961\mathrm{i}$	$-5.4984 + 21.4962\mathrm{i}$
6	$-6.0014 + 27.8552\mathrm{i}$	$-6.0014 + 27.8553\mathrm{i}$

Table A.4: First 6 roots of Eq. (2.16) for $a_1 = a_2 = a_3 = a_4 = 1$.

No.	Padé approximant	Newton-Raphson
1	$-0.1639 + 2.4749\mathrm{i}$	$-0.1639 + 2.4749\mathrm{i}$
2	$-2.3946 + 8.2369\mathrm{i}$	$-2.3946 + 8.2369\mathrm{i}$
3	$-2.8736 + 13.6232\mathrm{i}$	$-2.8736 + 13.6232\mathrm{i}$
4	$-2.6442 + 20.2466\mathrm{i}$	$-2.6442 + 20.2466\mathrm{i}$
5	$-3.2404 + 27.0141\mathrm{i}$	$-3.2404 + 27.0141\mathrm{i}$
6	$-3.8715 + 32.8327\mathrm{i}$	$-3.8703 + 32.8338\mathrm{i}$

Appendix B

Initial conditions in the presence of delayed terms

In applying averaging to conservative oscillators perturbed by terms with delays, we note that they are infinite dimensional for any nonzero ϵ. The solutions have infinitely many fast decaying components which rapidly converge to a slow invariant manifold, as shown schematically in Figure B.1. The slow flow equations for amplitude and phase obtained in chapter 3 capture only the dynamics on the slow manifold. Hence, for purposes of numerical comparison with the "full" solutions, the choice of the initial function for the DDEs requires attention.

The full-solution should not, as an extreme example, approach the slow manifold at the origin: in such cases there will be no slow dynamics observed at all. Moreover, initial conditions for the averaged equations should correspond to that trajectory on the slow manifold to which the full solution converges (adjustments in initial conditions may be required to achieve this). The idea is shown schematically in Figure B.1.

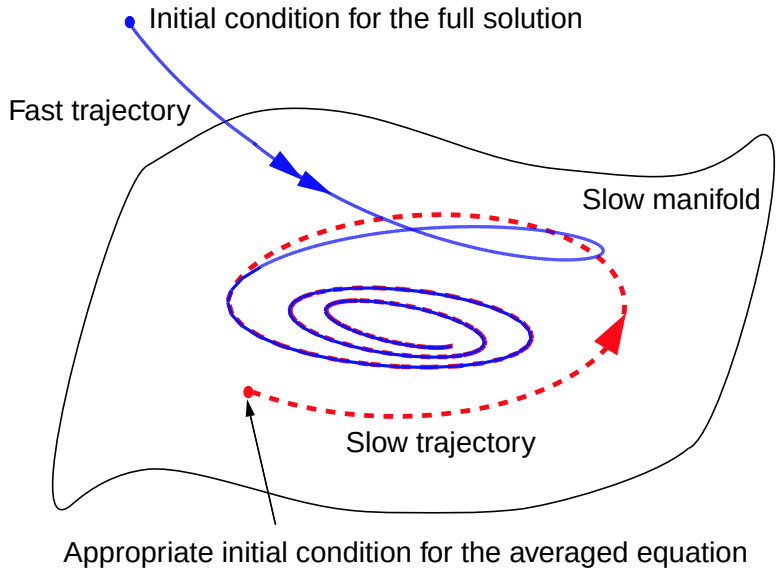

Figure B.1: Solution trajectories for a DDE. Double arrows represent the fast portion of the full-solution trajectory, which eventually converges to a slow manifold where it coincides with a slow trajectory (single arrow).

For example, consider a simple second order linear DDE,

$$\ddot{x}(t) + x(t) + \epsilon \dot{x}(t-1) = 0\,. \tag{B.1}$$

The corresponding averaged equations are

$$\dot{R} = -0.27015\, R\, \epsilon\,,$$

$$\dot{\phi} = 0.42074\,\epsilon\,.$$

The first three characteristic roots of this equation for $\epsilon = 0.05$ are $-0.01351 \pm i\,1.02176$, -4.56003 and $-5.17593 \pm i\,7.21996$. The slow manifold in this linear case is simply the subspace spanned by $e^{(-0.01351 \pm i\,1.02176)t}$. The behavior of any initial function which has no significant components along $e^{-4.56003t}$ or $e^{(-5.17593 \pm i\,7.21996)t}$ (neglecting the infinitely many roots which decay even faster) will be captured well by the averaged equations (see Figure B.2 (a)). However, for the initial function $e^{-4.56003t}$, the solution trajectory has no portion lying on the slow manifold, has little in common with the averaged solution (see Figure B.2 (b)).

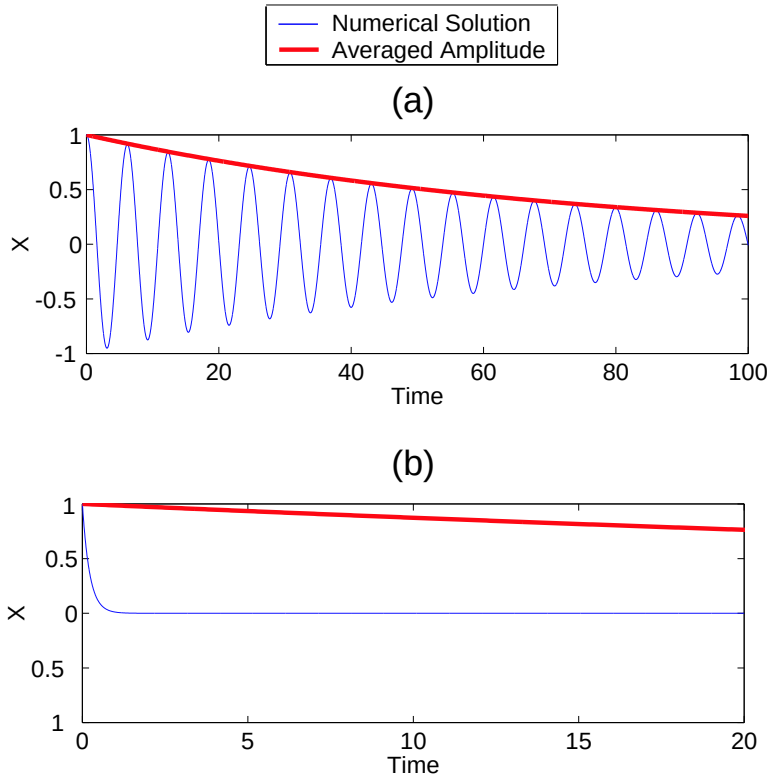

Figure B.2: Solution of Equation (B.1) and the corresponding averaged slow flow equations for $\epsilon = 0.05$. Initial conditions: (a) $x(\eta) = 1$, $\dot{x}(\eta) = 0$, for $\eta \in [-1, 0]$, $R(0) = 1$, (b) $x(\eta) = e^{-4.56003\eta}$, $\dot{x}(\eta) = -4.56003\,e^{-4.56003\eta}$, for $\eta \in [-1, 0]$, $R(0) = 1$.

Appendix C

Averaging with fractional order derivatives for general q

In chapter 3, we have used $q = 1/2$ in our fractional derivative terms, which is the value most encountered in structural dynamics. However, the procedure is applicable for $q \neq 1/2$. A procedural detail is that we will be required to evaluate

$$\int_0^t \frac{\sin\tau}{\tau^q} d\tau \quad \text{and} \quad \int_0^t \frac{\cos\tau}{\tau^q} d\tau$$

or equivalently,

$$\int_0^{t^{(1-q)}} \sin s^{1/(1-q)} ds \quad \text{and} \quad \int_0^{t^{(1-q)}} \cos s^{1/(1-q)} ds\,.$$

As before, only the behavior of the above as $t \to \infty$ is of interest to us. Using contour integration, it can be shown that

$$\int_0^{\infty} \sin s^{1/(1-q)} ds \; = \Gamma(1-q)\sin(q\pi/2)$$

and

$$\int_0^{\infty} \cos s^{1/(1-q)} ds \; = \Gamma(1-q)\cos(q\pi/2)\,.$$

The above integrals are also derivable from related results on page 110 of [104].

Appendix D

Invertibility of matrices A and $\mathbf{A_m}$ obtained in chapter 5

D.1 Invertibility of matrix A

In section 5.2 it is mentioned that $\mathbf{A\dot{a} + Ba} = 0$ is represented in the form $\mathbf{\dot{a} = Ca}$. Here it is assumed that $\mathbf{A}$ is invertible. Consider an M^{th} order DDE. It can be written as M first order equations, $M-1$ of which are of the form $x_{n+1} = \dot{x}_n$. It can be shown that the determinant of the matrix $\mathbf{A}$ constructed for this equation is given by $\frac{C_o}{2^{N-2}}\left(\frac{1}{3} - \frac{2}{\pi^2}\sum_{m=1}^{N-2}\frac{1}{m^2}\right)$ where C_o is the coefficient of the highest derivative in the equation (in all our examples, $C_o = 1$). Since all the terms in the sum are positive and $\frac{2}{\pi^2}\sum_{m=1}^{\infty}\frac{1}{m^2} = \frac{1}{3}$, the determinant of $\mathbf{A}$ is strictly positive for finite N, and hence $\mathbf{A}$ is invertible.

D.2 Invertibility of matrix $\mathbf{A_m}$

In section 5.4 we presumed that $\mathbf{A_m}$ is invertible and hence defined $\mathbf{C_m} = -\mathbf{A_m}^{-1}\mathbf{B_m}$. Like in section D.1 the determinant of $\mathbf{A_m}$ is $C_o \times \det(\hat{\mathbf{A}}_\mathbf{m})$, where $\hat{\mathbf{A}}_\mathbf{m}$ is the $N-1 \times N-1$ matrix which is the right bottom block of matrix $\mathbf{A_m}$. Finding an analytical expression for the determinant of the matrix $\hat{\mathbf{A}}_\mathbf{m}$ is difficult. But we can get some idea about the invertibility of $\mathbf{A_m}$ by looking at the condition number of $\hat{\mathbf{A}}_\mathbf{m}$. Figure D.1 shows the plot between the condition number and N on a log-log scale. It is seen that the condition number is proportional to N^2. Thus $\mathbf{A_m}$ is invertible for finite N.

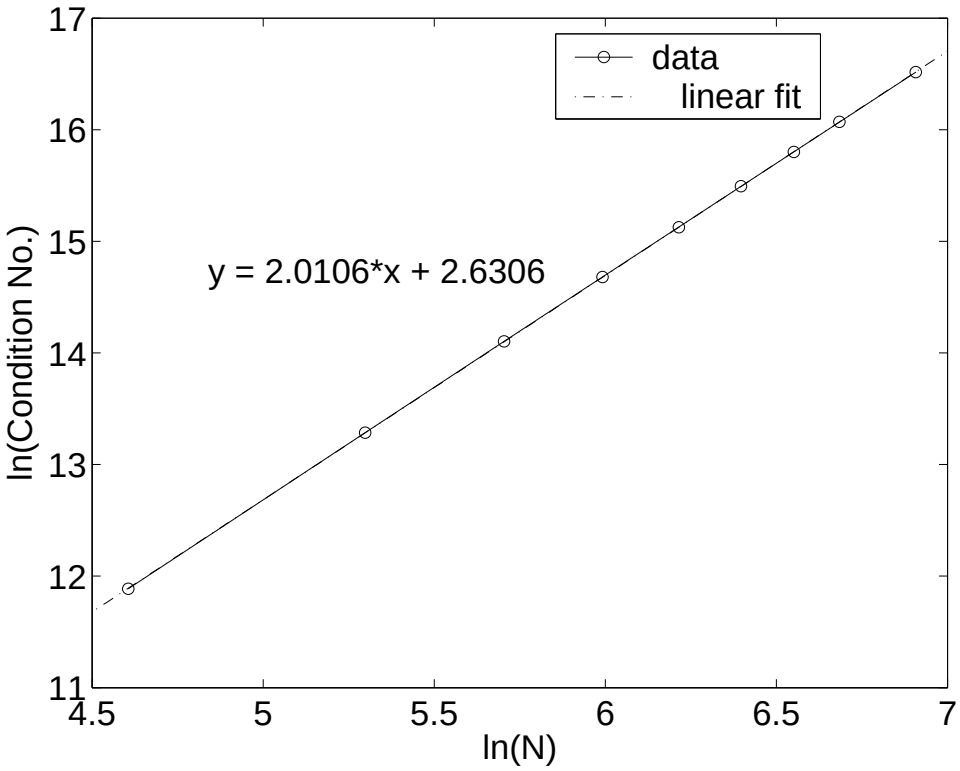

Figure D.1: Invertibility of $\hat{\mathbf{A}}_{\mathbf{m}}$.

Appendix E

What is ϵ?

Textbooks on perturbation methods discuss problems where the small term is already labeled (usually by the symbol ϵ). In practical applications of perturbation methods, however, we have problems with finite and nonzero parameter values; and which of these may be treated as small, and how small, is in some sense a modeling decision. In chapter 6 we have studied a problem where we arbitrarily chose a parameter of value 3/16 to be ϵ. There is no theoretical justification for this. The subsequent analysis made qualitative and quantitative predictions, and the final test of suitability for the choice of ϵ lay in comparison with numerical solutions.

To further clarify this issue, we present here a simple equation which we can solve using two different schemes for choosing ϵ. Consider

$$x^{1+a} = 1 + b,$$

where a and b are positive valued parameters. Let us consider the case $a = 1$ and $b = 1/2$, for which we have

$$x^2 = \frac{3}{2}, \tag{E.1}$$

with a positive root at $x = 1.2247$.

Let us now consider the equation

$$x^{1+\epsilon} = 1 + \frac{\epsilon}{2}, \tag{E.2}$$

which reduces to Equation (E.1) when $\epsilon = 1$. Note that we are here interested only in the strictly nonzero value of $\epsilon = 1$; any perturbation scheme for solving Equation (E.2) using a small-ϵ expansion will stand or fall based on its performance for $\epsilon = 1$.

Posing a solution for Equation (E.2) in the form

$$x = x_0 + \epsilon\, x_1 + \epsilon^2\, x_2 + \cdots,$$

we find using routine methods that

$$x = 1 + \frac{1}{2}\,\epsilon - \frac{1}{2}\,\epsilon^2 + \frac{3}{8}\,\epsilon^3 - \frac{11}{48}\,\epsilon^4 + \frac{19}{192}\,\epsilon^5 + \mathcal{O}(\epsilon^6),$$

which upon truncation and for $\epsilon = 1$ gives

$$x = 1.2448,$$

a reasonable approximation.

But the choice of what ϵ should be is in our hands. We could also consider, for example, the equation

$$x^{1 + \frac{\epsilon}{1-\epsilon}} = 1 + \epsilon, \tag{E.3}$$

which reduces to the desired Equation (E.1) for $\epsilon = 1/2$. A similar expansion for the solution now gives

$$x = 1 + \epsilon - \epsilon^2 - \frac{1}{2}\,\epsilon^3 + \frac{2}{3}\,\epsilon^4 - \frac{1}{12}\,\epsilon^5 + \mathcal{O}(\epsilon^6),$$

which upon truncation and for $\epsilon = 1/2$ gives

$$x = 1.2266,$$

a ten times better approximation.

Both solutions above, using Equations (E.2) and (E.3) respectively, are equally correct in that they are formally identical. The scaling used in the latter case appears to be better for the problem at hand for the specific, finite and nonzero values of a and b that are of interest. As far as we know there is no rigorous method of predicting, in advance, which of these is better.

In this sense, choice of ϵ in practical problems often involves a nonrigorous modeling decision that precedes the formal (or rigorous) part of the analysis.

Appendix F

A numerical scheme to obtain branches of periodic solutions of ODEs

F.1 Numerical search for periodic solutions of unknown period

Here, we explain the numerical procedure for a second order ODE only. The extension of the method to higher order ODEs and systems of ODEs is straightforward.

Consider the system to be

$$\ddot{x} + f(\alpha, x, \dot{x}) = 0\,, \tag{F.1}$$

where α is a parameter and $f(\alpha, x, \dot{x})$ is known and is such that Eq. (F.1) has a periodic solution. For each value of the parameter α, we seek the amplitude A and the time period T of the periodic solution. Hence, if we use $x(0) = A$ and $\dot{x}(0) = 0$ as initial conditions and numerically integrate the above equation for a time interval T, then $x(T)$ and $\dot{x}(T)$ should be equal to $x(0) = A$ and 0, respectively. Thus the desired amplitude A and time period T are required to satisfy the following equations:

$$x(T) - A \;=\; 0\,, \tag{F.2}$$

$$\dot{x}(T) \;=\; 0\,. \tag{F.3}$$

It is emphasized that $x(T)$ and $\dot{x}(T)$ are each actually functions of both A and T. Denoting

$$y = \begin{pmatrix} A \\ T \end{pmatrix},$$

we can write Eqs. (F.2) and (F.3) as

$$g(y) = 0. \tag{F.4}$$

Equation (F.4) can now be solved numerically using the Newton-Raphson method. Note that evaluation of g in the solution procedure involves background numerical solution of ODEs. If an analytical solution were available for the ODE, then the map g would be known and Runge-Kutta (or other numerical integration) would not be needed. However, the basic principle of obtaining the amplitude and the time-period of the unknown periodic solution of the ODEs remain the same.

For obtaining the amplitudes and time-period corresponding to periodic solutions for a range of values of the parameter α, we can use an arc-length based branch following technique. The method is described next.

F.2 Fixed arc-length based continuation scheme

Initially, we fix the parameter α at some particular value, say α_0, and obtain the corresponding amplitude A_0 and the time-period T_0 as explained above. Then we repeat the same procedure for another α value close to α_0. This new parameter value α and the corresponding new amplitude A and time-period T are required to satisfy both Eq. (F.4) as well as an arc-length constraint given by

$$\sqrt{(A - A_0)^2 + (T - T_0)^2 + (\alpha - \alpha_0)^2} = d, \tag{F.5}$$

where d is a small number that we have chosen. This parameter d represents the length of the arc in the three dimensional (A, T, α) space. The new values of α, A and T are now denoted byα_0, A_0 and T_0, and the process is repeated. This summarizes the fixed arc-length continuation technique.

Bibliography

[1] Tlusty, J., Polacek, A., Danek, C., and Spacek, J., 1962, *Selbsterregte Schwingungen an erkzeugmaschinen*, VEB Verlag Technik, Berlin.

[2] Tobias, S. A., 1965, *Machine-Tool Vibration*, Blackie and Sons Ltd., London.

[3] Kudinov, V. A., 1967, *Dynamics of Tool-Lathe* (in Russian), Mashinostroenie, Moscow.

[4] Hanna, N. H., and Tobias, S.A., 1974, "A theory of nonlinear regenerative chatter", *ASME Journal of Engineering for Industry*, **96**, pp. 247-255.

[5] Tlusty, J., and Ismail, F., 1981, "Basic non-linearity in machining chatter", *Annals of the CIRP*, **30**, pp. 299-304.

[6] kondo, Y., Kawano, O., and Sato, H., 1981, "Behavior of chatter due to multiple regenerative effect", *ASME Journal of Engineering for Industry*, **103**, pp. 324-329.

[7] Shi, M., and Tobias, S. A., 1984, "Theory of finite amplitude machine tool instability", *International Journal of Machine Tool Design and Research*, **24**, pp. 45-69.

[8] Stépán, G., 1997, "Delay differential equation models for machine tool chatter", in *Dynamics and Chaos in Manufacturing Processes*, F. C. Moon (ed.), Wiley, New York, pp. 165-191.

[9] Nayfeh, A. H., Chin, C., and Pratt, J., 1997, "Applications of perturbation methods to tool chatter dynamics", in *Dynamics and Chaos in Manufacturing Processes*, F. C. Moon (ed.), Wiley, New York, pp. 193-213.

[10] Pratt, J. R., and Nayfeh, A. H., 1999, "Design and modelling for chatter control", *Nonlinear Dynamics*, **19**, pp. 49-69.

[11] Pratt, J. R., and Nayfeh, A. H., 2001, "Chatter control and stability analysis of a cantilever boring bar under regenerative cutting conditions", *Proceedings of the Royal Society of London A*, **359**, pp. 759-792.

[12] Kalmár-Nagy, T., Stépán, G., and Moon, F. C., 2001, "Subcritical Hopf bifurcation in the delay equation model for machine tool vibrations", *Nonlinear Dynamics*, **26**, pp. 121-142.

[13] Fofana, M. S., 2003, "Delay dynamical systems and applications to nonlinear machine-tool chatter", *Chaos, Solitons and Fractals*, **17**, pp. 731–747.

[14] Stépán, G., 2001, "Modelling nonlinear regenerative effects in metal cutting", *Proceedings of the Royal Society of London A*, **359**, pp. 739-757.

[15] Moon, F. C., and Kalmár-Nagy, T., 2001, "Nonlinear models for complex dynamics in cutting materials", *Proceedings of the Royal Society of London A*, **359**, pp. 695-711.

[16] Steṕań, G., Szalai, R., and Insperger, T., 2004, "Nonlinear dynamics of high-speed milling subjected to regenerative effect", in *Nonlinear Dynamics of Production Systems*, G. Radons and R. Neugebauer (eds.), Wiley-VCH, Berlin, pp. 111-128.

[17] Balachandran, B., 2001, "Nonlinear dynamics of milling process", *Proceedings of the Royal Society of London A*, **359**, pp. 793-819.

[18] Jayaram, S., Kapoor, S. G., and DeVor, R. E., 2000, "Analytical stability analysis of variable spindle speed machining", *ASME Journal of Manufacturing Science and Engineering*, **122**, pp. 391-397.

[19] Zhao, M. X., and Balachandran, B., 2001, "Dynamics and stability of milling process", *International Journal of Solids and Structures*, **38**, pp. 2233-2248.

[20] Kalmár-Nagy, T., Pratt, J. R., Davies, M. A., and Kennedy, M. D., 1999, "Experimental and analytical investigation of the subcritical instability in metal cutting", *Proceedings of the DETC'99, 17th ASME Biennial Conference on Mechanical Vibration and Noise,* Las Vegas, Nevada, USA.

[21] Johnson, M. A., and Moon, F. C., 2001, "Nonlinear techniques to characterize prechatter and chatter vibrations in the machining of metals", *International Journal of Bifurcation and Chaos*, **11**(2), pp. 449-467.

[22] Insperger, T., Stépán, G., Bayly, P. V., and Mann, B. P., 2003a, "Multiple chatter frequencies in milling processes", *Journal of Sound and Vibration*, **262**, pp. 333-345.

[23] Insperger, T., Mann, B. P., Stépán, G., and Bayly, P. V., 2003b, "Stability of up-milling and down-milling, part 1: alternative analytical methods", *International Journal of Machine Tools and Manufacture*, **43**, pp. 25-34.

[24] Insperger, T., Mann, B. P., Stépán, G., and Bayly, P. V., 2003c, "Stability of up-milling and down-milling, part 2: experimental verification", *International Journal of Machine Tools and Manufacture*, **43**, pp. 35-40.

[25] Batzer, S. A., Gouskov, A. M., and Voronov, S. A., 2001, "Modelling vibratory drilling dynamics", *ASME Journal of Vibration and Acoustics*, **123**, pp. 435-443.

[26] Stépán, G., and Haller, G., 1995, "Quasiperiodic oscillations in robot dynamics", *Nonlinear Dynamics*, **8**, pp. 513-528.

[27] Insperger, T., and Stépán, G., 2000, "Remote control of periodic robot motion", *Proceedings of the Thirteenth Symposium on Theory and Practice of Robots and Manipulators*, Zakopane, pp. 197-203.

[28] Chaitanya, V. S. K., 2004, "Stability analysis of structurally stable man-machine system involving time delays", *Nonlinear Analysis: Real World Applications*, **6**, pp. 845-857.

[29] Landry, M., Campbell, S. A., Morris, K., and Aguilar, C. O., 2005, "Dynamics of an inverted pendulum with delayed feedback control", *SIAM Journal of Applied Dynamical Systems*, **4**(2), pp. 333-351.

[30] Sheridan, T. B., 1993, "Space Teleoperation through time delay: review and prognosis", *IEEE Transactions on Robotics and Automation*, **9**(5), pp. 592-606.

[31] Olgac, N., Elmali, H., Hosek, M., and Renzulli, M., 1997, "Active vibration control of distributed systems using delayed resonator with acceleration feedback", *ASME Journal of Dynamic Systems, Measurement, and Control*, **119**, pp. 380-389.

[32] Santos, O., and Mondié, S., 2000, "Control laws involving distributed time delays: robustness of implementation", *Proceedings of the American Control Conference*, Chicago, Illinois, pp. 2479-2480.

[33] Pyragas, K., 2002, "Analytical properties and optimization of time-delayed feedback control", *Physical Review E - Statistical Physics, Plasmas, Fluids, and Related Interdisciplinary Topics*, **66**(2), pp. 1-9.

[34] Park, J. H., and Kwon, O. M., 2005, "A novel criterion for delayed feedback control of time-delay chaotic systems", *Chaos, Solitons and Fractals*, **23**(2), pp. 495-501.

[35] Feng, Z. C., and Chicone, C., 2003, "A delay differential equation model for surface acoustic wave sensors", *Sensors and Actuators A*, **104**, pp. 171-178.

[36] Seo., D., Chicone, C., and Feng, Z. C., 2005, "Synchronization problem in delay-line oscillator SAW sensors", *Sensors and Actuators A*, **121**, pp. 44-51.

[37] Rodet, X., 1993, "Models of musical instruments from Chua's circuit with time delay", *IEEE Transactions on Circuits and Systems-II: Analog and Digital Signal Processing*, **40**(10), pp. 696-701.

[38] Barjau, A., Gibiat, V., and Grand, N., 1997, "Study of woodwind-like systems through nonlinear differential equations. Part I simple geometry", *Journal of Acoustical Society of America*, **102**(5), pp. 3023-3031.

[39] Barjau, A., and Gibiat, V., 2003, "Delayed models for simplified musical instruments", *Journal of Acoustical Society of America*, **114**(1), pp. 496-504.

[40] Hu, B., and Eberhard, P., 2004, "Simulation of longitudinal impact waves using time delayed systems", *ASME Journal of Dynamic Systems, Measurement, and Control*, **126**, pp. 644-649.

[41] Nagatani, T., and Nakanishi, K., 1998, "Delay effect on phase transitions in traffic dynamics", *Physical Review E - Statistical Physics, Plasmas, Fluids, and Related Interdisciplinary Topics*, **57**(6), pp. 6415-6421.

[42] Orosz, G., Wilson, R. E., and Krauskopf, B., 2004, "Global bifurcation investigation of an optimal velocity traffic model with driver reaction time", *Physical Review E - Statistical Physics, Plasmas, Fluids, and Related Interdisciplinary Topics*, **70**(2), pp. 026207-1-026207-10.

[43] Epstein, I. R., 1992, "Delay effects and differential delay equations in chemical kinetics", *International Reviews in Physical Chemistry*, **11**(1), pp. 135-160.

[44] Roussel, M. R., 1996, "Use of delay differential equations in chemical kinetics", *Journal of Chemical Physics*, **100**(20), pp. 8323-8330.

[45] Roussel, M. R., 1998, "Approximate state-space manifolds which attract solutions of systems of delay-differential equations", *Journal of Chemical Physics*, **109**(19), pp. 8154-8160.

[46] Balasubramanian, P., Kosuri, M. R., Pushpavanam, S., and Kienle, A., 2003, "Effect of delay on the stability of a coupled reactor-separator system", *Industrial and Engineering Chemistry Research*, **42**(16), pp. 3758-3764.

[47] Pieroux, D., Erneux, T., Gavrielides, A., and Kovanis, V., 2001, "Hopf bifurcation subject to a large delay in a laser system", *SIAM Journal on Applied Mathematics*, **61**(3), pp. 966-982.

[48] Vladimirov, A. G., Turaev, D., and Kozyreff, G., 2004, "Delay differential equations for mode-locked semiconductor lasers", *Optics Letters*, **29**(11), pp. 1221-1223.

[49] Yanchuk, S., 2005 "Properties of stationary states of delay equations with large delay and applications to laser dynamics", *Mathematical Methods in the Applied Sciences*, **28**(3), pp. 363-377.

[50] Giannakopoulos, F., and Zapp, A., 2001 "Bifurcations in a planar system of differential delay equations modeling neural activity", *Physica D: Nonlinear Phenomena*, **159**, (3-4), pp. 215-232.

[51] Shayer, L. P., and Campbell, S. A., 2001, "Stability, bifurcation, and multistability in a system of two coupled neurons with multiple time delays", *SIAM Journal on Applied Mathematics*, **61**(2), pp. 673-700.

[52] Mackey, M., and Glass, L., 1977, "Oscillations and chaos in physiological control systems", *Science*, **197**, pp. 287.

[53] Batzel, J. J., and Tran, H. T., 2000, "Stability of the human respiratory control system I. Analysis of a two-dimensional delay state-space model", *Journal of Mathematical Biology*, **41**, pp. 45-79.

[54] Nelson, P. W., and Perelson, A. S., 2002, "Mathematical analysis of delay differential equation models of HIV-1 infection", *Mathematical Biosciences*, **179**(1), pp. 73-94.

[55] Srividhya, J., and Gopinathan, M. S., 2003, "Modeling experimental oscillations in liquid membranes with delay equations", *Journal of Physical Chemistry B*, **107**(6), pp. 1438-1443.

[56] Gopalsamy, K., 1992, *Stability and Oscillations in Delay Differential Equations of Population Dynamics*, Kluwer Academic Publishers, Dordrecht.

[57] Szydlowski, M., and Krawiec, A., 2001, "The Kaldor-Kalecki model of business cycle as a two-dimensional dynamical system", *Journal of Nonlinear Mathematical Physics*, **8**, pp. 266-271.

[58] Tarng, Y. S., Young, H. T., and Lee, B. Y., 1994, "An analytical model of chatter vibration in metal cutting", *International Journal of Machine Tools and Manufacturing*, **28**, pp. 31-350.

[59] Fang, N., Jawahir, I. S., and Oxley, P. L. B., 2001, "A universal slip-line model with non-unique solutions for machining with curled chip formation and a restricted contact tool", *International Journal of Mechanical Sciences*, **43**, pp. 557-580.

[60] Taylor, F. W., 1907, "On the art of cutting metal", *Transactions of the American Society of Mechanical Engineers*, **34**(2), pp. 183-197.

[61] Wiercigroch, M., and Budak, E., 2001, "Sources of nonlinearities, chatter generation and suppression in metal cutting", *Proceedings of the Royal Society of London A*, **359**, pp. 663-693.

[62] Wiercigroch, M., 1997, "Chaotic vibration of a simple model of the machine tool cutting process system", *ASME Journal of vibration and Acoustics*, **119**, pp. 468-475.

[63] Grabec, I., 1988, "Chaotic dynamics of the cutting process", *International Journal of Machine Tools and Manufacturing*, **28**, pp. 19-32.

[64] Wiercigroch, M., and Krivtsov, A. M., 2001, "Frictional chatter in orthogonal metal cutting", *Proceedings of the Royal Society of London A*, **359**, pp. 713-738.

[65] Davies, M. A., and Burns, T. J., 1999, "The dynamics of chip formation in machining", in *New applications of Nonlinear and Chaotic Dynamics in Mechanics*, F. C. Moon (ed.), Kluwer Academics, Dordrecht, pp. 183-192.

[66] Davies, M. A., and Burns, T. J., 2001, "Thermomechanical oscillations in material flow during high speed machining", *Proceedings of the Royal Society of London A*, **359**, pp. 821-846.

[67] Pontryagin, L. S., 1955, "On the zeros of some elementary transcendental functions," *American Mathematical Society Translations*, Series 2, **1**, pp. 95-110.

[68] Hale, J. K., and Lunel, S. V., 1993, *Introduction to Functional Differential Equations*, Springer-Verlag, New York.

[69] Wahi, P., and Chatterjee, A., 2005, "Asymptotics for the characteristic roots of delayed dynamic systems", *ASME Journal of Applied Mechanics*, **72**(4), pp. 475-483.

[70] Wahi, P., and Chatterjee, A., 2002, "Computer Algebra for Characteristic Roots of Delay Differential Equations", presented at *First International Conference and Instructional Workshop on Industrial Mathematics*, Mumbai, India, December 06-10, 2002.

[71] Wahi, P., and Chatterjee, A., 2002, "On the characteristic roots of linear constant-coefficient DDE's", in *Proceedings of the 47th Congress of Indian Society of Theoretical and Applied Mechanics*, Dec 23-26, Guwahati, pp. 234-241.

[72] Wahi, P., and Chatterjee, A., 2004, "Averaging oscillations with small fractional damping and delayed terms", *Nonlinear Dynamics*, **38**, pp. 3-22.

[73] Wahi, P., and Chatterjee, A., 2005, "Galerkin projections for delay differential equations", *ASME Journal of Dynamic Systems, Measurement, and Control*, **127**(1), pp. 80-87.

[74] Wahi, P., and Chatterjee, A., 2003, "Galerkin projections for delay differential equations", in *Proceedings of the Ninteenth International ASME Biennial Conference on Mechanical Vibration and Noise*, Chicago, Illinois, USA, September 2-6, 2003.

[75] Wahi, P., and Chatterjee, A., 2004, "Performance of a Galerkin projection technique for DDEs", presented at *Tenth Conference on Nonlinear Vibrations, Stability, and Dynamics of Structures*, Blacksburg, VA, USA, July 25-28, 2004.

[76] Wahi, P., and Chatterjee, A., 2005, "Regenerative tool chatter near a codimension 2 Hopf point using multiple scales", *Nonlinear Dynamics*, **40**, pp. 323-338.

[77] Wahi, P., and Chatterjee, A., 2004, "Regenerative tool chatter near a codimension - 2 Hopf point", in *Proceedings of the Twenty-First International Congress of Theoretical and Applied Mechanics*, Warsaw, Poland, August 15-21, 2004.

[78] Bellman, R., and Cooke, K. L., 1963, *Differential Equations*, Academic press, New York.

[79] Driver, R. D., 1977, *Ordinary and Delay Differential Equations*, Springer-Verlag, New York.

[80] Stépán, G., 1989, *Retarded Dynamical Systems*, Longman Group, UK.

[81] Bhatt, S. J., and Hsu, C. S., 1966, "Stability criteria for second-order dynamical systems with time lag", *ASME Journal of Applied Mechanics*, **33**(1), pp. 113-118.

[82] Bhatt, S. J., and Hsu, C. S., 1966, "Stability charts for second-order dynamical systems with time lag", *ASME Journal of Applied Mechanics*, **33**(1), pp. 119-124.

[83] Hassard, B. D., 1997, "Counting roots of the characteristic equation for linear delay-differential systems", *Journal of Differential Equations*, **136**, pp. 222-235.

[84] Diekmann, O., Gils, S. V., Lunel, S. V., and Walther, H., 1995, *Delay equations: functional-, complex-, and nonlinear analysis*, Springer-Verlag, New York.

[85] Breda, D., Maset, S. and Vermiglio, R., 2004, "Computing the characteristic roots for delay differential equations", *IMA Journal of Numerical Analysis*, **24**, pp. 1-19.

[86] Engelborghs, K., and Roose, D., 2002, "On stability of LMS methods and characteristic roots of delay differential equations", *SIAM Journal of Numerical Analysis*, **40**(2), pp. 629-650.

[87] Sandquist, G. M., and Rogers, V. C., 1979, "Graphical solutions for the characteristic roots of the first order linear differential-difference equation", *SIAM Journal of Dynamic Systems, Measurements, and Control*, **101**, pp. 37-43.

[88] Minorsky, N., 1942, "Self-excited oscillations in dynamical systems possessing retarded actions", *ASME Journal of Applied Mechanics*, **9**), pp. A65-A71.

[89] Lam, J., 1993, "Model reduction of delay systems using Padé approximants", *International Journal of Control*, **57**(2), pp. 377-391.

[90] Wang, Z., and Hu, H., 1999, "Robust stability test for dynamic systems with short delays by using Padé approximation", *Nonlinear Dynamics*, **18**, pp. 275-287.

[91] Das, S. L., and Chatterjee, A., 2005, "Second order multiple scales for oscillators with large delay", *Nonlinear Dynamics*, **39**, pp. 375-394.

[92] Bagley, R. L., and Torvik, P. J., 1983, "A Theoretical basis for the application of fractional calculus to viscoelasticity", *Journal of Rheology*, **27**(3), pp. 201-210.

[93] Bagley, R. L., and Torvik, P. J., 1983, "Fractional calculus - A different approach to the analysis of viscoelastically damped structures", *AIAA Journal*, **21**(5), pp. 741-748.

[94] Bagley, R. L., and Torvik, P. J., 1985, "Fractional calculus in the transient analysis of viscoelastically damped structures", *AIAA Journal*, **23**(6), pp. 918-925.

[95] Koeller, R. C., 1984, "Application of fractional calculus to the theory of viscoelasticity", *ASME Journal of Applied Mechanics*, **51**, pp. 299-307.

[96] Kevorkian, J., and Cole, J. D., 1996, *Multiple Scales and Singular Perturbation Methods,* Springer-Verlag, New York.

[97] Plaut, R. H., and Hseih, J. C., 1987, "Nonlinear structural vibrations involving a time delay in damping", *Journal of Sound and Vibration*, **117**(3), pp. 497-510.

[98] Hu, H., Dowell, E. H., and Virgin, L. N., 1998, "Resonances of a harmonically forced duffing oscillator with time delay state feedback", *Nonlinear Dynamics*, **15**, pp. 311-327.

[99] Maccari, A., 2001, "The response of a parametrically excited van der Pol oscillator to a time delay state feedback", *Nonlinear Dynamics*, **26**, pp. 105-119.

[100] Li, G., Zhu, Z., and Cheng, C., 2001, "Dynamical stability of viscoelastic column with fractional derivative constitutive relation", *Applied Mathematics and Mechanics*, **22** (3), pp. 294-303.

[101] Sanders, J. A., and Verhulst, F., 1985, *Averaging Methods in Nonlinear Dynamical Systems*, Springer-Verlag, New York.

[102] Rossikhin, Y. A., and Shitikova, M. V., 1998, "Application of fractional calculus for analysis of nonlinear damped vibrations of suspension bridges", *Journal of Engineering Mechanics*, **124** (9), pp. 1029-1036.

[103] Chatterjee, A., 2003, "Harmonic balance based averaging: approximate realizations of an asymptotic technique", *Nonlinear Dynamics*, **32**, pp. 323-343.

[104] Oldham, K. B., and Spanier, J., 1974, *The Fractional Calculus - Theory and Applications of Differentiation and Integration to Arbitrary Order*, Academic Press, New York.

[105] Koh, C. G., and Kelly, J. M., 1990, "Application of fractional derivatives to seismic analysis of base-isolated models", *Earthquake Engineering and Structural Dynamics*, **19**, pp. 229-241.

[106] Yuan, L., and Agrawal, O. P., 1998, "A numerical scheme for dynamic systems containing fractional derivatives", *Proceedings of 1998 ASME Design Engineering Technical Conferences*, Atlanta, Georgia, September 13-16, 1998.

[107] Suarez, L. E., and Shokooh, A., 1997, "An eigenvector expansion method for the solution of motion containing fractional derivatives", *ASME Journal of Applied Mechanics*, **64**(3), pp. 629-635.

[108] Rand, R. H., 2001, *Lecture Notes on Nonlinear Vibrations*, version 36. Available online at http://tam.cornell.edu/randdocs/nlvibe36.pdf.

[109] Verhulst, F., 1990, *Nonlinear Differential Equations and Dynamical Systems*, Springer-Verlag, Berlin.

[110] Coppola, V. T., and Rand, R. H., 1990, "Averaging using elliptic functions : Approximation of limit cycles", *Acta Mechanica*, **81**, pp. 125-142.

[111] Engelborghs, K., 2000a, "DDE-BIFTOOL: a Matlab package for bifurcation analysis of delay differential equations", Technical Report TW-305, Department of Computer Science, Katholieke Universiteit Leuven, Leuven, Belgium. Available from *http://www.cs.kuleuven.ac.be/koen/delay/ddebiftool.shtml*.

[112] Engelborghs, K., 2000b, "Numerical bifurcation analysis of delay differential equations", *Ph.D. dissertation*, Department of Computer Science, Katholieke Universiteit Leuven, Leuven, Belgium.

[113] Bellen, A., and Zennaro, M., 1985, "Numerical solution of delay differential equations by uniform corrections to an implicit Runge-Kutta method", *Numerische Mathematik*, **47**, pp. 301-316.

[114] Cryer, C. W., 1974, "Highly stable multistep method for retarded differential equations", *SIAM Journal of Numerical Analysis*, **11**(4), pp. 788-797.

[115] Macdonald, N., 1995, "Harmonic Balance in delay-differential equations", *Journal of Sound and Vibration*, **186**(4), pp. 649-656.

[116] Gronbech-Jensen, N., Blackburn, J. A., Huberman, B. O., and Smith, H. J. T., 1992, "Josephson junction with delayed feedback", *Physics Letters A*, **172**, pp. 131-140.

[117] Saupe, D., 1983, "Global bifurcation of periodic solutions to some autonomous differential delay equations", *Applied Mathematics and Computation*, **13**, pp. 185-211.

[118] Layton, W., 1986, "The Galerkin method for the approximation of almost periodic solutions of functional differential equations", *Funkcialaj Ekvacioj*, **29**, pp. 19-29.

[119] Campbell, S. A., Bélair, J., Ohira, T., and Milton, J., 1995, "Complex dynamics and multi-stability in a damped harmonic oscillator with delayed negative feedback", *Chaos*, **5**(4), pp. 640-645.

[120] Fofana, M. S., 2001, "A unified framework for the study of periodic solutions of nonlinear delay differential equations", in *Proceedings of the DETC'01, ASME 2001 Design and Engineering Technical Conference and Computers and Information in Engineering Conference.* Pittsburgh, PA.

[121] Xu, J., and Lu, Q. S., 1999, "Hopf bifurcation of time-delay Lienard equations", *International Journal of Bifurcation and Chaos*, **9**(5), pp. 939-951.

[122] Wang, Z. H., and Hu, H. Y., 2001, "Dimensional reduction for nonlinear time-delayed systems composed of stiff and soft substructures", *Nonlinear Dynamics*, **25**, pp. 317-331.

[123] Faria, T., and Magalhaes, L. T., 1995a, "Normal forms for retarded functional differential equations and applications to Bogdanov-Takens singularity", *Journal of Differential Equations*, **122**, pp. 201-224.

[124] Faria, T., and Magalhaes, L. T., 1995b, "Normal forms for retarded functional differential equations with parameters and applications to Hopf bifurcation", *Journal of Differential Equations*, **122**, pp. 181-200.

[125] Faria, T., 1997, "Normal forms for periodic retarded functional differential equations", *Proceedings of the Royal Society of Edinburgh*, **127A**, pp. 21-46.

[126] Das, S. L., and Chatterjee, A., 2002, "Multiple scales without center manifold reductions for delay differential equations near Hopf bifurcations", *Nonlinear Dynamics*, **30**, pp. 323-335.

[127] Bayly, P. V., Halley, J.E., Mann, B. P., and Davies, M. A., 2003, "Stability of interrupted cutting by temporal finite element analysis", *ASME Journal of Manufacturing Science and Engineering*, **125**, pp. 220-225.

[128] Insperger, T., and Stépán, G., 2002, "Semi-discretization method for delayed systems", *International Journal for Numerical Methods in Engineering*, **55**, pp. 503-518.

[129] Insperger, T., 2002, "Stability analysis of periodic delay-differential equation modeling machine tool chatter", *Ph.D. dissertation*, Department of Applied Mechanics, Budapest University of Technology and Economics, Budapest, Hungary.

[130] Breda, D., Maset, S. and Vermiglio, R., 2001, "Numerical computation of characteristic roots for delay differential equations", in *Proceedings of the 3rd IFAC Workshop on Time Delay Systems*, Santa Fe, New Mexico (U.S.A.).

[131] Asl, F. M., and Ulsoy, A. G., 2003, "Analysis of a system of linear delay differential equations", *ASME Journal of Dynamic Systems, Measurement, and Control*, **125**, pp. 215-223.

[132] Sipahi, R., and Olgac, N., 2003, "Direct method implementation for the stability analysis of multiple time delayed systems", *Proceedings of 2003 IEEE Conference on Control Applications*, **1**, pp. 943-948.

[133] Engelborghs, K., and Roose, D., 1999, "Numerical computation of stability and detection of Hopf bifurcations of steady state solutions of delay differential equations", *Advances in Computational Mathematics*, **10**, pp. 271-289.

[134] Natarajan, V., and Chatterjee, A., 2005, "Finite elements for delay differential equations", *Unpublished Work*.

[135] Chatterjee, A., 2000, "An introduction to the proper orthogonal decomposition", *Current Science*, **78**(7), pp. 808-817.

[136] Cusumano, J. P., Sharkady, M. T., Kimble, B. W., 1994, "Experimental measurements of dimensionality and spatial coherence in the dynamics of a flexible-beam impact oscillator", *Proceedings of the Royal Society of London A*, **347**, pp. 421-438.

[137] Cazemier, W., Verstappen, R. W. C. P., and Veldman, A. E. P., 1998, "Proper orthogonal decomposition and low-dimensional models for driven cavity flows", *Physics of Fluids*, **10**(7), pp. 1685-1699.

[138] Yu, P., 2002, "Analysis on double Hopf bifurcation using computer algebra with the aid of multiple scales", *Nonlinear Dynamics*, **27**, pp. 19-53.

[139] Lewis, G. M., and Nagata, W., 2003, "Double Hopf bifurcations in the differentially heated rotating annulus", *SIAM Journal of Applied Mathematics*, **63**(3), pp. 1029-1055.

[140] Marques, F., Lopez, J. M., and Shen, J., 2002, "Mode interactions in an enclosed swirling flow: a double Hopf bifurcation between azimuthal wavenumbers 0 and 2", *Journal of Fluid Mechanics*, **455**, pp. 263-281.

[141] Moroz, I. M., and Brindley, J., 1982, "An example of two-mode interaction in a three-layer model of baroclinic instability", *Physics Letters A*, **91**(5), pp. 226-230.

[142] Cox, S. M., Leibovich, S., Moroz, I. M., and Tandon, A., 1992, "Hopf bifurcations in Langmuir circulations", *Physica D*, **59**, pp. 226-254.

[143] Davies, A., and Balachandran, B., 2000, "Impact dynamics in the milling of thin-walled structures", *Nonlinear Dynamics* **22**, pp. 375-392.